Protein Adsorption and Transport Kinetics in Novel Stationary Phases for Protein
Chromatography Based on the UNOsphere Architecture

A Dissertation

Presented to

the faculty of the School of Engineering and Applied Science

University of Virginia

---

in partial fulfillment

of the requirements for the degree

Doctor of Philosophy

by

Ernie X. Perez Almodovar

May

2012

APPROVAL SHEET

The dissertation
is submitted in partial fulfillment of the requirements
for the degree of
Doctor of Philosophy
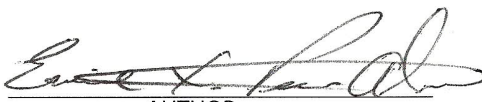
_____
AUTHOR

The dissertation has been read and approved by the examining committee:
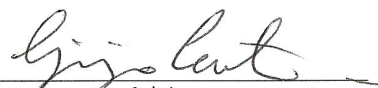
_____
Advisor

_____

_____

_____

_____

_____
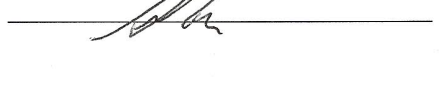
Accepted for the School of Engineering and Applied Science:
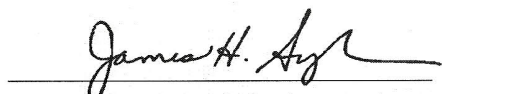
_____
Dean, School of Engineering and Applied Science

May
2012

Abstract

This work examines protein adsorption equilibrium and transport kinetics in a new class of stationary phases for protein chromatography based on a hydrophilic macroporous polymer bead, known as UNOsphere (Bio-Rad Laboratories, Hercules, CA), that possesses improved protein adsorption capacity, kinetics, and mechanical strength. Three different materials are considered: UNOsphere SUPrA, a protein A matrix, UNOsphere S, a cation exchanger based on a short ligand chemistry, and Nuvia S, which is based on essentially the same backbone matrix but contains grafted charged polymeric surface extenders.

The results for UNOsphere SUPrA show rapid IgG adsorption kinetics, which results primarily from the large-pore size and small particle size afforded by the relative rigidity of the UNOsphere backbone. A comprehensive model taking into account IgG binding on a distribution of protein A ligands with different accessibility was developed to describe IgG adsorption in batch and column systems. Coupled with a newly developed model describing the pressure-flow relationship in large diameter columns, the binding kinetics model allows rational design of process-scale units that maximize productivity while meeting specified pressure constrains.

The results for Nuvia S show that the backbone pores are essentially completely filled with a gel-phase formed by the grafted charged polymeric surface extenders. This phase is inaccessible by neutral macromolecules but provides readily accessible binding sites for adsorption of both small (e.g. lysozyme) and large (e.g. IgG) positively charged giving very high binding capacities. The adsorption kinetics of these proteins is also fast in Nuvia S, apparently as a result of a solid diffusion mechanism. Compared to UNOsphere S, which has large open pores, Nuvia S exhibits more than twice the protein binding capacity and much faster adsorption rates. For Nuvia S, however, the adsorption kinetics is a strong function of the protein type and charge, and of the nature of the counterion indicating that binding strength, which is strongly affected by these characteristics, is correlated with transport rates. A model was developed to describe protein adsorption kinetics in Nuvia S for single and multicomponent systems based on batch

adsorption and confocal microscopy measurements of intraparticle protein concentration profiles. The model, based on a Maxwell-Stefan description of diffusion fluxes, predicts, in agreement with the experimental data, rapid kinetics for the adsorption of a single protein on a clean particle and for the simultaneous adsorption of two or more proteins. Very slow rates are predicted, however, also in agreement with experimental data, when two proteins counterdiffuse within the particle as a result of the apparent inability of adsorbed protein molecules to pass each other in the spatially-constrained network defined by the grafted charged polymers.

Acknowledgements

I would like to thank my advisor, Giorgio Carta for his tolerance, and guidance throughout this project. You really made my time at University of Virginia one full of challenges and great memories. Thank you for believing in me and pushing me to be a better scientist and graduate student everyday.

I appreciate the assistance of my advisory committee members Prof. Gordon Laurie, Prof. Roseanne Ford, Prof. Inchan Kwon and Prof. John L. Hudson. Thanks for the valuable input and discussions.

Bio-Rad Laboratories supported this work and I would like to thank the following members: Mark Snyder, Russ Frost, Larry Cummings, Chris Foster and Kim Brisack. I want to also acknowledge the support from the NIH biotechnology training program and the program members. It was great to meet each of you and learn about other research activities on grounds.

Also, I want to thank all past and present members of the bioseparation group for the great discussions and help in the lab - Tim, Melani, Theresa, Yinying, Joe C., Chenny, Yige, Tarl, Bianca, Laura, Brian, Jessica, Gonül, Drew, Frank, and Mimi. I hope that you had as much of a blast as I did working with each of you.

To my UVa friends and classmates: Oliver, Howard, Carolina, Griselle, Ruthy, Arnaldo, Lydia, Simpson, Brittany, Tony, Jason, Xiaopu, Joe C., Sara, Joe K., David, Emily, Adrian,

Rose, Gerardo and Kristie, thanks for all the great times, for all your help on my struggles, advice, and more. To my girlfriend Olia thanks for your support and your words during this time.

Many thanks to the staff of the Chemical Engineering Department: Ricky, Vickie, Margaret, Teresa, and Kim you made a big difference in my life and it was my pleasure to work with you.

Finally, I would like to thank my family. To my parents (Lesbia, and Julio), thank you for believing in me and encouraging me to complete my PhD. To my brothers (Julio, Delvis and Luis) thanks for being there for me and for having the patience to have me far away for so long. To Erasmo Asencio and Doña Paquita: I am very lucky to have you in my life. To the rest of my family and friends in the world, thanks a lot for always keeping in touch and for the good times outside of the lab.

Table of Contents

List of Figures

List of Tables

Chapter 1

Motivation and Background

1.1. Motivation

Advances in fermentation and cell culture techniques used for the production of therapeutics proteins have shifted production constraints from upstream to the downstream purification processes. While theoretically feasible at very large scales [1], biopharmaceutical purification by chromatography remains challenging because column size is typically limited by mechanical and technological factors as well as the space constraints of GMP manufacturing suites. Overcoming these size constraints requires the development of alternative stationary phases that have higher protein binding capacities, faster adsorption kinetics, and high mechanical strength [2]. Many of the commonly used stationary phases for protein capture and purification are based on protein-A or ion exchange interaction and rely on the affinity or electrostatic interaction respectively between the protein and the surface.

Base matrices used to produce protein A and ion exchange adsorbents include inorganic materials, natural polymers, and synthetic polymers [3,4]. Inorganic materials like silica gel or porous glass are mechanically very strong but are not stable in alkaline solutions that are preferred for sanitation and cleaning. Natural polymers like cellulose, agarose, and dextran are often used. Their advantage is that they are highly hydrophilic and, thus, have low non-specific binding. The disadvantage of these softer materials is that they are compressible imposing limits to the attainable flow velocities. Synthetic polymers like polystyrene-divinylbenzene, while rigid, exhibit substantial non-specific binding of proteinaceous impurities because of their

hydrophobicity. However, other synthetic polymers based on polymethacrylates or polyacrylamide are hydrophilic, but have lower surface areas and, hence, lower binding capacities than those of natural polymers. These materials present a potentially valuable alternative to soft gels but surface modifications are needed to improve binding capacity. Moreover, compared to soft gels, these materials permit using smaller particles resulting in faster adsorption kinetics. Thus, alternative support matrices are desirable.

A new approach that is being studied to improve binding capacity and potentially adsorption kinetics in ion exchange media is the introduction of polymeric "surface extenders" in a porous framework [5]. Tethering charged polymers to the surface can enhance binding capacity by providing greater accessibility of the protein to the charged functional groups. This has been obtained with grafted dextran polymers as demonstrated for both experimental [6] and commercial [5,7] materials. A surprising result accompanying this increased capacity has been increased adsorption kinetics by as much as 10 times. The mechanisms underlying this effect are not completely understood but it has been hypothesized that, for certain conditions, protein molecules adsorbed through favorable interactions with the surface extenders retain diffusional mobility [8]. Although low, this mobility coupled with the high concentration driving force made possible by the large binding capacity results in rapid adsorption kinetics. While this hypothesis is qualitatively consistent with experimental observations, several open questions remain regarding the underlying transport mechanism for both single and multicomponent protein adsorption, for desorption, and with regards to the effects of counterion type.

The overall objective of this work is thus to investigate two newly developed chromatographic materials: UNOsphere SUPrA and Nuvia S. Both are based on hydrophilic acrylamide and vinyl copolymers forming a relatively rigid macroporous network which

provides low non-specific binding. In the case of UNOsphere SUPrA, the pore network is open allowing coupling of recombinant protein A as a ligand for the selective adsorption of immunoglobulin (e.g. IgG). The mechanical strength of the matrix allows using a smaller particle size, which result is faster adsorption kinetics. Nuvia S, on the other hand, is based on a similar polymeric backbone but its surface is functionalized with charged polymeric extenders providing favorable cation exchange interactions with oppositely charged proteins. Chapter 2 describes the results for UNOsphere SUPrA with two main objectives. The first is to characterize the adsorption equilibrium and kinetics and to develop a model to accurately predict the breakthrough behavior. The second objective is to obtain pressure flow curves in laboratory and large-scale columns and to develop a model to predict column pressure. Chapter 3, 4 and 5 are devoted to Nuvia S focusing on the effects of charged polymeric surface extenders on protein adsorption capacity and transport.

1.2. Background

1.2.1 Principles of adsorption of monoclonal antibodies on Protein A adsorbents

Antibodies are proteins produced by living organisms in response to an antigen. Our body has the capability of producing between 10^6 and 10^8 types of antibodies, each of them with the capacity to bind a different antigen [9]. An antigen is any foreign agent that is capable of eliciting such immunogenic response. Examples of common antigens are bacteria, virus particles, and proteins that are foreign to the organism. The basic structure of an antibody is shown in Fig. 1.1. It consists of four polypeptides linked by disulfide bonds. Two are heavy chains and two are light chains, each pair having the same primary structure. Digestion of antibodies with the enzyme papain produces two identical antigen-binding fragments (Fab) and one single crystallizable fragment, which represents the constant region (Fc-region) of the antibody. It is in
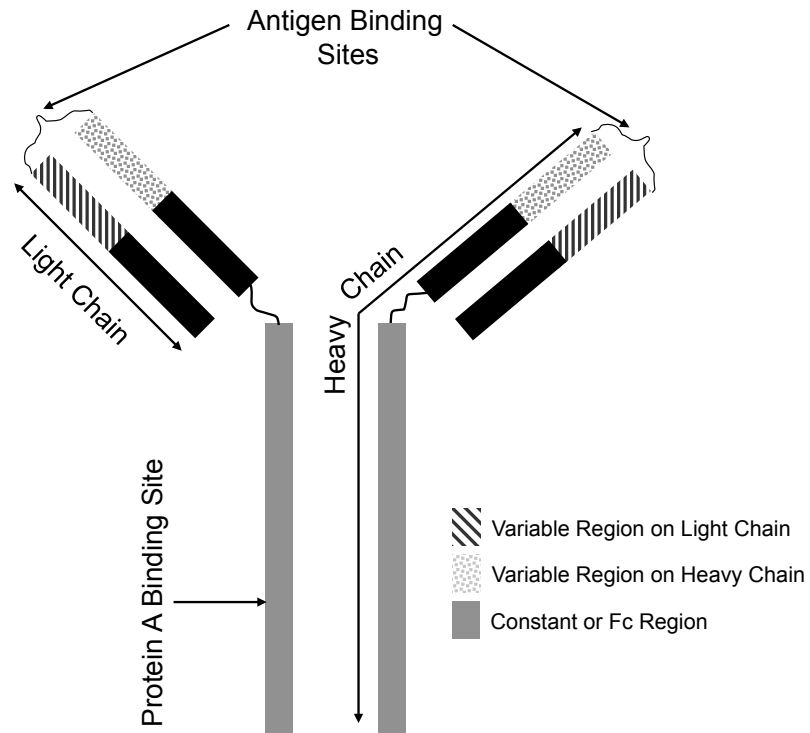
Fig. 1.1. Antibody structure, identification of each of the parts were made for better interpretation.

this region where binding of protein A occurs. Thus, different antibodies from the same clan but with different variable regions (Fab-region) will all bind to protein A. As a result adsorbents using immobilized protein A as a ligand to adsorb IgG can be used for generic or "platform" processes suitable for the purification of many different antibodies in the same clan.

Protein A is a type I cell wall-associated protein expressed on the surface of the bacterium *Staphylococcus aureus*. Protein A has high affinity to IgG from various species including human, rabbit and guinea pig [10]. On the other hand, Protein A does not bind all subclasses of IgG. For example human IgG3, mouse IgG3, sheep IgG1, bind only weakly or not at all. Wild type protein A contains five binding domains for the Fc-region of IgG that are known as A, B, C, D, and E. Recombinant versions of protein A exist and are available commercially and are typically used to produce adsorbents for industrial use.

The base matrix used to immobilize protein A plays an important role. Inertness, chemical stability, mechanical stability, pore size and particle size are the most important characteristics [3]. Inertness is necessary to avoid non-specific binding of other components. In general, this requires that the material be hydrophilic, to avoid hydrophobic interactions with additional proteins and uncharged in order to avoid ionic interactions. Chemical stability is needed to withstand sanitizing cleaning agents, usually acids and/or bases. Mechanical stability is needed to prevent swelling and shrinking in response to changes in operating conditions and to allow operations at high flow rates and with viscous feeds. The pore size of the support matrix must allow unhindered access to the antibody, and provide sufficient space for the antibody-protein A interaction. Finally, particle size is critical since it affects the overall mass transfer rate and the column dynamic binding capacity. Smaller values obviously improve mass transfer, but lead to higher pressures. Thus, particle size needs to be optimally chosen.

1.2.2 Transport mechanism in Protein A adsorbents

Adsorption of an antibody on a protein A adsorbent is potentially affected by three resistances:

1. Boundary layer mass transfer at the particle surface;

2. Diffusion within the particle pores; and

3. Kinetic resistance to binding of the antibody onto the protein A ligand.

Rate equations for each of these three mechanisms are as follows [11]:

Boundary layer mass transfer

$$J = k_f (C^* - C_s) \tag{1.1}$$

Pore Diffusion

$$J = -D_e \frac{\partial c}{\partial r} \tag{1.2}$$

Binding Kinetics

$$\frac{dq}{dt} = k\left(c(q_m - q) - \frac{q}{K}\right) \tag{1.3}$$

In these equations, J is the main transfer flux, k_f is the film mass transfer coefficient, C^* and C_s are the antibody concentration in the bulk fluid and at the particle surface, c is the antibody concentration in the particle pores, D_e is the effective pore diffusivity of the antibody, and k and K are the binding rate constant and equilibrium constant, respectively. q and q_m are the concentrations of bound antibody and the maximum binding capacity, respectively.

Several authors [12-14] have assumed that the binding kinetics is sufficiently fast that local equilibrium can be assumed to exist within the pores. In this case, setting $dq/dt=0$, eq. 1.3 yields:

$$q^* = \frac{q_m Kc}{1 + Kc} \tag{1.4}$$

which is analogous to the Langmuir isotherm. Accordingly, the adsorption kinetics in spherical

particles is described by the following equations and boundary conditions:

$$\varepsilon_p \frac{\partial c}{\partial t} + (1 - \varepsilon_p) \frac{\partial q^*}{\partial t} = \frac{D_e}{r^2} \frac{\partial}{\partial r}\left(r^2 \frac{\partial c}{\partial r}\right) \tag{1.5}$$

$$t=0 \ c=0 \ q=0 \tag{1.6}$$

$$r=0 \ \frac{\partial c}{\partial r} = 0 \tag{1.7}$$

$$r=r_p \quad D_e \frac{\partial c}{\partial r} = k_f(C - C_s) \tag{1.8}$$

where r_p is the particle radius, ε_p is the intraparticle porosity, $c|_{r=r_p} = C_s$, and

$$\frac{\partial q^*}{\partial t} = \frac{q_m K}{(1 + Kc)^2} \frac{\partial c}{\partial t} \tag{1.9}$$

When adsorption occurs in a finite bath, mixed batch vessel, eqs. 1.5-1.9 are coupled to the

following material balance:

$$\frac{dC}{dt} = -\frac{3k_f}{r_p} \frac{V_m}{V}(C - C_s) \tag{1.10}$$

$$t=0 \ C=C_0 \tag{1.11}$$

V_m and V are the volumes of particles and solution, respectively, and C_0 is the initial antibody

concentration in the bulk fluid. In general, a numerical algorithm is needed to solve these

coupled equations. Analytical solutions are available for limiting cases where the isotherm is

either linear ($KC_0 \ll 1$) or rectangular ($KC_0 \gg 1$) and are available in LeVan and Carta [11].

When adsorption occurs in a packed bed column, eqs. 1.5 to 1.9 are coupled to the following differential material balance and boundary conditions:

$$\varepsilon \frac{\partial C}{\partial t} + (1-\varepsilon)\frac{\partial \bar{q}}{\partial t} + \varepsilon v \frac{\partial C}{\partial z} = \varepsilon D_L \frac{\partial C}{\partial z} \tag{1.12}$$

$$t=0, C=0 \tag{1.13}$$

$$z=0, C=C_F \tag{1.14}$$

where ε is the extraparticle porosity, v is the fluid velocity, z is the axial coordinate, D_L is the axial dispersion coefficient and C_F is the feed antibody concentration. $\bar{q}$ is the average antibody concentration in the particle and is given by:

$$\frac{\partial \bar{q}}{\partial t} = \frac{3k_f}{r_p}(C - C_s) \tag{1.15}$$

A numerical algorithm is needed again to solve eqs. 1.5-1.9 and 1.12-1.15 for the general case. Limiting solutions are again available for linear isotherm case ($KC_0 \ll 1$) and for the rectangular isotherm case ($KC_0 \gg 1$) when $\varepsilon D_L \rightarrow 0$ [11].

1.2.3. Ion exchange chromatography

Chromatography separates proteins by taking advantage of differences in various physiochemical characteristics such as charge, size, hydrophobicity, and affinity. Ion exchange chromatography (IEC), which exploits charge differences, is used in more than 70% of industrial protein purification processes [15]. IEC has been widely used in protein purification for decades due to its relatively low costs, high capacity, high resolution, and scalability. Another feature of IEC, especially important for therapeutic applications, is the ability to operate under non-denaturing conditions [16].

In general, IEC can attain high protein binding capacities with soft gels, but these tend to have poor mechanical properties. These stationary phases are often made from cellulose, agarose, or dextran [3,4]. On the other hand, rigid porous media made from silica, methylmethacrylate, or other polymers have excellent flow properties [17-20], but have limited binding capacity. The ideal stationary phase would utilize the inherent advantages of each type of backbone. Composite matrices in which a soft-gel or grafted polymers are incorporated into a rigid support structure are of interest, since they exhibit the desirable characteristics of both materials, resulting in high capacity and excellent mechanical properties.

Several composite chromatographic matrices have been developed in recent years, including silica-dextran matrices [3], HyperD matrices, which incorporate a charged polyacrylamide gel in the pores of macroporous silica or ceramic beads [3,18,19], and grafted agarose matrices where ionically-functionalized carbohydrate polymers are attached to an agarose backbone [21,22]. The high binding capacity achieved with these materials can be explained by the increased interaction between the protein and the flexible charged polymers which provide a greater surface area and allow multilayer binding to occur [23].

Salts play an important role in IEC because counter ions compete with the protein for the binding sites. For this reason salt is used to adjust binding strength and facilitate elution [24]. Stone and Carta [25], in a study comparing dextran grafted stationary phases to those with short ligands, concluded that the transport rate for lysozyme decreases as the ionic strength is increased and suggest that electrostatic coupling of diffusional fluxes may play a role in the adsorption kinetics. However, the relationship between ionic strength, stationary phase composition, and the transport mechanism is not well understood, and more should be done to

understand if electrostatic coupling of diffusional fluxes is the responsible mechanism for transport in polymer grafted materials.

1.2.4. Transport mechanisms in ion exchange media

The kinetics of protein adsorption and desorption is typically dominated by intraparticle mass transfer. However, extraparticle effects can be in some cases important when the protein concentration is very low [26]. Diffusional transport of proteins in IEC stationary phases can occur through different mechanisms. "Pore diffusion" and "solid diffusion" are extreme cases, but combination are of course possible. The driving force for pore diffusion is the concentration gradient in protein concentration in the liquid contained within the pores. This mechanism has been observed to be dominant in resins with an open pore structure such as POROS 50, UNOsphere S, and SP-Sepharose-FF [7,19,27]. An estimate of the effective diffusivity for a protein in these macroporous matrices can be obtained using the following equation:

$$D_e = \frac{\psi_p D_0 \varepsilon_p}{\tau} \tag{1.16}$$

where ψ_p is the hindrance factor, D_0 the free solution diffusivity, ε_p the intraparticle porosity and τ a tortuosity factor. When the adsorption isotherm is highly favorable, the pore diffusion model will predict sharp intraparticle concentration profiles [6].

The driving force for solid diffusion is instead the gradient in adsorbed protein concentration. In this case the protein moves either by sliding along a surface or hopping between exchange sites without escaping from the electrostatic interactions with the charged functional groups. The solid diffusion model predicts a smooth and diffuse profile within the particle where protein molecules reach the center of the particle quickly but approach equilibrium only slowly. A significant number of publications have reported observing this behavior in IEC chromatographic media [28-30]. Generally the investigated stationary phases are

composite resins that incorporate a soft gel phase within a rigid porous structure or dextran polymers grafted onto an agarose base matrix. In other cases, parallel diffusion has been proposed as the mechanism responsible for very fast uptake rates. Even if parallel diffusion can describe very fast protein uptake, Stone and Carta [25] have suggested that other mechanisms such as the Nernst-Planck effect can be responsible for the fast adsorption of proteins observed in composite media.

The separation of a mixture of proteins is the final goal in chromatography, making multicomponent models a necessity for accurately describing actual separations. If pore diffusion is the dominant mechanism (macroporous resin) for the multicomponent adsorption, the displacement of an adsorbed protein by another should happen very fast. This situation was investigated by Tao et al. [7] who explored both simultaneous and sequential adsorption of two deamidated mAbs with different binding strengths for UNOsphere S. The process was described as a continuous displacement where the more weakly bound species diffuse toward the center of the particle ahead of the more strongly bound component. This behavior has also been observed for the system of cytochrome c and lysozyme in SP-Sepharose-FF [31]. Although a very fast displacement is observed for macroporous stationary phases, a different behavior is expected when transport occurs in the adsorbed phase (solid diffusion).

If solid diffusion is the dominant transport mechanism, the protein molecules transfer rapidly from an occupied adsorption site to an adjacent empty site as shown schematically in Fig. 1.2a, producing diffuse profiles under microscopic observation. In this case the behavior will be similar whether only one protein is adsorbed or two or more proteins are simultaneously co-adsorbed. However, sequential adsorption where a preadsorbed weakly bound protein is displaced by a more strongly bound one should be much slower because the displaced protein

molecules do not have any available exchange sites (Fig. 1.2b). Tao et al. [32] observed this behavior for the adsorption of mAb variants in Capto S, a dextran grafted cation exchanger. This behavior can be explained with Fig. 1.2b, which shows that the mAb B can displace mAb A but inter-site transfer can't occur because the next binding site is occupied. Here transport will occur in a "single file diffusion" (SFD) fashion where diffusion will be dependent on occupancy of the adsorption sites. This model has been described for adsorption in zeolitic structures [33-38], but has been extended to protein adsorption by Tao and Carta [39].

1.2.5. Experimental techniques to study protein transport in ion exchangers

Several experimental techniques are available for the study of protein adsorption and desorption and can be divided into two categories: macroscopic and microscopic techniques. Macroscopic methods include batch uptake and column dynamic experiments. In both cases, mass balances are used to relate the experimentally observed behavior to a mechanistic model. These techniques provide information regarding the rates at which proteins are adsorbed or desorbed. However since the macroscopically observed behavior is generally insensitive to the nature of the mechanism chosen to represent the rate, it is not possible to discriminate among potential transport modes [20,40].

On the other hand, microscopic methods involve a determination of protein concentration profiles in the stationary phase. In this case, it is still necessary to compare the experimental results with a mechanistic model. However, the behavior is expected to depend strongly on which particular mechanism is assumed. For example, when the adsorption isotherm is rectangular or highly favorable the pore diffusion mechanism predicts a sharp intraparticle protein concentration profile [41], while the solid diffusion mechanism predicts diffuse profiles [28,41].
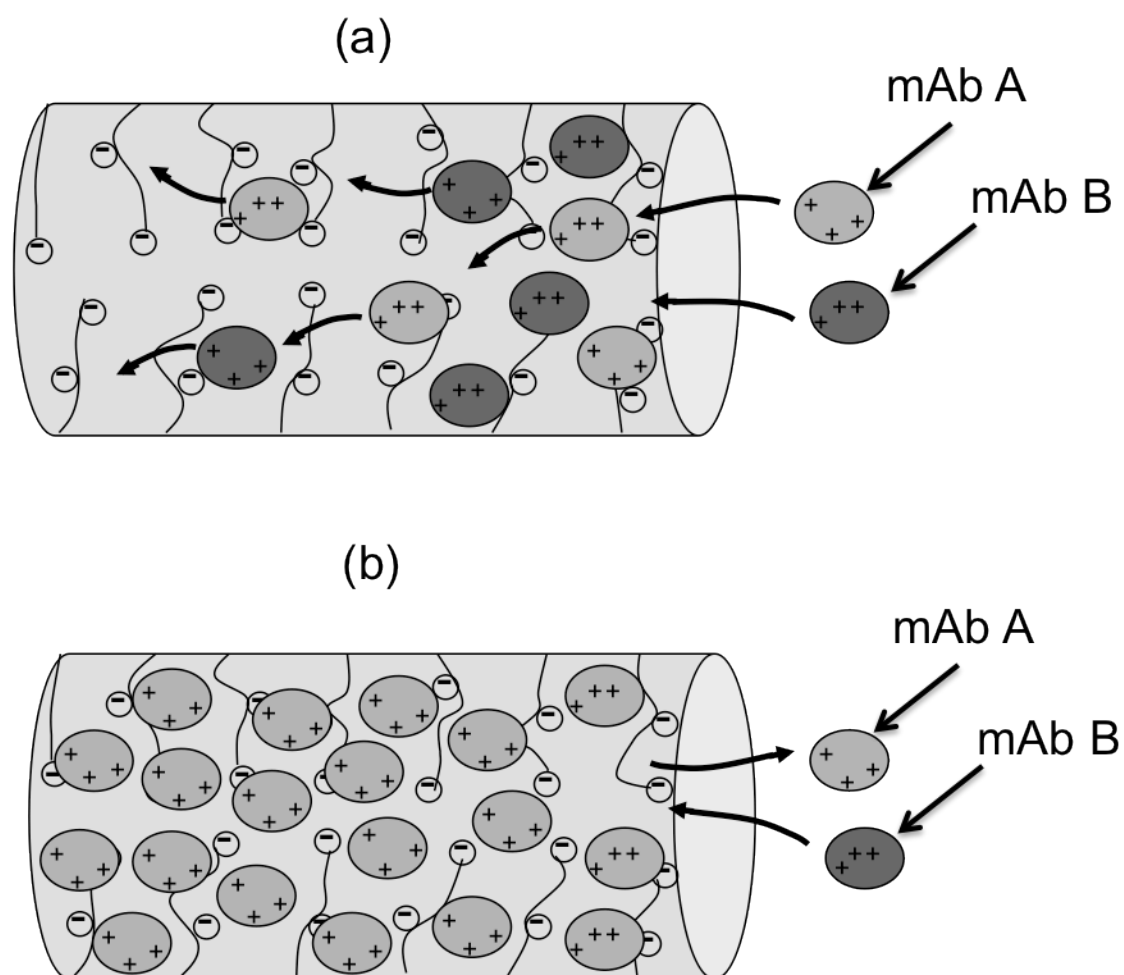
Figure 1.2. Drawing of (a) solid diffusion hopping mechanism for the coadsorption of two mAbs with different binding affinity and (b) sequential adsorption of two mAbs with different binding affinity where no binding sites are available for the molecule to hop.

Refractive index based microscopy (RIB) and confocal laser scanning microscopy (CLSM) have been used in recent years to observe intraparticle profiles for different stationary phases. RIB microscopy exploits the difference in refractive index of the protein-free and protein-saturated adsorbent matrix providing a view of the advancing interface when the adsorption front is sharp using an ordinary light microscope. RIB microscopy can be implemented with unmodified proteins. However, it is limited to one component adsorption and can only be used when the adsorption front is sharp [42]. CLSM requires a tracer obtained by conjugating a fluorescent dye to the protein and uses a special microscope that collects the fluorescent light emitted only by a thin optical section of the adsorbent particle by the tracer [43]. Some of the challenges presented by CLSM are that the labeled protein can interact differently with the stationary phase and the presence of signal attenuation caused light adsorption and light scattering, especially when the particles are opaque. If the labeled protein has a different affinity for the stationary phase than the native one, the fluorescent intensity profiles are disturbed and no longer represent the true intraparticle protein concentration profile [44,45]. For IEC, it has been shown that some dyes can have a great effect on the protein-surface interaction [29,46] while others, especially those with zero net charge, have minimal effects [39,47,48]. The signal attenuation and light scattering can also be significant problems. Attenuation correction equations based on both theoretical [49] and empirical approaches [50] have been developed to account for this effect.

1.3. List of symbols

c protein concentration in particle pores (mg/mL)

C^* protein concentration in solution (mg/mL)

C_s protein concentration at the particle surface (mg/mL)

D_e effective pore diffusivity (cm^2/s)

D_L axial dispersion coefficient (cm^2/s)

D_0 free solution diffusivity (cm^2/s)

K adsorption constant in Langmuir model (mL/mg)

k_f film mass transfer coefficient (cm/s)

q adsorbed protein concentration (mg/mL)

$q*$ adsorbed protein concentration in Langmuir model (mg/mL)

q_m maximum adsorption capacity in Langmuir model (mg/mL)

r radius (cm)

r_p particle radius (cm)

t time (s)

v interstitial mobile phase velocity (cm/s)

V volume of solution (mL)

V_m volume of particles (mL)

Greek Symbols

ε extraparticle porosity

ε_p intraparticle macroporosity

τ tortuosity factor for pore diffusion

ψ_p hindrance parameter for pore diffusion

1.4. References

[1]   J.J. Kelley, G. Wang, H. Wang. ACS Symposium Series 14 (1986) 193.

[2]   P. Gagnon, Bioprocess Int. 8 (2010) 22.

[3]   E. Boschetti, J. Chromatogr. A 658 (1994) 207.

[4]   M. Leonard, J. Chromatogr. B 699 (1997) 3.

[5]   E. Müller, J. Chromatogr. A 1006 (2003) 229.

[6]   M.C. Stone, G. Carta, J. Chromatogr. A 1146 (2007) 202.

[7]   Y. Tao, G. Carta, G. Ferreira, D. Robbins, J. Chromatogr. A 1218 (2011) 1530.

[8]   A.M. Lenhoff, Langmuir 24 (2008) 5991.

[9]   I. Roitt, P. Delves, Essential Immunology, Wiley, New York, 2001.

[10]   D. Richman, P. Cleveland, M. Oxman, K. Johnson, J. Immunol., 128 (1982), 2300.

[11]   M.D. LeVan, G. Carta, in: D.W. Green, R.H. Perry (Eds.), Perry's Chemical Engineers'

        Handbook, Section 16: Adsorption and Ion Exchange, eighth ed., McGraw-Hill, New

        York, 2007.

[12]   J. McCue, G. Kemp, D. Low, I. Quinones-Garcia, J. Chromatogr. A, 989 (2003) 139.

[13]   B. H. Arve, A. I. Liapis, Biotechnol. and Bioeng., 30 (1987) 638.

[14]   R. Hahn, R. Schlegel, A. Jungbauer, J. Chromatogr. B, 790 (2003) 35.

[15]   C. Wang, L. Wang, X. Geng, Biomed. Chromatogr. 12 (2007) 1291.

[16]   L. Bai, S. Burman, L. Gledhill, J. Pharm. And Biomed. Anal. 22 (2000) 605.

[17]   J. Horvath, E. Boschetti, L. Guerrier, N. Cooke, J. Chromatogr. A 679 (1994) 11.

[18]   M.A. Fernandez, G. Carta, J. Chromatogr. A 746 (1996) 169.

[19]   L.E. Weaver, G. Carta, Biotechnol. Prog. 12 (1996) 342.

[20]   E.X. Perez-Almodovar, G. Carta, J. Chromatogr. A 1216 (2009) 8348.

[21]   J. Thommes, Biotechnol. Bioeng. 62 (1999) 358.

[22]   A. Staby, I. H. Jensen, J. Chromatogr. A 908 (2001) 149.

[23]   B.D. Bowes, H. Koku, K.J. Czymmek, A.M. Lenhoff, J. Chromatogr. A 1216 (2009)

        7774.

[24]   J.X. Huang, G. Guiochon, J. Chromatogr. A 492 (1989) 431.

[25]   M.C. Stone, Y. Tao, G. Carta, J. Chromatogr. A 1216 (2009) 4465.

[26]   R.K. Lewus, G. Carta, J. Chromatogr. A 865 (1999) 155.

[27]   A.R. Ubiera, G. Carta, Biotechnol. J. 1 (2006) 665.

[28]   S.R. Dziennik, E.B. Belcher, G.A. Barker, M.J. DeBergalis, S.E. Fernandez, A.M. Lenhoff, PNAS. 100 (2003) 420.

[29]   C.A. Teske, M. Schroeder, R. Simon, J. Hubbuch. J. Phys. Chem. B 109 (2005) 13811.

[30]   Y. Tao, G. Carta, G. Ferreira, D. Robbins, J. Chromatogr. A 1218 (2011) 1530.

[31]   C. Martin, G. Iberer, A. Ubiera, G. Carta, J. Chromatogr. A 1079 (2005) 105.

[32]   Y. Tao, E.X. Perez-Almodovar, G. Carta, G. Ferreira, D. Robbins, J. Chromatogr. A 1218 (2011) 8027.

[33]   W.R. Qureshi, J. Wei. J. Catalysis 126 (1990) 126.

[34]   W.R. Qureshi, J. Wei. J. Catalysis 126 (1990) 147.

[35]   J.G. Tsikoyiannis, J. Wei, Chem. Eng. Sci. 46 (1991) 233.

[36]   K.D. Dahlke, G. Emig. Catal. Today 8 (1991) 439.

[37]   J. Wei, Ind. Eng. Chem. Res. 33 (1994) 2467.

[38]   L.J.P. Van den Broeke, AIChE J. 41 (1995) 2399.

[39]   Y. Tao, N. Chen, G. Ferreira, D. Robbins, G. Carta, AIChE J. (2011) DOI 10.1002/aic.1371.

[40]   W.D. Chen, X.Y. Dong, Y. Sun. J. Chromatogr. A 962 (2002) 29.

[41]   G. Carta, A. Jungbauer. "Protein chromatography: Process development and Scale-up" Wiley-VCH, Weinheim, Germany (2010).

[42]   T.E. Bankston, M.C. Stone, G. Carta, J.Chromatogr. A 1188 (2008) 242.

[43]   M.G. Kula, J. Hubbuch. Bioprocess Biosyst. Eng. 31 (2008) 241.

[44]   G. Carta, A.R. Ubiera, T.M. Pabst, Chem. Eng. Technol. 28 (2005) 1252.

[45]   C.A. Teske, E. von Lieres, M. Schroeder, A. Ladiwala, S.M. Cramer, J. Hubbuch, Biotechnol. Bioeng. 95 (2006) 58.

[46]   A. Ljunglof, K.M. Lacki, J. Mueller, C. Harinarayan, R. Reis, R. Fahrner, J.M.V. Alstine, Biotechnol. Bioeng. 96 (2007) 515.

[47]   S.M. Russell, G. Carta, AIChE J. 51 (2005) 2469.

[48]   E.X. Perez-Almodovar, Y. Tao, G.Carta, Biotechnol. Prog. (2011) online.

[49]   K. Yang, Y. Sun, Biochem. Eng. J. 39 (2008) 258.

[50]   S.R. Dziennik, E.B. Belcher, G.A. Barker, A.M. Lenhoff, Biotechnol. Bioeng. 91 (2005) 139.

Chapter 2

IgG Adsorption on UNOsphere SUPrA: Equilibrium, Kinetics, and Pressure-flow Curves

2.1. Introduction

Protein A based adsorbents are used extensively for the capture and purification of antibodies. They are critical components of several published industrial downstream processing schemes for a variety of existing biopharmaceuticals [1, 2] and are elements of proposed generic platform processes [3-5]. Interest in these adsorbents is heightened by their selectivity for antibodies and Fc-fusion proteins, by their practically universal applicability to human IgG1 and IgG2 class antibodies, and by the simplicity of their use, which typically involves binding and wash at neutral pH and step elution at low pH.

A variety of protein A adsorbents are commercially available based on different backbone matrices including agarose, porous glass, polystyrene, and silica gel. Several authors have compared the properties of these materials in terms of capacity, mass transfer properties, process performance, and lifetime [6-11]. Mass transfer properties are especially important in these comparisons, since, for a given adsorbent, they often limit the overall rate of IgG adsorption and the productivity in capture applications [11]. As a result they have been examined in detail both macroscopically [7,10] and microscopically [12].

Despite the success of available protein A adsorbents, future challenges to the industrial purification of antibodies are expected as a result of increased cell culture titers [13] and of

practical limits to the size of available chromatography columns [4], which, combined, make downstream process rates limiting in many modern antibody production processes. Increasing the binding capacity is a way to overcome such limitations and significant advances in this direction have been made in recent years with several commercially available protein A adsorbents achieving IgG equilibrium binding capacities in excess of 60 mg/mL [7, 9]. While higher capacities are obviously advantageous from the productivity viewpoint, very high protein concentrations are attained during step elution, which, in turn, can sometimes lead to aggregate formation. This problem can be alleviated by implementing elution with a pH gradient, although this also adds some complexity to the process. Another approach is to increase mass transfer rates. In this case, the capture process can be operated faster, thereby enabling the processing of multiple batches in the same time. On the other hand, smaller diameter particles and larger pore matrices can provide a suitable compromise of reasonable capacity and rapid mass transfer, as long as adequately low column pressures can be obtained in large-diameter columns. The design of large-scale columns for protein A capture is, of course, subject to constraints, principal among which is often the column pressure. In practice, this is generally limited to only a few bars. As a result, reducing the adsorbent particle size to improve the adsorption kinetics must be balanced against the correspondingly reduced hydraulic permeability and thus increased column pressure.

The design and scale-up of adsorption columns to meet specified pressure constrains is generally straightforward when the adsorbent particles are rigid. In this case, under the laminar flow conditions that are encountered in practice, the column pressure is proportional to the ratio uL/d_p^2, where u is the superficial velocity, L is the column length, and d_p is the particle diameter, and is independent of column diameter for a given value of this ratio [14]. For conditions where intraparticle diffusion is the dominant band-broadening factor, the dynamic binding capacity is

instead dependent on the ratio L/ud_p^2 [15,16]. As a result, since for a given flow rate u varies in inverse proportion with the square of the column diameter, d_c, adsorption columns can be designed to handle smaller particles with specified pressure constraints and for a given residence time by choosing a suitably large aspect ratio L/d_c that makes the ratio uL/d_p^2 and, hence, the pressure fall within acceptable limits.

In practice, however, many of the stationary phases used in biochromatography are compressible and exhibit a non-linear relationship between column pressure and flow rate [17]. Moreover, in many cases the column pressure exhibits a complex dependence on column diameter [18], which is not predictable based on laboratory scale column data and requires extensive experimentation.

In this chapter we have investigated the adsorption properties and scalability of a new protein A adsorbent, known as UNOsphere SUPrA (Bio-Rad Laboratories, Hercules, CA, USA). This adsorbent consists of macroporous beads based on hydrophilic polymers with coupled recombinant protein A. The polymer is synthesized from acrylamido and vinyl monomers and with a hydrophilic porogen, which are expected to provide low non-specific binding. The resulting polymer beads have large pore size and small particle size with a narrow particle size distribution to permit fast processing of IgG feedstocks. The results obtained on this chapter will provide a complete characterization of the new protein A adsorbent. Moreover, the experimental and theoretical developments provide a general framework for characterization, modeling, scale-up, and optimization of other materials.

2.2. Experimental methods

2.2.1 Materials

UNOsphere SUPrA media was obtained from Bio-Rad Laboratories (Hercules, CA, USA). The particle size distribution of this material is quite narrow with volume-average particle diameter d_p = 57±6 μm as determined in this study from microphotographs at 100 x magnification.

Polyclonal immunoglobulin (IgG) from Sigma-Aldrich (St. Louis, IL, USA, Cat No. G4386) was used as a model protein. Prior to use in the experiments, the IgG was purified using a MabSelect column from GE Healthcare (Piscataway, NJ, USA) to remove IgG-3 and other impurities that do not bind to protein A. Although the protein A - purified sample is likely heterogeneous, containing multiple IgG subclasses and, possibly, different modified isoforms, we assume that the different forms have the same binding behavior with protein A. Dextran probes for inverse size exclusion chromatography (iSEC) were obtained from GE Healthcare. Chemicals used for buffer preparations (sodium phosphate, phosphoric acid, sodium chloride, and glycine) were purchased from Fisher Scientific (Fair Lawn, NJ, USA).

All IgG adsorption experiments were performed at room temperature (22±2°C) with a mobile phase consisting of 10 mM Na_2HPO_4, adjusted to pH 7.4 with phosphoric acid, with the addition of 150 mM NaCl. Desorption was obtained with a 100 mM glycine buffer at pH 3.0.

Pressure flow curves were obtained for laboratory scale columns packed with UNOsphere SUPrA media. Measurements with larger columns up to 45 cm diameter were conducted with the base matrix used to prepare the protein A media. The particle size distribution is the same for both materials. Additionally, laboratory scale experiments showed the same column pressure with both materials. Pressure-flow curves were obtained at room

temperature (22±2 °C) for water and for a 10% glycerol solution having a viscosity of 1.37 mPa s in order to simulate a more viscous, clarified cell culture broth. Glycerol was purchased from Fisher Scientific (Fair Lawn, NJ, USA).

2.2.2 Methods

The external and internal structures of the adsorbent particles were characterized from scanning electron micrographs (SEM) and transmission electron micrographs (TEM). SEM's were obtained for dry particles coated with gold using a Hitachi Model S-3000H (Schaumburg, IL, USA) scanning electron microscope. TEM's were obtained for 80 nm sections derived from beads dehydrated in an ethanol gradient and embedded in Spurr's resin as discussed in ref. [19]. This procedure has been shown to preserve structural features that depend on hydration giving images that are representative of the actual structure that exists under aqueous process conditions.

Inverse size exclusion chromatography (iSEC) was used to determine the accessible pore size using glucose and dextrans with molecular masses ranging from 10 to 500 kDa. For this purpose the adsorbent particles were packed in a 0.5 x 5 cm Tricorn column from GE Healthcare with a bed height of approximately 5 cm. A Waters HPLC System (Milford, MA, USA), with a Waters Model R401 refractive index detector was used to determine the retention volume of individual dextran samples for 20 μL injections of 5 mg/mL dextran solutions at 0.25 mL/min. The distribution coefficient, $K_D = \left(V_e/V_c - \varepsilon\right)/\left(1 - \varepsilon\right)$, was then calculated based on the ratio of elution V_e volume (obtained from the peak first moment) and column volume V_c. The extraparticle porosity, $\varepsilon = 0.35$, was obtained from the experimental relationship between column pressure and flow rate using the Carman-Kozeny equation as described in ref. [19].

The IgG adsorption isotherm was obtained by adding a known weight of hydrated particles to vials containing either 1.5 or 3 mL of protein solution with a known concentration sealed and rotated at a few rpm. The supernatant was analyzed after 48 hr with a UV spectrophotometer at 280 nm and the amount of protein adsorbed calculated by material balance. Prior to weighing each sample of particles, the extraparticle fluid was removed by placing the sample in a microcentrifuge filter tube spun at 5,000 rpm for 10 min. The density of the hydrated particles was also determined with a picnometer and used to convert the amount of protein adsorbed from a mass basis to units of mg per mL of hydrated particle volume.

The IgG adsorption kinetics was determined from batch uptake measurements made in a stirred vessel agitated with a small paddle stirrer at 300 rpm as described in ref. [20]. The volume of the protein solution used was varied between 20 and 40 mL and the amount of adsorbent used was adjusted to reach a final concentration equal to about one half of the initial value. The protein concentration was obtained by circulating a stream of the solution through a UV spectrophotometer at 280 nm (GE Healthcare, Model UV1). The absorbance was then used to calculate the amount adsorbed by material balance. The effective pore diffusivity was determined by comparing the experimental uptake curves with various models as described in the adsorption kinetics section of this paper. The effective pore diffusivity was also determined from van Deemter curves in a 100 mM glycine buffer at pH 3.0 where IgG binding does not occur. For this determination, the adsorbent was packed in 0.5 x 10 cm GE Healthcare Tricorn chromatography column operated at flow rates of 0.1 to 1.0 mL/min with an AKTA Explorer 10 workstation (GE Healthcare). 20 μL injections of IgG were made and the UV detector signal at 280 nm was used to calculate the height equivalent to a theoretical plate (HETP) based on the

moment method. Finally, the effective diffusivity was obtained from the slope of HETP versus mobile phase velocity as illustrated, for example, in ref. [20].

Breakthrough experiments with different IgG feed concentrations, flow rates, and bed heights were performed with the AKTA Explorer 10 system using 0.5 cm-diameter GE Healthcare Tricorn columns with bed heights between 2.0 and 5.7 cm that flow-packed at 1,220 cm/h. After each run, elution of the bound IgG was conducted with 100 mM glycine at pH 3.0.

Pressure-flow curves were obtained in our laboratory for small scale columns. However, for the larger-scale work, we used the process column testing facility of Bio-Rad Laboratories (Hercules, CA, USA). Small scale data were obtained with a 1 X 10 cm Tricorn column and an AKTA Explorer 100 workstation, both from GE Healthcare (Piscataway, NJ, USA). Column pressure was measured with a calibrated in-line pressure gauge with 1-psi resolution.

Three preparative scale columns with diameters of 20, 30, and 45 cm where used for the larger scale studies using a process chromatography skid from Bio-Rad Laboratories (Hercules, CA, USA). The 20 and 45 cm diameter columns were InPlace^{TM} columns from Bio-Rad and have a motorized top header with an air-inflated seal and bed-height indicator while the 30 cm column was a BPG^{TM} column from GE Healthcare (Piscataway, NJ, USA). In all three cases pressures were determined with the skid instrumentation. Bed heights were obtained either from the bed height indicator or with a ruler through the clear wall. A schematic of the InPlace^{TM} columns and a photograph of the 45 cm-diameter column used for this work are shown in Fig. 2.1.
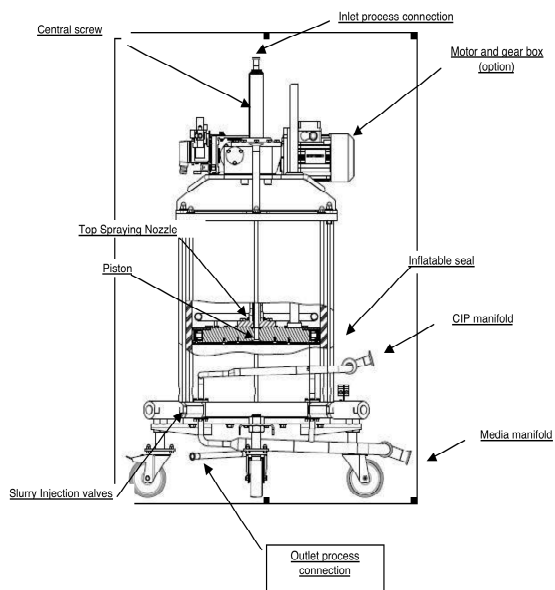
Fig. 2.1. Schematic and photograph of 45 cm diameter column used to obtained pressure-flow curves.

The laboratory scale columns were packed by pouring in a measured amount of a 50% slurry of the resin suspended in water, allowing gravity settling for 10 min in order to obtain 1 to 2 cm of clear mobile phase at the top, inserting the top column header, and immediately flowing water at a 300 cm/h superficial velocity for approximately 10 min until attaining a stable bed height. After achieving a consolidated bed, the flow was stopped and the column header lowered until contact with the particles. Following packing, the flow rate was increased gradually while holding the top header in place and recording pressure and packed bed height. For the preparative scale columns the first step was also to pour in a measured volume of 50% slurry in water. Consolidation of the bed was then conducted according to the following procedures. For the 30 cm-diameter BPG^{TM} column, the top header was inserted immediately after pouring in the slurry and allowing it to settle for 10 min to obtain a 2 to 3 cm layer of clear liquid above the particles. After this step, the mobile phase was pumped in at 300 cm/h for 10 min. At this point the height of the consolidated bed was marked, the flow was stopped and the header lowered until contact with the stationary phase and locked in position. Since there was some rebound of the bed height when the flow was stopped, the steps of pumping at 300 cm/h and lowering the header were repeated a few times until achieving the previously marked packed bed height. A slightly different procedure was used to pack the InPlace^{TM} columns, since these columns have a motorized header. In this case, after loading the slurry, allowing settling for 10 min, inserting the header, and activating the inflatable seal with compressed air at 4 bar, consolidation of the bed was obtained by continuously lowering the header at a velocity of 200 cm/h while flowing water at a 100 cm/h until achieving a stable bed height. The net result of this process is a combined packing flow rate of 300 cm/h analogous to that used for the 1 cm and the 30 cm diameter columns. However, because of the continuous header movement, rebound of the bed was

avoided and there was no need for further adjustments. After packing, all three preparative scale columns were subjected to a flow-conditioning processes during which 3 column volumes of water were pumped in upflow followed by 3 column volumes in downflow at 100 cm/h. Pressure-flow curves were then obtained by incrementally changing the pump speed from zero to high values each time recording the new bed height. Following experiments with water during which the flow rate was increased to maximum values ranging between 500 and 800 cm/h, dependent on initial column height, the resin was re-expanded to the original bed height obtained when the column was first packed in water by flowing the 10% glycerol solution in alternating up and down directions.

For both laboratory and preparative scale units, pressure-flow curves were also obtained for each empty column. The corresponding pressure was subtracted from the total pressure to determine the pressure drop across the packed bed alone.

2.3. Results and discussion

2.3.1. Particle properties

Figure 2.2 shows representative electron micrographs. Figures 2.2a and 2.2b are SEM's of whole particles at different magnifications while Fig. 2.2c shows a representative TEM of a section near the particle surface. In the TEM image the darker areas represent the matrix backbone and the lighter the embedding resin. The few visible circular lighter spots are imperfections resulting from the sectioning process. As seen in these images, the particles have a microgranular structure defining a macroporous network with fairly wide, open pores.

Figure 2.3a shows the peaks obtained with the different dextran probes and glucose. As seen from this graph, the dextrans are only partially resolved and even dextran with 500 kDa
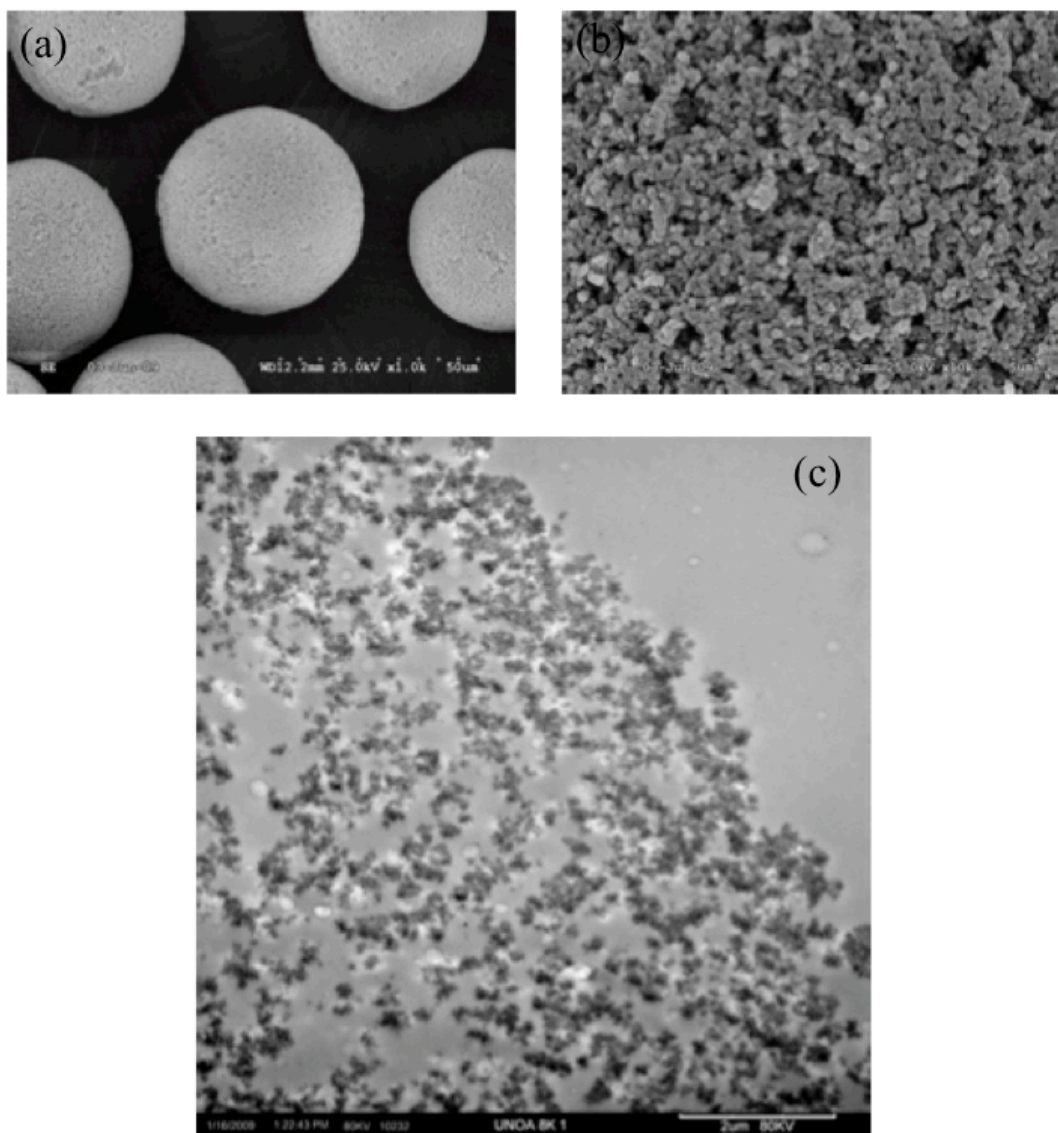
Fig. 2.2. Electron micrographs of UNOsphere SUPrA. (a) and (b) Exterior views by scanning electron microscopy (SEM) at 1,000X (a) and 10,000X (b) magnifications (images courtesy of Bio-Rad Laboratories). (c) Interior structure by transmission electron microscopy (TEM).
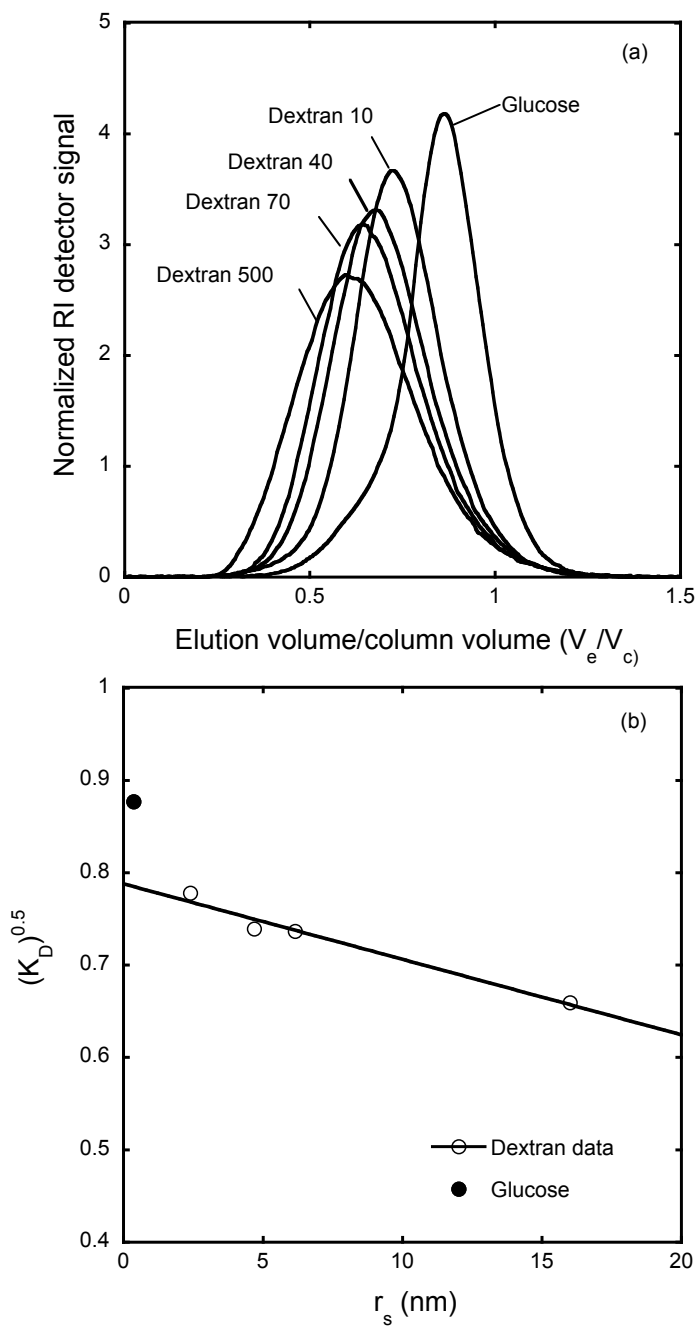
Fig. 2.3. Inverse size exclusion results. (a) Dextran and glucose peaks. (b) Linearized plot K_D vs. dextran radius according to eq. 2.1.

molecular mass is retained and gains access to a substantial fraction of the particle volume. Obtaining the pore size distribution from these data is not straightforward since different assumed distributions give nearly identical fit of the data [21]. Thus, for simplicity, we determined macroporosity, ε_p, and average pore radius, r_{pore}, by assuming a single cylindrical pore model. Accordingly, K_D is described by the following equation [21, 22]:

$$K_D = \varepsilon_p \left(1 - \frac{r_s}{r_{pore}} \right)^2 \tag{2.1}$$

where r_s is the dextran radius. Figure 2.3b shows a plot of $\sqrt{K_D}$ as a function of r_s based on this equation, where the r_s-values were calculated as the average of the dextran viscosity radii estimated from the equations in Hagel et al. [21] and Squire [23]. The corresponding values of ε_p and r_{pore}, based on the slope and intercept of a linear regression of the dextran data were 0.621±0.001 and 96±11 nm, respectively. Note that the glucose data was not included in the regression since this small probe likely gains access to the micropores in the polymer network of the base matrix from which macromolecules are completely excluded.

2.3.2. Adsorption isotherm

The IgG adsorption isotherm is shown in Fig. 2.4 and is highly favorable as is typical for IgG binding to protein A. The graph also shows the IgG adsorption capacities attained after 2,500 s in the batch uptake experiments, which are described later. A fit of the 48 hr data according to the Langmuir isotherm:

$$q = \frac{q_m K C}{1 + K C} \tag{2.2}$$

is also shown in Fig. 2.4. The regressed parameter values are $q_m = 46\pm1$ mg/mL and $K = 72\pm4$ mL/mg. The K-value determined from these data is somewhat smaller than the range of values
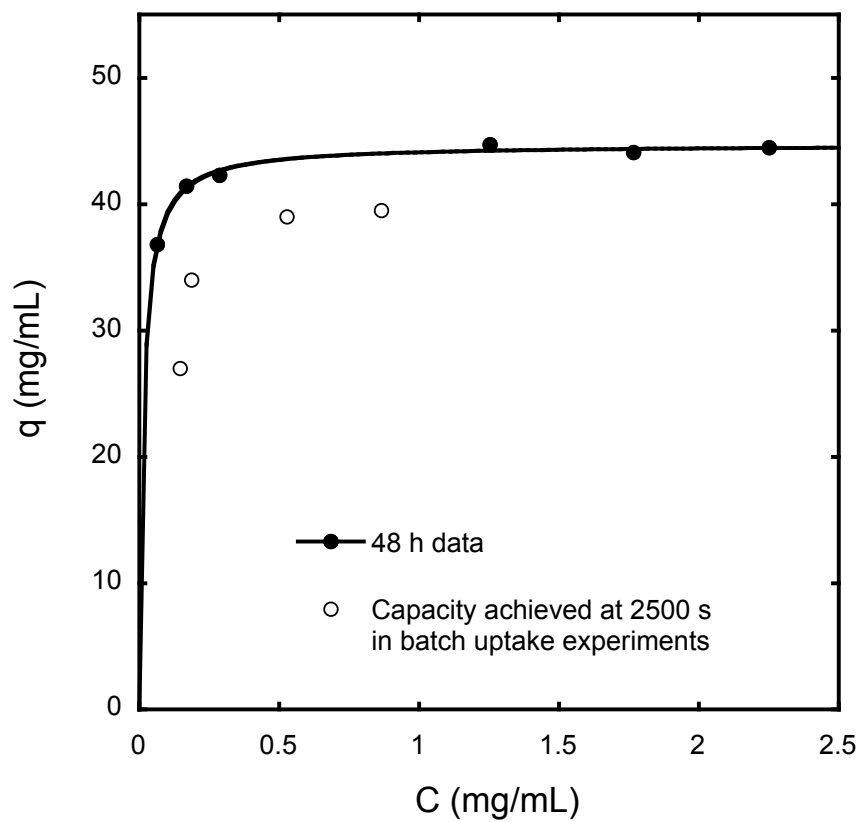
Fig. 2.4. Adsorption isotherm and capacities attained after 2,500 s. The solid line is based on the Langmuir model. See text for parameter values.

reported by other authors for IgG binding to immobilized protein A (1.8-9.4x10^7 M^{-1} or 120–630 mL/mg [12, 24]). This result could suggest that equilibrium was not completely established at low concentrations even after 48 h. However, our K-value is considerably larger than the value reported by Hahn et al. [8,10] for several commercial protein A adsorbents. This discrepancy may be due to the fact that insufficient time (8 h) was allowed by these authors to attain equilibrium at low concentrations.

2.3.3. Adsorption kinetics

The overall kinetics of IgG binding is expected to be controlled by diffusional mass transfer [10] with a potential contribution of the kinetics of formation of the complex between the protein A ligand and the IgG molecules. In order to ascertain the relative importance of these effects, diffusional mass transfer effects were first determined for non-binding conditions where binding kinetics effects are absent. The chromatographic peaks obtained for pulse injections under non-binding conditions and the corresponding dimensionless van Deemter plot ($h = HETP/d_p$ vs. $v' = vd_p/D_0$) are shown in Fig. 2.5. As expected, the peaks become progressively broader and asymmetrical as the flow rate is increased since less time is available for diffusion of IgG in and out of the particle pores. The effective pore diffusivity, D_e, is obtained by comparing the experimental results with the following equation [16]:

$$h = a + \frac{1}{30}\frac{\varepsilon}{1-\varepsilon}\left(\frac{k'}{1+k'}\right)^2\left(\frac{10}{Sh}+\frac{D_0}{D_e}\right)v'$$

(2.3)

where the retention factor $k' = (\mu - V_0)/V_0$ is calculated using the peak first moment, μ, and the extraparticle column volume, $V_0 = \varepsilon V_c$. The Sherwood number ($Sh = k_f d_p/D_0$) is estimated from the following correlation for mass transfer in packed beds [16]:
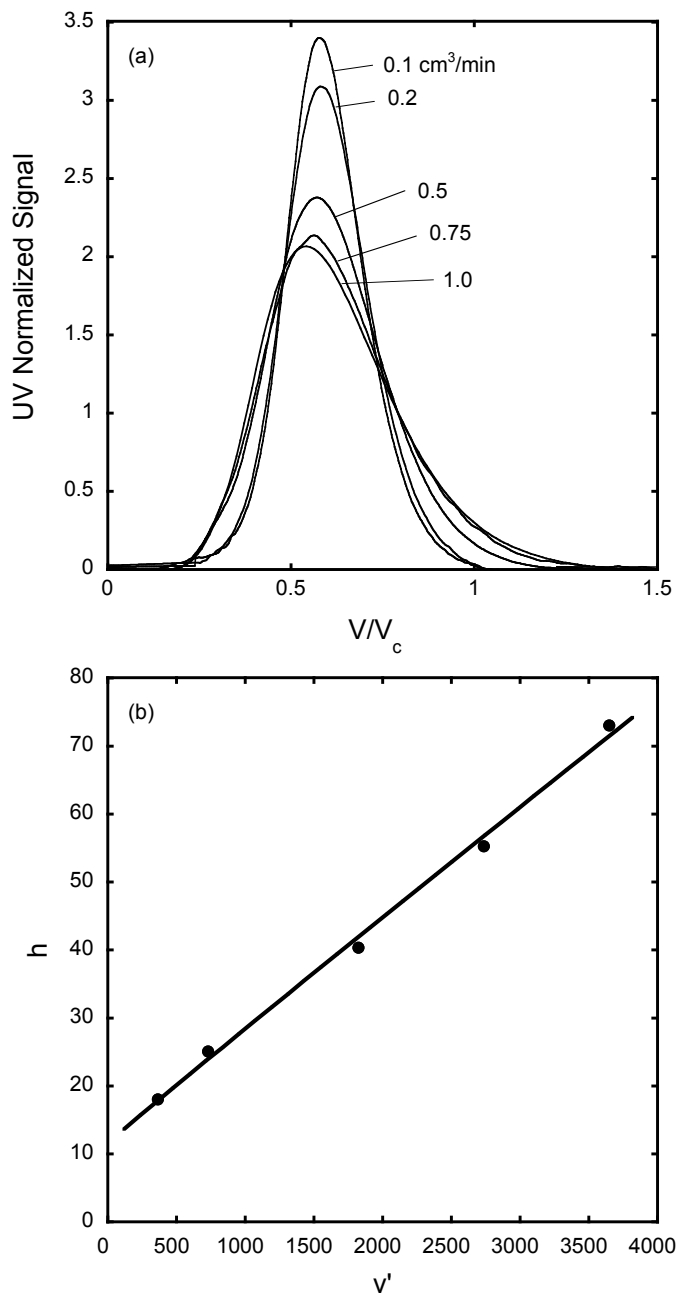
Fig. 2.5. (a) Pulse response peaks obtained for IgG under non-binding conditions. (b) van Deemter plot on dimensionless $h=H/d_p$ and $v'=vd_p/D_0$ showing fit according to eq. 2.3.

$$Sh = \frac{1.09}{\varepsilon}\left(\frac{\rho u d_p}{\eta}\right)^{0.33}\left(\frac{\rho}{\eta D_0}\right)^{0.33} \tag{4}$$

while the free solution diffusivity, $D_0 = 3.7 \times 10^{-7}$ cm^2/s, is estimated from Tyn and Gusek [25]. The best-fit line regressed according to eq. 2.3 is shown in Fig. 2.5b with $D_e = 8.0 \pm 0.3 \times 10^{-8}$ cm^2/s. In turn, D_e is related to the intraparticle porosity and tortuosity factor, τ_p, by $D_e = \varepsilon_p D_0 / \tau_p$. Since $\varepsilon_p = 0.62$, we obtain $\tau_p = 2.8 \pm 0.1$. This relatively small value indicates the absence of significant diffusional hindrance and is consistent with the fairly open pore structure and large pore size determined by TEM and iSEC experiments.

We next determined the kinetics of IgG adsorption from batch uptake experiments at varying initial protein concentration. The results are shown in Fig. 2.6 on both linear (a) and logarithmic (b) scales. As seen in these figures the adsorption rate increases as the IgG concentration increases. The q-values obtained at 2,500 s are summarized in Fig. 2.4. Obviously, equilibrium is not attained during this timeframe, especially at low concentrations. Even at higher concentrations, however, close inspection of the results shows that the amount of IgG adsorbed continues to rise very slowly for longer times. This behavior of slow approach to equilibrium is sometimes seen even for protein adsorption on ion exchangers when the adsorbent has a broad distribution of particle sizes [26]. In our case, however, the particle size distribution is very narrow and is unlikely to have a significant effect. Thus it is possible that a kinetic resistance to binding affects the long-times results.

Three different models were used to describe these data. All three consider pore diffusion as the dominant intraparticle transport mechanism, but differ in the way in which adsorption equilibrium and kinetics are treated. The first of these models is the "shrinking core model",
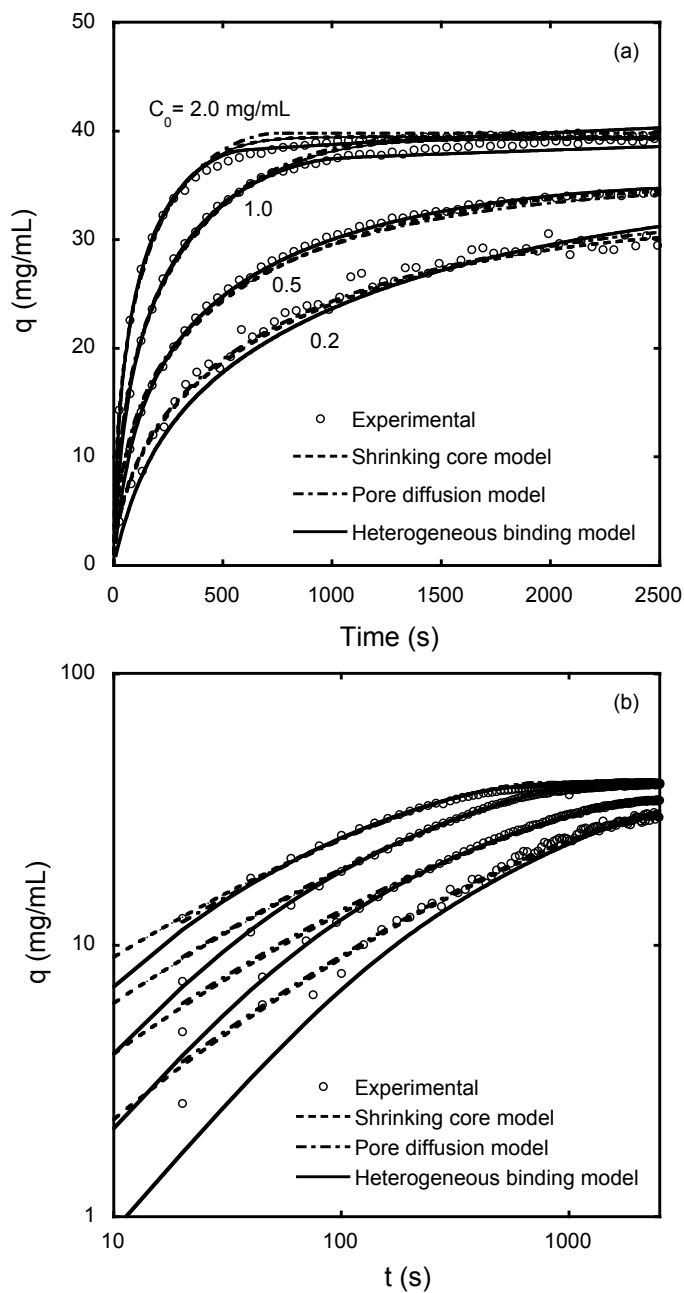
Fig. 2.6. Batch uptake curves for IgG at different initial protein concentrations on linear (a) and logarithmic scales (b). Lines are calculated with parameters in Table 2.1.

which assumes that the isotherm is rectangular, that the amount of protein held in the pore liquid is negligible, and that there is no kinetic resistance to binding. The second is the "pore diffusion model", which assumes that the isotherm is described by the Langmuir model, but still neglect the kinetic resistance to binding. The third considers the kinetics of IgG binding on a heterogeneous distribution of binding sites. Such heterogeneity could arise because of different reasons leading to reduced accessibility or even complete inaccessibility by IgG, including non-directional attachment of the protein A ligand on the adsorbent surface, attachment within pores that are too small to allow formation of the protein A- IgG complex, and partial deactivation of the protein A ligand during the coupling process. For simplicity, in our work, we consider only two types of independent binding sites, with concentrations q_{m1} and q_{m2}, such that $q_{m1} + q_{m2} = q_m$. We assume that both have the same affinity for IgG (i.e. equal K), but that have fast and slow binding kinetics, respectively. A fourth model was also considered based on the assumption that there is only one type of binding site with slow binding kinetics. This model, however, did not provide predictions consistent with the data since the only significant effect was a generally slower approach to equilibrium, which would then require a higher and concentration-dependent effective diffusivity of IgG in order to fit the data. The equations for the three models used are as follows:

Shrinking core model (adapted from ref. [27]):

$$\frac{C_0}{q^*}\frac{D_e t}{r_p^{\ 2}} = \left(1-\frac{1}{Bi}\right)I_2 - I_1 \tag{2.5}$$

$$I_1 = \frac{1}{6\lambda\Lambda}\ln\left[\frac{\lambda^3 + \beta^3}{\lambda^3 + 1}\left(\frac{\lambda+1}{\lambda+\beta}\right)^3\right] + \frac{1}{\lambda\Lambda\sqrt{3}}\left[\tan^{-1}\left(\frac{2\beta-\lambda}{\lambda\sqrt{3}}\right) - \tan^{-1}\left(\frac{2-\lambda}{\lambda\sqrt{3}}\right)\right] \tag{2.5a}$$

$$I_2 = \frac{1}{3\Lambda}\ln\left(\frac{\lambda^3 + \beta^3}{\lambda^3 + 1}\right) \tag{2.5b}$$

$$\beta = \left(1 - \frac{q}{q^*}\right)^{1/3} \tag{2.5c}$$

$$\lambda = \left(\frac{1}{\Lambda} - 1\right)^{1/3} \tag{2.5d}$$

$$\Lambda = \frac{V_M q^*}{V C_0} \tag{2.5e}$$

$$Bi = \frac{k_f r_p}{D_e} \tag{2.5f}$$

Pore diffusion model (adapted from ref. [16]):

$$\left[\varepsilon_p + \frac{q_m K}{(1 + Kc)^2}\right]\frac{\partial c}{\partial t} = \frac{D_e}{r^2}\frac{\partial}{\partial r}\left(r^2 \frac{\partial c}{\partial r}\right) \tag{2.6}$$

$$r = 0, \quad \frac{\partial c}{\partial r} = 0$$

(2.6a)

$$r = r_p, \quad D_e \frac{\partial c}{\partial r} = k_f(C - c) \tag{2.6b}$$

$$\frac{dC}{dt} = -\frac{3V_M}{r_p V} k_f \left(C - c\big|_{r=r_p}\right) \tag{2.7}$$

Heterogeneous binding model (this work):

$$\varepsilon_p \frac{\partial c}{\partial t} + \frac{\partial(q_1 + q_2)}{\partial t} = \frac{D_e}{r^2}\frac{\partial}{\partial r}\left(r^2 \frac{\partial c}{\partial r}\right) \tag{2.8}$$

$$r = 0, \quad \frac{\partial c}{\partial r} = 0$$

(2.8a)

$$r = r_p, \quad D_e \frac{\partial c}{\partial r} = k_f(C - c) \tag{2.8b}$$

$$\frac{\partial q_1}{\partial t} = k_1 \left[(q_{m1} - q_1)c - \frac{q_1}{K} \right] \qquad (2.9)$$

$$\frac{\partial q_1}{\partial t} = k_2 \left[(q_{m2} - q_2)c - \frac{q_2}{K} \right] \qquad (2.10)$$

$$\frac{dC}{dt} = -\frac{3V_M}{r_p V} k_f \left(C - c|_{r=r_p} \right) \qquad (2.11)$$

In these equations, q^* is the adsorbed protein concentration attained at equilibrium, k_f is the external mass transfer coefficient, r_p is the particle radius, V_M and V are the volumes of adsorbent and solution, respectively, and k_1 and k_2 are rate constants for IgG binding on fast and slow sites, respectively. A numerical solution is required for both the pore diffusion model and for the heterogeneous binding model and was obtained by finite differences as described in ref. [28]. The shrinking core and pore diffusion models are the same as those used by McCue et al. [7] and Hahn et al. [10] and neglect any kinetic resistance to binding. The heterogeneous binding model is similar to the model proposed by Boi et al. [29] for IgG adsorption on affinity chromatography membranes. In their case, however, the heterogeneity was attributed to non-specific binding which resulted in an almost even distribution of weak and strong binding sites.

For all three models described above, the external mass transfer coefficient, k_f, was estimated based on previous measurements for lysozyme adsorption at low concentrations in the same laboratory apparatus but with ion exchange particles approximately 100 μm in diameter [30]. The adsorption kinetics was very fast in this case, allowing a precise determination of k_f at low protein concentrations. The corresponding Sherwood number was 28 [30]. To account for the different particle size and protein diffusion coefficient pertaining to our system we assumed that the Sherwood number has the functional dependence predicted by the correlation of Armenante and Kirwan [31] for mass transfer to small particles suspended in agitated vessels.

Accordingly, we estimate $Sh = 27$ and $k_f = 1.8 \times 10^{-3}$ cm/s for IgG adsorption on UNOsphere

SUPrA. Using this value of k_f, the three models were compared to the experimental batch uptake

data as follows. For the shrinking core model, q^* and D_e were fitted to the data at each initial

protein concentration as in refs. [7] and [10]. For the pore diffusion model, q_m and D_e were fitted

at each initial protein concentration while assuming that the isotherm parameter K is the same as

that determined from the 48 h data in Fig. 2.4. Finally, for the heterogeneous binding model, we

used the D_e-value obtained for non-binding conditions. In this case, the ratio q_{m2}/q_m and k_2

were used as fitting parameters assuming a value of $k_1 = 10$ mL/mg s, that is so large that its

actual magnitude did not affect the numerical results. Thus, the only kinetic resistance to binding

is assumed to be that associated with q_{m2}. The resulting fitted parameter values are summarized

in Table 2.1 and model-calculated lines are shown in Fig. 2.6. Obviously, all three models are

capable of fitting the data reasonably well, although deviations occur for the shrinking core and

the pore diffusion model when saturation is approached. On the other hand, both of these models

show a consistent and unexpected trend where D_e increases as the protein concentration is

reduced. Since the solution viscosity is low for all these cases and the adsorption capacity is

nearly the same over the range of IgG concentrations studied, such a trend is unexpected,

especially in view of the large pore size of the adsorbent. Moreover, both models require

adjustment of adsorption isotherm parameters (q^* or q_m). These unexpected results suggest that

the basic assumption in these models that the binding sites are homogeneous is likely inadequate.

On the other hand, the heterogeneous binding model provides a good description of all the data

with the same values of D_e (equal to the value determined under non-binding conditions), k_2, and

q_{m2}/q_m -values, all independent of the IgG concentration. According to these model results, the

distribution of binding sites is 83% fast and 17% slow. The reason why all three models provide

Table 2.1. Parameters obtained by fitting the batch uptake data with different model.

Run	Shrinking core model		Pore diffusion model		Heterogeneous binding model[a]	
C_0 (mg/mL)	q^* (mg/mL)	D_e (10^{-8} cm^2/s)	q_m (mg/mL)	D_e (10^{-8} cm^2/s)	$\dfrac{q_{m2}}{q_m}$	k_2 (10^{-4} mL/mg s)
0.2	31	8.5	34	8.7	0.17	2.0
0.5	36	7.3	39	7.5		
1.0	39	6.5	40	7.1		
2.0	40	6.2	41	7.0		

[a] $q_m = 46$ mg/mL, $D_e = 8.0 \times 10^{-8}$ cm^2/s

reasonable fits is that over the time scale of the batch uptake runs (2,500 s), only a fraction of the slow binding sites play a role, so that for these experiments the contribution of fast sites to IgG adsorption is dominant and mass transfer is almost completely limiting. Over longer time scales, however, such as those used to determine the isotherm, even the slow binding sites become occupied. Between these two time scales, the heterogeneous binding model is the only one of the three that can describe the overall adsorption kinetics.

2.3.4. Breakthrough behavior

Breakthrough curves for IgG were obtained for a range of feed concentrations (0.2 to 4 mg/mL), column lengths (2 to 5.7 cm), and flow rates, (0.2 to 4 mL/min or 60 to 1,200 cm/h). Representative results for a short column with 2.1 mg/mL feed concentration are shown in Fig. 2.7a. Results for other conditions were qualitatively similar. As seen in this figure, the breakthrough curves become increasingly shallow as the flow rate is increased, primarily as a result of mass transfer limitations. Note, however, that even at low flow rates the breakthrough curve approaches the feed concentration very slowly, not quite reaching it even after loading 70 mg of protein per mL of column. The dynamic binding capacity (*DBC*), expressed in mg/mL of column volume, obtained for a range of column lengths and feed concentrations is shown in Fig. 2.7b. As seen in this graph, when plotted as a function of residence time the *DBC* is essentially independent of feed concentration and column length, as expected for pore diffusion control with a very favorable adsorption isotherm [16, 20].

Fig. 2.8 shows the experimental breakthrough curves obtained at 0.2 and 4 mL/min in 5.5 and 2 cm-long columns, respectively. The corresponding residence times are 323 and 5.9 s, respectively, the largest and smallest values used in this work. The results are compared with
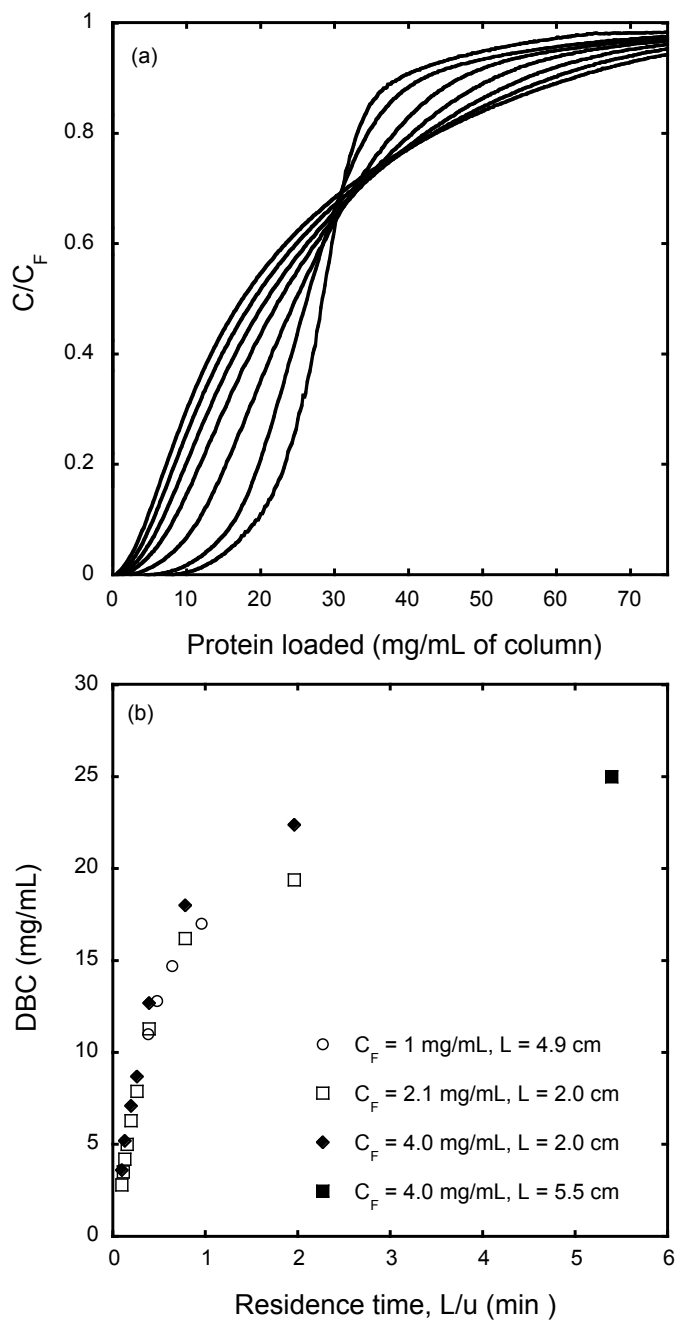
Fig. 2.7. Breakthrough behavior of IgG. (a) Breakthrough curves for 2.1 mg/mL IgG in a 2.0 cm column operated at 0.2, 0.5, 1, 2, 2.5, 3, 3.5 and 4 mL/min. (b) Dynamic binding capacity (*DBC* in mg/mL of column volume) at C/C_F=0.1 plotted vs residence time for a range of column lengths and feed concentrations.

predictions based on the shrinking core model using $D_e = 8.0\text{x}10^{-8}$ cm²/s, determined for non-binding conditions, and the true isotherm capacity. The relevant equations are given by Weber and Chackraborty [32] and are as follows:

$$n_{pore}\left(1-\tau_1\right) = +\frac{15}{2}\ln\left[1+\left(1-X\right)^{\frac{1}{3}}+\left(1-X\right)^{\frac{2}{3}}\right]-\frac{15}{\sqrt{3}}\tan^{-1}\left[\frac{2}{\sqrt{3}}\left(1-X\right)^{\frac{1}{3}}+\frac{1}{\sqrt{3}}\right]$$
$$-\frac{n_{pore}}{n_{film}}\left[\ln(X)+1\right]+\frac{5\pi}{2\sqrt{3}}-\frac{5}{2} \tag{2.12}$$

for constant pattern conditions or long residence times and:

$$n_{pore} = +\frac{15}{2}\ln\left[1+\left(1-Y\right)^{\frac{1}{3}}+\left(1-Y\right)^{\frac{2}{3}}\right]-\frac{15}{\sqrt{3}}\tan^{-1}\left[\frac{2}{\sqrt{3}}\left(1-Y\right)^{\frac{1}{3}}+\frac{1}{\sqrt{3}}\right]-\frac{n_{pore}}{n_{film}}\left[\ln(Y_0)+1\right]$$
$$-\frac{15}{2}\ln\left[1+\left(1-Y_0\right)^{\frac{1}{3}}+\left(1-Y_0\right)^{\frac{2}{3}}\right]+\frac{15}{\sqrt{3}}\tan^{-1}\left[\frac{2}{\sqrt{3}}\left(1-Y_0\right)^{\frac{1}{3}}+\frac{1}{\sqrt{3}}\right]+\frac{n_{pore}}{n_{film}}\left[\ln(Y_0)+1\right] \tag{2.13}$$

with

$$n_{pore}\tau_1 = 5\left[1.5-1.5\left(1-Y_0\right)^{\frac{2}{3}}-\left(1-\frac{n_{pore}}{5n_{film}}\right)Y_0\right] \tag{2.14}$$

for non-constant pattern conditions or short residence times. In these equations, X, τ_1, n_{pore}, and n_{film} are defined by the following:

$$X = \frac{C}{C_F} = \frac{Y}{Y_0} \tag{2.15}$$

$$\tau_1 = \frac{\dfrac{ut}{L}-\varepsilon}{\left(1-\varepsilon\right)q_F\big/C_F} \tag{2.16}$$
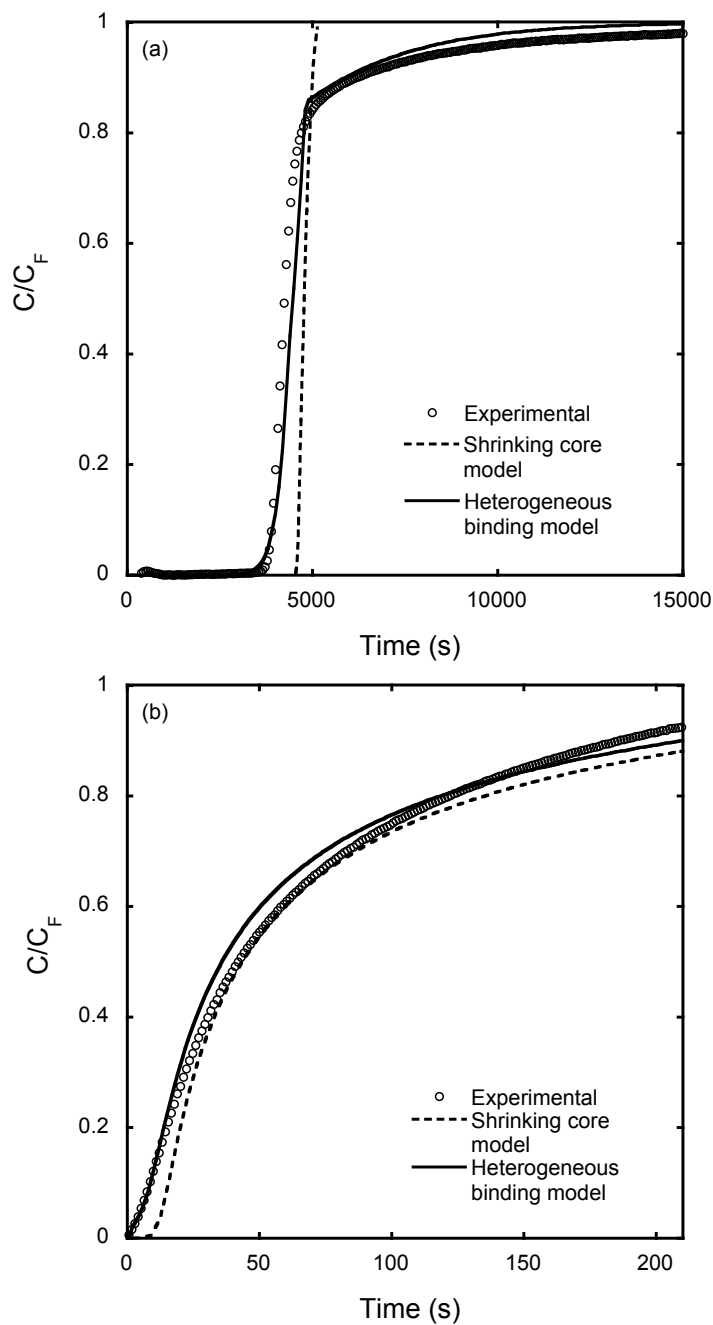
Fig. 2.8. Comparison of experimental breakthrough curves with model predictions. (a) $C_F = 2.1$ mg/mL, L=5.5 cm, 0.2 mL/min ($u = 60$ cm/h). (b) $C_F = 2.1$ mg/mL, $L = 2.0$ cm, 4 mL/min ($u = 1200$ cm/h).

$$n_{pore} = \frac{60(1-\varepsilon)D_e}{d_p^2} \frac{L}{u} \tag{2.17}$$

$$n_{film} = \frac{6(1-\varepsilon)k_f}{d_p} \frac{L}{u} \tag{2.18}$$

Note that the non-constant pattern case requires a trial and error calculation where at each time Y_0 is first determined from eq. 2.14, then used to determine Y from eq. 2.13, which, in turn is used to determine X from eq. 2.15. Conversely, a direct calculation is possible from eq. 2.12 for constant pattern conditions since in this case $Y_0 = 1$.

As seen in Fig. 2.8b, the shrinking core model does a reasonable job predicting the breakthrough curve with $D_e = 8.0 \times 10^{-8}$ cm²/s for the low residence time case. For these conditions, the time scale of the experiment (total duration ~ 210 s) was very short and insufficient for the slow binding sites to play a significant role. On the other hand, the shrinking core prediction deviates dramatically from the experimental result for the high residence time case. As seen in Fig. 2.8a, for these conditions the experimental breakthrough curve consists of a sharp rise, which we hypothesize corresponds to the saturation of the fast binding sites, followed by a long tail that eventually reaches the feed concentration, the latter corresponding to the saturation of the slow binding sites. In order to test this hypothesis, the equations describing the heterogeneous binding model were combined with the following column material balances:

$$\varepsilon \frac{\partial C}{\partial t} + (1-\varepsilon)\frac{\partial \overline{q}}{\partial t} + u\frac{\partial C}{\partial z} = 0 \tag{2.19}$$

$$\frac{\partial \overline{q}}{\partial t} = \frac{3}{r_p}k_f(C - C_s) \tag{2.20}$$

The resulting set of equations (eqs. 2.7 to 2.10, 2.19 and 2.20) were then solved numerically discretizing the particle coordinate by finite differences as in ref. [28] and the column axial

coordinate by backwards finite differences, using a discretization grid sufficiently fine that the numerical results were not affected by significant numerical dispersion. The resulting system of ordinary differential equations was integrated using subroutine DIVPAG in the International Mathematical and Statistical Library (IMSL, Visual Numerics, Inc., Houston, TX, USA). All calculations were performed with a FORTRAN program available in our laboratory.

The numerical results are shown in Fig. 8a and b using the parameters in Table 2.1 and the true isotherm in Fig. 2.4. It is apparent that the heterogeneous binding model captures the experimental behavior quite closely predicting a sharp rise followed by a long tail corresponding to saturation of the slow binding sites when the residence time is long (Fig. 2.8b). For short residence times, when conditions deviate from constant pattern, the breakthrough curve is highly asymmetrical even in the absence of a heterogeneous binding mechanism. In this case, neglecting the kinetic resistance provides a good prediction, but only if the equilibrium binding capacity is appropriately adjusted to fit the results. It should be noted that the parameters for the heterogeneous binding model could predict the results over a broad range of conditions. For example, data and predicted results are shown in Fig. 2.9 for a 5.6 cm long column with a 0.2 mg/mL operated at 1 mL/min and for a 2.0 cm long column with a 2.1 mg/mL operated at 0.2 mL/min.

The tailing behavior of the IgG breakthrough curve is not unique to the adsorbent studied in this work and has been found to occur with several other commercial protein A adsorbents, for example, by McCue et al. [7] and Hahn et al. [10]. In their work too, fitting the batch adsorption kinetics with models that did not consider a kinetic resistance to binding resulted in apparent effective diffusivities that, unexpectedly, increased dramatically at low IgG concentrations.
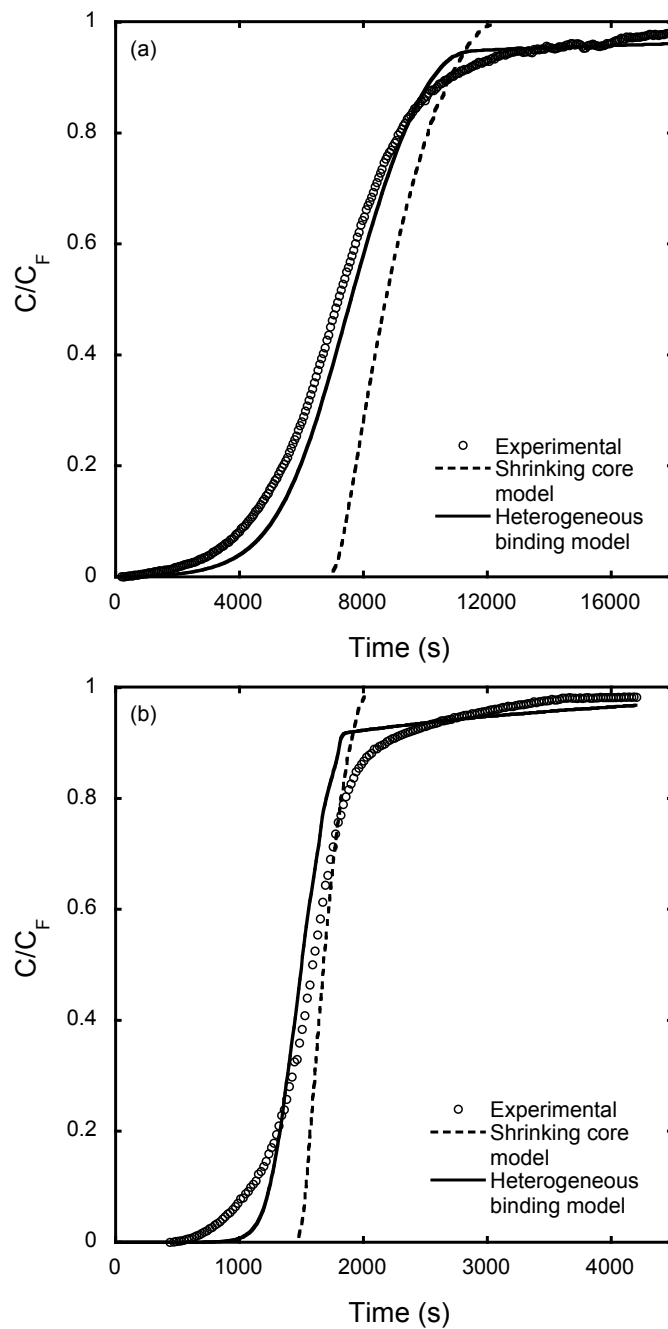
Fig. 2.9. Comparison of experimental breakthrough curves with model predictions. (a) $C_F = 0.2$ mg/mL, $L = 5.7$ cm, 1.0 mL/min ($u = 300$ cm/h). (b) $C_F = 2.1$ mg/mL, $L = 2.0$ cm, 0.2 mL/min ($u = 1200$ cm/h).

Moreover, similarly to our observations, attempts by these authors to predict the breakthrough curve with ordinary pore diffusion without kinetic resistance required using binding capacities lower than the true equilibrium values and could only match the early rising portion of the experimental breakthrough curve.

2.3.5. Experimental pressure-flow curves

Figure 2.10 shows the results obtained with a 1-cm diameter column packed to an initial bed height of 9.8 cm. The pressure-flow curve exhibits some deviation from linearity as soon as the packing velocity is increased above 300 cm/h, although these deviations are limited. In fact, even at 1200 cm/h the bed height is reduced by less than about 10%. Figures 2.11-2.13 show representative results obtained for the preparative scale columns with different initial bed height. In each case, the pressure-flow curve is initially linear and then increases more rapidly as the flow velocity is increased beyond the initial packing velocity. As expected, the column pressure is higher with 10% glycerol because of the higher viscosity. As seen in these figures, the non-linearity of the pressure-flow curves is accompanied by a reduction in packed bed height, which is more pronounced for the 10% glycerol case. This behavior was not visible in the 1-cm column experiments over the same range of flow velocities likely because, in that case, the wall provided substantial support making the material appear less compressible.
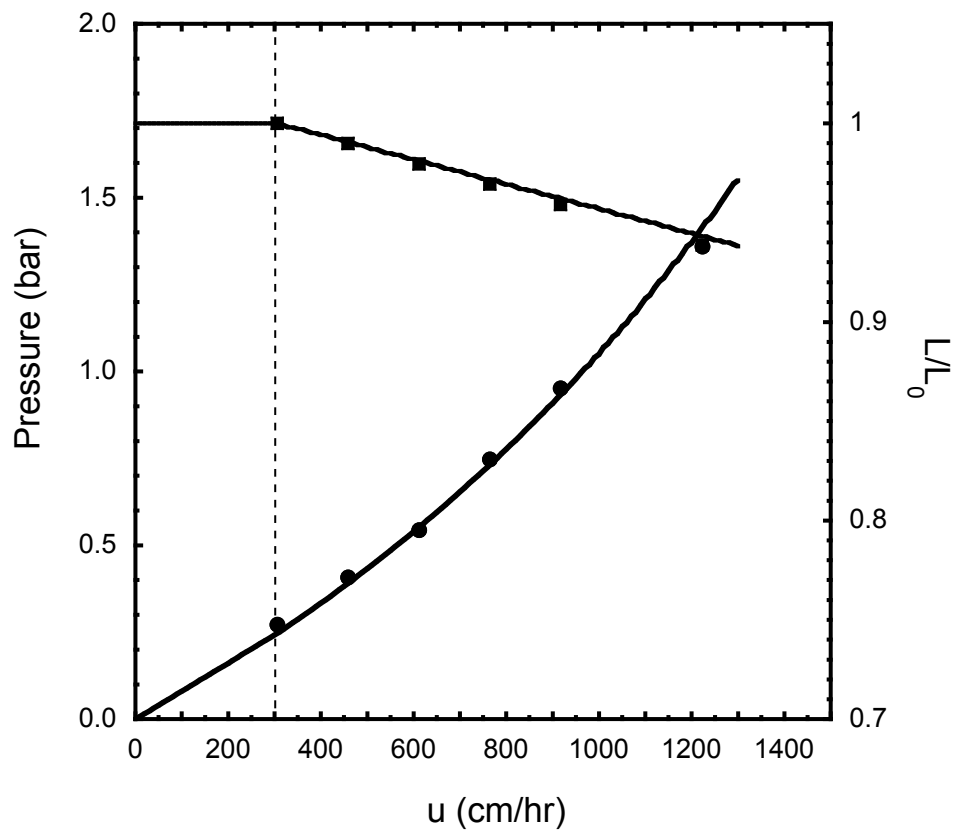
Fig. 2.10. Pressure-flow curve and bed height for a 1.0 cm diameter column. L_0 = 9.8 cm. Lines are calculated from eqs. 2.21-2.24 with parameters in Table 2.2.
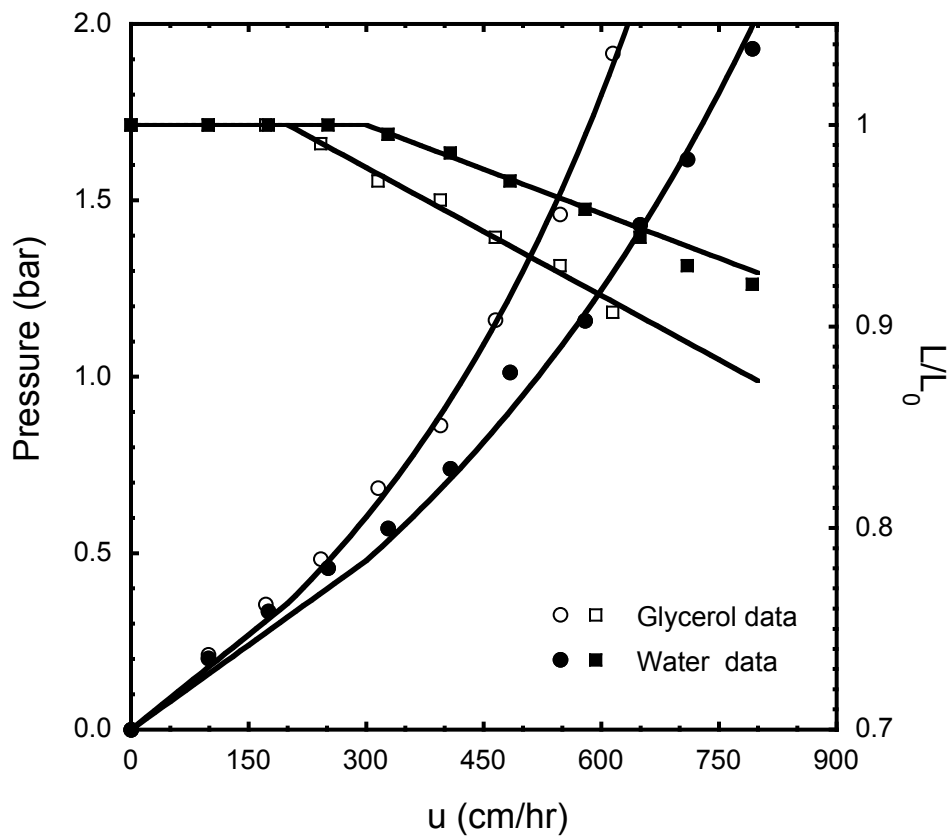
Fig. 2.11. Pressure-flow curve and bed height for a 20 cm diameter column. L_0 = 21.5 cm. Lines are calculated from eqs. 2.21-2.24 with parameters in Table 2.2.
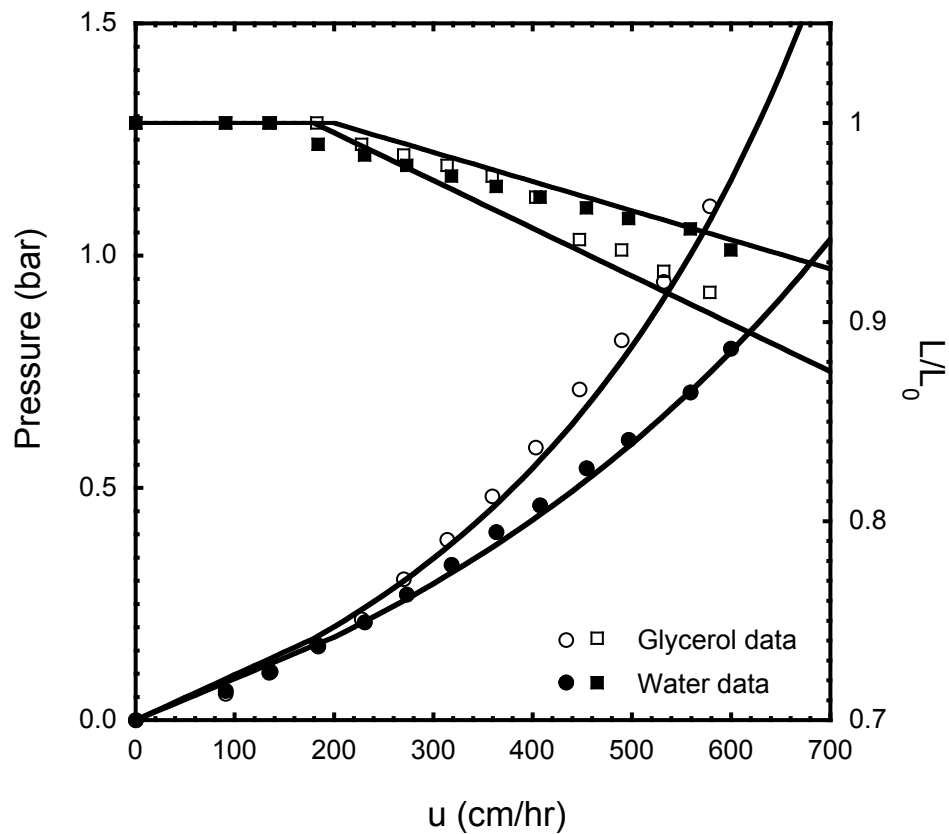
Fig. 2.12. Pressure-flow curve and bed height for a 30 cm diameter column. L_0 = 9.4 cm. Lines are calculated from eqs. 2.21-2.24 with parameters in Table 2.2.
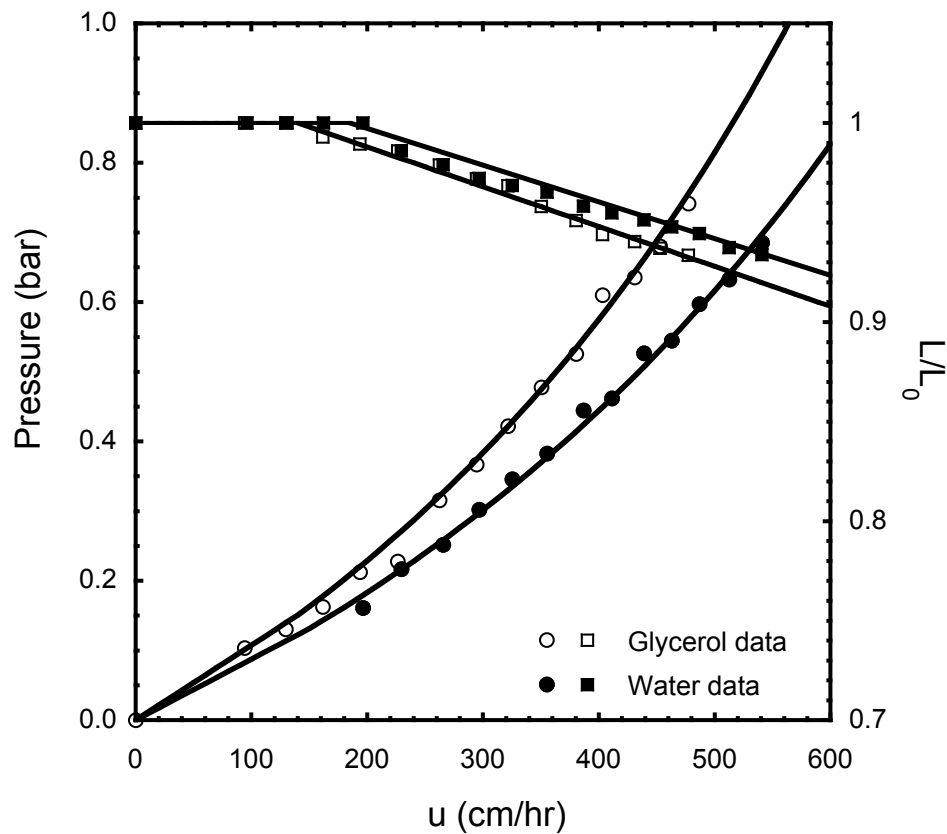
Fig. 2.13. Pressure-flow curve and bed height for a 45 cm diameter column. $L_0 = 14.3$ cm. Lines are calculated from eqs. 2.21-2.24 with parameters in Table 2.2.

2.3.6. Model development

Although, as seen in Fig. 2.10-2.13, the pressure remained below 2 bar for bed depths up to 20 cm and flow velocities up to 500 cm/h, it obvious that the compressibility of the packing cannot be neglected in the design of large columns. A few different models are available in the literature to describe pressure-flow relationship for soft packings [18,33,34]. These models are based on the assumption that a maximum or "critical" velocity, u_{cri}, exists and that this velocity is a function of initial bed height and column diameter, which, in turn, can be related to the properties of the initial, gravity-settled bed. In our work, however, a critical velocity was not attained even in 45 cm diameter columns. Moreover, instead of relying on gravity settling, our columns were consolidated under flow so that even in the initial state there was some degree of compression. Thus, a modified version of the model of Stickel and Fotopoulos [18] was used to describe our results. The modified model is based on three key assumptions. The first is that the incremental compression or "strain" of the packed bed, $\lambda = (L_0 - L)/L_0$, is directly proportional to the flow velocity, u, and to the viscosity of the packing fluid, η . Accordingly, we have:

$$\frac{L_0 - L}{L_0} = \gamma\eta(u - u_0) \tag{2.21}$$

where L_0 and u_0 are the initial bed height and packing velocity, respectively, L is the actual bed height, and γ is a parameter that describes the compressibility of the stationary phase. The product $\gamma\eta$ is equivalent to the ratio λ_{cri}/u_{cri} defined by Stickel and Fotopoulos [18]. As seen in Figs. 2.11-2.13, this assumption is justified by the experimentally observed linear dependence of L on u, which suggests that over the range of flow rates studied experimentally, the consolidated stationary phase behaves like an elastic body.

The other two assumptions are the same as those made by Stickel and Fotopoulos [18]. The first of these is that the change in extraparticle porosity is directly related to the strain and that this change occurs without a change in particle volume or substantial deformation of the individual particles. Accordingly, we have:

$$\frac{L_0 - L}{L_0} = \frac{\varepsilon_0 - \varepsilon}{1 - \varepsilon} \tag{2.22}$$

or:

$$\varepsilon = 1 - (1 - \varepsilon_0)\frac{L_0}{L} \tag{2.23}$$

where ε_0 and ε are the column extraparticle porosities at the initial packing velocity and at the current flow velocity, respectively. The second of these assumptions is that the pressure across the packed bed is described by the Karman-Cozeny equation, which is given by the following expression [14]:

$$\Delta P = 150\frac{(1 - \varepsilon)^2}{\varepsilon^3}\frac{\eta u L}{d_p^2} \tag{2.24}$$

where L and ε are calculated from eqs. 2.21 and 2.23, respectively, for $u > u_0$. The general characteristics of this model are illustrated qualitatively in Fig. 2.14. At velocities lower than the initial packing velocity ($u < u_0$) at which the consolidated bed was locked in place, both L and ε remain constant equal to L_0 and ε_0, respectively. For these conditions, the pressure is linearly related to u according to eq. 2.24. On the other hand, as the flow velocity exceeds u_0, the bed is compressed further with a linear decrease in bed height, described by eq. 2.21, and a non-linear decrease in ε, described by eq. 2.23. For these conditions, the pressure increases rapidly and non-linearly as a result of the strong dependence of ΔP on ε predicted by eq. 2.24.

Obviously, the trends of Fig. 2.14 are in qualitative agreement with those observed experimentally. In order to obtain a quantitative comparison of these equations to the experimental data, ε_0 was first calculated from eq. 2.24 using the initial slope of the pressure-flow curves for $u < u_0$. Since, as shown in Fig. 2.14, ε has a very strong effect on ΔP according to eq. 2.24, such determination of ε_0 is expected to be rather accurate. The remaining model parameter γ was then determined from the slope of the L/L_0 vs. u data. A summary of these parameters is given in Table 2.2 and corresponding model predictions are shown in Figs. 2.10-2.13. It should be noted that during the measurement of pressure-flow curves, a small degree of compression occurred at velocities somewhat lower than the initial packing velocity, suggesting that some relaxation of the consolidated bed may have occurred during the flow-conditioning steps. Thus, somewhat different values of u_0 were used in fitting the data. As seen in Figs. 2.10-2.13, despite this deviation from the model assumptions, eqs. 2.21-2.24 provides an accurate description of the experimental results. More importantly, for the large-scale columns (20 cm diameter and larger) both ε_0 and γ appear to be essentially independent of column size, initial aspect ratio, and mobile phase viscosity. The relatively small difference in the γ-values appears to be statistically insignificant and is within the error of the experimental determinations of pressure. This result is different from the results of Mohammad et al. [34] and Stickel and Fotopoulos [18] who found that their model parameters were dependent on column aspect ratio and, in the case of Stickel and Fotopoulos [18], on mobile phase viscosity. This difference is perhaps due to the relative rigidity of UNOsphere SUPrA compared to the much softer resins used by these previous authors.

Table 2.2. Parameters obtained by fitting the pressure-flow curves with eqs. 2.21-2.24

Column. diam. (cm)	L_0 (cm)	ε_0	$\gamma\,(10^{-4}$ h/cm·mPa·s)
Data for water ($\eta = 1.00$ mPa·s)			
1.0	9.8	0.39	0.62
20	21.5	0.40	1.5
30	9.4	0.37	1.5
30	17.2	0.36	1.3
45	8.6	0.40	1.8
45	14.4	0.41	1.7
45	18.0	0.39	2.6
Average values for preparative columns =		0.39±0.02	1.7±0.5
Data for 10% glycerol ($\eta = 1.37$ mPa·s)			
20	21.5	0.41	1.5
30	9.4	0.39	1.8
30	17.2	0.37	1.6
45	8.6	0.39	1.8
45	14.4	0.42	1.5
45	18.0	0.37	1.5
Average values for preparative columns =		0.39±0.02	1.6±0.2
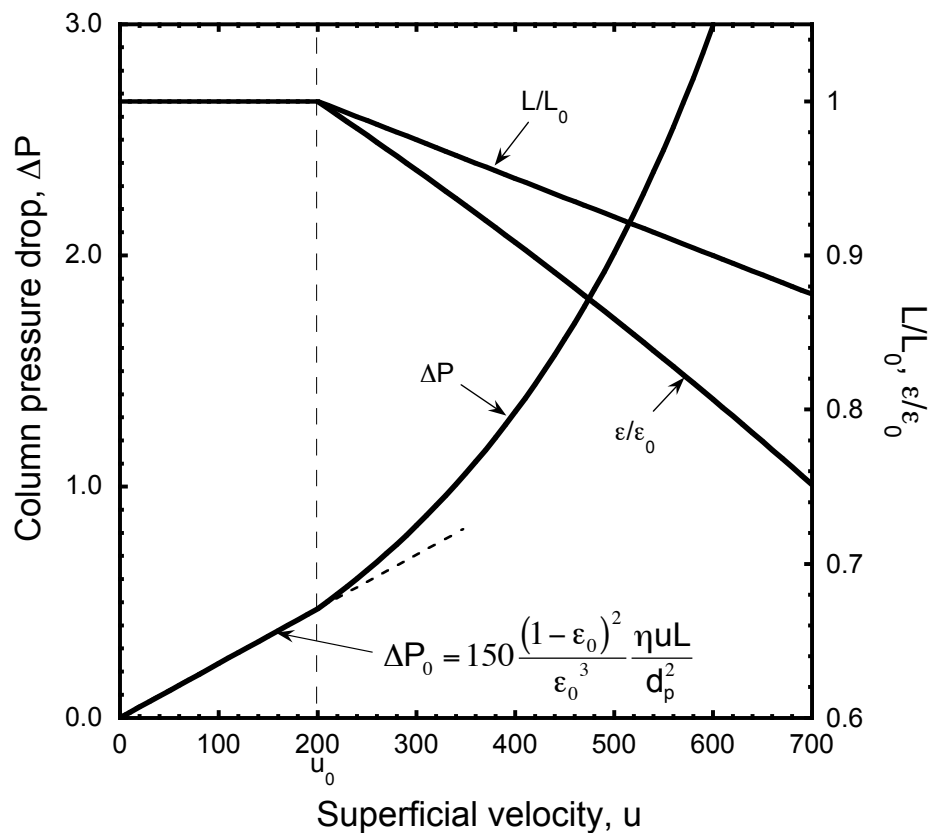
Fig. 2.14. General relationship between column pressure, porosity, and bed length and superficial velocity predicted by Eqs. (2.21-2.24). Note that according to the model, L/L_0 and $\varepsilon/\varepsilon_0$ are constant and ΔP is linear for $u < u_0$.

The 1-cm column, on the other hand, gave a much lower γ for UNOsphere SUPrA suggesting that in this case, the column wall provides substantial support to the packed bed giving the appearance of a less compressible matrix. Finally, it should be noted that γ could, in principle, depend on the way in which the bed is initially consolidated. However, given its relative constancy for preparative-scale columns of rather different diameters and proportions, such dependence is not expected to be large in practice unless very large deviations from the bed consolidation protocols used in this work are used.

2.3.7. Optimization of productivity

The maximum productivity attainable for a cyclic adsorption-desorption operation is useful as a tool to compare different resins. Moreover, when the adsorbent is particularly expensive, conditions that maximize productivity can also be close to the true economic optimum. The specific productivity, P, is defined as the amount of protein product recovered upon elution divided by the adsorbent volume and by the total processing time. The latter includes the times needed to load the feed on the column, t_{Load}, wash unretained impurities, t_{Wash}, desorb the product, t_{Desorb}, and clean and reequilbrate the adsorbent, t_{Clean} and t_{Equil}, respectively. Accordingly:

$$P = \frac{\text{Amount of protein recovered}}{\text{Column volume} \times \text{Total cycle time}} \qquad (2.25)$$

where:

$$\text{Total cycle time} = t_{Load} + t_{Wash} + t_{Desorb} + t_{Clean} + t_{Equil} \qquad (2.26)$$

In some instances, a "strip" step is also included prior to cleaning, although this is not considered explicitly in this work. Several models are available in the literature to predict P as a function of operating conditions [35-37]. Our approach is similar to that of Yamamoto and Sano [35]. Following these authors, we assume that the amount of protein recovered can be expressed as the

amount of protein retained in the adsorption column times a recovery ratio, η_E, which reflects product losses due to leakage from the column and irreversible binding. Accordingly, the amount of protein recovered is given by $\eta_E \times DBC \times V_c$, where V_c is the column volume and DBC is the dynamic binding capacity at a specified percentage of breakthrough. The latter is usually small, typically 10% or less, so that, in practice, little leakage of the product occurs prior to breakthrough. We also assume that t_{Wash}, t_{Desorb}, and t_{Equil} can be expressed as a function of the number of column volumes of wash, desorb and reequilibrate solutions, so that the time for each of these steps can be expressed as the product of the number of column volumes (CV) required for that step times the corresponding residence time, L/u. This assumption is justified below. Finally, in our work, we also consider the time needed to clean the adsorbent between successive feed loads. This time is generally not dependent on the number of column volumes of cleaning solution passed and remains expressed as the time of exposure to the cleaning solution. The final expression for P derived on the basis of the above considerations is as follows:

$$P = \frac{\eta_E \times DBC}{\dfrac{DBC}{C_F}\dfrac{L}{u_{Load}} + \left(CV_{Wash} + CV_{Desorb} + CV_{Equil}\right)\dfrac{L}{u_E} + t_{Clean}} \tag{2.27}$$

In this equation, C_F is the protein feed concentration and t_{Load} is expressed as:

$$t_{Load} = \frac{DBC \times V_c}{C_F \times Q_{Load}} = \frac{DBC}{C_F}\frac{L}{u_{Load}} \tag{2.28}$$

where L is the column length and Q_{Load} is the protein feed flow rate. Note that, for simplicity, we have assumed the same residence time, L/u_E, for wash, desorb, and reequilibrate steps. When mass transfer is controlling, the DBC is an increasing function of residence time, L/u_{Load}. Since this function appears in eq. 2.27 both in the numerator and in the denominator where it is multiplied times L/u_{Load}, it is obvious that there is a value of L/u_{Load} that maximizes P.

A detailed model was already developed in this chapter to describe the IgG adsorption kinetics and predict the breakthrough curves for UNOsphere SUPrA. This model required numerical solution of the governing equations taking into account the IgG binding kinetics. A simpler semi-empirical model can also be used to describe the dynamic binding capacity when the time scale of the load step is sufficiently short that adsorption on slow binding sites can be neglected. This assumption is conservative and actual results could be expected to exceed predictions made on this basis. As shown in this work, this occurs at IgG concentrations about 1 mg/mL or higher and for residence times smaller than about 5 min. In this case, the adsorption isotherm can be considered rectangular and band broadening is virtually completely dominated by intraparticle diffusion. For these conditions, the *DBC* model of Carta et al. [20] can be used for both constant-pattern and non-constant pattern conditions. Accordingly, the *DBC* at 10% of breakthrough is given by the following expressions:

$$DBC = \begin{cases} EBC \times \left(0.36n - 0.061n^2 + 0.0042n^3\right) & \text{for} \quad n < 2.5 \\ EBC \times \left(1 - 1.03/n\right) & \text{for} \quad n > 2.5 \end{cases} \quad (2.29)$$

where, in this case, *EBC* is the apparent equilibrium binding capacity and *n* is the number of transfer units. In turn, the *EBC* is related to the adsorption capacity, q_m, and the extraparticle void fraction, ε, by the following equation:

$$EBC = \varepsilon C_F + \left(1 - \varepsilon\right)q_m \quad (2.30)$$

while *n* is related to the effective intraparticle diffusivity, D_e , and the particle diameter, d_p, by the equation:

$$n = 60\left(1 - \varepsilon\right)\frac{D_e}{d_p^2}\frac{L}{u} \quad (2.31)$$

DBC data at 10% of breakthrough were obtained for UNOsphere SUPrA and are presented in Section 2.3.4 for columns with $\varepsilon = 0.35$. The results are shown in Fig. 2.15 in

comparison with eq. 2.29 with apparent values of *EBC* and D_e obtained by non-linear least square fit of the data. The corresponding fitted values, *EBC* = 25 mg/mL (corresponding to q_m = 38 mg/mL) and D_e = 5.8x10^{-8} cm^2/s are both lower than the true values determined in Section 2.3.3 of this chapter (q_m = 46 mg/mL and D_e = 8.0x10^{-8} cm^2/s). Nonetheless, the model provides an adequate semi-empirical description of the relationship between *DBC* and L/u.

The last parameters needed to determine conditions that maximize productivity are the column volumes required for wash, desorption, and reequilibration. This determination was made empirically, based on laboratory-scale data. Figure 2.16 shows representative results for a 4.9 cm UNOsphere SUPrA column fully loaded with 1 mg/mL IgG showing the wash and desorption steps conducted, respectively, with 150 mM NaCl in 10 mM Na$_2$HPO$_4$ at pH 7.4 and with 100 mM glycine at pH 3.0. The experiments were conducted at superficial velocities of 300, 460, 611, and 765 cm/h, corresponding to residence times between 0.96 and 0.38 min. During desorption, the UV detector became saturated at concentration greater than 10 mg/mL so that the actual maximum product concentration could not be determined from the UV traces. Nonetheless, it is apparent that the wash and desorption curves are practically independent of residence times down to 0.38 min and are virtually complete within about 4 CV's each. Reequilibration was also quite fast and fewer than 4 CV's were sufficient to restore the initial conditions in equilibrium with the phosphate buffer.
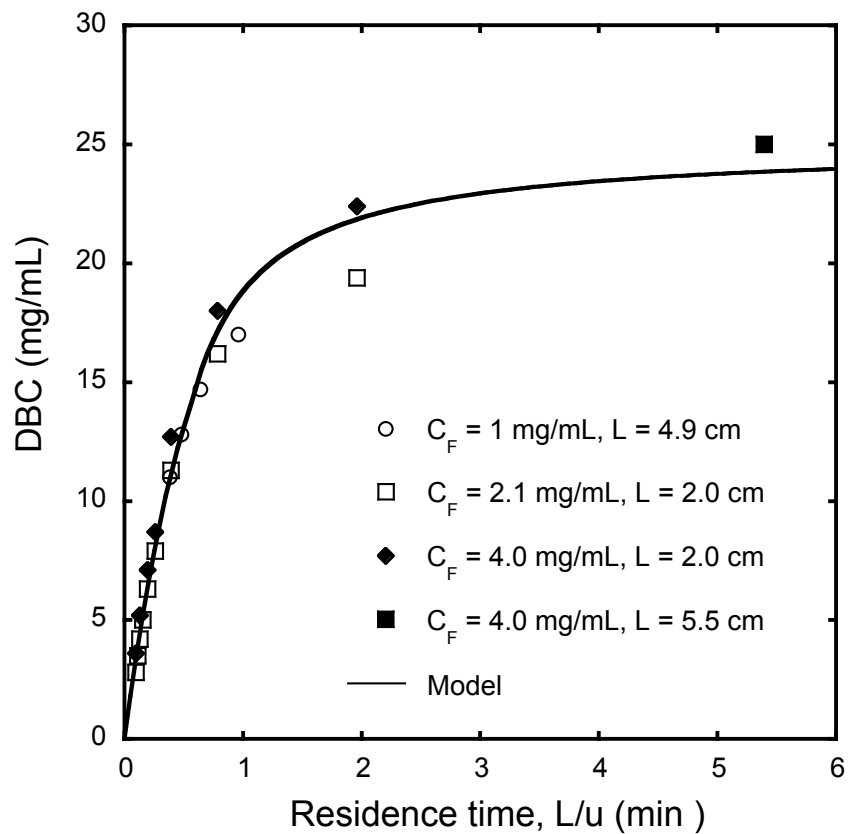
Fig. 2.15. Relationship between dynamic binding capacity and residence time determined from results in the adsorption kinetics section of this chapter. The line is calculated from eq. 2.29 with $EBC = 25$ mg/mL and $D_e = 5.8 \times 10^{-8}$ cm^2/s.
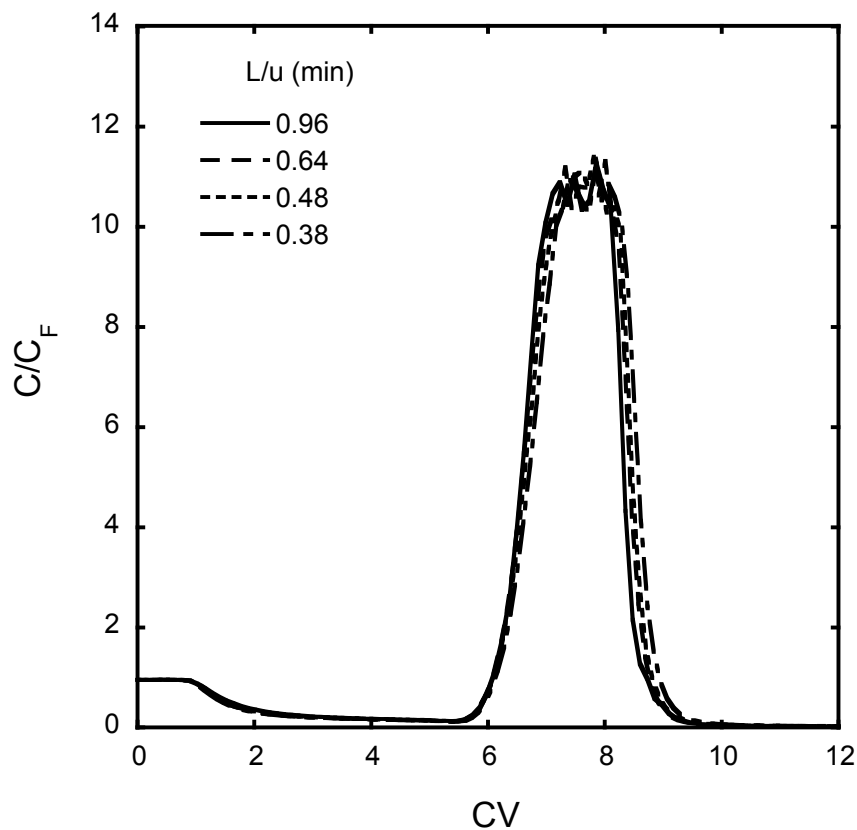
Fig. 2.16. Wash and desorption curves obtained at different flow rates for a 0.5x4.9 cm UNOsphere SUPrA column fully saturated with 1 mg/mL IgG. Wash with 150 mM NaCl in 10 mM Na_2HPO_4 at pH 7.4 for 5CV and desorption with 100 mM glycine at pH 3.0 for 5 CV. Values of $C/C_F > 10$ are unreliable because of saturation of the UV detector.

Figure 2.17 shows a plot of productivity as a function of the load step residence time calculated from eq. 2.27 for L/u_E =1 min and assuming a 2 mg/mL IgG feed concentration and ε = 0.39. The latter value corresponds to columns packed at 300 cm/h (Table 2.2). t_{Clean} was assumed to be 20 min. The results show a maximum productivity at a residence time of about 1 min and this value occurs when the ratio DBC/EBC is about 0.8. The trends are similar at different IgG feed concentrations, although the optimum residence time shifts to higher values per eq. 2.27.

2.3.8. Column design example

Actual preparative column designs that maximize productivity and satisfy specified pressure constraints can be obtained based on the results of this work. An illustrative numerical example follows for the conditions of Fig. 2.16 assuming a feed viscosity of 1.37 mPa s and imposing a maximum ΔP constraint of 2 bar. From Fig. 2.17, the optimum residence time was found to be 1.1 min. Thus, the remaining design parameter is the actual column length, which requires a trial and error calculation. This calculation is done as follows. Based on eq. 2.21, we have $(1-\varepsilon)L = (1-\varepsilon_0)L_0$. Thus, within the bounds of our determinations, the number of transfer units (see eq. 2.31) is unaffected by compression of the packing and is equal to 4.3. The main effect is, thus, on the EBC, which varies with compression according to eq. 2.30. We begin by assuming that the optimum n remains the same for the compressed columns. In this case, by trial and error we obtain ΔP = 2 bar for L_0 = 13.5 cm with ε_0 = 0.39, which corresponds to u = 736 cm/h. At this velocity, using the average value of γ = 1.6x10^{-4} h/cm·mPa·s (Table 2.2), we calculate L = 12.2 cm and ε = 0.325, based on eqs. 2.21 and 2.23. The corresponding column pressure drop is calculated from eq. 2.24. Based on eq. 2.27, for these conditions the L/u that maximizes P is predicted to decrease from the initially guessed value.
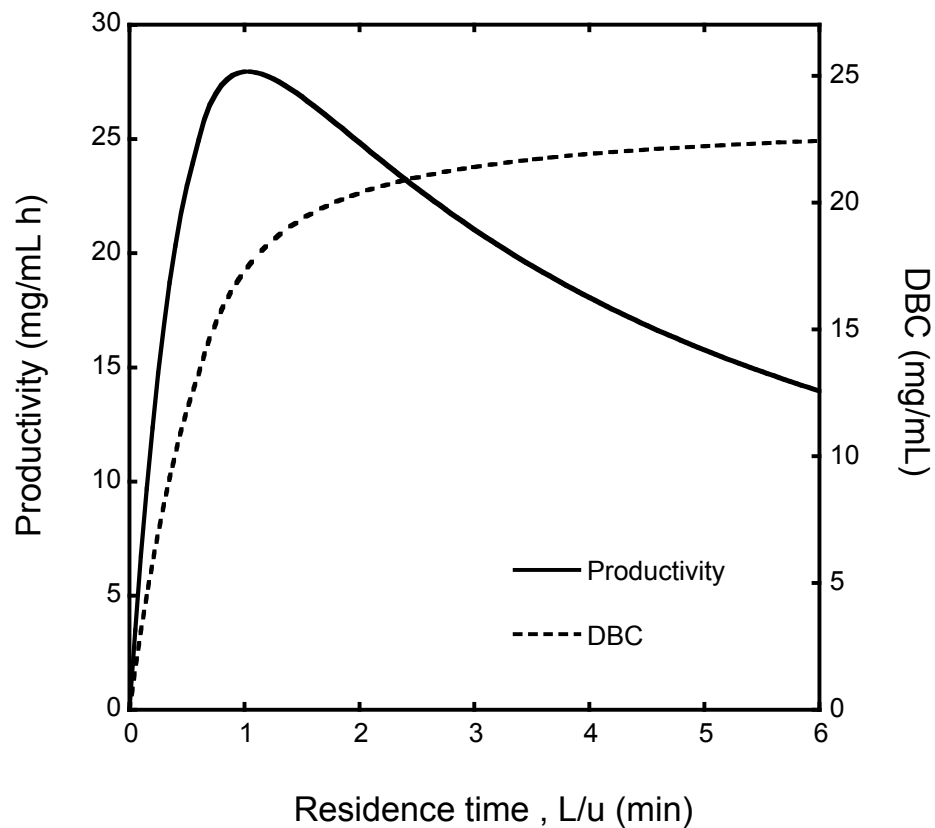
Fig. 2.17. Productivity and *DBC* curves calculated from eq. 2.27 and 2.29 with $C_F = 2$ mg/mL,

$\eta_E = 1$, $CV_{Wash} = CV_{Desorb} = 5$, $CV_{Equil} = 4$, $L/u_E = 1$ min, $\varepsilon = 0.39$, $t_{Clean} = 20$ min.

However, this decrease is very slight so that the same value of $L/u = 1.1$ is adequate. The productivity increases, however, to about 27 mg/mL h as a result of the higher EBC caused by the lower ε in the compressed column.

2.4. Conclusions

The new protein adsorbent considered in this work is characterized by a relatively large pore size and small particle size with a narrow particle size distribution. The IgG batch adsorption kinetics is relatively fast achieving adsorbed concentrations of 40 mg/mL in less than 1,800 s at a 1 mg/mL solution concentration, primarily as a result of the relatively small particle size and high intraparticle effective diffusivity. Additional IgG, up to a total of about 46 mg/mL, is adsorbed on a much longer time scale, likely as a result of a kinetic resistance to binding on slow binding sites. The breakthrough curves obtained in short columns show substantial dynamic binding capacity at residence times as short as 30 s as a result of rapid mass transfer in the relatively small particles. The tailing behavior of the breakthrough curves, evident especially at longer residence times, appears consistent with the existence of slow and fast binding sites, the former constituting a relatively small percentage of the total binding capacity. The heterogeneous binding model developed in this chapter provides a quantitative description of both batch adsorption kinetics and breakthrough curves with only two fitted parameters that remain invariant over a broad range of conditions tested. Based on this result, we conclude that the intraparticle effective diffusivity of IgG is unaffected by the protein solution concentration and is the same for binding and non-binding conditions, likely as a result of the large pore size of the support matrix.

Furthermore, the results show that the UNOsphere SUPrA is compressible to some extent especially in preparative scale columns, 20 to 45 cm in diameter. However, the compressibility

of the packing is predictable using a modified version of the model of Stickel and Fotopoulos [18] as a function of viscosity, initial bed height, and flow velocity. Surprisingly, the results show that the column diameter does not influence the compression of the packing for the range of preparative scale columns considered. As a result, column pressure can be readily predicted as a function of scale. The productivity model developed based on *DBC*-data allows the selection of operating conditions that maximize productivity. The combination of the pressure flow model with the *DBC*-model provides column designs that maximize productivity while satisfying specified column pressure constrains.

2.5. List of symbols

c protein concentration in particle pores (mg/mL)

C protein concentration in solution (mg/mL)

C_F protein feed concentration (mg/mL)

C_0 initial protein concentration (mg/mL)

DBC dynamic binding capacity (mg/mL of column volume)

D_e effective pore diffusivity (cm^2/s)

D_0 free solution diffusivity (cm^2/s)

d_p particle diameter (cm)

EBC equilibrium binding capacity (mg/mL of column volume)

k' retention factor

K adsorption constant in Langmuir model (mL/mg)

K_D distribution coefficient based on particle volume

L bed height (cm)

L_0 initial packed bed height (cm)

n_{pore} number of transfer units for pore diffusion, $\dfrac{60(1-\varepsilon)D_e}{d_p^2}\dfrac{L}{u}$

n_{film} number of transfer units for film mass transfer, $\dfrac{6(1-\varepsilon)k_f}{d_p}\dfrac{L}{u}$

q adsorbed protein concentration (mg/mL)

q_m maximum adsorption capacity in Langmuir model (mg/mL)

r_p particle radius (cm)

r_{pore} pore radius (cm)

r_s molecule radius (cm)

Sh Sherwood number, $\dfrac{k_f d_p}{D_0}$

u superficial velocity (cm/s)

u_0 initial packing velocity (cm/s)

t time (s)

Greek symbols

γ parameter describing the compressibility of the consolidated bed, eq. 1 (s cm^{-1} Pa^{-1})

ε extraparticle porosity

ε_0 initial extraparticle porosity

ε_p Intraparticle macroporosity

η viscosity (Pa s)

η_E fractional product recovery

2.6. References

[1]   R.L. Fahrner, H.L. Knudsen, C.D. Basey, W. Galan, D. Feuerhelm, M. Vanderlaan, G.S. Blank, Biotechnol. Gen. Eng. Rev. 18 (2001) 301.

[2]   G. Blank, Recovery of Biological Products X Conference, Cancun, Mexico, 2001.

[3]   S. Ghose, M. Allen, B. Hubbard, C. Brooks, S.M. Cramer, Biotechnol. Bioeng. 92 (2005) 665.

[4]   A.A. Shukla, B. Hubbard B, T. Tressel , S. Guhan, D. Low J. Chromatogr. B. 848 (2007) 28.

[5]   N. Tugcu, D.J. Roush, K.E. Gocklen, Biotechnol. Bioeng. 99 (2007) 599.

[6]   R.L. Fahrner, D.H. Whitney, M. Vanderlaan, G.S. Blank, Biotechnol. Appl. Biochem. 30 (1999) 121.

[7]   J.T.McCue, G. Kemp, D. Low, I. Quinones-Garcia, J.Chromatogr. A 989 (2003) 139.

[8]   R. Hahn, R. Schlegel, A. Jungbauer, J. Chromatogr. B 790 (2003) 35.

[9]   A. Jungbauer, R. Hahn, Curr. Opin. Drug Disc. Dev. 7 (2004) 248.

[10]   R. Hahn, P. Bauerhansl, K. Shimahara, C. Wizniewski, A. Tscheliessnig, A. Jungbauer, J. Chromatogr. A 19093 (2005) 98.

[11]   K. Swinnen, A. Krul, I. Goidsenhoven, N. van Tichelt, A. Rosen, K. van Houdt, J. Chromatogr. B. 848 (2007) 97.

[12]   T. E. Bankston, M. C. Stone, G. Carta, J. Chromatogr. A 1188 (2008) 242.

[13]   F. Wurm, Nat. Biotechnol. 22 (2004) 1393.

[14]   R.B. Bird, W.E. Stewart, E.N., Lightfoot, Transport Phenomena, Wiley, New York, 1960, pp. 196-200.

[15]   G. Sofer, L. Hagel, Handbook of Process Chromatography: A Guide to Optimization, Scale-up and Validation, Academic Press, San Diego, 1997, pp. 100-101, 361-365.

[16]   M.D. LeVan, G. Carta, in: D.W. Green, R.H. Perry (Eds.), Perry's Chemical Engineers' Handbook, Section 16: Adsorption and Ion Exchange, eighth ed., McGraw-Hill, New

York, 2007.

[17]   G.K. Sofer, L.E. Nystrom, Process Chromatography- a Practical Guide, Academic Press, San Diego, 1989, p.56.

[18]   J.J. Stickel, A. Fotopoulos, Biotechnol. Progr. 17 (2001) 744.

[19]   A.K. Hunter, G. Carta , J. Chromatogr. A 897 (2000) 65.

[20]   G. Carta, A.R. Ubiera, T.M. Pabst, Chem. Eng. Technol. 28 (2005) 1.

[21]   L. Hagel, M. Ostberg, T. Andersson, J. Chromatogr. A 743 (1996) 33.

[22]   W.W. Yau, J.J. Kirkland, D.D. Bly, Modern Size Exclusion Liquid Chromatography, Wiley, New York, 1979.

[23]   P.G. Squire, J. Chromatogr. 210 (1981) 433.

[24]   M.P. Schwartz, S.D. Alvarez, M.J. Sailor, Anal. Chem. 79 (2007) 327.

[25]   M.Y. Tyn, T.W. Gusek, Biotechnol. Bioeng. 35 (1990) 327.

[26]   G. Carta, A. R. Ubiera, AIChE J. 49 (2003) 3066.

[27]   N.K. Teo, D.M. Ruthven, Ind. Eng. Chem. Process Des. Dev. 25 (1986) 17.

[28]   M.C. Stone, Y. Tao, G. Carta, J. Chromatogr. A 1216 (2009) 4465.

[29]   C. Boi, S. Dimartino, G. Sarti, J. Chromatogr. A 1162 (2007) 24.

[30]   M.C. Stone, G. Carta, J. Chromatogr. A 1146 (2007) 202.

[31]   P. Armenante, D.J. Kirwan, Chem. Eng. Sci. 44 (1989) 2781.

[32]   T.S. Weber, R.K. Chakravorti, AIChE J. 20 (1974) 228.

[33]   M.K. Joustra, A. Emneus, P. Tibbling, Protides Biol. Fluids 15 (1967) 575.

[34]   A.W. Mohammad, D.G. Stevenson, P.C. Wankat, Ind. Eng. Chem. Res. 31 (1992) 549.

[35]   S. Yamamoto, Y. Sano, J. Chromatogr. 597 (1992) 173.

[36]   A.E. Rodrigues, J.M. Loureiro, C. Chenou, M.R. De La Vega, J. Chromatogr B 664

(1995) 233.

[37]   R.L. Fahrner, H.V. Iyer, G.S. Blank, Biopr. Eng. 21 (1999) 287.

Chapter 3

Characterization of Nuvia S and Single-component Adsorption

3.1. Introduction

As discussed in Chapter 1, increasing titers obtained from advances in fermentation and cell culture used for the manufacture of recombinant therapeutic proteins have shifted production constraints from upstream to downstream processing [1-3]. While feasible at very large scales [4], biopharmaceutical purification remains challenging because column size is typically limited by mechanical and technological factors as well as by the space constraints of GMP manufacturing suites. Thus, alternative stationary phases that have higher protein binding capacities, fast adsorption kinetics, and high mechanical strength are desirable [5]. In general, high protein binding capacities in ion exchange can be attained with soft gels, but these tend to have poor mechanical properties. Rigid porous media, on the other hand, tend to have excellent flow properties, but have limited binding capacity. Thus, composite matrices, where either a soft-gel or grafted polymers are incorporated in a rigid support structure are of interest, since they can combine both desirable properties, resulting in high capacity and excellent mechanical properties.

The objective of this work is to investigate the effects of charged polymeric surface extenders on protein adsorption capacity and transport in stationary phases based on a rigid backbone matrix. Specifically, we have studied the adsorption equilibrium and rate behavior of

two model proteins, lysozyme and a monoclonal antibody (mAb), in two stationary phases that are based on essentially the same macroporous structure – one without surface extenders and the other with charged polymeric extenders. Macroscopic and microscopic results show that adsorption equilibrium and kinetics are not only quantitatively different but they are driven by different mechanisms apparently originating from interactions with the surface extenders.

3.2. Experimental methods

3.2.1. Materials

The two cation exchangers used in this work are UNOsphere S and Nuvia S both from Bio-Rad Laboratories (Hercules, CA, USA). Both are based on similar crosslinked polyacrylamide copolymers. However, while UNOsphere S has an open macroporous structure Nuvia S contains proprietary sulfonated polymeric surface extenders. Thus, while Nuvia S is the principal objective, UNOsphere S is used as a control. Micrographs of these materials are shown in Fig. 3.1. In both cases, the particles are primarily spherical and have similar particles size distributions, but different mean diameters of 75±13 and 85±10 μm, for UNOsphere S and Nuvia S, respectively. An experimental sample containing an unsulfonated version of the polymeric surface extender of Nuvia S was also obtained from Bio-Rad Laboratories.

Hen egg white lysozyme ($M_r \sim 14.5$ kDa, pI~11) was obtained from Sigma-Aldrich (St. Louis, MO, USA, Catalog No. L-6876). A monoclonal antibody ($M_r \sim 150$ kDa, pI~8.6) was obtained from Pfizer (St. Louis, MO). Both the lysozyme and the mAb were >99 % monomer as determined by size exclusion chromatography with a Superdex 200 column (GE Healthcare, Piscatway, NJ, USA). All other chemicals were purchased from Fisher Scientific (Pittsburgh, PA, USA). Adsorption experiments were done at room temperature, 22±2 °C. Protein solutions
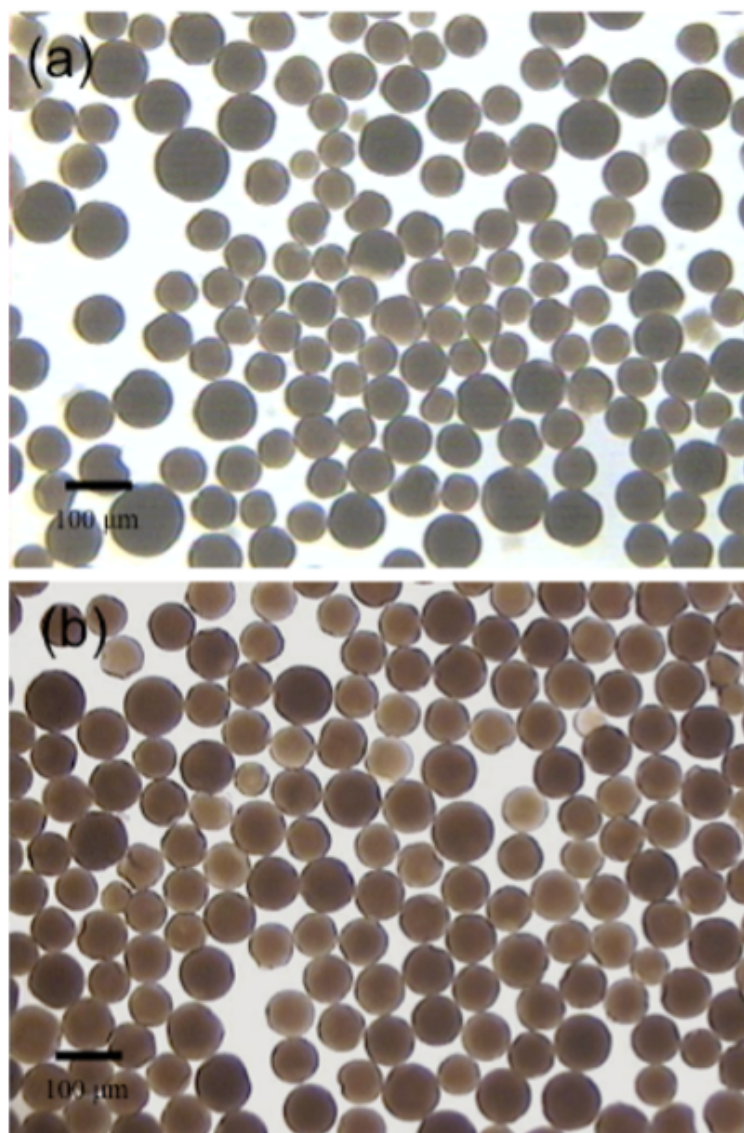
Fig. 3.1. Micrographs of UNOsphere S (a) and Nuvia S (b). Scale bar is 100 μm.

were prepared in buffers containing 10 mM Na_2HPO_4 adjusted to pH 6.5 with phosphoric acid for lysozyme and in 20 mM $NaCH_3COO$ adjusted to pH 5.0 with acetic acid for the mAb.

3.2.2. Methods

3.2.2.1. Transmission electron microscopy

Transmission electron microscopy (TEM) was done by first dehydrating the beads in a water-ethanol gradient increasing from 0 to 100% anhydrous ethanol, followed by saturating the particles with a 50% (v/v) mixture of ethanol and LRWhite embedding resin (obtained from London Resin Company Ltd, London, UK), and by 100% LRWhite resin. After curing overnight, the samples were microtomed (80 nm) and viewed with a JEOL 100 CX transmission electron microscope.

3.2.2.2. Inverse size exclusion chromatography

Inverse size exclusion chromatography (iSEC) was done using neutral dextran standards obtained from Amersham Biosciences (Piscataway, NJ, USA) and Spectrum Chemicals (New Brunswick, NJ, USA) and glucose to determine the accessible pore as described in detail elsewhere [14]. The extraparticle porosity, ε, was determined by measuring the column pressure drop as a function of flow rate in conjunction with the Karman-Cozeny equation.

3.2.2.3. Adsorption isotherms

Adsorption isotherms were determined by equilibrating samples of the adsorbents with solutions containing different initial protein concentrations for 24 to 40 hours. For this purpose, adsorbent samples were first equilibrated in either the sodium acetate or sodium phosphate buffers as needed, then placed in 1.5 ml filter centrifuge tubes obtained from Millipore (Billerica, MA, USA), and centrifuged at 5000 rpm for 10 min to remove the extraparticle liquid. Samples

of the centrifuged particles (5 to 15 mg) were then weighed and added into 1.5 or 3.0 ml vials containing protein solutions with known initial concentration and rotated slowly end-over-end on a rotator at a few rpm. After equilibration, the supernatant was analyzed spectrophotometrically at 280 nm with a Nanovue spectrophotometer (GE Healthcare, Piscataway, NJ, USA) and the amount of protein adsorbed determined by material balance. The mass of particles used was converted to the corresponding particle volume using the density of the hydrated particles determined with a pycnometer. The latter was 1.08±0.01 g/mL for both materials.

3.2.2.4. Adsorption kinetics

Protein uptake rates were measured by suspending a known amount of adsorbent (determined as described in Section 3.3) in 20 mL of protein solutions in a stirred batch apparatus described elsewhere [14, 15]. The amount of adsorbent added was different in each case, varying between 15 and 70 mg, with the actual amount chosen based on the adsorption isotherms to yield a final protein concentration about equal to one half of the initial value. The amount of protein bound at each time step was determined by material balance from the initial and current solution concentration obtained from the UV absorbance at 280 nm.

3.2.2.5. Confocal microscopy

Following prior work [16-20], confocal laser scanning microscopy (CLSM) was used to image the movement of the mAb within the beads. For this purpose, the mAb was conjugated with Rhodamine Red™-X dye obtained from Invitrogen (Carlsbad, CA, USA) according to the dye supplier instructions. For this purpose, the mAb was incubated with a dye-to-protein molar ratio of 3:1 in a pH 8.5 sodium bicarbonate buffer for 1 hour at room temperature. The unreacted dye was separated by size exclusion chromatography using PD 10 desalting columns from GE Healthcare. An average labeling ratio of 0.21 was obtained, as quantified by UV/Vis

spectrophotometry. Gradient elution cation exchange chromatography of the conjugated and free

mAb was done with a 1 mL Source 30S column with a sodium chloride gradient at pH 5.0.

Confocal microscopy was carried out using a Zeiss LSM 510 microscope with a Plan-

Apochromat 63x/1.4NA oil objective (Carl Zeiss MicroImaging, LLC, Thornwood, New York,

NY, USA). Measurements were made batchwise. For this purpose samples of the particles were

incubated in protein solutions (10 mL) in a 15 mL tube and rotated end-over-end on a rotator. At

periodic time intervals a 400 μL sample was removed from the tube and rapidly centrifuged to

separate the particles from the supernatant. The particles were then rapidly placed in a buffered

40% (w/w) sucrose solution selected to provide an approximate match of the particle refractive

index as indicated by the optical clarity gained by the particles in this solution. The labeled

protein was diluted with the corresponding unlabeled protein to yield a 1 to 40 molar ratio of

labeled to unlabeled. Because of the different binding capacities and particle sizes, different laser

transmission and gain settings were used in each experiment in order to optimize CLSM

performance and avoid saturating the CCD detector. Confocal scans were obtained and

equatorial optical sections collected and digitized using ImageJ analysis software [21].

Although a detailed theory has been presented to account for refraction and fluorescence

attenuation effects [22], the following empirical approach similar to that of Dziennik et al. [23]

was used in this work. Digitized intensity profiles were first normalized by the maximum

intensity at the particle surface (I_m) and then corrected for signal attenuation effects using the

intensity profile obtained for protein-saturated particles. For this purpose, the raw intensity

profile of the saturated particles was correlated with a parabolic function of radial distance from

the particle center. The actual profiles for non-saturated particles were then obtained dividing the

normalized intensity profile by the correlated intensity of the saturated particles at the same radial position.

3.3. Results and discussion

3.3.1. Particle properties

Figure 3.2 shows representative TEM's of sections of the two materials. Only the backbone matrix is apparently visible, but not the surface extenders in Nuvia S. In both cases, the backbone structure is similar to that previously reported by Hunter and Carta [24] for a UNOsphere S prototype and consists of irregular microparticulate aggregates defining an apparently random pore network with some pores as large as 500 nm. The reasons why the polymeric extenders in Nuvia S are not visible are not known. One possibility is that the polymer grafts collapsed during the drying and embedding process. Another is that their density is insufficient to obtain adequate contrast in the electron microscope. It should be noted that the structure was apparently uniform through the beads with obviously open pores all the way from the center to the external bead surface.

Figure 3.3 compares the iSEC results for the two materials at low ionic strength. For UNOsphere S, the dextran peaks are partially resolved, and even dextran with 500 kDa molecular mass appears to gain access to a significant fraction of the pore volume consistent with the open structure visible in the TEM. On the other hand, Nuvia S excludes almost completely dextrans with molecular mass of 40 kDa or larger. Only 10 kDa dextran and glucose gain significant access; the others elute close to the extraparticle void volume, ε. This result is consistent with low-density polymeric surface extenders forming a gel-like structure that fills nearly completely the entire macropore volume. Similar size exclusion properties have
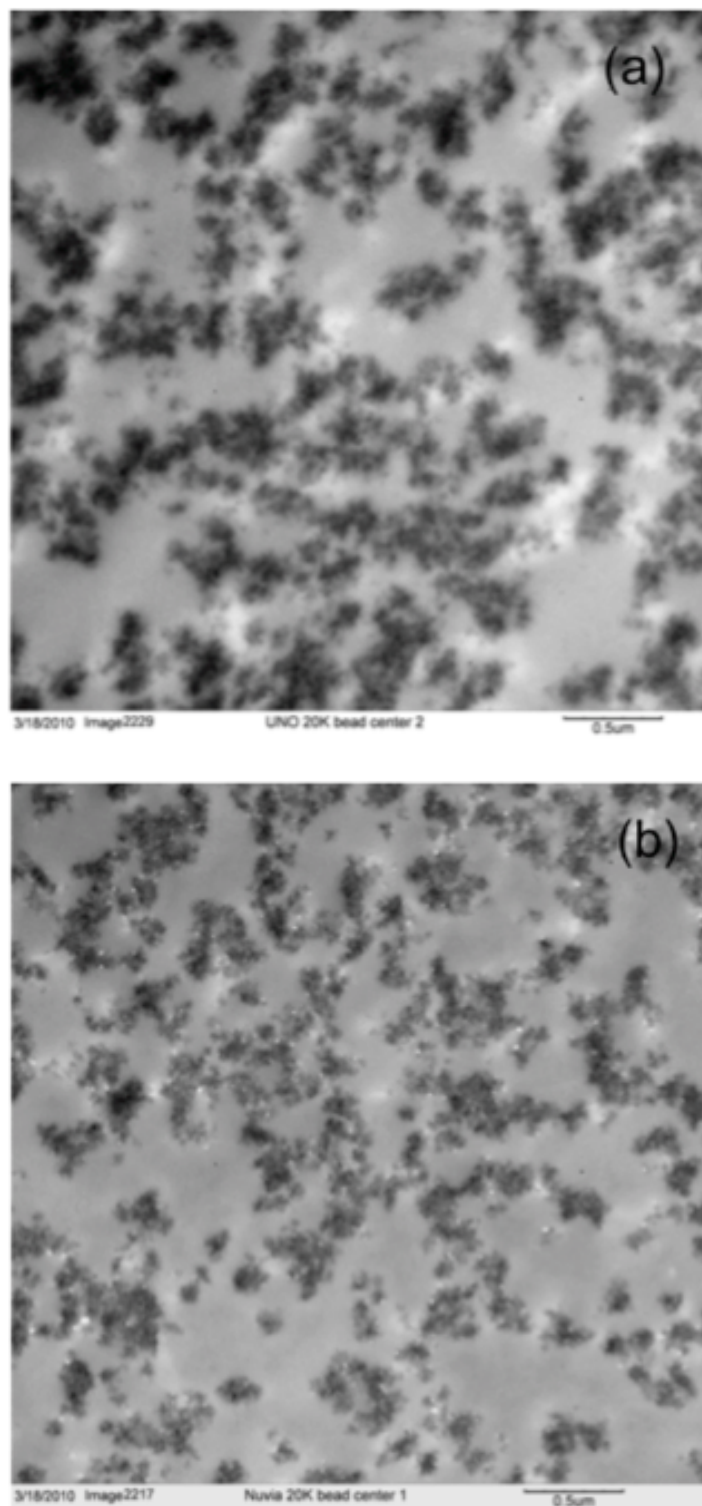
Fig. 3.2. TEM images of center sections of UNOsphere S (a) and Nuvia S (b) particles. Light grey areas are the embedding resin. Scale bar is 0.5 μm.
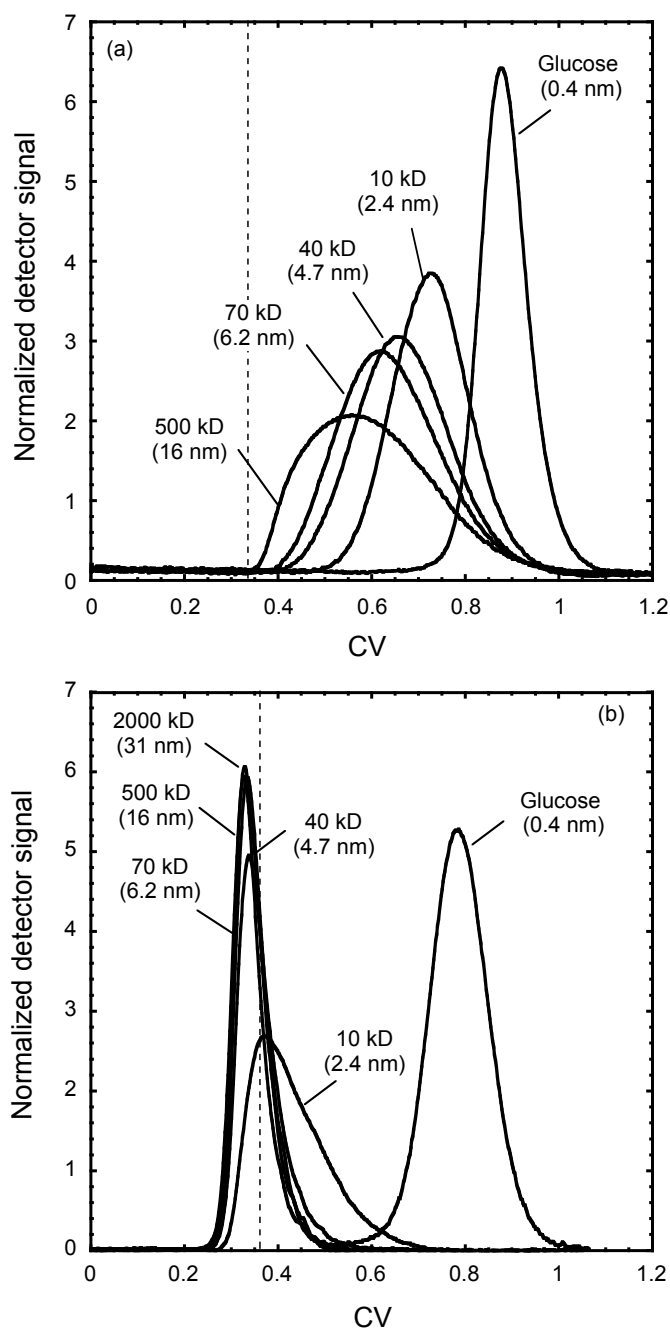
Fig. 3.3. iSEC results at low ionic strength for UNOsphere S (a) and Nuvia S (b). Dashed lines show the extraparticle porosities determined from pressure drop measurements ($\varepsilon = 0.33$ and $\varepsilon = 0.37$ for a and b respectively). Curve labels give dextran molecular mass and hydrodynamic radius estimated as the average values given by Squire [25] and Hagel et al [26].

previously been reported for other polymer-grafted media, including experimental agarose-based matrices [13-14] and commercial materials such as SP-Sepharose-XL [12, 25] and Capto S [28].

Some insight about the nature of the Nuvia S polymeric surface extenders can be obtained by comparing the iSEC results shown in Fig. 3.4 obtained in 0 M NaCl for a resin sample containing only unsulfonated surface extenders and for Nuvia S, which contains sulfonated surface extenders, in 1 M NaCl. The unsulfonated version (Fig. 3.4a) gives a good separation of the dextran standards allowing access to 70 kDa dextran and indicating a much more open pore structure than Nuvia S. Apparently, the uncharged surface extenders are at least partially collapsed on the surface even at low ionic strength. On the other hand, ionic strength had a small but significant effect on Nuvia S. In this case, adding 1 M NaCl (Fig. 3.4b) provided some accessibility to 40 kDa dextran. For the 10 kDa dextran (2.4 nm radius) the effect was even greater. In this case, retention increased from about 0.45 CV without NaCl to about 0.65 CV in 1 M NaCl. Correspondingly, the distribution coefficient K_D, calculated as $K_D = (CV - \varepsilon)/(1 - \varepsilon)$ where ε is the extraparticle void fraction, increased from 0.13 to 0.44. Sulfonation apparently causes the grafted polymers to extend away from the surface preventing access by large neutral probes. Adding NaCl likely shielded electrostatic repulsion between the negatively charged surface extenders, causing some degree of retraction toward the surface [14].

Unfortunately, these results do not provide the means for an accurate calculation of pore size for Nuvia S, since most of the probes used were completely or almost completely excluded. Nevertheless, the complete size exclusion of the 40 kDa dextran suggests radius of about 5 nm, similar to the hydrodynamic radius of the mAb (~5 nm), but larger than the hydrodynamic radius of lysozyme (~2 nm). By comparison, UNOsphere S has a mean pore radius around 68 nm [28], much larger than the hydrodynamic radius of either test protein used in this work.
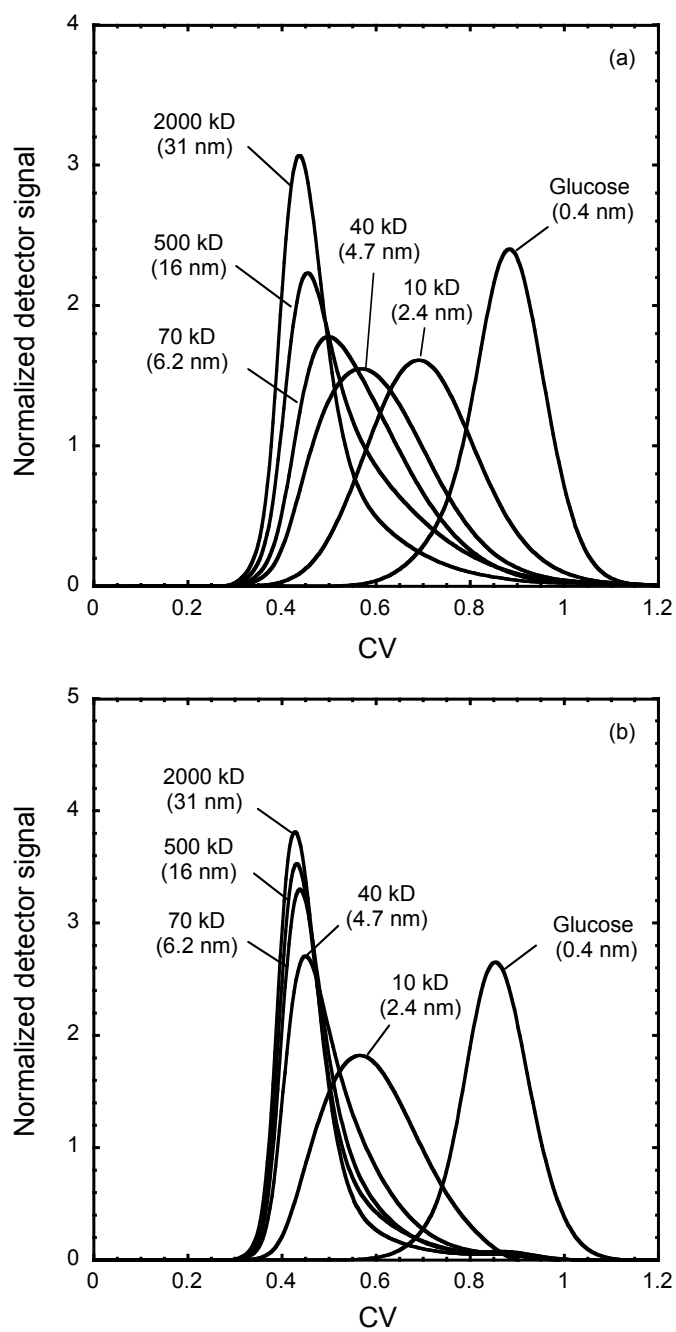
Fig. 3.4. iSEC results for the unsulfonated precursor of Nuvia S in 0 M NaCl (a) and for Nuvia S

in 1 M NaCl (b). Curve labels give dextran molecular mass and hydrodynamic radius estimated

as the average values given by Squire [25] and Hagel et al [26].

3.3.2. Adsorption isotherms

Figure 3.5 shows the adsorption isotherms for lysozyme and the mAb in phosphate buffer at pH 6.5 and in acetate buffer at pH 5.0, respectively. q is given in mg of protein bound per mL of particle volume. The corresponding binding capacities for a packed column can be found by multiplying q times the quantity $(1 - \varepsilon)$. Curves based on the Langmuir isotherm are shown to correlate the data. Both stationary phases are characterized by very sharp isotherms for these conditions. However, the binding capacity of Nuvia S is approximately double that of UNOsphere S for lysozyme and more than double for the mAb. Comparing the lysozyme and mAb behavior provides some insight. For UNOsphere S, the mAb binding capacity (120±10 mg/mL) is significantly lower than that of lysozyme (170±10 mg/mL), suggesting that the mAb is excluded from a portion of the pores and thus from a portion of the total surface area. On the other hand, the Nuvia S binding capacity is the same for both proteins (320±10 mg/mL), despite the 10-fold difference in molecular mass. This equivalence of capacities suggests a multilayer packing of the protein molecules, rather than a surface-limited adsorption mechanism.

3.3.3. Batch adsorption kinetics

Figures 3.6 and 3.7 compare the batch adsorption kinetics of lysozyme and the mAb, respectively, for the two stationary phases. For both proteins, the adsorption rate is substantially higher for Nuvia S. Moreover, the rate shows little dependence on the protein concentration in solution. Interestingly, lysozyme and the mAb exhibit almost identical adsorption kinetics on Nuvia S despite the very different molecular size. The UNOsphere S uptake curves could be described accurately by the general pore diffusion model with the same effective diffusivity regardless of initial protein concentration. Lines calculated from this model are shown in Fig. 3.6a and 3.7a. The corresponding effective pore diffusivities are $D_e = (2.6 \pm 0.3) \times 10^{-7}$ cm^2/s and
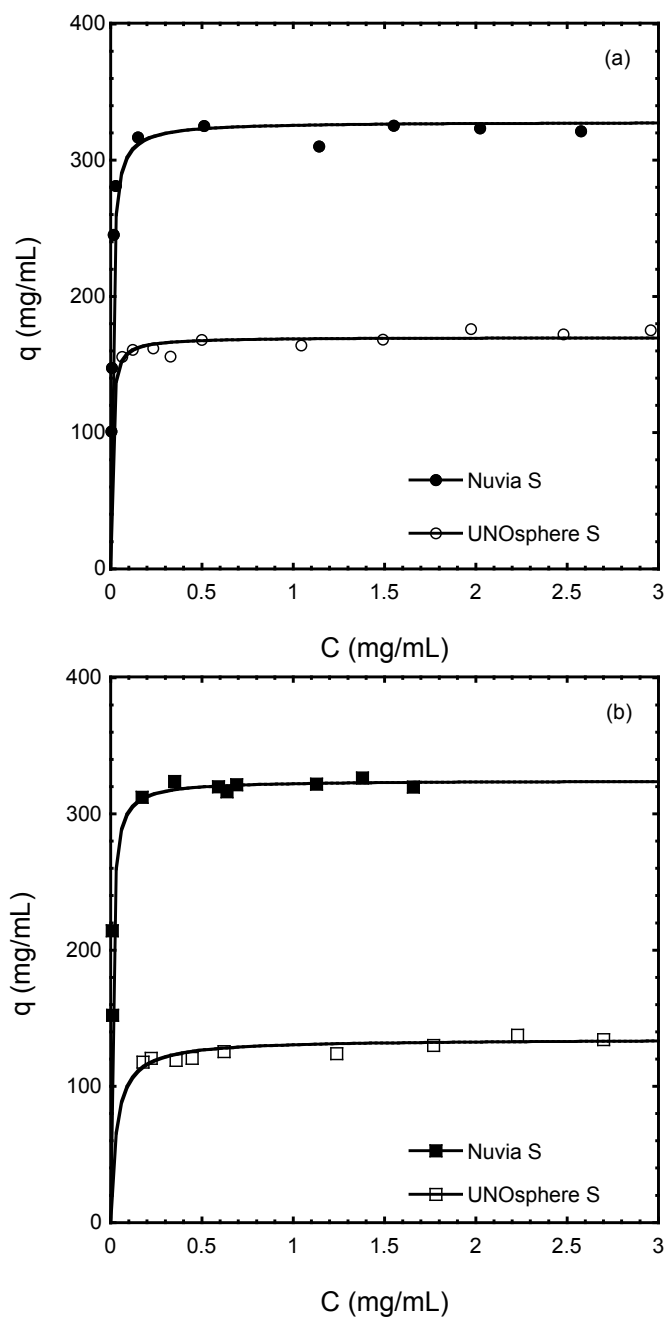
Fig. 3.5. Adsorption isotherms for (a) lysozyme in the sodium phosphate buffer at pH 6.5 and (b) mAb in the sodium acetate buffer at pH 5.0. Curves are the fitted Langmuir isotherm model, $q = q_m K/(1 + KC)$.

$(4.5\pm0.5)\times10^{-8}$ cm^2/s, for lysozyme and the mAb, respectively. Normalizing by the corresponding free solution diffusivity, D_0, estimated from the correlations in Tyn and Gusek [30], these values yield $D_e/D_0 = 0.24\pm0.03$ and 0.12 ± 0.01 for lysozyme and the mAb, respectively, which are typical for ordinary pore diffusion of proteins in ion exchangers [15].

For Nuvia S, on the other hand, neither the time trend nor the relative independence on protein solution concentration could be described accurately by the pore diffusion model. An approximate fit of the data gave D_e-values increasing from about 5×10^{-7} cm^2/s at 1 mg/mL initial concentration to 4×10^{-6} cm^2/s at 0.2 mg/mL. These values are 2 to 10 times larger than those obtained for UNOsphere S and become several fold larger than the free solution diffusivity at low protein concentrations. Qualitatively, the Nuvia S results are consistent with a solid diffusion model where the driving force is given by the adsorbed protein concentration gradient [15, 31-34]. As a result, since the adsorbed protein concentration is virtually flat (see Fig. 3.5), the adsorption rate becomes essentially independent of liquid-phase protein concentration [9].

3.3.4. CLSM

CLSM was used to follow the movement of protein molecules within the beads. Interpretation of the results requires a careful analysis since fluorescent labeling can alter the protein adsorption properties potentially resulting in artifacts [15, 35]. Additionally, fluorescence attenuation, scattering and light refraction within the beads can affect the results [19, 22-23]. Figures 3.8 and 3.9 show the results of two key control experiments. The first shows the Source 30S cation exchange chromatography of free and conjugated mAb with detection at 280 and 570 nm, respectively. The latter wavelength corresponds to the absorbance maximum of the fluorescent dye. Since the unconjugated protein does not absorb light significantly at this wavelength, the 570 nm signal provides the behavior of the conjugated protein only. As seen in
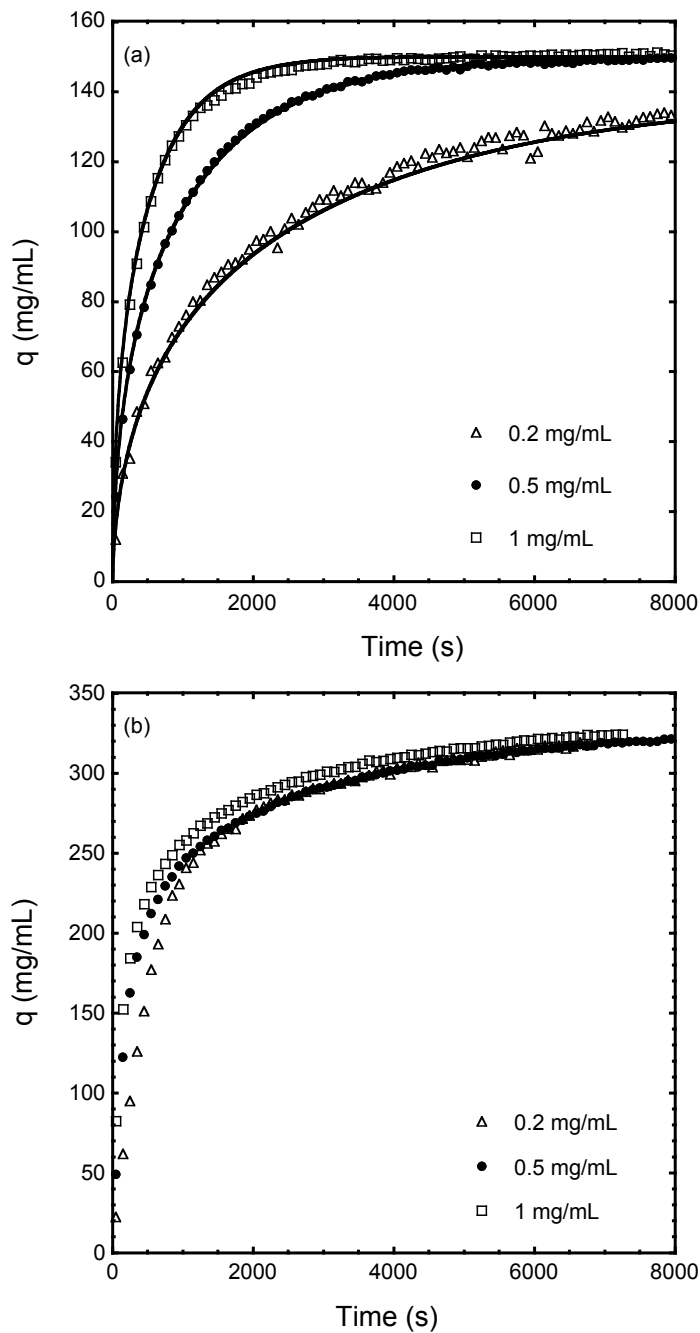
Fig. 3.6. Batch uptake curves for lysozyme on UNOsphere S (a) and Nuvia S (b) in the sodium phosphate buffer at pH 6.5. Legends indicate the initial protein solution concentration. Note the different vertical scales for the two graphs.
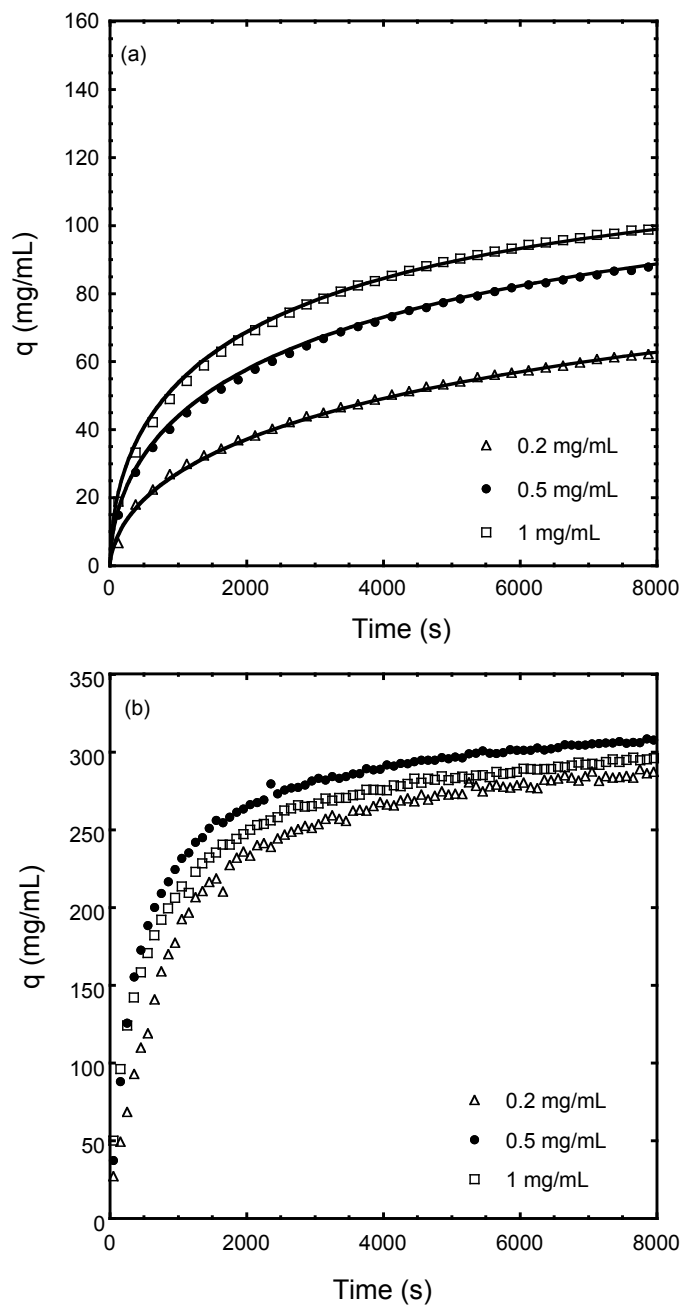
Fig. 3.7. Batch uptake curves for the mAb on UNOsphere S (a) and Nuvia S (b) in the sodium acetate buffer at pH 5.0. Legend indicates the initial protein concentration. Note the different vertical scales for the two graphs.

this figure, the bulk of the labeled protein has exactly the same retention behavior as the native one. However, the 570 nm peak is broader suggesting that conjugation introduces a degree of heterogeneity or perhaps hydrophobicity, which are responsible for the tailing behavior. The significance of the apparent heterogeneity introduced by conjugation with the fluorescent dye is discussed below.

Figure 3.9 shows CLSM images for UNOsphere S and Nuvia S beads saturated with 1 mg/mL mAb with and without sucrose. Without sucrose, the beads are opaque and the bead center remains dark in both cases. Much less signal attenuation is, however, seen when the beads are saturated in 40% sucrose allowing detection of fluorescence at the particle center. In separate experiments we confirmed that adding 40% sucrose to protein- saturated beads did not cause the protein to desorb determined from the absence of changes in the UV absorbance of the supernatant solution.

Figures 3.10 and 3.11 show the CLSM images for transient mAb adsorption on UNOsphere S and Nuvia S, respectively, and the corresponding attenuation-corrected profiles. Note that different but similarly sized particles were sampled at each time. Actual sizes are included in the figure caption. The UNOsphere S profiles are very sharp with a very clear demarcation between the advancing protein-saturated layer and a shrinking protein-free core. On the other hand, despite the fact that the isotherm is very sharp, the Nuvia S intraparticle concentration profiles are diffuse with protein reaching the particle center well before complete saturation is attained. It can be seen that for long times the UNOsphere S fluorescence intensity increases near the particle surface. This phenomenon is likely due to the presence of minor
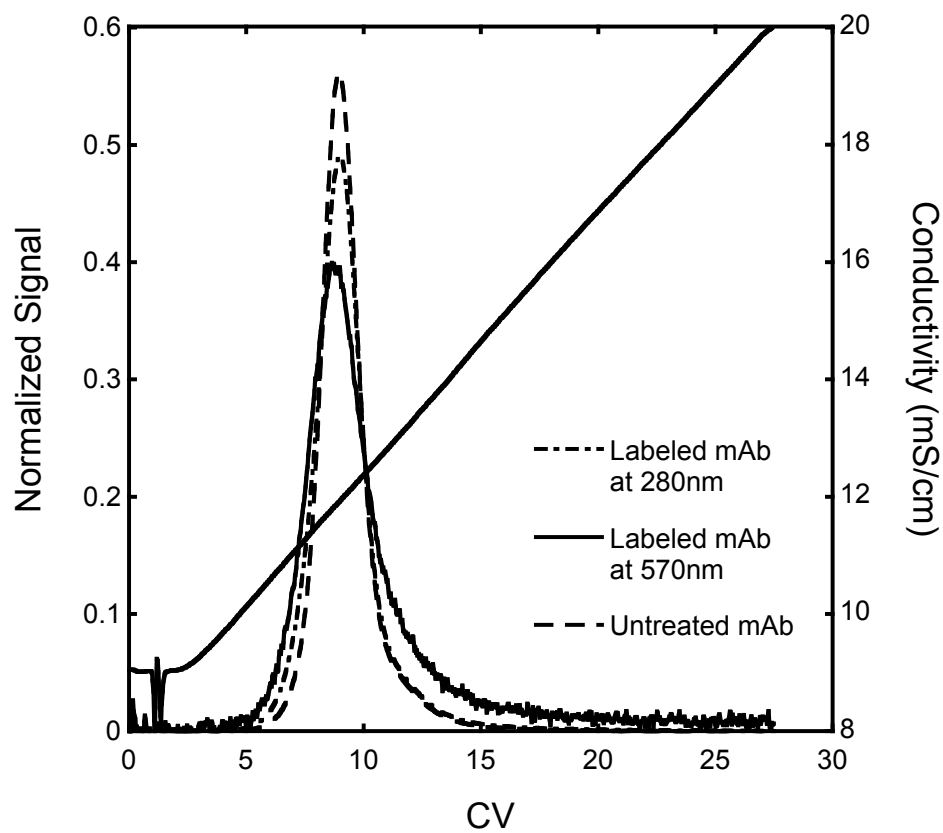
Fig. 3.8. Source 30S cation exchange chromatography of untreated (280 nm) and dye labeled (280 and 570 nm) mAb.
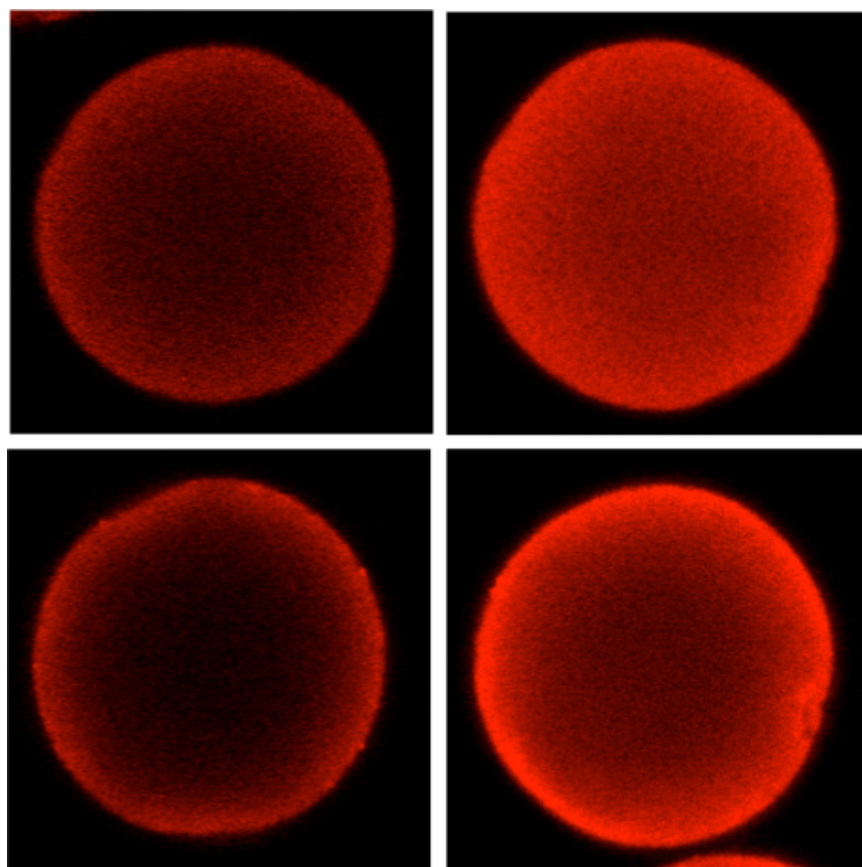
Fig. 3.9. CLSM images UNOsphere S (top) and Nuvia S (bottom) saturated with 1.0 mg/mL mAb in the sodium acetate buffer at pH 5.0. Left images are without sucrose. Right images are after adding 40% (w/w) sucrose.

amounts of stronger binding species formed during dye conjugation (possibly multiply labeled species), which resulted in the tailing chromatographic peak shown in Fig. 3.8, and which compete with the native protein for binding at the particle surface. The presence of these apparently minor impurities obviously did not affect the behavior of the bulk protein, whose adsorptive behavior is represented closely by the fluorescence signal. Based on the shrinking core model [15,29], which is expected to describe transport in UNOsphere S, the dimensionless position of the adsorption front, $\rho_s = r_s/r_p$, in the particles is related to time by the following equation:

$$f(\rho_s) = 2\rho_s^3 - 3\rho_s^2 + 1 = \frac{6D_e C_0 t}{q_m r_p^2}$$

(3.1)

where C_0 and q_m are the protein solution concentration and binding capacity, respectively, r_s is the radial position of the adsorption front and r_p is the particle radius. Figure 3.12 shows a plot of $f(\rho_s)$ vs. $C_0 t / q_m r_p^2$ for UNOsphere S obtained from measurements over time for differently sized particles. The plot is linear ($R^2 = 0.983$) and the slope gives $D_e = (4.9 \pm 0.8) \times 10^{-8}$ cm^2/s, which is consistent with the values derived from the batch uptake data (see Section 3.3.3).

For Nuvia S the profiles are diffuse and do not conform to the shrinking core model, despite the nearly rectangular shape of the isotherm (cf. Fig. 3.5). Thus, assuming that the fluorescence intensity is proportional to protein concentration, we calculated the average adsorbed protein concentration, $\bar{q}$, from the following equation:

$$\frac{\bar{q}}{q_m} = \left[3 \int_0^1 \frac{I}{I_m} \rho^2 \, d\rho \right]$$

(3.2)
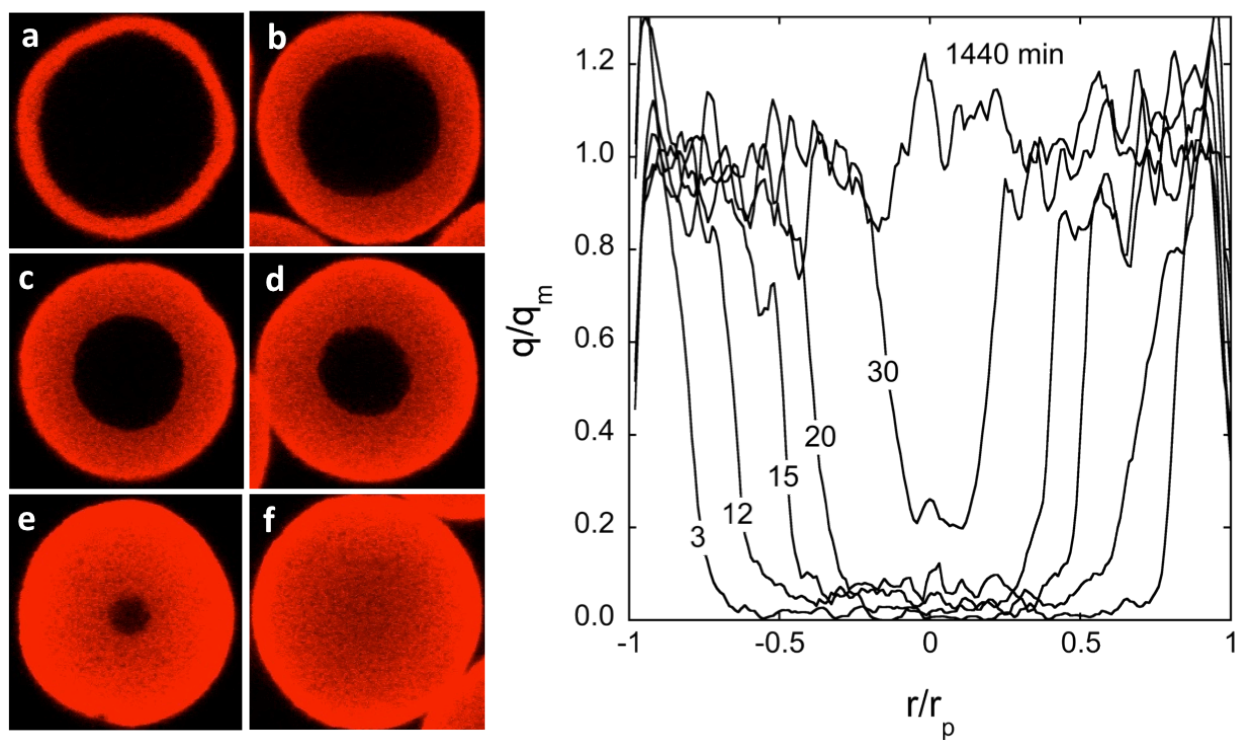
Fig. 3.10. CLSM images of 1.0 mg/mL mAb adsorption on UNOsphere S in the sodium acetate buffer at pH 5.0. Different particles were observed at different times; (a) 3 min, 54 μm, (b) 12 min, 56 μm , (c) 15 min, 56μm, (d) 20 min, 52 μm, (e) 30 min, 51 μm, and (f) 1440 min, 51 μm.
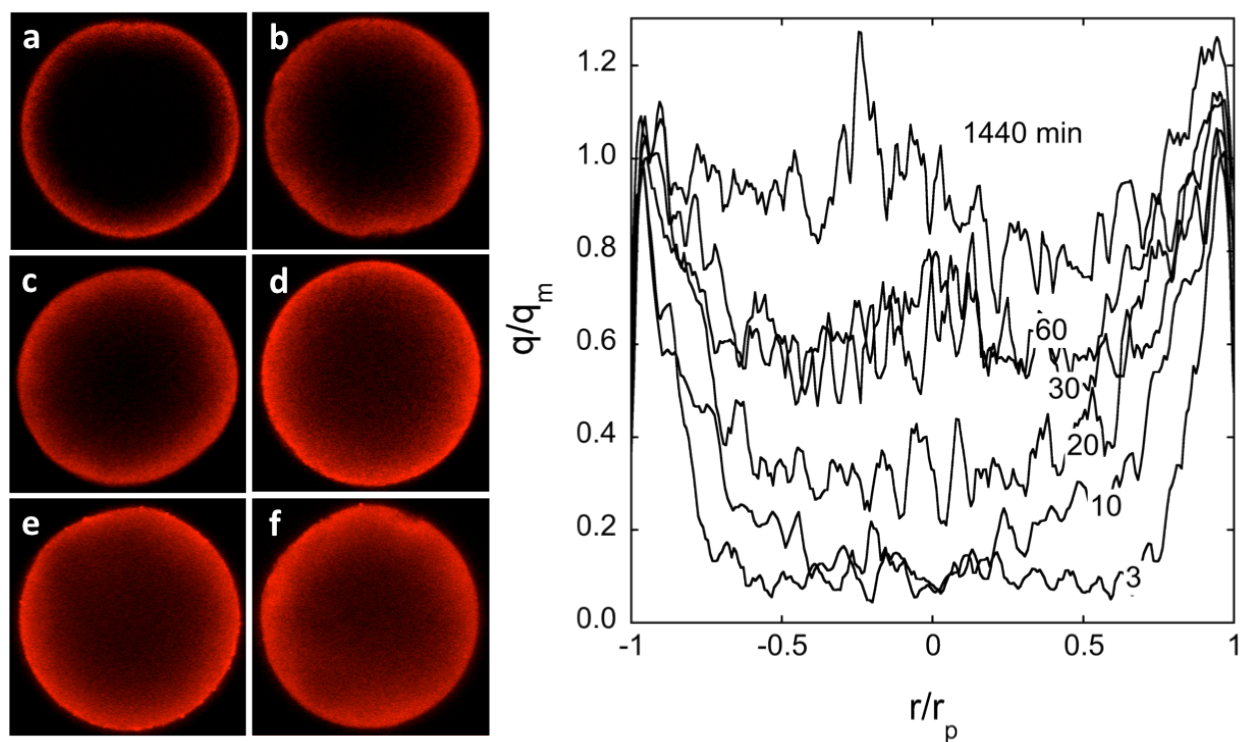
Fig. 3.11. CLSM images of 1.0 mg/mL mAb adsorption on Nuvia S in the sodium acetate buffer at pH 5.0. Different particles were observed at different times: (a) 3 min, 70 μm, (b) 10 min, 64 μm, (c) 20 min, 68 μm, (d) 30 min, 67 μm, (e) 60 min, 77 μm, and (f) 1440 min, 79 μm.

where I/I_m is the attenuation-corrected intensity at dimensionless radial position $\rho = r/r_p$, where r is the radial coordinate. The results are shown in Fig. 3.13 as a function of t/r_p^2 in comparison with the 1 mg/mL batch uptake results. Since diffusional mass transfer is known to vary inversely with the square of the particle size [29], plotting the results as a function of t/r_p^2 allows a proper comparison between the batch uptake data obtained for the bulk adsorbent sample and the CLSM data obtained for individual particles with different sizes. The close agreement corroborates the quantitative validity of the CLSM measurements. Unfortunately, the noise of the digitized profile is substantial and likely prevents an exact determination of $\bar{q}/q_m$. However, although the CLSM-derived data are affected by considerable scatter, largely due to the noise in the digitized profiles and to the fact that the results were obtained only for a few individual particles, the trends and time scales are very similar indicating that the CLSM results are representative of the actual kinetic processes occurring within the particle.
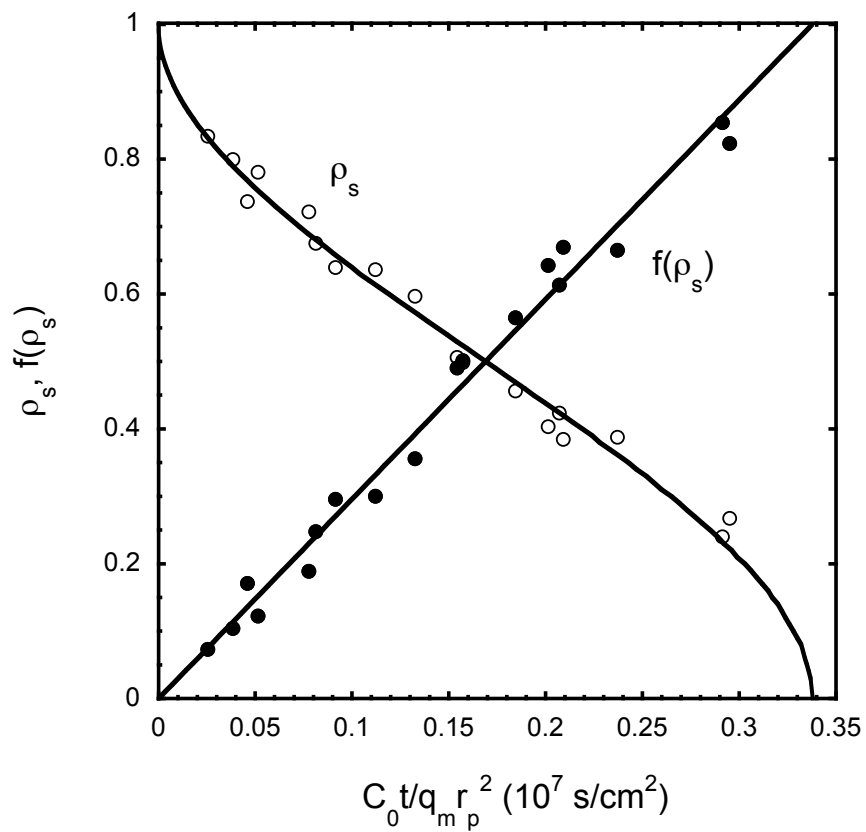
Fig. 3.12. Plot of dimensionless front position ρ_s and function $f(\rho_s)$ vs. $C_0 t / q_m r_p^2$ for UNOsphere S CLSM mAb data according to Eq. 3.1.
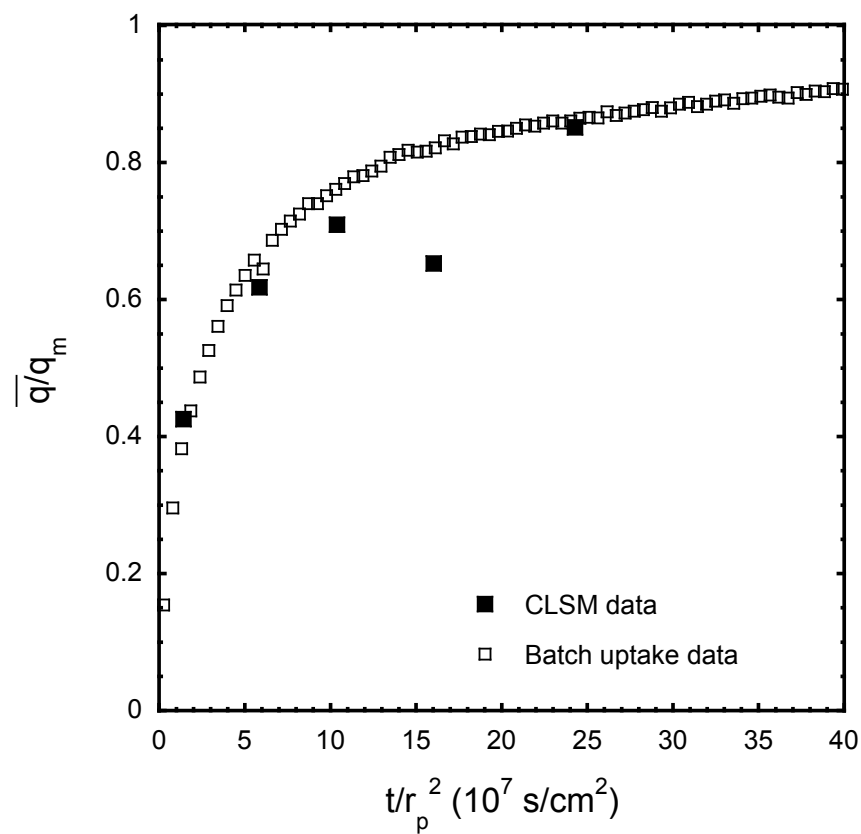
Fig. 3.13. Plot of $\overline{q}/q_m$ vs t/r_p^2 for Nuvia S mAb data comparing results obtained by integrating

the CLSM intraparticle concentration profiles with those obtained from the batch uptake data at 1

mg/mL solution concentration using the mean particle radius.

3.4. Conclusions

Charged polymeric surface extenders incorporated in a rigid pore matrix impart unique properties with regards to the mechanism of protein adsorption. The protein binding capacity is increased dramatically and the kinetics of protein adsorption is enhanced. The underlying mechanism for both phenomena appears to be the result of a "partitioning" mechanism, where protein molecules are adsorbed and diffuse while continuously interacting with the charged polymeric surface extenders. While similarly sized neutral molecules are excluded from the matrix, oppositely charged proteins are favorably partitioned and diffuse rapidly. The CLSM images comparing the behavior of macroporous and polymer-grafted media provide a stark contrast. Although the backbone matrix is very similar, the intraparticle protein concentration profiles are very sharp and consistent with the shrinking core model for the former, but diffuse and qualitatively consistent with a solid diffusion mechanism for the latter. The reasons for these differences are clearly associated with the polymeric surface extenders, which apparently create an environment where protein molecules are favorably partitioned but retain sufficient diffusional mobility that, coupled with a large driving force, results in a rapid adsorption kinetics.

3.5. List of symbols

C_0 fluid phase protein concentration (mg/mL)

CV number of bed volumes passed through the column

D_e effective pore diffusivity (cm^2/s)

f function defined by eq. 3.1

I fluorescence intensity signal

I_m maximum fluorescence intensity signal at particle surface

K Langmuir isotherm adsorption constant (mL/mg)

K_D distribution coefficient

q adsorbed protein concentration (mg/mL)

$\bar{q}$ particle-average adsorbed protein concentration (mg/mL)

q_m protein binding capacity (mg/mL)

r_p particle radius (cm)

r_s radial position of adsorption front (cm)

t time (s)

ρ_s dimensionless radial position of adsorption front

3.6. References

[1]   A.A. Shukla, J. Thommes, Trends Biotechnol. 28 (2010) 253.

[2]   B. Kelley, MABS. 1 (2009) 443.

[3]   U. Gottschalk, Process scale purification of antibodies, Wiley & Sons, Hoboken, NJ, USA, 2009.

[4]   B. Kelley, Biotechnol. Prog. 23 (2007) 995.

[5]   P. Gagnon, Bioprocess Int. 8 (2010) 22.

[6]   E. Boschetti, P. Girot, L. Guerrier, J. Chromatogr. A 523 (1990) 35.

[7]   E. Boschetti, J. Chromatogr. A 658 (1994) 207.

[8]   M.A. Fernandez, G. Carta, J. Chromatogr. A 746 (1996) 169.

[9]   L.E. Weaver, G. Carta, Biotechnol. Prog. 12 (1996) 342.

[10]   J. Thommes, Biotechnol. Bioeng. 62 (1999) 358.

[11]   A. Staby, I.H. Jensen, J. Chromatogr. A 908 (2001) 149.

[12]   B.D. Bowes, H. Koku, K.J. Czymmek, A.M. Lenhoff, J. Chromatogr. A 1216 (2009)

7774.

[13] M.C. Stone, Y. Tao, G. Carta, J. Chromatogr. A 1216 (2009) 4465.

[14] M.C. Stone, G. Carta, J. Chromatogr. A 1160 (2007) 206.

[15] G. Carta, A.R. Ubiera, T.M. Pabst, Chem. Eng. Technol. 28 (2005) 1252.

[16] A. Ljunglof, R. Hjorth, J. Chromatogr. A 743 (1996) 75.

[17] T. Linden, A. Ljunglof, M.E. Kula, J. Thommes, Biotechnol. Bioeng. 65 (1999) 622.

[18] J. Hubbuch, T. Linden, E. Knieps, J. Thommes, M.R. Kula, J. Chromatogr. A 1021 (2003) 105.

[19] S.R. Dziennik, E.B. Belcher, G.A. Barker, M.J. de Bergalis, S.E. Fernandez, A.M. Lenhoff, Proc. Nat. Acad. Sci. 100 (2003) 420.

[20] A. Ljunglof, K.M. Lacki, J. Mueller, C. Harinarayan, R. van Reis, R. Fahrner, J.M. Van Alstine, Biotechnol. Bioeng. 96 (2007) 515.

[21] M.D. Abramoff, P.J. Magelhaes, S.J. Ram. Biophotonics Int. 11 (2004) 36.

[22] K. Yang, Y. Sun. Biochem. Eng. J. 39 (2008) 258.

[23] S.R. Dziennik, E.B. Belcher, G.A. Barker, A.M. Lenhoff, Biotechnol. Bioeng. 91 (2005) 139.

[24] A.K. Hunter, G. Carta, J. Chromatogr. A 897 (2000) 65.

[25] P.G. Squire, J. Chromatogr. A 210 (1981) 433.

[26] L. Hagel, M. Ostberg, T. Andersson, J. Chromatogr. 743 (1996) 33.

[27] A. Ubiera, G. Carta, Biotechnol. J. 1 (2006) 665.

[28] Y. Tao, G. Carta, G. Ferreira, D. Robbins, J. Chromatogr. A 1218 (2011) 1519.

[29] G. Carta, A. Jungbauer, Protein chromatography – Process development and Scale-up, Wiley-VCH, Weinheim, Germany, 2010.

[30]   M.T. Tyn, T.W. Gusek, Biotechnol. Bioeng. 35 (1990) 327.

[31]   C. Chang, A.M. Lenhoff. J. Chromatogr. A 827 (1998) 281.

[32]   X.P. Zhou, W. Li, Q.H. Shi, Y. Sun, J. Chromatogr. A 1103 (2006) 110.

[33]   A.M. Lenhoff, Langmuir 24 (2008) 5991.

[34]   Y. Tao, G. Carta, G. Ferreira, D. Robbins, J. Chromatogr. A 1218 (2011) 1530.

[35]   C.A. Teske, M. Schroeder, R.E. Simon, J. Hubbuch, J. Phys. Chem. B 109 (2005) 13811.

Chapter 4

Multicomponent Adsorption on Nuvia S

4.1. Introduction

The separation of a mixture of proteins is the final goal in chromatography, making multicomponent analysis a necessity for accurately modeling separations. However, studying multicomponent adsorption is also important to understand transport mechanisms. The information acquired from the experimental observations can help identify the mechanisms responsible for protein transport in chromatographic materials. The structure of the chromatographic materials is expected to influence multicomponent transport as well.

In macroporous resin, where pore diffusion is the dominant mechanism, multicomponent adsorption can occur with simultaneous displacement of an adsorbed protein by another. Tao et al. [1], for example, explored both simultaneous and sequential adsorption of two mAb isoforms having different binding strengths on UNOsphere S. The process was found to occur via a continuous displacement with the more weakly bound species diffusing toward the center of the particle ahead of the more strongly bound component. This behavior has also been observed for the co-adsorption of cytochrome c and lysozyme in SP-Sepharose-FF [2]. In both cases, transport rates were found to be similar whether the two components were co-adsorbed simultaneously on a clean particle or sequentially adsorbed on a particle presaturated with the more weakly bound species.

A different behavior can be expected, however, when transport occurs in the adsorbed phase according to a solid diffusion mechanism. In this case, protein molecules can transfer

rapidly from an occupied adsorption site to an adjacent empty site, producing diffuse concentration profiles within the particle. This mechanism should be the same whether only one protein is adsorbed or two or more proteins are simultaneously co-adsorbed on an initially clean particle. However, what will happen in sequential adsorption, where a preadsorbed weakly bound protein is displaced by a more strongly bound one, is less easily predicted. In this case there are no or few empty adsorption sites. Thus, low rates of counter transport can be expected. Tao et al. [1] observed this behavior for the adsorption of mAb charge variants in Capto S, a dextran grafted cation exchanger. While co-adsorption of two isoforms occurred rapidly, sequential adsorption occurred extremely slowly suggesting that mass transfer fluxes are coupled thereby leading to rates that depend on the direction of transport. A "single file diffusion" (SFD) model was developed by Tao et al. [3] to describe this situation. This model, previously used to describe adsorption in zeolitic structures [4-9], assumes that adsorbed molecules cannot pass each other and that diffusion occurs at a rate that depends on the availability of empty adsorption sites.

In Chapter 3 we investigated both macroscopically and microscopically the single component adsorption of a mAb at pH 5.0 on UNOsphere S and Nuvia S. As previously explained, the former is a rigid matrix with a large pore architecture, while the latter is based on the same backbone but with the addition of charged polymeric surface extenders. Because of the lack of selectivity observed between the two available mAbs at pH 5.0, the behavior of mixture adsorption was studied at pH 6.0 for two different monoclonal antibodies. Macroscopic and microscopic experiments were performed for each mAb individually and for the mixture for both simultaneous and sequential adsorption cases. CLSM was then used to understand the transport mechanism responsible for simultaneous and sequential adsorption in both resins. CLSM results

for Nuvia S will be compared qualitatively with a single file diffusion model that incorporates the steric mass action (SMA) model.

4.2. Experimental methods

4.2.1. Materials

The two cation exchangers used in the work described in this chapter are UNOsphere S and Nuvia S, both from Bio-Rad Laboratories (Hercules, CA, USA). Both are based on a similar crosslinked polyacrylamide backbone. However, while UNOsphere S has an open macroporous structure, Nuvia S contains proprietary sulfonated polymeric surface extenders. A complete description and characterization of the materials can be found in Chapter 3.

Two mAbs, identified as mAbT and mAbY, with pI=8.2 and 8.6 respectively were used for the experiments. Both mAbs were >99% monomer as determined by size exclusion chromatography with a Superdex 200 column (GE Healthcare, Piscatway, NJ, USA). All other chemicals were purchased from Fisher Scientific (Pittsburgh, PA, USA). Adsorption experiments were done at room temperature, 22±2 °C. Protein solutions were prepared in buffers containing 10, 15, 20 and 35 mM Na_2HPO_4 adjusted to pH 6.0 with phosphoric acid.

4.2.2. Methods

4.2.2.1. Adsorption isotherms

Protein adsorption isotherms were determined from batch experiments. For this purpose, samples of each resin with mass (M_W) between 5 and 15 mg were mixed with solutions containing different initial protein concentrations and equilibrated for 24 hours in 1.5 mL vials slowly rotated end over end. The resin samples were first equilibrated in sodium phosphate buffers as needed, then placed in 1.5 mL filter centrifuge tubes obtained from Millipore (Billerica, MA, USA), and centrifuged at 5000 rpm for 10 min to remove the extraparticle liquid.

Samples of the centrifuged particles were then weighed and added into 1.5 mL vials containing protein solutions ($V = 1.0$ mL) with known initial concentration (C_0), sealed and rotated end-to-end on a rotator at a few rpm.   After equilibration, the supernatant was analyzed spectrophotometrically at 280 nm with a Nanovue spectrophotometer (GE Healthcare, Piscataway, NJ, USA) and the amount of protein adsorbed by the media was calculated from the expression:

$$\tilde{q} = \frac{V}{M_W}(C_0 - C_F) \tag{4.1}$$

The mass of particles used was converted to the corresponding volume of particles using the density of the hydrated particles determined with a pycnometer. The latter was 1.081 ± 0.012 g/mL for both materials, giving us a q expressed in terms of hydrated particle volume. Equilibrium experiments were conducted over a range of different salt concentrations for both one mAb and two mAb adsorption for Nuvia S. For the two-component case, the supernatant was analyzed by cation exchange with a Source 30S (0.5 x 5 cm) Tricorn column from GE Healthcare (Piscataway, NJ, USA). A gradient elution was used with 10 mM Na_2HPO_4 at pH 6.0 solution as buffer A and 10 mM Na_2HPO_4 containing 500 mM NaCl at pH 6.0 as buffer B. 60 µL of sample were injected into the column and eluted at 1mL/min with a 0-30 % B linear gradient in 40 column volumes (CV) followed by a strip at 100% B.

4.2.2.2. Adsorption kinetics

Protein uptake rates were measured by suspending a known amount of adsorbent in 20 mL of protein solutions in a stirred batch apparatus described elsewhere [10, 11]. The amount of adsorbent added was different in each case with the actual amount chosen based on the adsorption isotherms to yield a final protein concentration about equal to one half of the initial

value. The total amount of protein bound at each time step was determined by material balance from the initial and current solution concentration obtained from the UV absorbance at 280 nm. Mixture data were obtained by HPLC analysis of the supernatant using a Source 30S column as described in Section 4.2.2.1.

4.2.2.3. Confocal microscopy

As described in detail in prior work [12-16], confocal laser scanning microscopy (CLSM) was used to image the movement of the two mAbs within the resin beads. For this purpose, mAbT and mAbY were conjugated with Rhodamine Green[TM]-X and Rhodamine Red[TM]-X dyes, respectively, following the dye supplier instructions. Each of the mAbs was incubated in a solution containing a reactive dye with a dye-to-protein molar ratio of 3:1 in a pH 8.5 sodium bicarbonate buffer for 1 hour at room temperature. The unreacted dye was separated by size exclusion chromatography as described in Section 3.2 and the average labeling ratio was calculated based on absorbances obtained by UV/Vis spectrophotometry.

Figure 4.1 shows the gradient elution cation exchange chromatogram for a mixture of native, red dye conjugated mAbY and green dye conjugated mAbT on a 0.5 x 9.8 cm UNOsphere S column at pH 6.0. Very similar retention times are seen for labeled and unlabeled mAbs indicating that labeling does not have a significant effect in the interaction of each mAb with the resin. Confocal microscopy for one component and two component adsorption was carried out batch-wise using 40 % sucrose as a refractive index matching fluid (see Section 3.2) and results were analyzed as described in detail in Section 3.2. For sequential experiments different amounts of resin samples were initially equilibrated with mAbT solutions for 24 hours to obtain complete saturation, one half and one third of the mAbT equilibrium binding capacity.
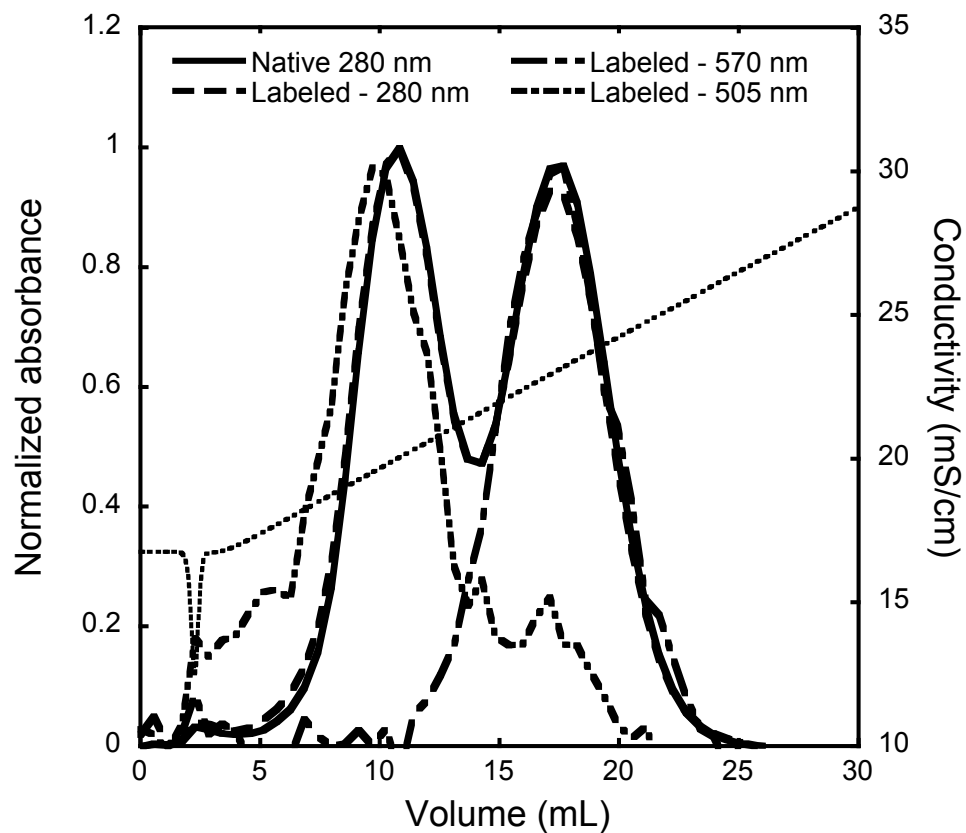
Fig. 4.1. UNOsphere S gradient elution cation exchange chromatography of a mixture of native (280 nm), Rhodamine Red-mAbY dye labeled (280 nm and 570 nm), and Rhodamine Green-mAbT dye labeled (280nm and 505 nm) at pH 6.0.

After equilibration, the resin samples were separated from the mAbT solutions and added to an excess volume (10 mL) of a 1 g/L mAbY solution. The same procedure described in Section 3.2 for the one component case was then followed to take the samples and image the fluorescence intensity profiles on each particles equatorial section.

4.2.2.4. Linear gradient elution

Linear gradient elution (LGE) was used to determine, according to the procedure of Yamamoto [17], the number of ion exchange functional groups that interact with each mAb at pH 6.0. In these experiments, 100 µL samples containing approximately 2 g/L of each mAb were injected into a 0.5 x 9.7 cm Nuvia S column 10 mM Na_2HPO_4 buffer at pH 6.0 and eluted with sodium phosphate gradients. A 10 mM Na_2HPO_4 to 50 mM Na_2HPO_4 in 5, 10, 15, 20 and 30 CVs was used for mAbT and 10 mM Na_2HPO_4 to 175 mM Na_2HPO_4 in 5, 10, 15, 20 and 30 CVs was used for mAbY. The mobile phase flow rate was kept constant at 1 mL/min. In each case the Na^+ concentration at peak elution, C_R^I, was determined from the conductivity signal using appropriate correlations.

4.3. Results and discussion

4.3.1. Adsorption isotherms

Figure 4.2 shows the adsorption isotherms for UNOsphere S and Nuvia S at pH 6.0. The adsorbed concentration q, is given in mg of protein bound per mL of particle volume. Very sharp isotherms are obtained for both stationary phases at this pH and Na^+ concentration. However the binding capacity of Nuvia S is much higher for both mAbs when compared with that of UNOsphere S. Since the backbone of both resins is essentially the same, these results suggest a multilayer packing of the protein molecules in Nuvia S, rather than a surface-limited adsorption
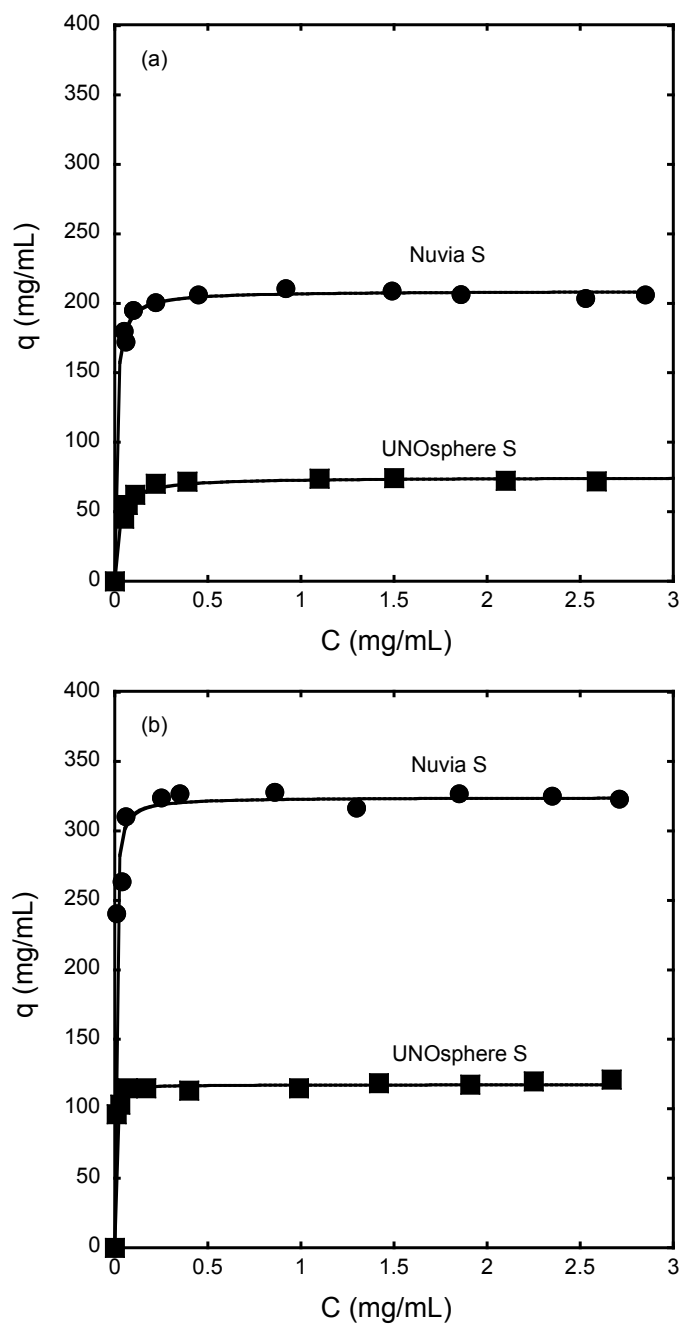
Fig. 4.2. Adsorption isotherms for (a) mAbT and (b) mAbY in 10 mM Na$_2$HPO$_4$ buffer at pH 6.0. Lines are drawn as guides.

mechanism. This is consistent with the results at pH 5.0 in Chapter 3. Although the two mAbs have the same molecular mass, mAbT has a lower binding capacity on both materials compared with mAbY. This is likely due to the fact that mAbT has a lower pI (8.2) compared to mAbY (8.6) and is thus less basic resulting in weaker binding.

4.3.2. Adsorption kinetics

Figure 4.3 shows the one-component batch uptake curves for 1 mg/mL mAbT and mAbY obtained for UNOsphere S (a) and Nuvia S (b) at pH 6.0. In addition to having a higher ultimate binding capacity for both mAbs, Nuvia S has also faster adsorption kinetics than UNOsphere S. For mAbY equilibrium was achieved in about 2,000 s for Nuvia S, while it took about 6,000 s for UNOsphere S. A similar behavior was observed for mAbT. Since both mAbs have similar molecular mass, the rate is expected to be similar for both in UNOsphere S where pore diffusion is the dominant mechanism. Figure 4.3 also shows lines calculated from the pore diffusion model assuming a rectangular isotherm and taking into account the particle size distribution of each resin sample. The relevant equations are given by Carta and Jungbauer [18]. For UNOsphere S the uptake curves could be described almost perfectly by this model. The corresponding effective pore diffusivities obtained by fitting the model to the data are $D_e = (0.65 \pm 0.02) \times 10^{-7}$ cm^2/s and $D_e = (0.66 \pm 0.04) \times 10^{-7}$ cm^2/s for mAbT and mAbY respectively. Normalizing by the free solution diffusivity, D_0, obtained by dynamic light scattering as discussed in Chapter 5, $D_0 = 5.44 \times 10^{-7}$ cm^2/s, these values yield $D_e/D_0 = 0.12 \pm 0.02$ and 0.12 ± 0.03 for mAbT and mAbY respectively, which are typical for ordinary pore diffusion of proteins in macroporous ion exchangers [11].
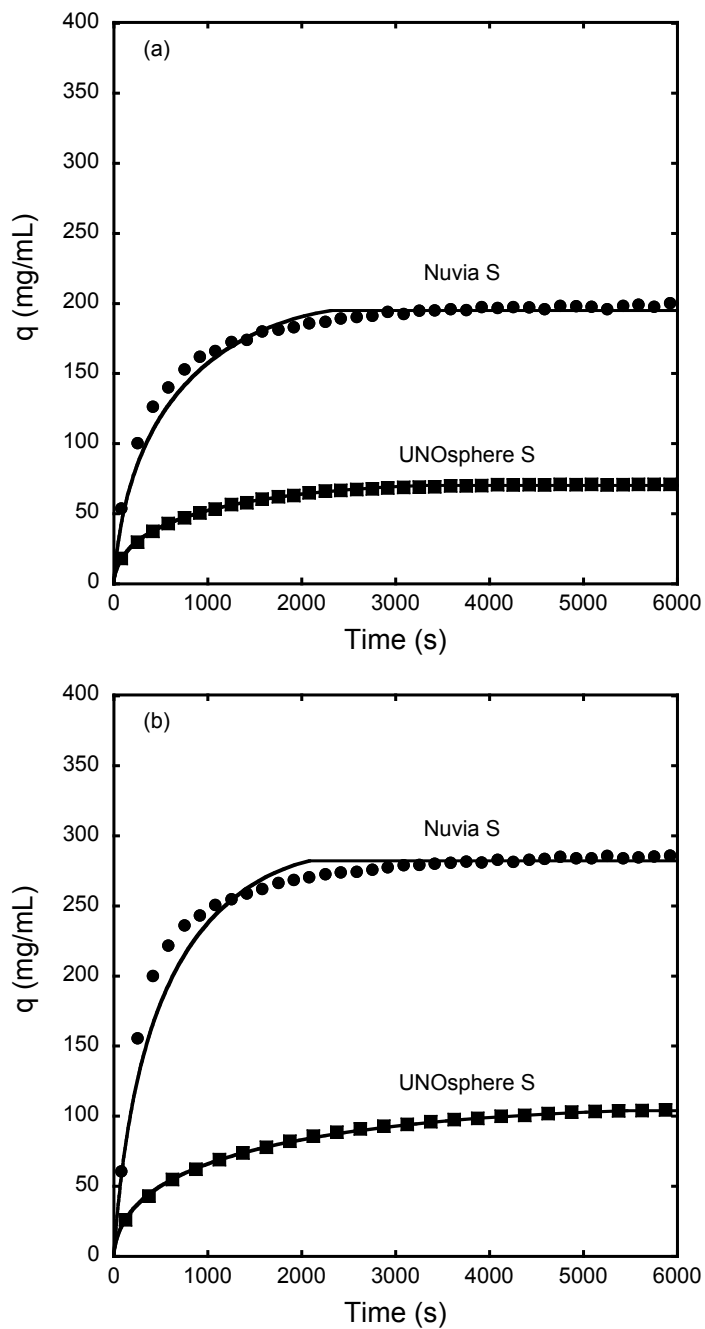
Fig. 4.3. One-component batch uptake curves for 1 g/L mAbT (a) and 1 g/L mAbY (b) in 10 mM Na$_2$HPO$_4$ buffer at pH 6.0. Solid lines are based on the pore diffusion model assuming a rectangular isotherm.

For Nuvia S, the results are also consistent with those obtained at pH 5.0 in Chapter 3. In this case, also the pore diffusion model provides only a rough description of the data (see lines in Fig. 4.3). Fitting this model to the data gave apparent effective pore diffusivities $D_{e,app}$ = (3.2 ±0.4) x 10^{-7} cm^2/s and (8.1 ± 0.3) x 10^{-7} cm^2/s for mAbT and mAbY, respectively. These values are 5 to 12 times larger than those obtained for UNOsphere S and the mAbY value is actually larger than its free solution diffusivity. Qualitatively, the Nuvia S results are consistent with a "solid diffusion" mechanism [18], likely the result of a "hopping" process in the grafted polymeric surface extenders with the driving force given by the adsorbed protein concentration gradient. In this case the apparent effective pore diffusivity $D_{e,app}$ is approximately related to an adsorbed-phase diffusivity, D_s by the following equation [20]:

$$D_{e,app} \sim D_s \frac{q_m}{C_0} \tag{4.2}$$

where q_m is the binding capacity and C_0 the protein concentration in solution. Thus, a smaller $D_{e,app}$ would be expected for mAbT, whose capacity is about 60% of that of mAbY on Nuvia S (see Fig. 4.2). The actual $D_{e,app}$ of mAbT is, however, less than 60% of that of mAbY suggesting that the D_s values may also be different for the two mAbs.

4.3.3. Confocal laser scanning microscopy

Figure 4.4 show the results for adsorption of a mixture containing 1 mg/mL each of mAbT and mAbY at pH 5.0. The profiles are quite sharp for UNOsphere S but fairly smooth for Nuvia S, consistent with pore diffusion and solid diffusion mechanisms, respectively. However at this pH there is little separation of the two mAbs in discrete bands within the UNOsphere S particles as it would be expected if one mAb were displacing the other within the particles [1]. To ascertain whether there is selectivity between the two mAbs at this pH, mixtures of 1 mg/mL of each mAb where equilibrated with both resins as discussed in Section 4.3.1. After

(A) UNOsphere S
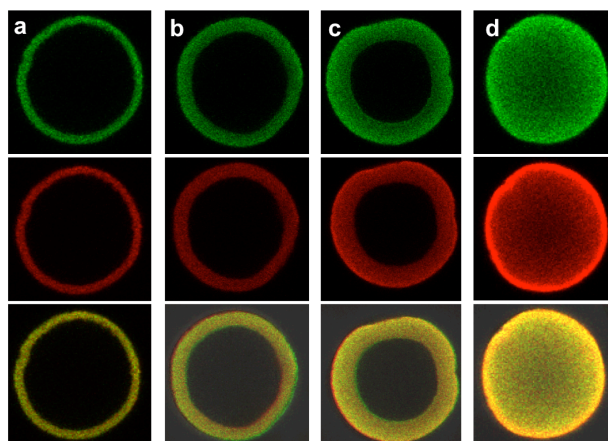
(B) Nuvia S
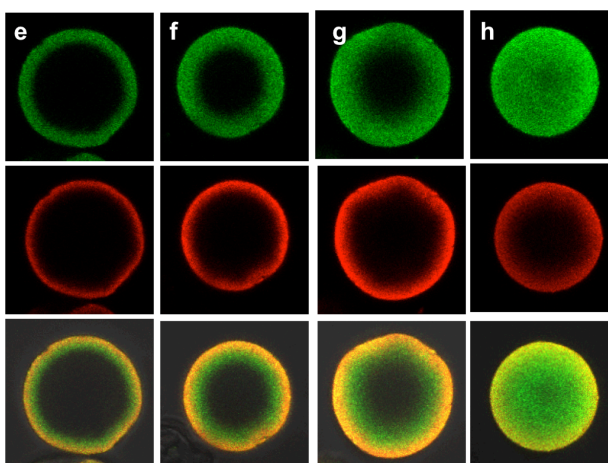
Fig. 4.4. Representative CLSM images of two-component simultaneous adsorption of 1 mg/mL mAbT (top row, green) and 1 mg/mL mAbY (middle row, red) adsorbed on UNOsphere S (A) and Nuvia S (B) at pH 5.0. Bottom rows in each panel are composite of green and red resolved images. Particle diameters and time of observation are as follows: a=2 min, 62 μm ,b=10 min, 66 μm, c=30 min, 80 μm, d=75 min, 71 μm, e=2 min, 74 μm, f=6 min,74 μm, g=12 min, 82 μm, h=24 min, 66 μm.
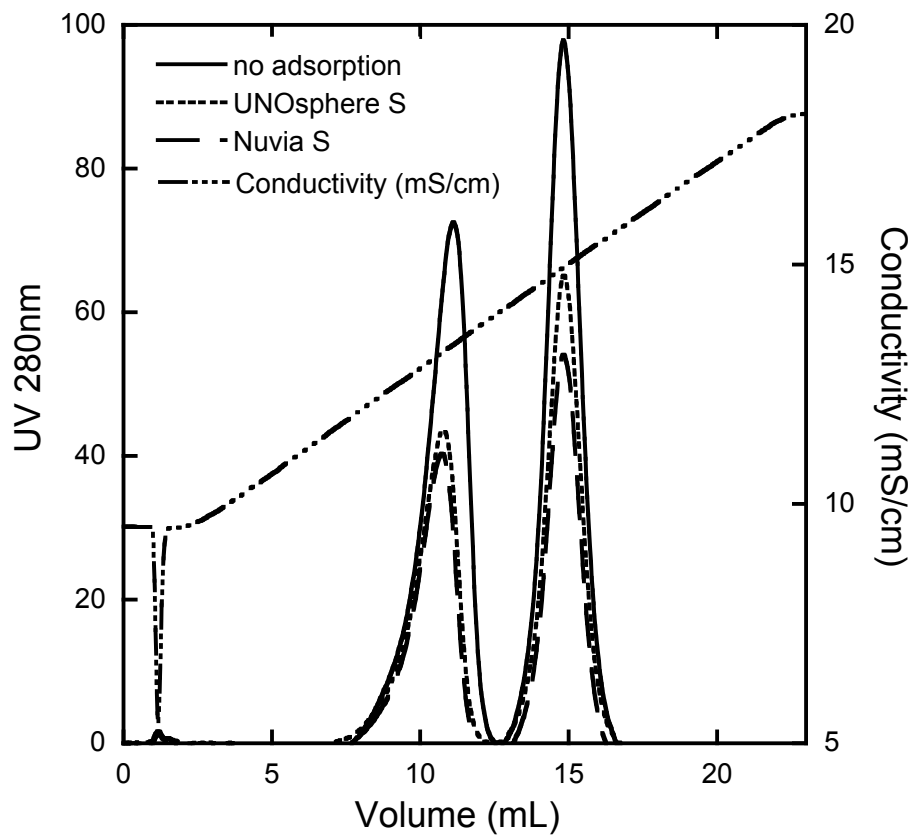
Fig. 4.5 LGE analysis on Source 30S of a 1 mg/mL mixture of mAbT and mAbY.

equilibration for 24 hrs, gradient elution on cation exchange chromatography was performed on a Source 30S column to separate the mixture and calculate how much of each protein was adsorb by the resin. As seen in Fig. 4.5 the results obtained showed minimal selectivity.

Figures 4.6 to 4.9 show the CLSM results for one-component adsorption at pH 6.0 along with the normalized concentration profiles obtained as discussed in Section 3.3. The profiles for UNOsphere S are very sharp for mAbY (Fig. 4.8) but somewhat less sharp for mAbT (Fig. 4.6), but both with a clear demarcation between an advancing protein-saturated layer and a shrinking protein-free core. This behavior is consistent with a pore diffusion mechanism where adsorbed protein molecules have no mobility and diffusion occurs only within the liquid-filled pores [18,19]. On the other hand, the Nuvia S profiles (Figs. 4.8 and 4.9) are diffuse, with some protein molecules apparently reaching the particle center well before complete saturation is attained.

Quantitative analyses of the CLSM results for UNOsphere S were done using the shrinking core model as described in Section 3.3. For mAbT, a distinct overshoot in fluorescence intensity can be observed at the adsorption front (see Fig. 4.6) which is likely due to a slightly weaker binding of labeled mAbT compared to the native mAbT (cf. Fig. 4.1) causing a competitive displacement front. Thus, for the analysis we assumed, as suggested by Carta et al. [11], that the outer edge of the overshoot ring represents the adsorption front of the largely dominant unlabeled protein. The position of this front is then related to time by the following equation:

$$f(\rho_s) = 2\rho_s^3 - 3\rho_s^2 + 1 = \frac{D_e C_0}{q_m r_p^2} t \tag{4.3}$$

where $\rho_s = r_s / r_p$ is the dimensionless position of the adsorption front. Figure 4.10 shows the plots of ρ_s and $f(\rho_s)$ vs $C_o t / q_m r_p^2$ for mAbT (a) and mAbY (b) respectively. The slope of $f(\rho_s)$
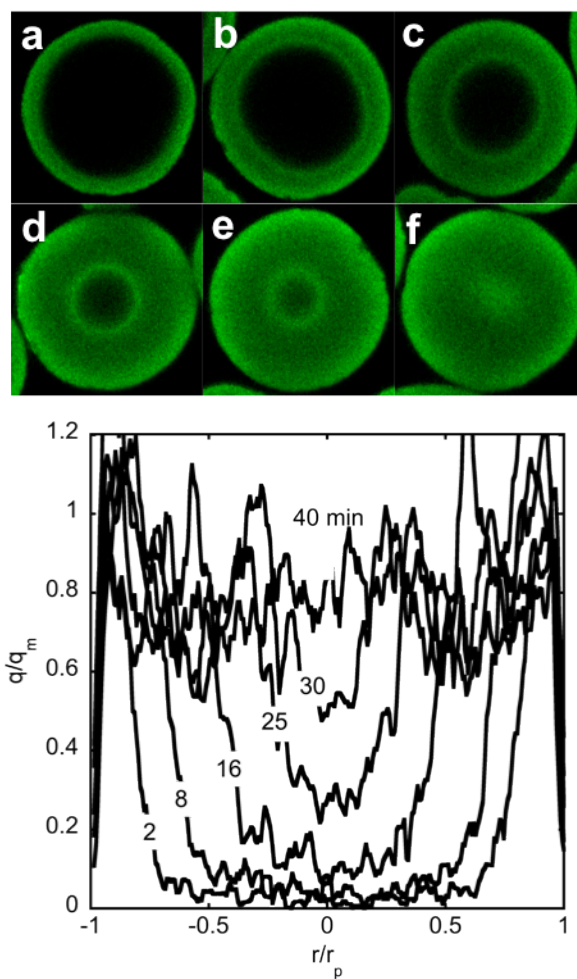
Fig. 4.6. CLSM images of 1.0 mg/mL mAbT adsorption on UNOsphere S in 10 mM Na_2HPO_4 buffer at pH 6.0. Different particles were observed at different times: (a) 2 min, 69 μm, (b) 8 min, 71 μm, (c) 16 min, 69 μm, (d) 25 min, 70 μm, (e) 30 min, 72 μm, (f) 40 min, 70 μm.
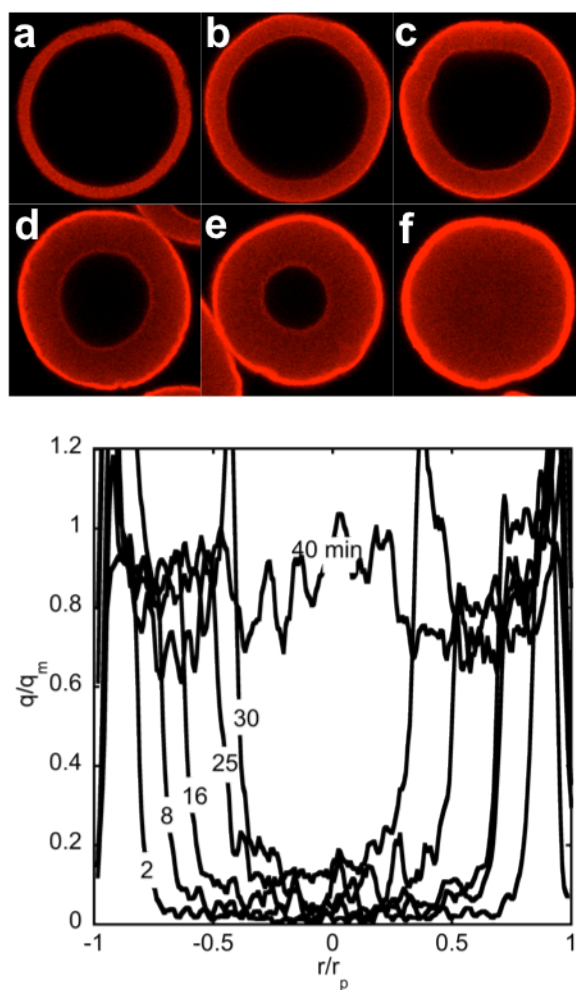
Fig. 4.7. CLSM images of 1.0 mg/mL mAbY adsorption on UNOsphere S in 10 mM Na_2HPO_4 buffer at pH 6.0. Different particles were observed at different times: (a) 2 min, 69 μm, (b) 8 min, 74 μm, (c) 16 min, 73 μm, (d) 20 min, 69 μm, (e) 30 min, 68 μm, (f) 40 min, 69 μm.
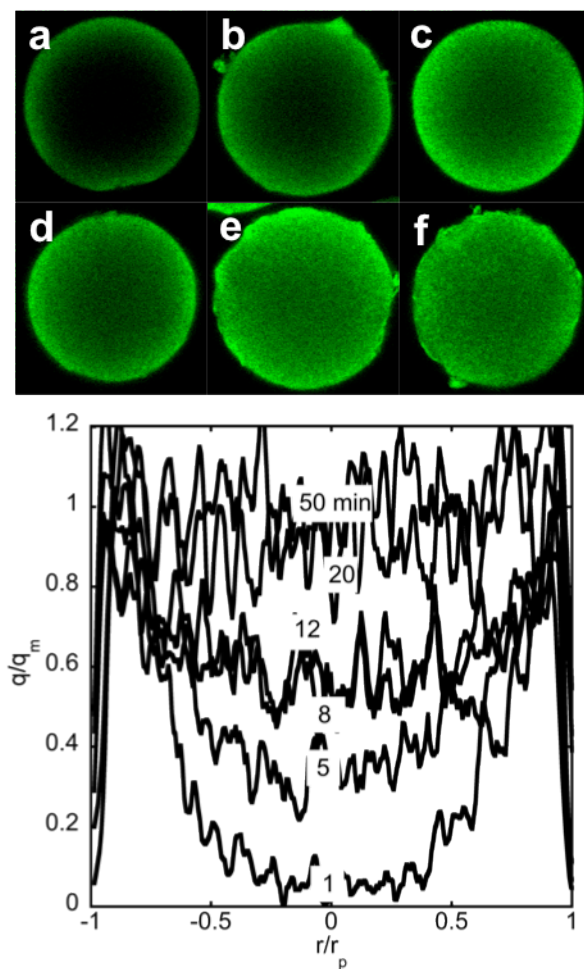
Fig. 4.8. CLSM images of 1.0 mg/mL mAbT adsorption on Nuvia S in 10 mM Na_2HPO_4 buffer at pH 6.0. Different particles were observed at different times: (a) 1 min, 71 μm, (b) 5 min, 73 μm, (c) 8 min, 70 μm, (d) 12 min, 72 μm, (e) 20 min, 76 μm, (f) 50 min, 73 μm.
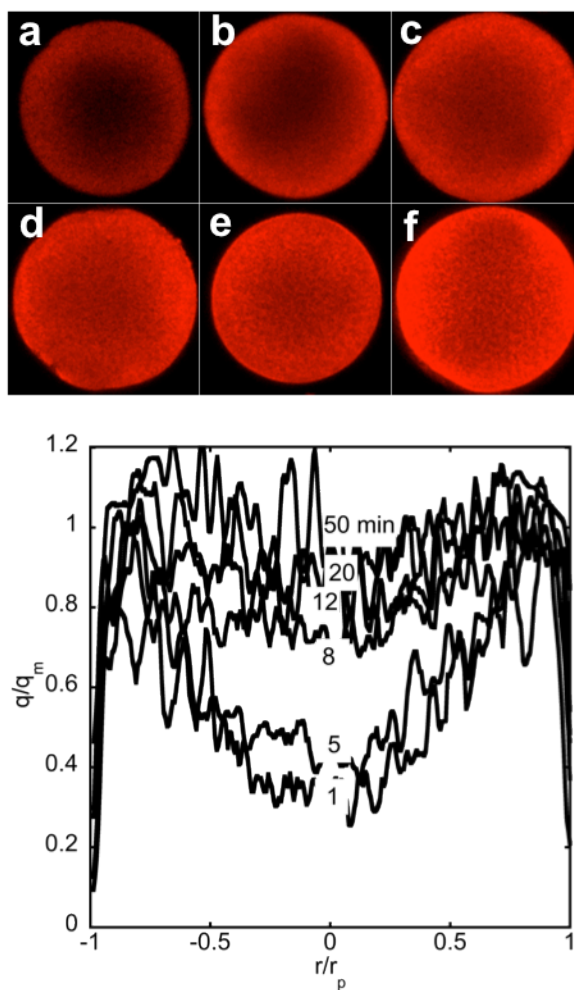
Fig. 4.9. CLSM images of 1.0 mg/mL mAbY adsorption on Nuvia S in 10 mM Na$_2$HPO$_4$ buffer at pH 6.0. Different particles were observed at different times: (a) 1 min, 73 μm, (b) 5 min, 77 μm, (c) 8 min, 81 μm, (d) 12 min, 78 μm, (e) 20 min, 73 μm, (f) 50 min, 78 μm.
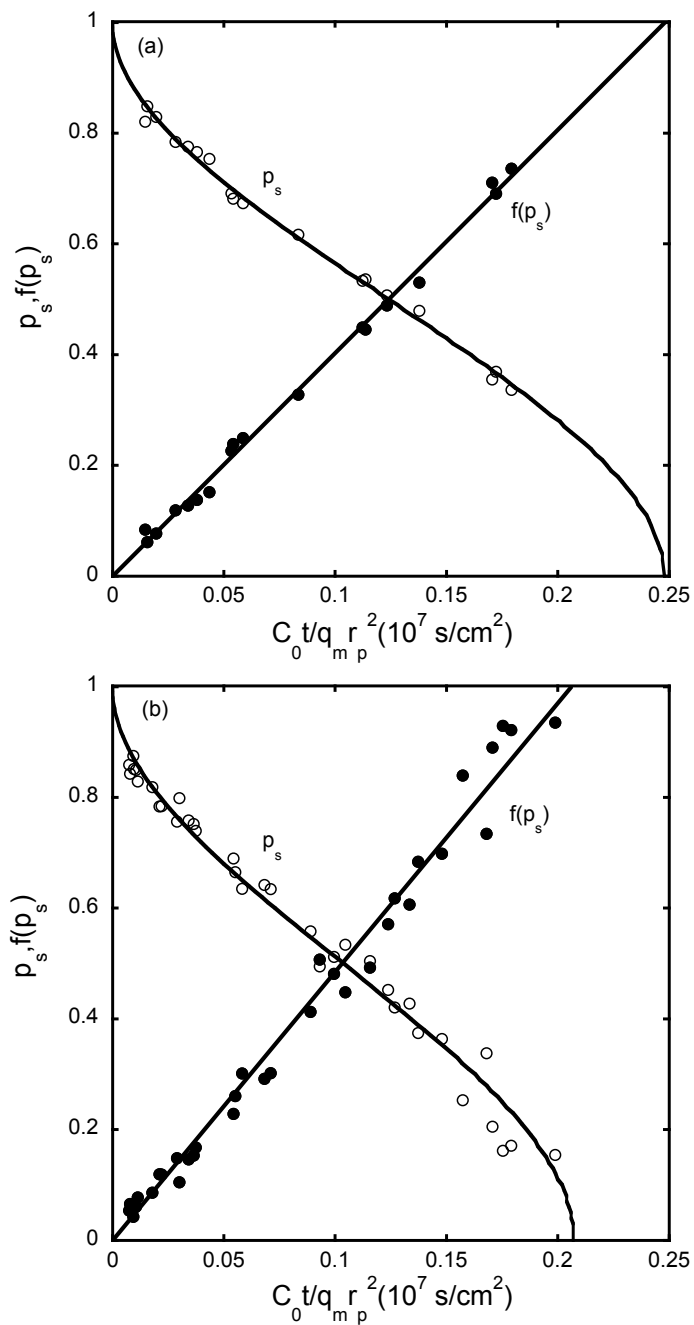
Fig. 4.10. Plot of dimensionless position of the adsorption front in the particle ρ_s and function $f(\rho_s)$ vs. $C_0t/q_mr_p^2$ obtained by CLSM for UNOsphere S with mAbT (a) and mAbY (b).

yields $D_e = (0.76 \pm 0.12)$ x 10^{-7} cm^2/s and $D_e = (0.68 \pm 0.06)$ x 10^{-7} cm^2/s, which are consistent with the values obtained by fitting the batch uptake data (see Section 4.3.2). Since the profiles are smooth, the same analysis could not be performed for Nuvia S. Thus, the procedure described in Section 3.3 to compare the CLSM results with the batch uptake curves was used instead. The results are shown in Fig. 4.11 as a function of t/r_p^2. Because diffusional mass transfer is known to vary inversely with the square of the particle size [18], plotting the results as a function of t/r_p^2 allows a proper comparison between the batch uptake data and the CLSM data. The CLSM data trends and time scales for both mAbT and mAbY are in excellent agreement with the batch uptake results confirming that the CLSM results represent the actual kinetic processes occurring within the particle.

Figures 4.12 and 4.13 show the two-component simultaneous and sequential adsorption results for UNOsphere S and Nuvia S, respectively. Green (mAbT) and red (mAbY) resolved images as well as color composite images are shown for each case. Differences in the signal intensities observed are related to the different laser transmissions used. For UNOsphere S it is apparent that the adsorption of the two mAbs occurs with a continual displacement of mAbT by mAbY within the particle. In the simultaneous adsorption case (Fig. 4.12A), mAbT diffuses ahead of the mAbY adsorption front and temporarily concentrates toward the center of the particle. In the final picture (60 min) it can be observed that almost no green (mAbT) is left adsorbed on the particle. Continuous displacement can be observed for the sequential adsorption case (Fig. 4.12B), when particles presaturated with mAbT were exposed to the more strongly bound mAbY. Since the time scale is nearly the same for both simultaneous and sequential adsorption experiments, it can be concluded that the transport mechanism in UNOsphere S is independent of the direction of transport thereby corroborating the finding that the exchange
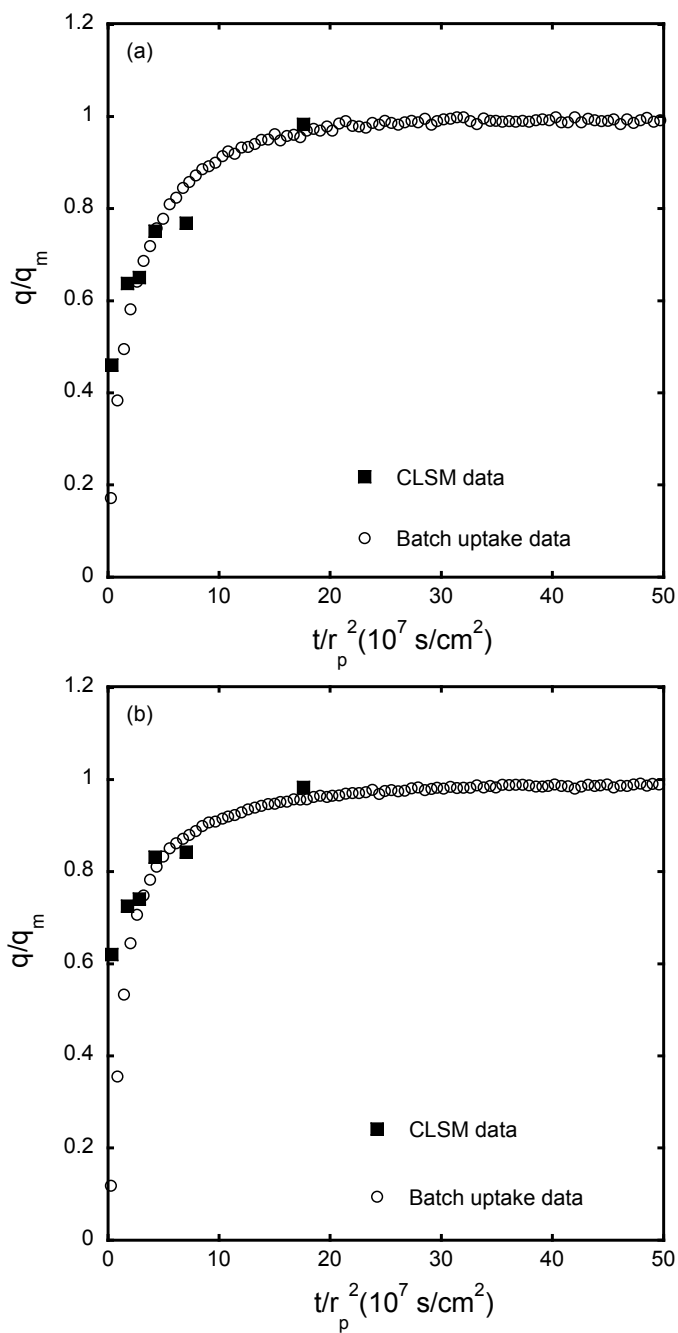
Fig. 4.11. Plot of q/q_m vs t/r_p^2 for 1 mg/mL mAbT (a) and mAbY (b) adsorption on Nuvia S comparing results obtained by integrating the CLSM intraparticle concentration profiles with those obtained from the batch uptake data.

(A) Simultaneous adsorption

(B) Sequential adsorption
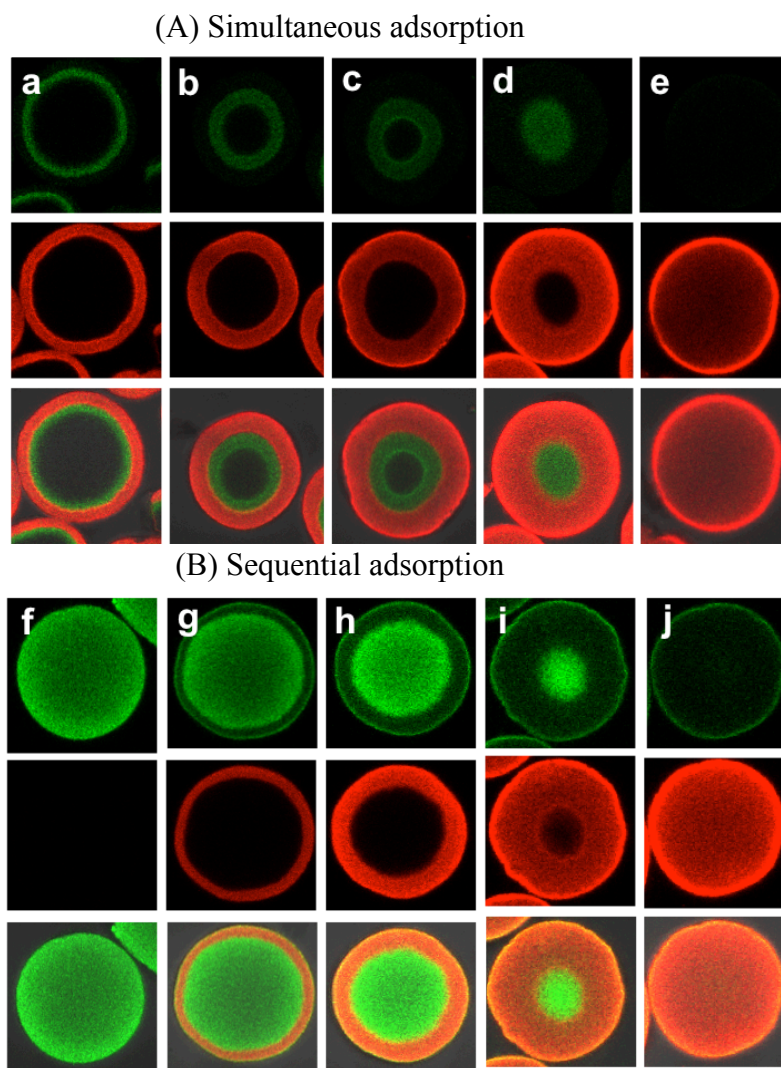
Fig. 4.12. Representative CLSM images of two-component adsorption in UNOsphere S at pH 6.0 (A) simultaneous adsorption mixtures containing 1 mg/mL each of mAbT and mAbY (B) sequential adsorption of 1 mg/mL mAbY on beads presaturated with 1 mg/mL mAbT. In each panel, top row images (green) are for mAbT, middle row (red) are for mAbY, and bottom images are composites of green and red resolved images. Particle diameters and time of observation are as follows: a=4 min, 62 μm, b=10 min, 66 μm, c=20 min, 80 μm, d=30 min, 71 μm, e=60 min, 74 μm, f=saturated, 74 μm, g=4 min, 82 μm, h=10 min, 66 μm, i=25 min, 65 μm, j=40 min, 62 μm.

process is controlled by diffusion in the particle macropores and that displacement of one protein by another is diffusion limited.

The results for simultaneous adsorption in Nuvia S (Fig. 4.13A) show diffuse profiles with little or no separation of the two mAbs within the particle. This result suggests that immediately after entering the particle mAbT and mAbY co-diffuse without further separation. The time scale of this co-adsorption process is very similar to that of the single component case suggesting that the underlying mechanism is the same whether one protein or multiple ones diffuse in the same direction. A completely different result is obtained, however, for the sequential adsorption case on Nuvia S (Fig. 4.13B). In this case displacement of mAbT by mAbY occurs very slowly. The time needed to reach equilibrium is obviously longer than the 150 min tested, suggesting that counter-diffusion of the two mAbs is severely hindered. Additionally, it can be seen that some mAbY is adsorbed very quickly near the surface of the particles, with additional adsorption occurring very slowly. The reason for this phenomenon can be related to the differences in binding capacities by the two mAbs. The Nuvia S-mAbT capacity is around 30% lower than that of mAbY so that some adsorption sites were available at the start of the experiment for mAbY.

Figure 4.14 shows the results of sequential adsorption experiments where the Nuvia S particles were only partially presaturated with mAbT. As seen in the images at time zero, mAbT is initially uniformly distributed throughout the particle even though the particles contained one half and one third, respectively, of the amount needed to achieve the equilibrium binding capacity. As seen in Fig. 4.14, when these particles are exposed to the mAbY solution the preadsorbed mAbT is displaced by mAbY and accumulates toward the center of the particle.

(A) Simultaneous adsorption

(B) Sequential adsorption
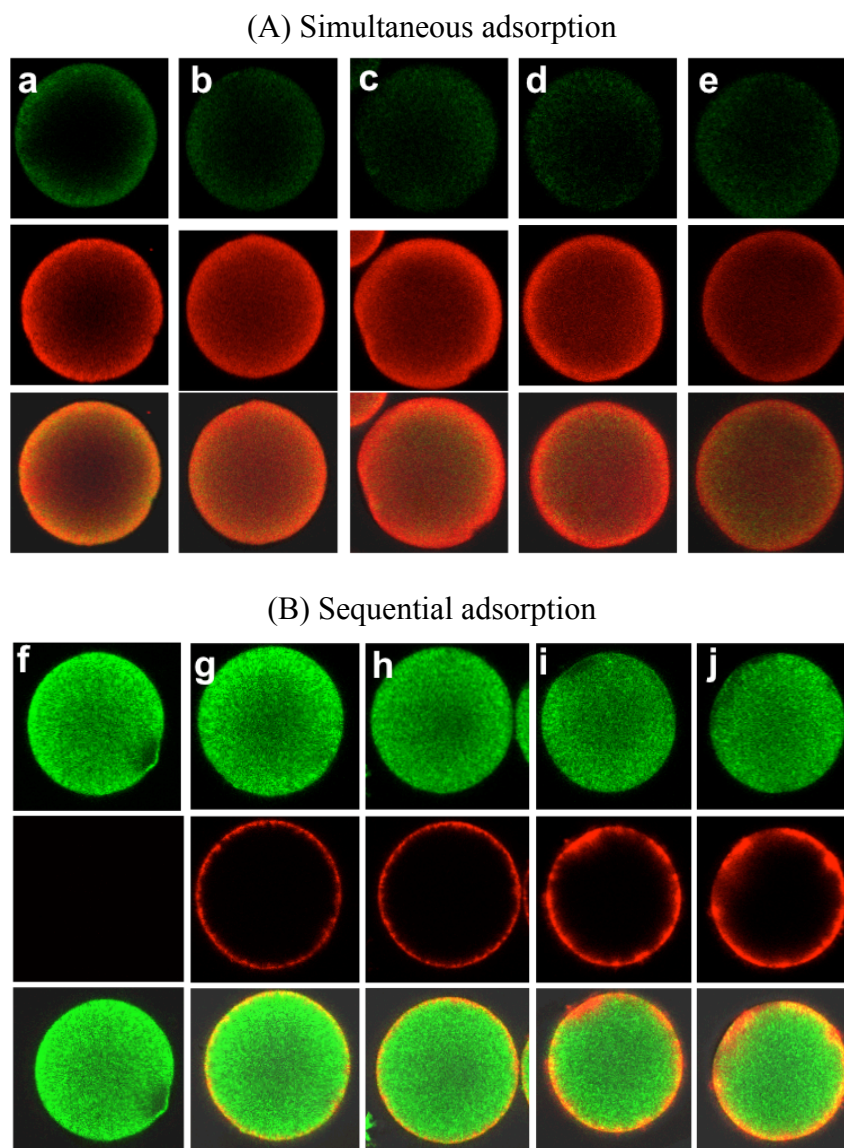
Fig. 4.13. Representative CLSM images of two-component adsorption in Nuvia S at pH 6.0 (A) simultaneous adsorption mixtures containing 1 mg/mL each of mAbT and mAbY (B) sequential adsorption of 1 mg/mL mAbY on beads presaturated with 1 mg/mL mAbT. In each panel, top row images (green) are for mAbT, middle row (red) are for mAbY, and bottom images are composites of green and red resolved images. Particle diameters and time of observation are as follows: a=2 min, 82 μm, b=5 min, 69 μm, c=13 min, 79 μm, d=18 min, 82 μm, e=25 min, 81 μm, f=saturated, 68 μm, g=10 min,73 μm, h=20 min, 70 μm, i=40min, 67 μm, j=150min, 68 μm.

(A) Sequential adsorption on particles initially loaded with mAbT to one half of the equilibrium binding capacity.

(B) Sequential adsorption on particles initially loaded with mAbT to one third of the equilibrium binding capacity.
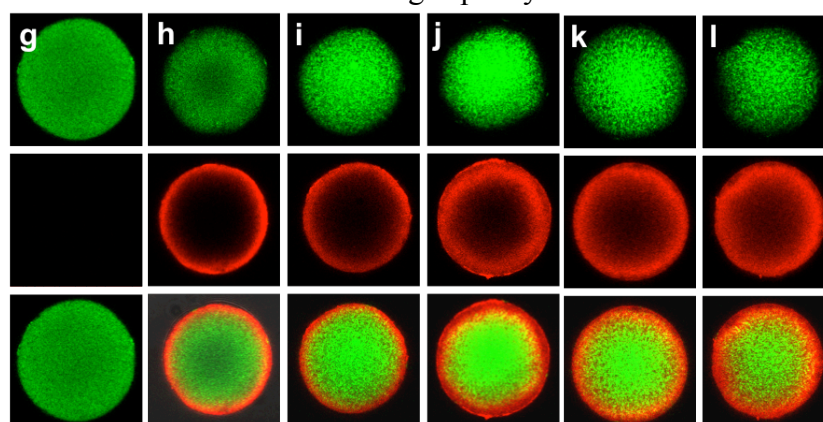
Fig. 4.14. Representative CLSM images of sequential adsorption in Nuvia S at pH 6.0 (A) particles initially loaded with mAbT to one half of the equilibrium binding capacity (B) particles initially loaded with mAbT to one third of the equilibrium binding capacity. In each panel, top row images (green) are for mAbT, middle row (red) are for mAbY, and bottom images are composites of green and red resolved images. Particle diameters and time of observation are as follows: a=0 min, 74 μm, b=3 min, 72 μm, c=12 min, 70 μm, d=25 min, 74 μm, e=50 min, 68 μm, f=120 min, 72 μm, g=0 min, 66 μm, h=3 min, 67 μm, i=12 min, 69 μm, j=25 min, 76 μm, k=80 min, 77 μm, l=180 min, 75 μm.

Further adsorption of mAbY occurs much more slowly suggesting again that strong diffusional hindrance occurs when the two mAbs counterdiffuse.

Batch adsorption measurements was also made to corroborate the CLSM results. Firstly, two-component adsorption equilibrium experiments were performed to determine the selectivity for the two mAbs and the results are shown in Fig. 4.15. These experiments were done by allowing resin and solution to mix for 24 h. Although this time is sufficient to attain equilibrium for the one component case, since counter diffusion appears to be very slow in Nuvia S it is not certain that equilibrium was in fact attained in these experiments. Nevertheless, it is obvious that for these conditions Nuvia S strongly prefers mAbY, so that little mAbT is adsorbed when both mAbs are present in solution.

Secondly, two component batch uptake experiments were performed with Nuvia S to confirm the kinetic behavior seen by CLSM and the results are shown in Fig. 4.16. Figure 4.16a-c show the simultaneous adsorption results for mixtures of mAbT and mAbY in different initial concentration ratios while Fig. 4.16d shows the results for a sequential adsorption experiment. For the simultaneous adsorption case, both mAbs appear to be rapidly coadsorbed during the initial phase of the process with mAbT reaching a slight maximum before gradually decline and mAbY continuing to increase reaching capacities only slightly lower than those observed for the one-component case (see Fig. 4.3). For the sequential adsorption case (Fig. 4.16d), the amount of mAbY adsorbed increases approximately linearly but at very slow rate while little desorption of mAbT takes place. These results are qualitatively consistent with the CLSM images confirming that counter diffusion is very severely hindered in Nuvia S.
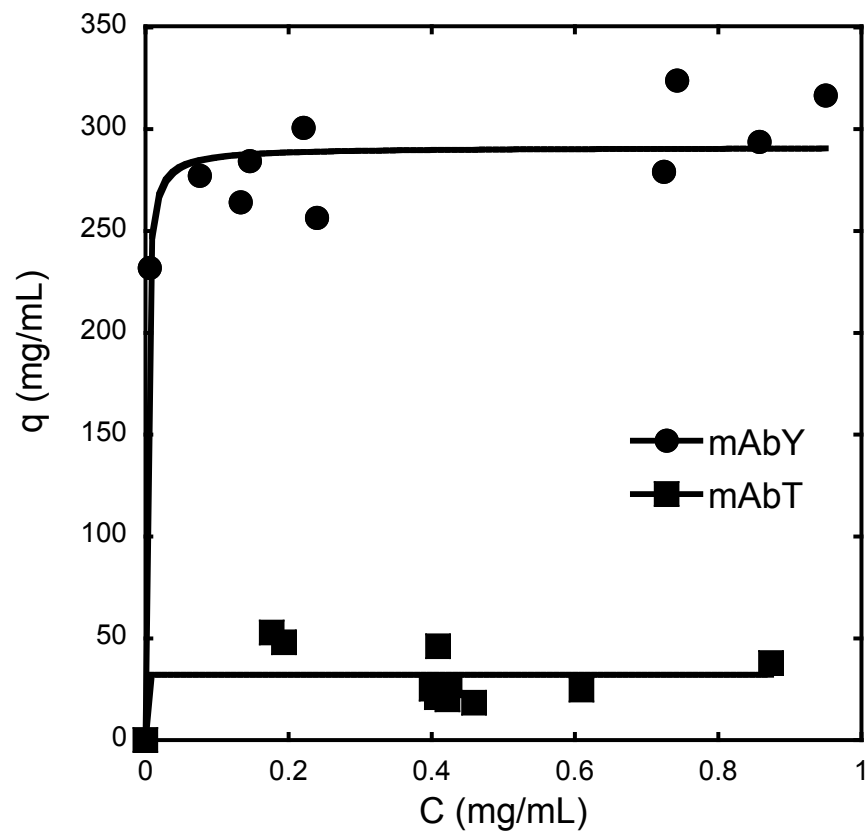
Fig. 4.15 Isotherm for mixture of mAbY and mAbT on Nuvia S at pH 6.0 The solid lines are drawn as guides.
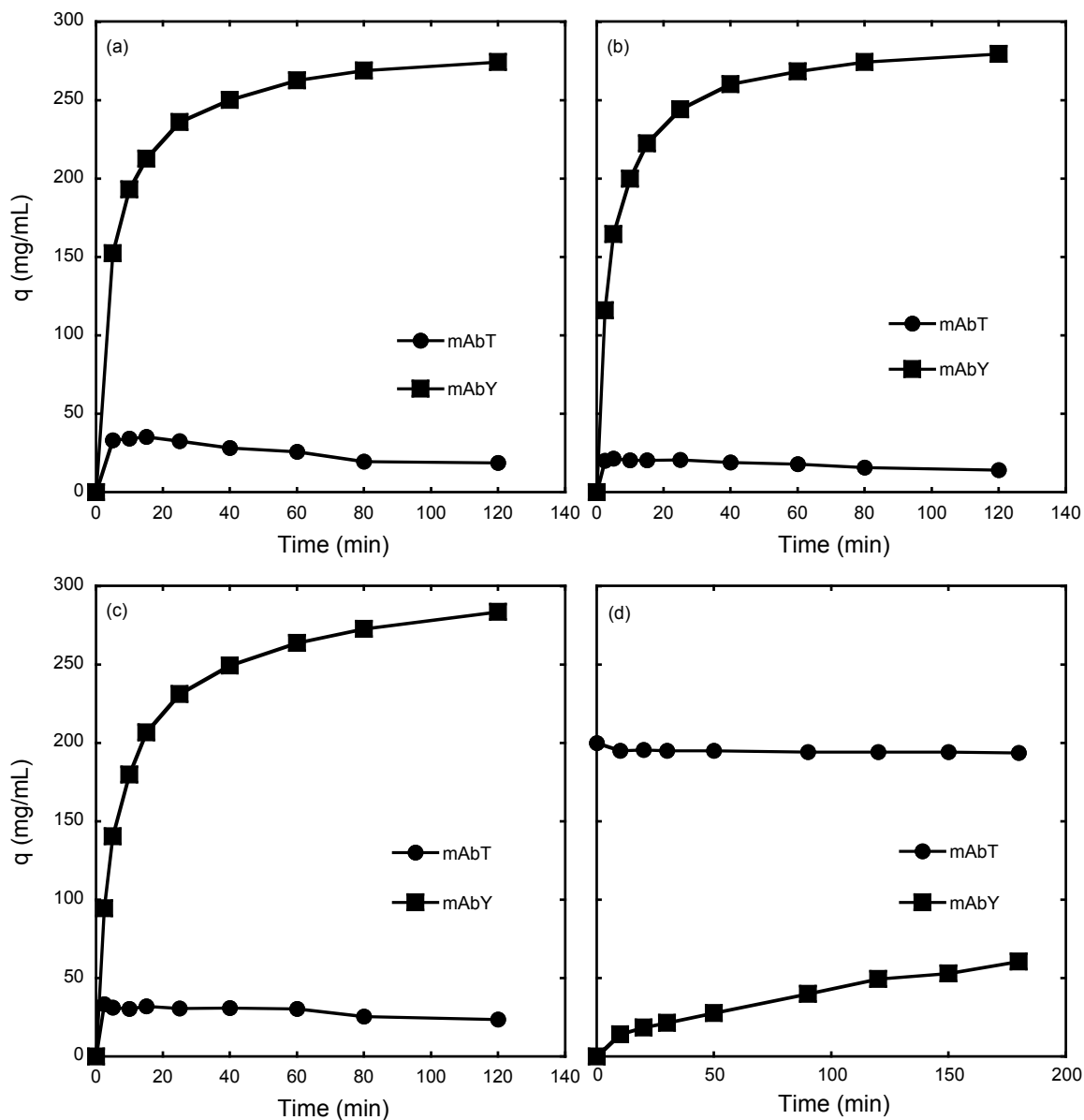
Fig. 4.16. Nuvia S two-component adsorption of mAbT and mAbY a-c show the results of simultaneous adsorption while d shows the results for sequential adsorption. Initial solution concentrations were as follows: (a) 1 g/L of each mAb, (b) 1 g/L mAbT and 2 g/L mAbY, (c) 2 g/L mAbT and 1 g/L mAbY, (d) 1 g/L of mAbY. For case d the particles were presaturated with 1 g/L of mAbT. Lines are shown to guide the eyes.

4.3.4. Quantitative analysis of CLSM data

The quantitative analysis of the CLSM data for UNOsphere S was done based on the shrinking core model for two-component adsorption of Martin et al. [21]. Accordingly, for simultaneous adsorption of a two-component mixture (component B more strongly bound), the positions of the two adsorption fronts are given by the following equations:

$$f(\rho_B) = 2\rho_B^3 - 3\rho_B^2 + 1 = \frac{6C_B^0 D_{e,B} t}{q_B^* r_p^2} \tag{4.4}$$

$$f(\rho_A) = 2\rho_A^3 - 3\rho_A^2 + 1 = (1+\beta)\frac{q_{m,A} - q_A^*}{q_{m,A}} \frac{6C_B^0 D_{e,B} t}{q_B^* r_p^2} \tag{4.5}$$

where
$$\beta = \frac{q_B^*}{q_{m,A} - q_A^*} \frac{C_A^0 D_{e,A}}{C_B^0 D_{e,B}} \tag{4.5a}$$

In these equations, ρ_i is the dimensionless position of the adsorption front of component i, C_i^0 is the liquid phase protein concentration of component i, $D_{e,i}$ its pore diffusivity, $q_{m,i}$ the binding capacity of component i by itself and q_i^* the binding capacity of component i when present in the two-component mixture. For our work mAbT is component A and mAbY is component B.

As shown in Fig. 4.17, plots of $f(\rho_B)$ vs. $C_B^0 t / q_B^* r_p^2$ according to eq. 4.4 for the strongly bound mAbY (obtained by measuring the distance of the red-boundary from the particle surface) are linear for both simultaneous and sequential adsorption cases. The $D_{e,B}$-value can thus be obtained from the slope of these plots. The results were $D_{e,B}$ = (0.76 ± 0.12) x 10^{-7} cm^2/s and (0.72 ± 0.09) x 10^{-7} cm^2/s for the simultaneous and sequential adsorption cases, respectively. These results are consistent with the ones obtained for mAbY from the analysis on the adsorption kinetics and the single-component CLSM measurements (see Sections 4.3.2 and 4.3.3, respectively). A linear plot of $f(\rho_A)$ vs. $C_B^0 t / q_B^* r_p^2$ is also obtained experimentally for the more-weakly bound mAbT for the simultaneous case (Fig. 4.18), as determined by measuring the
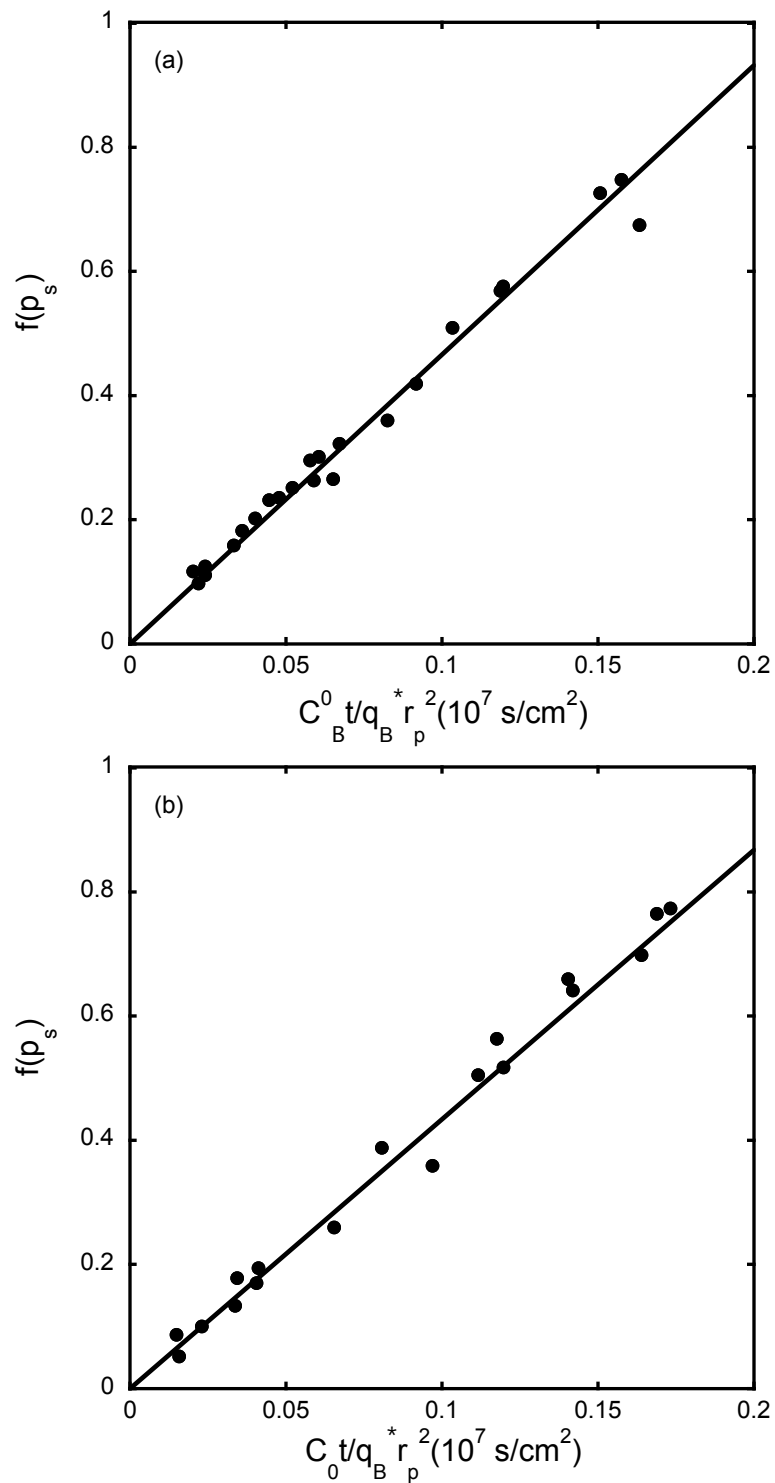
Fig. 4.17 Multicomponent analysis of UNOsphere S CLSM data for the strongly bound component mAbY (a) simultaneous and (b) sequential adsorption at pH 6.0 according to eq. 4.4.
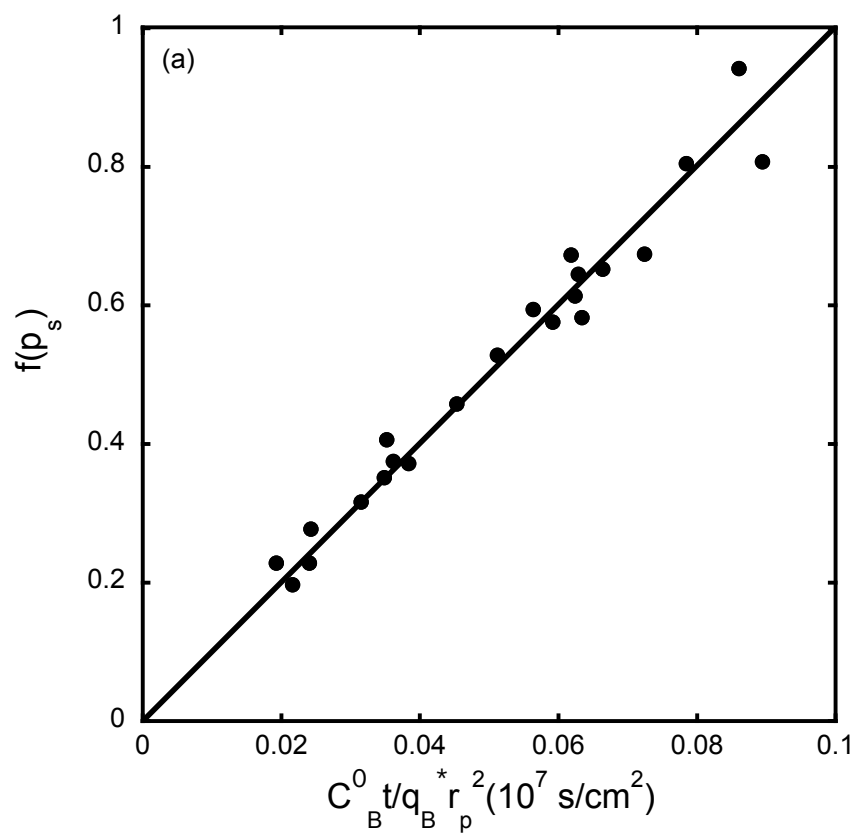
Fig. 4.18 Multicomponent analysis of UNOsphere S CLSM simultaneous adsorption data for the weakly bound component mAbT at pH 6.0 according to eq. 4.5.

position of the mAbT (green) ring. The D_e-value for mAbT can thus also be determined according to eq. 4.5. The value obtained was $D_e = (0.69 \pm 0.07)$ x 10^{-7} cm^2/s which coincides with the value obtained from single component batch and CLSM measurements. Thus, the UNOsphere S multicomponent results follow the pore diffusion model both qualitatively and quantitatively. The results for Nuvia S reveal, however, a complex behavior where the rate of adsorption depends strongly on the direction of transport. This behavior is analyzed in the following section.

4.3.5. Modeling transport in Nuvia S

As described above, for macroporous matrices like UNOsphere S transport occurs in the liquid filled pores. Since the pores are large, protein molecules can pass by the adsorbed ones. As a result the adsorption kinetics occurs over similar time scales whether one protein is adsorbed, two or more proteins are coadsorbed on a clean particle, or one protein replaces another more weakly bound one [1]. This behavior could be described quantitatively by the shrinking core model with two adsorption fronts as described in Section 4.3.4.

A different mechanism can be hypothesized however for transport in polymer grafted media, such as Nuvia S, where, due to the restricted access, protein molecules cannot pass the adsorbed ones. In this case, very different kinetics can be expected for simultaneous versus sequential adsorption where one protein displaces another. Tao et al. [3] recently introduced a single file diffusion (SFD) model to explain an analogous behavior observed for the simultaneous and sequential adsorption of the charge variants of a mAb on the cation exchanger Capto S. This stationary phase is based on agarose, but also contains charged dextran grafts as surface extenders. Its iSEC behavior is similar to that of Nuvia S [22], and mAb binding capacities determined for Capto S are also very high. Finally, very different rates were observed

for simultaneous and sequential adsorption. Thus, a similar analysis was applied to our Nuvia S data.

The SFD model has been used before to model adsorption in zeolitic structures where the size of the adsorbate is similar to the zeolite channel size [4-7]. The model assumes that diffusional transport is as a function of the chemical potential gradient. Accordingly, for the two component system of A and B, the vector of diffusion fluxes **J** is given by:

$$J = - \begin{bmatrix} \overline{D}_{s,A}(q_A,q_B) & 0 \\ 0 & \overline{D}_{s,B}(q_A,q_B) \end{bmatrix} \begin{bmatrix} \dfrac{q_A}{RT}\dfrac{\partial \mu_A}{\partial q_A} & \dfrac{q_A}{RT}\dfrac{\partial \mu_A}{\partial q_B} \\ \dfrac{q_B}{RT}\dfrac{\partial \mu_B}{\partial q_A} & \dfrac{q_B}{RT}\dfrac{\partial \mu_B}{\partial q_B} \end{bmatrix} \nabla q \tag{4.6}$$

where $\overline{D}_{s,i}(q_A,q_B)$ and $\mu_i = \mu_i^0 + RT\ln c_i$ are the Maxwell-Stefan diffusivity and the chemical potential, respectively [9]. In scalar form, eq. 4.6 can be written as follows:

$$J_A = -\overline{D}_{s,A}(q_A,q_B)\dfrac{q_A}{C_A}\left(\dfrac{\partial C_A}{\partial q_A}\nabla q_A + \dfrac{\partial C_A}{\partial q_B}\nabla q_B\right) \tag{4.7}$$

$$J_B = -\overline{D}_{s,B}(q_A,q_B)\dfrac{q_B}{C_B}\left(\dfrac{\partial C_B}{\partial q_A}\nabla q_A + \dfrac{\partial C_B}{\partial q_B}\nabla q_B\right) \tag{4.8}$$

where the partial derivatives $\partial C_i / \partial q_j$ are obtained from the adsorption isotherm. Following Tao et al. [3], we hypothesize that two-component adsorption equilibrium for our mAbT and mAbY system can also be described by the steric mass action (SMA) model, which is given by:

$$C_i = \dfrac{q_i \big/ q_0}{\dfrac{K_{e,i}q_0^{z_i-1}}{C_I^{z_i-1}}\left[1 - \sum_j (z_j + \sigma_j)\dfrac{q_i}{q_0}\right]^{z_i}} \tag{4.9}$$

where C_i is the protein solution concentration, q_i the adsorbed protein concentration, $K_{e,i}$ the equilibrium constant describing the exchange of protein for sodium ion, C_I is the sodium

concentration, q_0 the concentration of ionogenic groups in the adsorbent, z_i is the protein binding charge, and σ_i is the steric hindrance factor. For the composition dependence of the Maxwell-Stefan diffusivities Tao et al. [3] assumed the following:

$$\overline{D}_{s,i}(q_A,q_B) = \overline{D}_{s,i}(0)\left[1 - \sum_j (z_j + \sigma_j)\frac{q_j}{q_0}\right]^{\xi_i} = \overline{D}_{s,i}(0)(q_I)^{\xi_i} \tag{4.10}$$

which suggests that $\overline{D}_{s,i}(q_A,q_B)$ is smaller than the diffusivity at infinite dilution $\overline{D}_{s,0}(0)$, by a factor, given in brackets, that depends on the concentration of unoccupied sites. This equation is empirical and is justified by Tao et al. [3] who assumed that $z_A = z_B = \xi_A = \xi_B$. Equation 4.10 predicts that $\overline{D}_{s,i}$ goes to zero when the adsorbent is fully saturated. The final result is obtained by calculating the derivatives $\partial C_i/\partial q_j$ from eq. 4.9 and combining the results with eq. 4.7 and 4.8 yields:

$$J_A = -\overline{D}_{s,A}(0)(q_I)^{\xi_A}\left[\frac{q_I + z_A(z_A + \sigma_A)q_A}{q_I}\nabla q_A + \frac{z_A(z_B + \sigma_B)q_A}{q_I}\nabla q_B\right] \tag{4.11}$$

$$J_B = -\overline{D}_{s,B}(0)(q_I)^{\xi_B}\left[\frac{z_B(z_A + \sigma_A)q_B}{q_I}\nabla q_A + \frac{q_I + z_B(z_B + \sigma_B)q_A}{q_I}\nabla q_B\right] \tag{4.12}$$

we assume that these equations also describe mAb transport in within the grafted polymer layer of Nuvia S, which in turn, is assumed to occupy a fraction ϕ_G of the particle volume equal to the backbone porosity. These expression for the fluxes are then combined with the following material balances for the particles to obtain a description of the adsorption kinetics:

$$\frac{\partial q_i}{\partial t} = -\frac{1}{r^2}\frac{\partial}{\partial r}\left(r^2 J_i\right) \tag{4.13}$$

$$\left.\frac{\partial q_i}{\partial r}\right|_{r=0} = 0 \tag{4.13a}$$

$$\frac{dC_i}{dt} = -\frac{3V_M \phi_G}{V r_P} J_i \Big|_{r=r_p} \tag{4.14}$$

$$C_i \Big|_{t=0} = C_i^0 \tag{4.14a}$$

$$q_i \Big|_{r=r_p} = q_i^* \left(C_A, C_B \right) \tag{4.14b}$$

Equation 4.14 neglects the external mass transfer resistance, while eq. 4.14b assumes that equilibrium exists at the particle surface. These equations contain several unknowns including the parameters in the SMA model (q_0, z_i, σ_i, and $K_{e,i}$) and $\overline{D}_{s,i}(0)$, and ζ_i. The SMA equilibrium parameters were obtained as follows. q_0 = 0.25 mol/L gel was obtained as discussed in Section 5.3. z_i was obtained for each protein from LGE experiments. Finally, $K_{e,i}$ and σ_i were obtained for each mAb from isotherms obtained at different Na$^+$ concentrations. The results of these determinations are given below.

4.3.5.1. Determination of z_i from LGE

Figure 4.19 shows the LGE peaks obtained with different gradient slopes for mAbT and mAbY on Nuvia S at pH 6.0, while Fig. 4.20 shows the Na$^+$ concentration at elution (C_I^R) versus the normalized gradient slope $\gamma = \left(C_I^f - C_I^0 \right) L / v t_G$. As expected, both mAbs elute at higher Na$^+$ concentration values when the gradient slope is steeper (larger γ). Based on the steric mass action (SMA) model, at low protein loads the isotherm is linear and given by:

$$q_i = K_{e,i} \left(\frac{q_0}{C_I} \right)^{z_i} C_I \tag{4.15}$$

Accordingly in LGE, the Na$^+$ concentration at which the peak elutes is approximated by [22]:

$$C_I^R \sim \left[\phi(z_i + 1) K_{e,i} q_0^{z_i} \gamma \right]^{\frac{1}{(z_i+1)}} \tag{4.16}$$
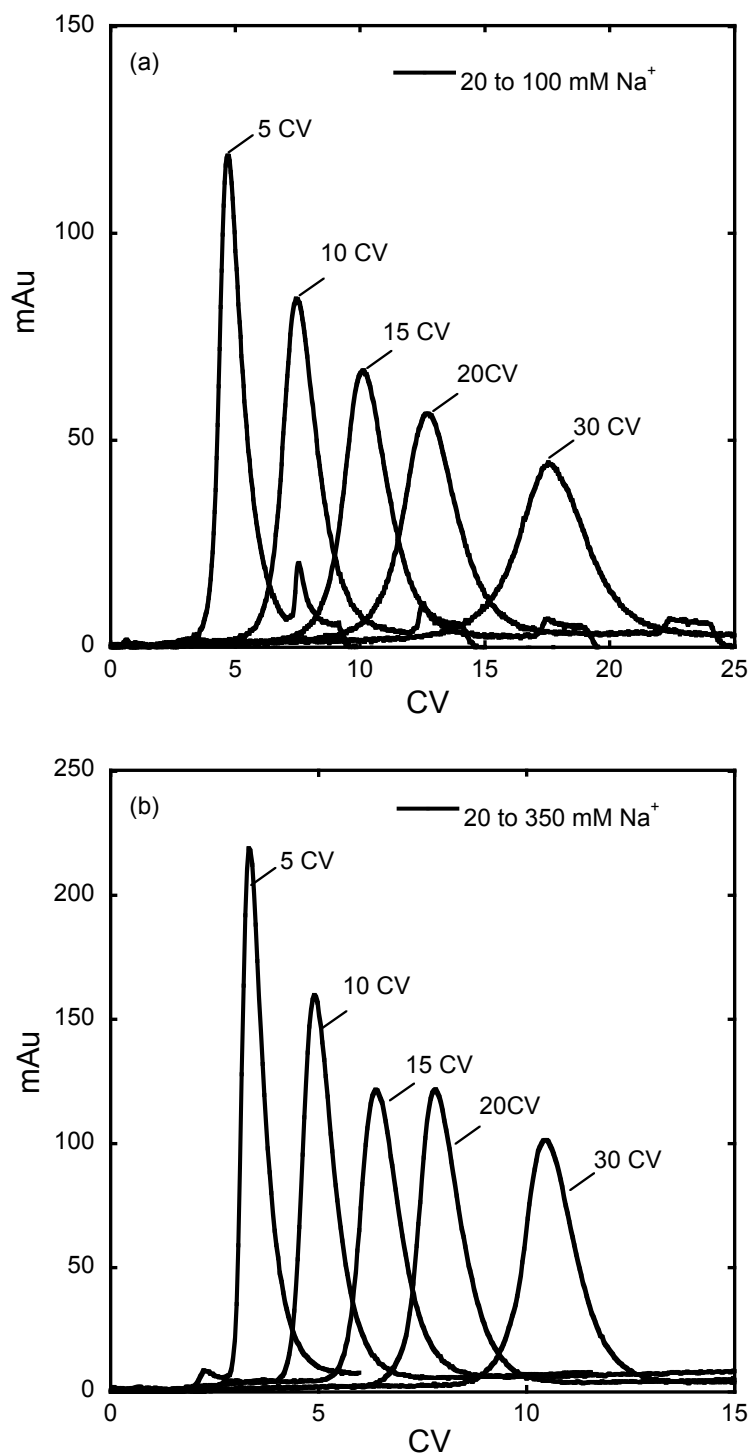
Fig. 4.19. Linear gradient elution (LGE) peaks of mAbT (a) and mAbY (B) on Nuvia S. Initial and final sodium concentration on the gradient and gradient durations in CV are on the legend.
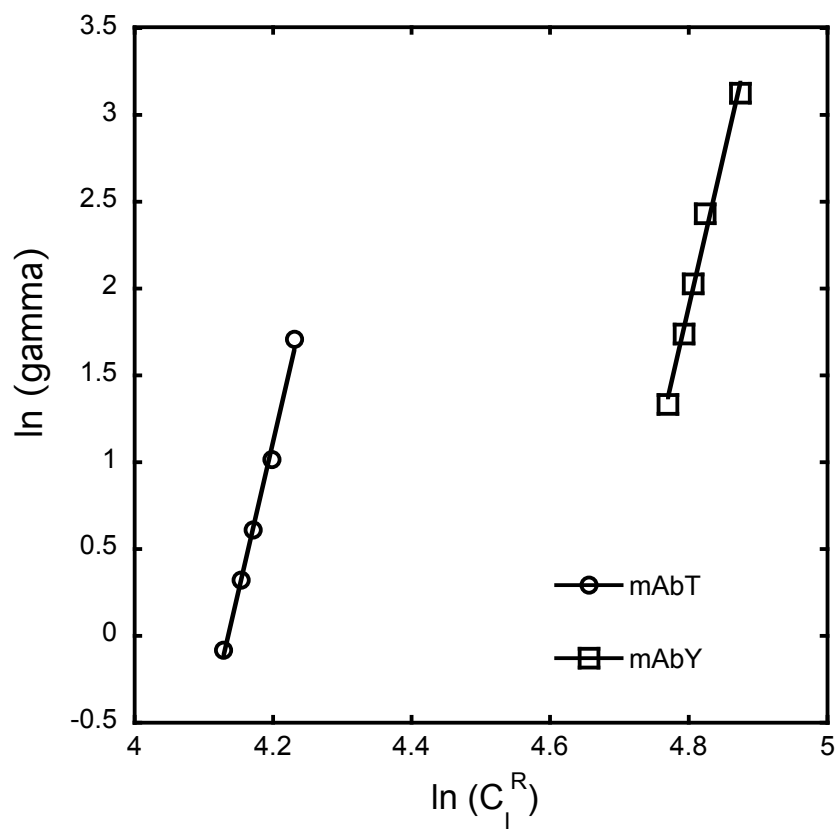
Fig. 4.20. LGE retention data for Fig. 4.19 plotted according to eq. 4.16.

Thus, a plot of ln γ vs ln C_I^R should yield a straight line with slope $z_i + 1$ and intercept $-$ln [

$\phi(z_i + 1) K_{e,i} q_0^{z_i}$]. As seen in Fig. 4.20 these plots are linear for both mAbs. Their slope give z-

values of 18 ± 2 and 25 ± 3 for mAbT and mAbY, respectively. The lower z-value for mAbT

compared to that of mAbY is consistent with the lower pI of mAbT compared to mAbY. It

should be noted that since the lines in Fig. 4.20 are extremely steep it is not possible to obtain the

K_e-values with any reasonable accuracy from these data alone.

4.3.5.2. Determination of K_e and σ from adsorption isotherms

      Adsorption isotherms were obtained at pH 6.0 and different salt concentrations for both

mAbs on Nuvia S and are shown in Fig. 4.21. Although increasing the buffer concentration

decreases the amount of mAb bound, the isotherms remain highly favorable even at the higher

Na^+ concentrations in the range studied. mAbT is more strongly affected by the buffer Na^+

concentration over the range shown. The SMA model, given by eq. 4.9, was fitted to the data

using the average z-values calculated from the LGE experiments yielding K_e and σ as regressed

parameters for each mAb. The parameters obtained from the data fitting were $K_e = 2.0x10^{-8}$,

and $\sigma = 72$ for mAbT, and $K_e = 8.0x10^{-5}$, and $\sigma = 42$ for mAbY. Calculated curves given in Fig.

4.21 show that the SMA model provides a reasonable fit of the isotherms with an average

relative deviation of ± 5%.

4.3.5.3. SFD modeling parameters and results

      The remaining parameters in the SFD model are the Maxwell-Stefan diffusivities at zero

coverage, $\bar{D}_{s,i}(0)$, and the parameter ζ_i in eq. 4.10 that defines the composition dependence of

the diffusivity. For the adsorption of one component on an initially clean bead, the former is

related to the initial steepness of the batch uptake curve while the latter determines the much
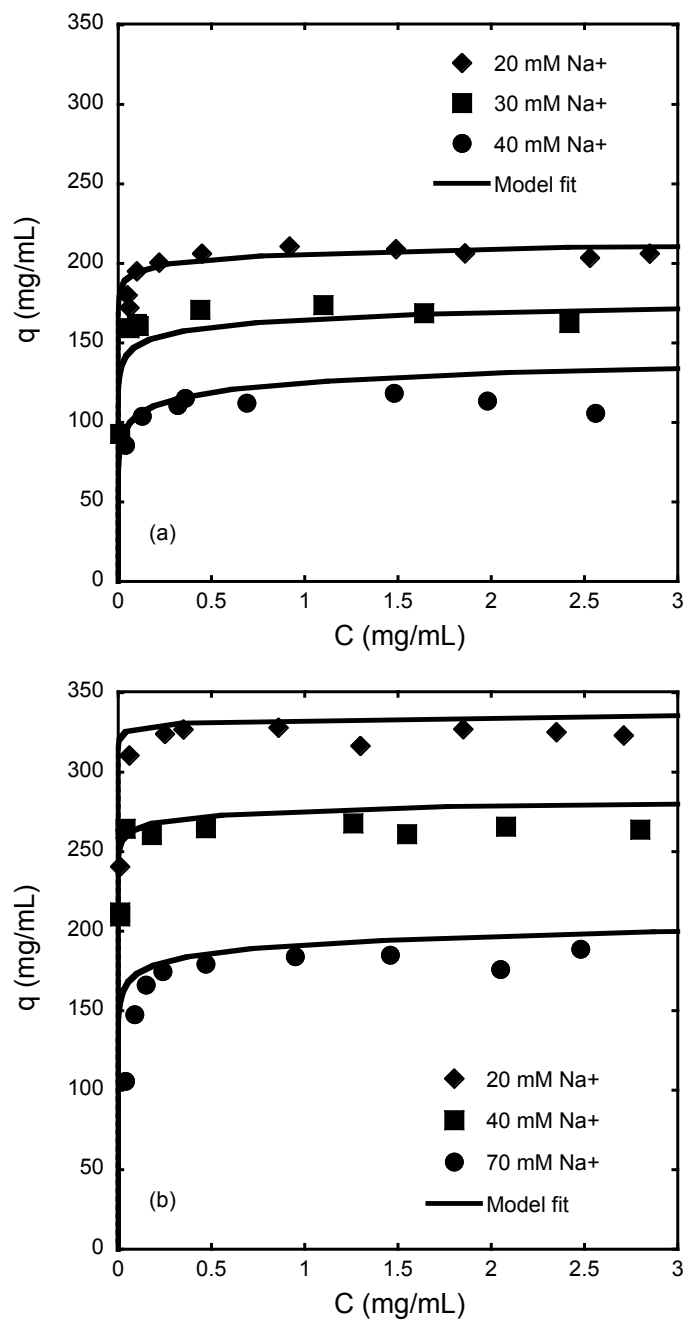
Fig. 4.21. Single component Nuvia S adsorption isotherms of mAbT (a) and mAbY (b) with different Na_2HPO_4 buffer concentrations at pH 6.0. Lines are based on the SMA model.

more gradual approach to equilibrium for long times. Approximate values of these parameters were thus obtained by matching experimental and calculated uptake curves. A FORTRAN program available in our laboratory was used to perform the calculations. The program uses a finite difference scheme to discretize the particle conservation equations (eq. 4.13-4.14b) with fluxes given by eqs. 4.11 and 4.12 for each component. Subroutine DIVPAG in the IMSL library was used to integrate the resulting set of ordinary differential equations in time. 200 spatial discretization intervals were chosen for the calculations as larger numbers did not affect the numerical results.

Figure 4.22 compares the single component batch uptake curves for the two mAbs on Nuvia S with curves calculated with the SFD model. The fitted parameter values were $\overline{D}_s(0) = 0.28x10^{-8}$ cm^2/s and $\zeta = 4.5$ for mAbT, and $\overline{D}_s(0) = 1.0x10^{-8}$ cm^2/s and $\zeta = 6.0$ for mAbY. These values are similar in magnitude to those obtained by Tao et al. [3] for the SFD model description of adsorption of two mAb charge variants on Capto S at pH 7.5. These authors found that $\overline{D}_s(0) = 4.5 \times 10^{-8}$ cm^2/s and $\zeta = 8.3$ for both mAb variants could successfully predict both single component and two-component adsorption kinetics. As seen in Fig. 4.22, the values determined in our work provide a fairly accurate description of the single component experimental data. Figure 4.23 shows a comparison of the experimental data for the sequential adsorption case, with particles initially completely saturated with mAbT and then exposed to 1 mg/mL of mAbY, with curves predicted from the SFD model without further adjustment of the parameters.
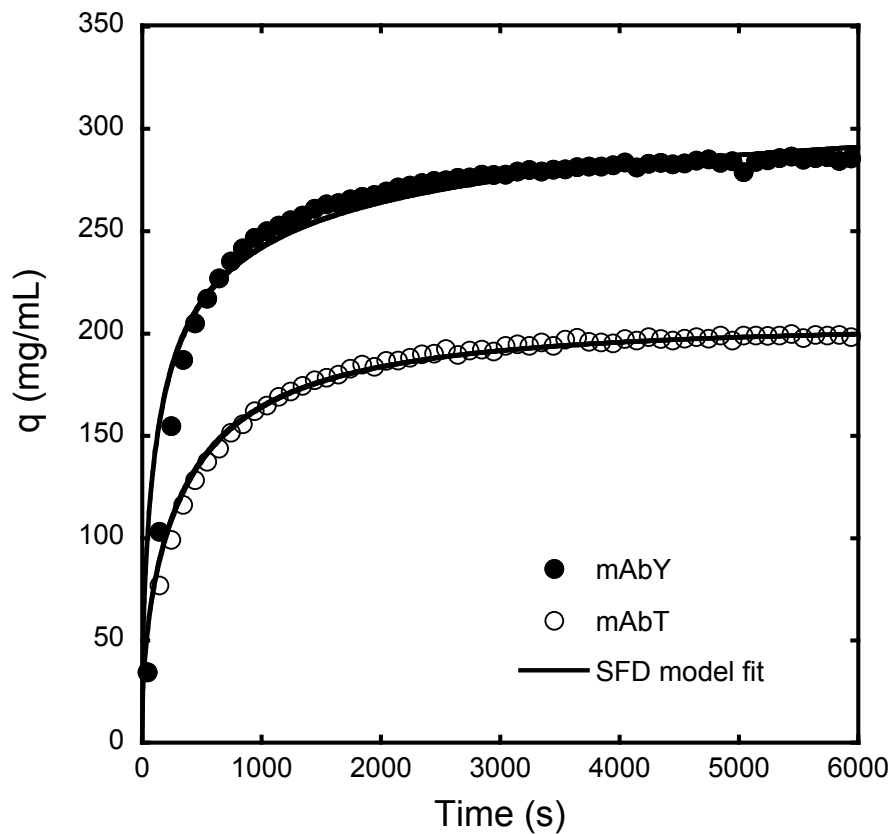
Fig. 4.22. Comparison of experimental single component batch uptake curves for mAbT and mAbY on Nuvia S and curves calculated with the SFD model. Data are from Fig. 4.3. See text for SFD model parameters.
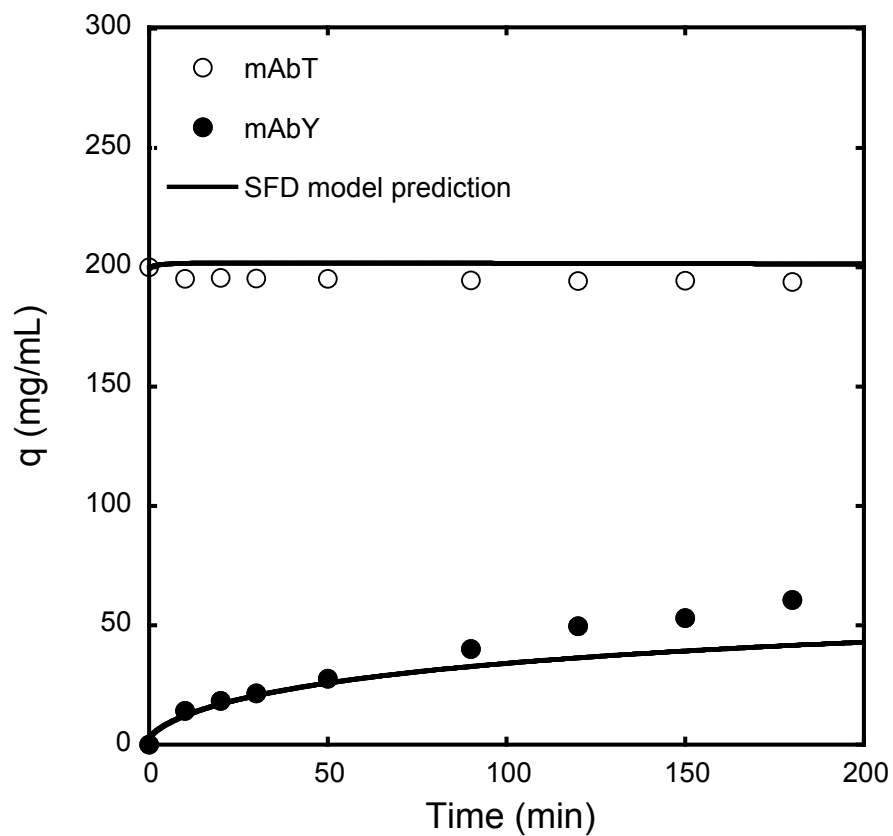
Fig. 4.23. Comparison of experimental batch uptake curves for sequential adsorption of mAbY on Nuvia S particles initially completely saturated with mAbT and curves predicted with the SFD model. Data are as in Fig. 4.16. See text for SFD model parameters.

In approximate agreement with the experimental data, the SFD model predicts essentially no desorption of the more weakly bound mAbT and only very slow adsorption of mAbY. In the SFD model, this occurs because the Maxwell-Stefan diffusivities $\bar{D}_{s,i}$ drop to low values when the adsorbent approaches saturation. Physically, this occurs because the two mAb molecules are not able to pass each other as they try to diffuse counter to each other in the gel-matrix defined by the polymeric surface extenders in Nuvia S. The agreement is only semi-quantitative but the model is obviously able to capture the main trends.

It is of interest to also compare the intraparticle concentration profiles predicted by the SFD model with the CLSM images for the sequential adsorption case with particles initially fully saturated with mAbT at 1 mg/mL solution concentration, with particles saturated with one-half of the equilibrium amount, and with particles saturated with one-third of that amount, shown in Figs. 4.13B, 4.14A, and 4.14B, respectively. These images show little penetration of mAbY (red) in the particles for the fully saturated case, but greater penetration of mAbY accompanied by an overshoot of mAbT (green) near the center of the particles for the particles that initially contained one-half and one-third of the mAbT equilibrium amount. Profiles predicts by the SFD model at 100 min (without adjusting the parameter values) are shown in Fig. 4.24 for the three different cases. In all three cases, the model predicts little desorption of mAbT from the particle. Any mAbT displaced by the adsorbed mAbY moves toward the center of the particle where adsorbed concentrations higher than the initial value are attained. In the SFD model, this occurs because mAbY is strongly bound and the concentration of empty adsorption sites is low at the particle surface (cf. Fig. 4.2). In turn, this greatly reduces the Maxwell-Stefan diffusivity, nearly completely preventing the more-weakly bound mAbT from leaving the particle. This behavior is also seen in the physical system, where accumulation of mAbT near the particle center above the
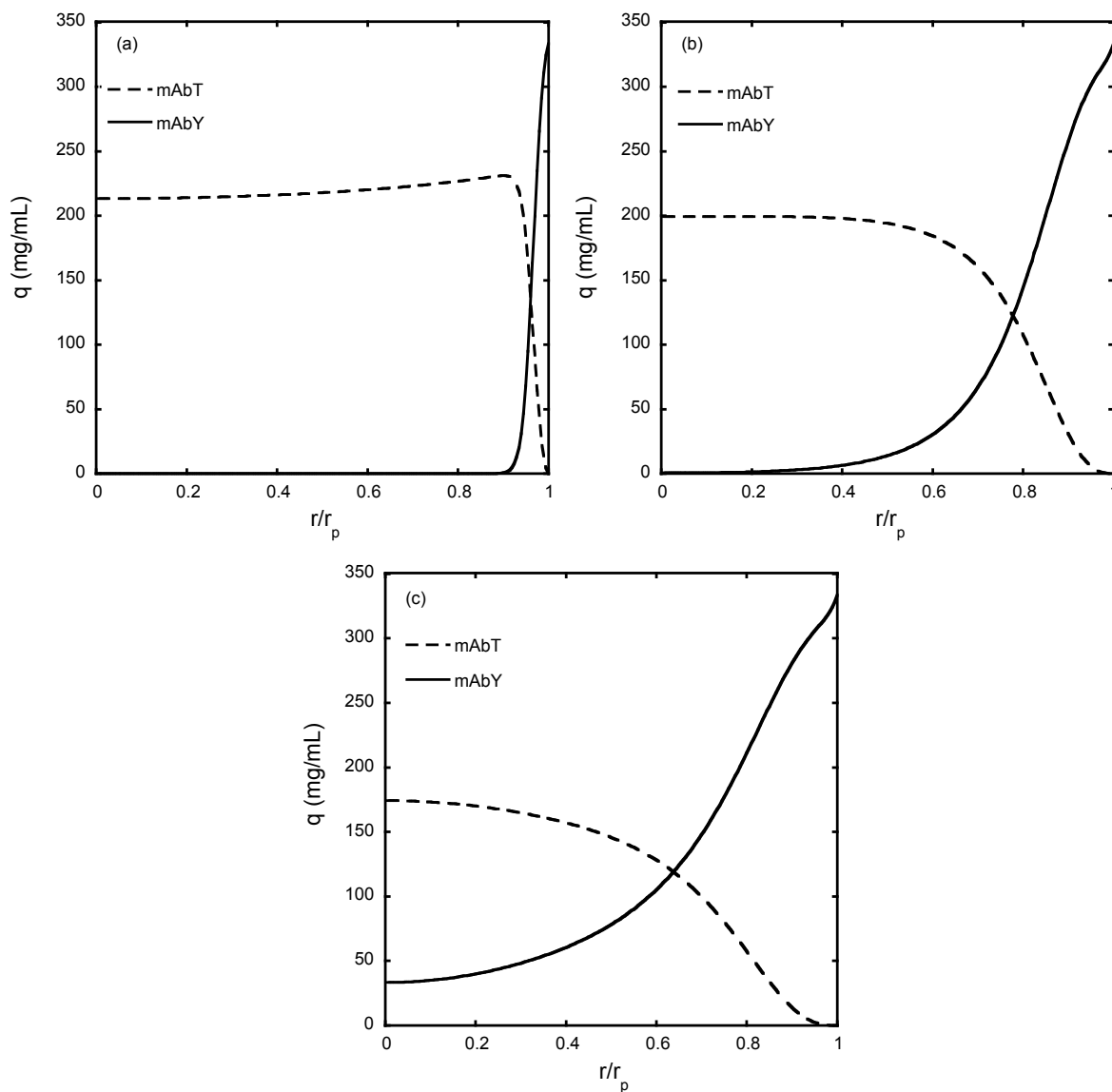
Fig. 4.24. Intraparticle concentration profiles predicted at 100 min by the SFD model for the sequential adsorption of mAbY on Nuvia S particles containing different adsorbed concentrations of mAbT. The initially adsorbed mAbT is assumed to be uniformly distributed through the particles. Initial adsorbed concentrations of mAbT were (a) 200 mg/mL (corresponding to saturation with a 1 mg/mL mAbT solution); (b) 100 mg/mL (corresponding to one half of the equilibrium amount); and (c) 67 mg/mL (corresponding to one-third of the equilibrium amount).

initial adsorbed concentration is manifested by the substantial overshoot in fluorescence intensity above the initial value. In agreement with the SFD model predictions, the experimental images also show greater penetration of mAbY (red) with a smooth profile when the particles were initially only partially saturated with mAbY. Physically, this occurs because the displaced mAbT molecules cannot pass the counterdiffusing mAbY molecules due to the physical constraints imposed by the polymeric surface extenders. Thus, the mAbT molecules move toward the center of the particle where they accumulate reaching adsorbed concentrations higher than the initial values. Despite the excellent agreement with the sequential adsorption kinetics data, the SFD model, however, was unable to quantitatively predict the two-component simultaneous adsorption behavior. In this case, the SFD model could predict only the rapid uptake of mAbY seen experimentally while almost no adsorption was predicted for mAbT although the experimental measurements showed that a small but apparently significant amount of mAbT was also adsorbed (see Figs. 4.13 and 4.16). The reason for this discrepancy is that, for the parameter values determined from the LGE experiments and the single component isotherms at different buffer concentrations, the SMA model predicts little or no equilibrium binding of mAbT when both mAbs are present in solution. Thus, the inability of the SFD model to describe the simultaneous adsorption kinetics seems to be related to the apparent inability of the SMA model to accurately describe the two-component equilibrium in this system. The reasons for this discrepancy are not known. One possibility is that a certain number of adsorption sites in Nuvia S are not accessible by mAbY, which, for these conditions has a greater binding charge than mAbT (25 vs 18). On such sites, competitive binding of the two mAbs cannot take place so that a certain amount of mAbT can still be bound even though the overall selectivity greatly favors mAbY. Such adsorption heterogeneity is not at all accounted for by the SMA model.

4.4. Conclusions

The charged polymeric surface extenders incorporated in Nuvia S provide the material with higher equilibrium binding capacities and transport kinetics for both mAbs compared to UNOsphere S. For UNOsphere S it looks like both single component and multi-component transport mechanisms are controlled by ordinary pore diffusion. On the other hand, transport on the Nuvia S material looks to be controlled by a transport mechanism where protein molecules are favorably partitioned but retain sufficient diffusional mobility to hop from one site to another, and coupled with the large driving force related to the adsorbed capacity results in a rapid adsorption kinetics. This can explain why mAbY shows higher transport kinetics than mAbT under the same condition. The SFD model can describe qualitatively the single and multi-component results obtained for mAbT and mAbY on Nuvia S. At this point a more complex model should be developed to quantify the Nuvia S results.

4.5. List of symbols

C protein concentration in solution (mg/mL)

C_F feed protein concentration (mg/mL)

C_I concentration of counterions in solution (mmol/L)

C_0 fluid phase protein concentration (mg/mL)

D_e effective pore diffusivity (cm^2/s)

D_s adsorbed phase diffusivity in solid diffusion model (cm^2/s)

$\bar{D}_s$ Maxwell-Stefan diffusivity (cm^2/s)

f function defined by eq. 4.3

J mass-transfer flux (g/cm^2 s)

k_f boundary layer film mass-transfer coefficient (cm/s)

K_e equilibrium constant in SMA model

M_W mass of stationary phase (mg)

q adsorbed protein concentration (mg/mL)

q_I concentration of unoccupied charged groups in stationary phase (mmol/L)

$\tilde{q}$ protein adsorbed by the media (mg/mL)

q_m protein binding capacity (mg/mL)

r_p particle radius (cm)

r_s radial position of adsorption front (cm)

R gas law constant (J/mol K)

t time (s)

T absolute temperature (K)

V solution volume (mL)

V_m volume of stationary phase (mL)

z protein effective charge in SMA model

Greek Symbols

ϕ_g volume fraction of adsorbent phase in the particle

γ normalized gradient slope ($= \beta L / v$), mol/L

μ chemical potential (J/mol)

ρ_s dimensionless radial position of adsorption front

σ steric hindrance parameter in SMA model

4.6. References

[1] Y. Tao, E.X. Perez-Almodovar, G. Carta, G. Ferreira, D. Robbins, J. Chromatogr. A. 1218 (2011) 8027.

[2] C.Martin, G. Iberer, A. Ubiera, G.Carta, J. Chromatogr. A. 1079 (2005) 105.

[3] Y. Tao, N. Chen, G. Carta, G. Ferreira, D. Robbins, AIChE J. doi: 10.1002/aic.13718.

[4] W.R. Qureshi, J. Wei, J. Catal. 126 (1990) 126.

[5] W.R. Qureshi, J. Wei, J. Catal. 126 (1990) 147.

[6] J.G. Tsikoyiannis, J. Wei, Chem. Eng. Sci. 46 (1991) 233.

[7] K. Dahlke, G. Emig, Catal. Today. 8 (1991) 439.

[8] J. Wei, Eng. Chem. Res. 33 (1994) 2467.

[9] L.J.P. van den Broeke, AIChE J. 41 (1995) 2399.

[10] M.C. Stone, G. Carta, J. Chromatogr. A. 1160 (2007) 206.

[11] G. Carta, A.R. Ubiera, T.M. Pabst, Chem. Eng. Technol. 28 (2005) 1252.

[12] A. Ljunglöf, R. Hjorth, J. Chromatogr. A. 743 (1996) 75.

[13] T. Linden, A. Ljunglöf, M.E. Kula, J. Thommes, Biotechnol. Bioeng. 65 (1999) 622.

[14] J. Hubbuch, T. Linden, E. Knieps, J. Thommes, M.R. Kula, J. Chromatogr. A. 1021 (2003) 105.

[15] S.R. Dziennik, E.B. Belcher, G.A. Barker, M.J. de Bergalis, S.E. Fernandez, A.M. Lenhoff, Proc. Natl. Acad. Sci. 100 (2003) 420.

[16] A. Ljunglöf, K.M. Lacki, J. Mueller, C. Harinarayan, R. van Reis, R. Fahrner, J.M. Van Alstine, Biotechnol. Bioeng. 96 (2007) 515.

[17] S.Yamamoto, Biotechnol. Bioeng. 48 (1995) 444.

[18] G. Carta, A. Jungbauer, Protein Chromatography- Process Development and

Scale-up, Wiley-VCH, Weinheim, Germany, 2010.

[19] E.X. Perez Almodovar, Y. Tao, G. Carta, Biotechnol. Prog. DOI 10.1002/btpr.643.

[20] Y. Tao, G. Carta, G. Ferreira, D. Robbins, J. Chromatogr. A. 1218 (2011) 1530.

[21] C. Martin, G.Iberer, A. Ubiera, G. Carta, J. Chromatogr. A. 1079 (2005) 105.

[22] Y. Tao, G. Carta, G. Ferreira, D. Robbins, J. Chromatogr. A. 1218 (2011) 1519.

Chapter 5

Counterion Effects on Protein Adsorption and Transport

5.1. Introduction

As noted in Chapter 1, ion exchangers are used extensively in the analytical and process scale capture and purification of proteins [1-3]. At the process scale, binding capacity and adsorption rates are generally critical since they, together, define the dynamic binding capacity and productivity [4]. As recently reviewed by Lenhoff [5] polymer-functionalized ion exchangers, where charged polymers are introduced by grafting to a support matrix or by in-situ polymerization within a porous support, have attracted considerable attention in recent years since in many instances they exhibit both high protein binding capacity and faster protein adsorption rates compared to more traditional macroporous matrices. These characteristics provide a large potential for higher productivity benefits in process applications. The exact mechanism responsible for the higher capacity and faster adsorption rates is not known [5]. However, it has been suggested that the charged polymers in these materials act as surface extenders forming a continuous three-dimensional network, akin to a hydrogel, which is stabilized by the support matrix and where protein binding and transport occur simultaneously [4-6]. The key assumption is that protein molecules retain diffusional mobility within the polymer phase leading to faster mass transfer because of the large driving force as observed for an homogeneous diffusion process [7-8].

Although van der Waals, hydrogen bonding, and steric interactions are likely contributing factors, the fundamental driving force for protein binding in ion exchangers is a stoichiometric

exchange with counterions [9-10]. This effect is readily evident in frontal analysis and displacement chromatography experiments at protein loadings and is captured qualitatively by the stoichiometric displacement [11]. Despite its seemingly important role, the effect of the counterion type on protein adsorption and transport in ion exchangers has received surprisingly little attention. Sodium ion is most commonly used in protein cation exchange chromatography of proteins. However, the potential practical usefulness of other cations has been suggested. Arakawa et al. [12], for example, noted that higher valence cations could be used effectively to modulate elution. The same authors also suggested using arginine, which is cationic at pHs typically used for protein cation exchange, to help prevent aggregate formation. Annathur et al. [13] also suggested using arginine as an efficient eluent in the cation exchange chromatographic purification of a PEGylated peptide. In their study, compared to sodium chloride, arginine acetate in the load buffer actually reduced somewhat the peptide binding capacity. However, since arginine had a stronger eluting power, sharper peaks were obtained upon elution, which, in turn decreased the PEGylated peptide hydrodynamic radius and thus improved mass transfer out of the particle pores. Addition of arginine and guanidine to mobile phases used in cation exchange chromatography has also been studied by Holstein et al. [14]. Significant effects of these species were seen on retention, but the behavior was highly protein-specific leading to the suggestion by these authors that these effects are caused by preferential interactions of arginine with specific regions on the protein surfaces and its effects on the surrounding hydration layer.

One aspect not explicitly investigated so far is the role of the counterion type on protein binding and transport. These effects are expected to be particularly important for polymer-functionalized ion exchangers, where protein transport occurs while simultaneously interacting with the charged polymer chains. Since protein binding equilibrium and transport are likely to be

intimately coupled in these systems, it is reasonable to expect that the nature of the counterion will affect both. In this study we consider the effects of four different counterions on the binding behavior of a monoclonal antibody (mAb) in the commercial polymer-functionalized cation exchanger Nuvia S. The counterions studied include sodium, arginine, and tetrabutyl ammonium ion, which are monovalent at the pH used, and calcium as an example of a divalent counterion. These species are different in size and aqueous diffusivity. Our measurements encompass inverse size exclusion chromatography to determine potential effects on the structure of the polymer phase, frontal analysis counterion exchange experiments to determine the relative affinity of each counterion for the stationary phase, linear gradient elution experiments to determine the protein effective charge, mAb adsorption isotherms to determine the effects of binding capacity, and mAb batch uptake rates to determine the impact of the counterion on intraparticle transport. The results are then extended to other matrices, with and without functionalizing polymers, and to two other model proteins, lysozyme and lactoferrin.

5.2. Experimental

5.2.1. Materials

5.2.1.1. Stationary phases

The cation exchangers used in this work are the same Nuvia S and UNOsphere S from Bio-Rad Laboratories (Hercules, CA, USA) considered in Chapter 3 and 4. However, Capto S from GE Healthcare (Piscataway, NJ, USA) was also used in this study. As noted earlier, Nuvia S and UNOsphere S are based on a similar macroporous polymeric backbone. However, Nuvia S contains grafted, charged polymeric surface extenders. Capto S is based instead on an agarose backbone but is also grafted with charged dextran polymers. All three materials contain SP-

functional groups. Mean particle sizes are 85, 75, and 89 μm for Nuvia S, UNOsphere S, and Capto S, respectively. Other relevant properties of these materials are given in refs. [15-16].

Figure 5.1 shows transmission electron micrographs of 80 nm sections of Nuvia S obtained as described by Perez-Almodovar et al. [15] by embedding the particles in LRWhite resin (obtained from London Resin Company, London, UK) and ultramicrotoming. The top panel is for a clean particle with its edge toward the bottom of the image. The light grey area represents the embedding resin, while the darker areas are the backbone matrix, which consists of dense aggregates defining a macroporous network. The grafted polymers are not visible, likely because of insufficient density contrast with the embedding resin. The bottom panel is for a mAb-saturated particle. The backbone matrix is still visible. However, it now appears to be completely surrounded by a different phase that fills the pores consistent with a hydrogel structure made visible by the higher density of the bound protein. Based on these images, the porosity of the backbone matrix and, hence, the hydrogel volume is estimated to be around 70% of the particle volume.

5.2.1.2. Proteins and buffers

A purified mAb (M_r ~ 150 kDa, pI ~ 8.2) available in our laboratory, hen egg white lysozyme (M_r ~15 kDa, pI ~ 11) from Sigma Aldrich (St Louis, MO, USA), and lactoferrin (M_r ~ 78 kDa, pI ~9.5) from DMV-International (Dehli, NY, USA) were used in this work. Acetate buffers at pH 5.0 containing fixed concentrations of tetrabutyl ammonium, sodium, arginine, and calcium ion were prepared from analytical reagent grade tetrabutyl ammonium hydroxide (TBAH), sodium acetate, free-base arginine, calcium acetate, and acetic acid obtained from Sigma-Aldrich (St. Louis, MO) and Fisher Scientific (Pittsburg, PA). Relevant properties are summarized in Table 5.1. TBAH is a strong base and is completely protonated at pH 5. Arginine

8/18/2011 Image 17029   NuviaS mAb 20K 6   0.5um
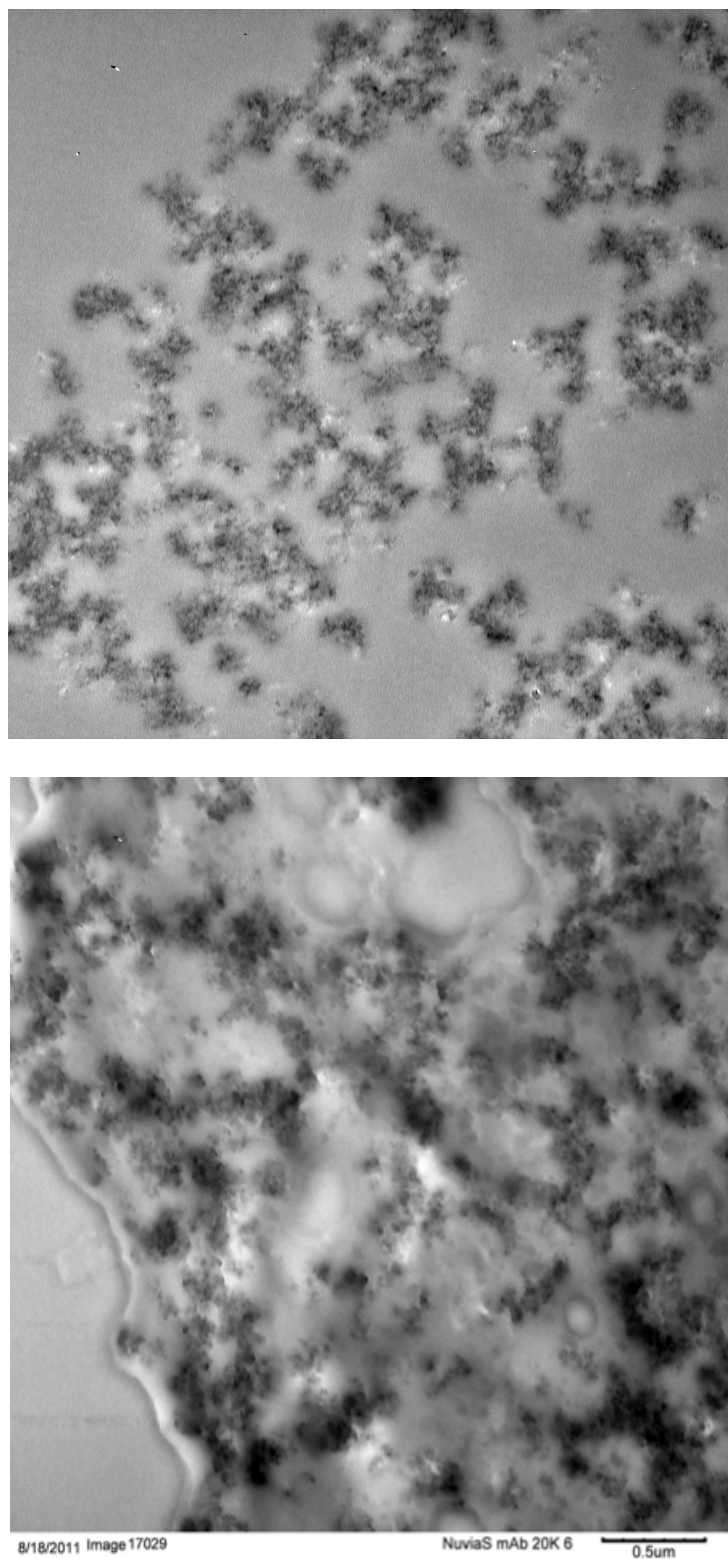
Fig. 5.1. TEM images of sections of clean (top) and mAb-saturated (bottom) Nuvia S particles.

Table 5.1. Properties of the counterions used in this work.

Counterion	Structure	Charge at pH 5.0	Aqueous diffusivity at 25 °C (cm^2/s)	Molecular radius (nm)[c]
Sodium	Na$^+$	+1	1.3x10^{-5}[a]	0.17
Arginine		+1	0.60x10^{-5}[b]	0.36
TBAH		+1	0.42x10^{-5}[b]	0.52
Calcium	Ca^{++}	+2	0.79x10^{-5}[a]	0.28
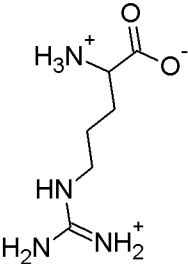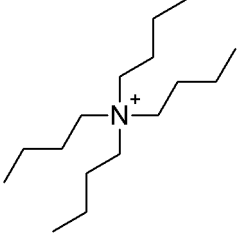
[a] Given in ref. [16]
[b] Estimated from the Wilke-Chang equation [16]
[c] Estimated from the Stokes-Einstein equation [16]

is also monovalent at this pH since its pK_as are 2.17, 9.04, and 12.48. Since the pKa of acetic acid is 4.76, solutions containing 20 mequi/L concentrations of each of these counterions contained 31.3 mM concentrations of total acetic acid.

5.2.2 Methods

Dynamic light scattering **(**DLS) analyses were performed at 25 $^{\circ}$C with a DynaPro NanoStar instrument from Wyatt Technology Corporation (Santa Barbara, CA). Inverse size exclusion chromatography (iSEC) experiments were conducted for Nuvia S as described in ref. [15] by packing the resin in a 0.5x10 cm Tricorn column from GE Healthcare and injecting 20 μL of 5 g/L dextran samples and glucose at a flow rate of 0.5 mL/min with a Waters Mod. 2595 HPLC unit. Dextran with molecular masses of 10, 40, 70, 500, and 2,000 kDa, obtained from Amersham Biosciences (Upsala, Sweden), were used as standards. Detection was with a Water Mod. 2414 refractive index detector. The extraparticle column porosity used in data analysis, $\varepsilon =$ 0.37, was based on the retention volume of 2,000 kDa dextran, which is assumed to be completely excluded.

Frontal analysis experiments were conducted with the packed Nuvia S column at a flow rate of 1 mL/min (300 cm/h) using an AKTA Explorer 10 unit from GE Healthcare. The column was first equilibrated with the desired acetate salt at 20 mequiv/L concentration and then supplied with 20 mM arginine acetate. Detection of arginine breakthrough and subsequent elution was by UV at 220 nm. Acetate also absorbs UV light at this wavelength, but since its concentration was kept constant, the UV220 signal was directly related to the arginine concentration.

Linear gradient elution (LGE) experiments were conducted with the same column and equipment used for the counterion frontal analysis experiments but at a flow rate of 0.5 mL/min

(150 cm/h). For these experiments the column was initially equilibrated with acetate buffers at pH 5.0 containing 10 mequiv/L of the different counterions and then subjected to 5, 10, 15, 20, and 30 CV acetate gradients to acetate buffers containing counterion concentrations of 300 mequiv/L for Na^+, Arg^+, and Ca^{++} and 700 mequiv/L for $TBAH^+$. In each case, the counterion concentration at elution was obtained from the conductivity signal using appropriate correlations.

Adsorption isotherms were obtained by suspending small samples of particles (2 − 25 mg) in 1 mL samples of protein solutions of known initial concentration held in 1.5 mL tubes. The resin samples used in these experiments had been previously equilibrated in the desired buffer and then spin in a microcentrifuge filter tube to remove the extraparticle solution. After rotating the tubes end-over-end for 24 hours, the amount of protein adsorbed after 24 hours was then determined by material balance based on the residual protein concentration obtained from the UV280 of the supernatant. Finally, the bound protein concentration per unit of particle volume was calculated based on a particle density of 1.08 g/mL determined with a picnometer [15].

Batch uptake rate experiments were conducted in a small open stirred vessel as described in ref. [17] following the protein concentration in the supernatant from the UV280 for a period of 2 hours. A small correction was applied to correct for water evaporated from the stirred vessel, which was less than 3% during the 2 hour period. All experiments, except DLS measurements, were conducted at room temperature, 22±2 $^{\circ}$C.

5.3. Ion exchange equilibrium theory

The mass action (MA) law provides a general framework for the description of ion exchange equilibrium [18]. Accordingly, the exchange equilibrium for a counterion A with charge z_A replacing a counterion B with charge z_B is described by the following equation:

$$K_{A,B} = \frac{q_A (C_B)^{z_A/z_B}}{C_A (q_B)^{z_A/z_B}} \tag{5.1}$$

subject to the conditions:

$$q_0 = z_A q_A + z_B q_B \tag{5.2}$$

$$C_0 = z_A C_A + z_B C_B \tag{5.3}$$

where $K_{A,B}$ is an equilibrium constant, q_0 the exchanger charge density, and C_0 the equivalent co-ion concentration. For equivalent exchange, the exchange process is favorable when $K_{A,B} > 1$, regardless of concentration. On the other hand, for heterovalent exchange, when $z_A > z_B$, the exchange process is favorable at low concentrations and unfavorable at high concentrations. In principle, the same approach can be used to describe the ion exchange equilibrium when A is a protein. There are three substantial differences, however, when compared to the exchange of small counterions. The first is that for such macromolecules the charge z_A is generally different from the net charge as a result of the heterogeneous distribution of charges on the proteins surface. z_A is then referred to as the effective charge [10-11] and should be thought of as the equivalent number of counterions B replaced by a protein molecule. The second difference is that protein binding can either hinder or completely block a number of fixed charged groups in the exchanger as a result of its bulkiness [11]. Accordingly, eq. 5.2 is replaced by:

$$q_0 = (z_A + \sigma_A) q_A + z_B q_B \tag{5.4}$$

where σ_A is the number of blocked functional groups. The third difference is that, because of the relatively high buffer concentrations used in practice and the large protein molecular mass, the equivalent protein concentration in solution is small so that $C_0 \sim z_B C_B$. Taking into account these factors the following well-known Steric Mass Action (SMA) model is obtained [11]:

$$K_{P,B} = \frac{q_P \left(z_B C_B \right)^{z_P/z_B}}{C_P \left[q_0 - \left(z_P + \sigma_P \right) q_P \right]^{z_P/z_B}}$$ (5.5)

where P has been used in lieu of A to denote that this equation applies to protein ion exchange. At high C_B-values, eq. 5.5 reduces to the following linear isotherm limit:

$$q_P = \frac{K_{P,B} \left(q_0 \right)^{z_P/z_B}}{\left(z_B C_B \right)^{z_P/z_B}} C_P$$ (5.6)

It should be noted that when these equations are used to describe equilibrium in heterogeneous matrices like Nuvia S, care must be taken to properly define the adsorbent volume as the basis for the adsorbed concentration, q. If ϕ_g is the volume fraction of the actual adsorbent phase in the particle, adsorbed concentrations averaged over the entire particle volume are obtained as $\hat{q} = \phi_g q$. In this work, since the backbone matrix pores appear to be filled with the charged grafted polymers, we assume that $\phi_g = \varepsilon_p$ where $\varepsilon_p = 0.7$ is the porosity of the backbone matrix.

5.4. Results and discussion

5.4.1. Results

5.4.1.1. Dynamic light scattering

Dynamic light scattering (DLS) was used to determine potential effects of the different counterions on the protein diffusivity in solution. Indirectly, this also provides information about potential changes in protein structure. Table 5.2 shows the D_0-values determined for the mAb from a cumulant fit of the autocorrelation function of the scattered light intensity along with the

Table 5.2. Aqueous diffusivity at 25 $^{\circ}$C and hydrodynamic radius of mAb in acetate buffers at pH 5.0 containing different counterions in 20 mequiv/L concentration.

Counterion	D_0 (10^{-7} cm^2/s)	r_s (nm)
TBAH$^+$	5.49±0.02	4.46±0.02
Na$^+$	5.45±0.08	4.50±0.06
Arg$^+$	5.57±0.05	4.41±0.04
Ca^{++}	5.24±0.03	4.69±0.03
Average	5.44±0.14	4.51±0.12

corresponding hydrodynamic radius obtained from the Stokes-Einstein equation [16]. Obviously, there is no significant effect of the counterion type on the mAb aqueous diffusivity, D_0, and, as a consequence, on its hydrodynamic radius, r_s, suggesting that none of these counterions affect the protein structure in a detectable way.

5.4.1.2. Inverse size exclusion chromatography

Inverse size exclusion chromatography (iSEC) was done with several neutral dextran probes and glucose to determine the effects of the couterion type on the structural characteristic of the charged polymer grafts in Nuvia S. Figure 5.2 shows the results for TBAH$^+$, Na$^+$, and Ca^{++}. The results are very similar for the different counterions, with glucose ($r_s \sim 0.4$ nm) gaining access to a large portion of the particle volume and dextran T40 ($r_s \sim 4.7$ nm) being almost completely excluded. Accessibility by dextran T10 ($r_s \sim 2.4$ nm), as measured by the intermediate elution CV, is limited and varies slightly with the type of counterion. Based on the dextran exclusion limits, the effective pore size of Nuvia S is about 6 nm in Na$^+$, increasing only slightly when Na$^+$ is replaced by Ca^{++} and decreasing when replaced by TBAH$^+$.

5.4.1.3. Counterion exchange equilibrium

Column frontal analysis experiments were used to determine the equilibrium constant for different pairs of counterions. The results, shown in Fig. 5.3, show different wave shapes dependent on the direction of the exchange process and the counterions involved. Since mass transfer of small counterions is fast, local equilibrium conditions can be assumed to apply. As a result the shape of concentration profiles at column outlet obtained in response to step changes at the column entrance can be used to determine the relative affinity of the different ions and the
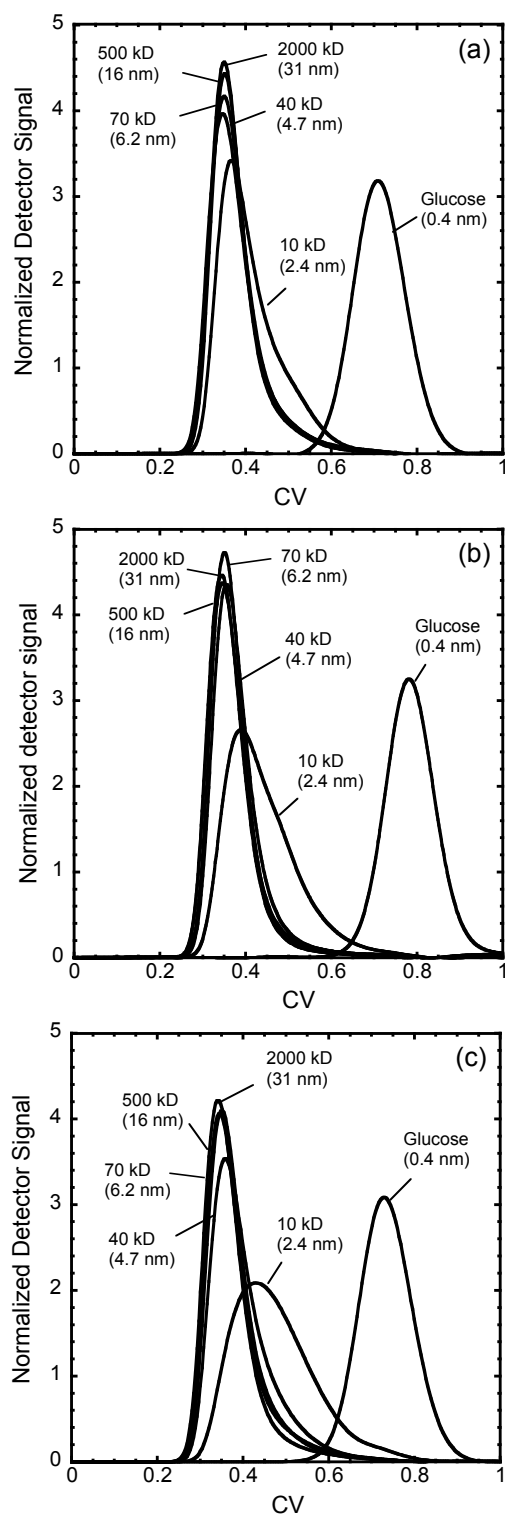
Fig. 5.2. iSEC results for Nuvia S in acetate buffers at pH 5.0 containing 20 mequiv/L concentrations of different counterions (a) TBAH$^+$, (b) Na$^+$, (c) Ca^{++}.
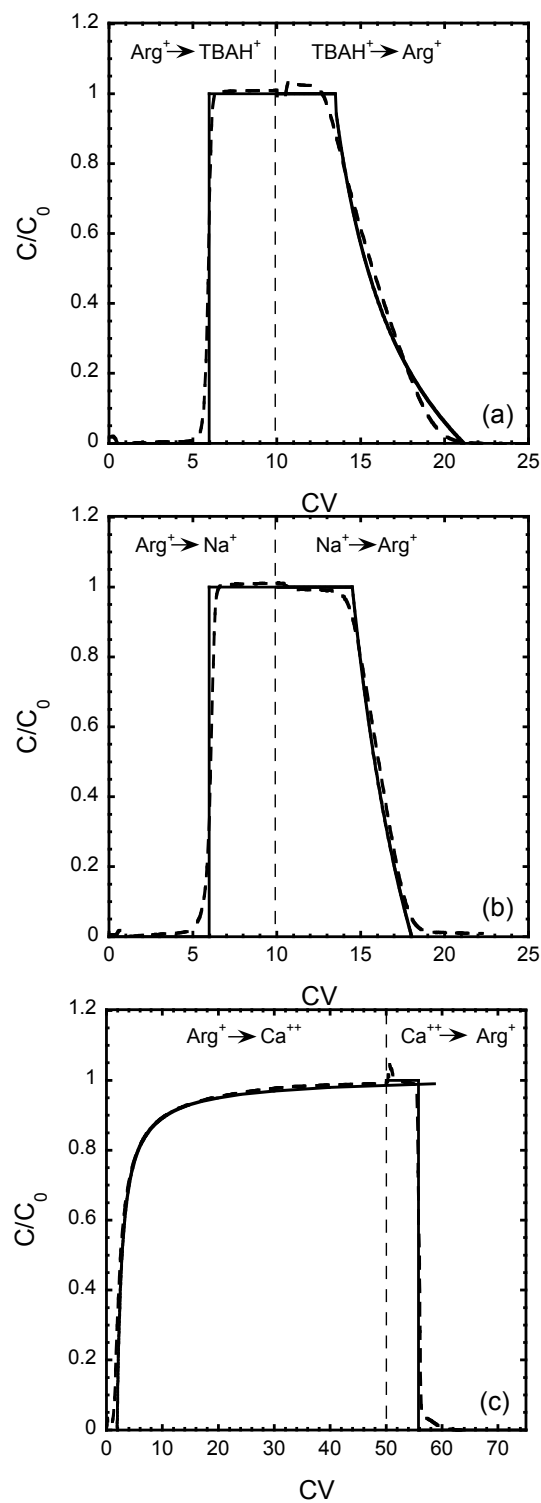
Fig. 5.3. Frontal analysis results for (a) $Arg^+/TBAH^+$, (b) Arg^+/Na^+, and (c) Arg^+/Ca^{++} exchanges in acetate at pH 5.0. $C_0 = 20$ mM.

value of the equilibrium constant. A shock front is expected when the replacing ion is favored, while a gradual wave is expected when the ion initially in the column is favored. As seen in Fig. 5.3, Nuvia S favors Arg^+ relative to $TBAH^+$ and Na^+. However, largely because of the electroselectivity effect [18], for these conditions Nuvia S favors Ca^{++} over Arg^+. For the favorable exchanges, the shock velocity is given by [6]:

$$v_{sh} = \frac{v}{1 + \frac{1-\varepsilon}{\varepsilon} \frac{\phi_g q_0}{C_0}}$$
(5.7)

where v is the mobile phase velocity, or , in terms of column volumes

$$CV_{sh} = \varepsilon + \left(1-\varepsilon\right)\frac{\phi_g q_0}{C_0}$$
(5.8)

Conversely, for the unfavorable exchanges, the wave velocity is:

$$v_c = \frac{v}{1 + \frac{1-\varepsilon}{\varepsilon} \phi_g \frac{dq_A}{dC_A}}$$
(5.9)

or

$$CV_c = \varepsilon + \left(1-\varepsilon\right)\phi_g \frac{dq_A}{dC_A}$$
(5.10)

where the derivative dq_A/dC_A is obtained from eq. 5.1. Lines calculated from these equations are shown in Fig. 5.3 using parameters q_0 and $K_{i,j}$ fitted to the experimental data and summarized in Table 5.3. Since Na^+ is commonly used in typical buffers for protein chromatography, the $K_{i,Na}$ -values derived from the proper ratios of fitted K's are also shown. As seen from these values, Nuvia S has a counterion preference in the order $Arg^+ > Na^+ > TBAH^+$. For the conditions studied ($C_0 = 20$ mM), Ca^{++} is also strongly favored over Na^+ as a result of its divalent nature.

Table 5.3. Ion exchange equilibrium constants derived from frontal analysis experiments with Nuvia S with q_0=0.25±0.01 mequiv/mL.

Fitted K-values	Derived K_{i,Na^+} values	
$K_{Arg,TBAH} = 1.9$	TBAH$^+$	0.79
$K_{Arg,Na} = 1.5$	Arg$^+$	1.5
$K_{Arg,Ca} = 0.74$	Ca^{++}	2.0

The reasons for the selectivity observed with the monovalent counterions are not known. As pointed out by Helfferich [18], many factors affect ion exchange selectivity including the size of the hydrated ions, which affects osmotic pressure, and specific interactions with the exchanger matrix. For styrene-DVB resins, ammonium ion is generally favored over Na^+ and our results are consistent with this trend. However, tetrabutyl ammonium ion is favored over Na^+ in these hydrophobic resins [19], which is not what we observe for Nuvia S. It is possible that for this species, shielding of the charged quaternary ammonium ion by the butyl chains reduces its affinity for the SP groups in the hydrophilic Nuvia S matrix, while hydrophobic interactions increase its affinity in hydrophobic matrices.

5.4.1.4. LGE results

The linear gradient elution (LGE) experiments were used to determine the protein effective charge according to the method of Yamamoto [20]. Following the formulation of Carta and Jungbauer [4], at low protein loads, the general relationship between the normalized gradient slope, $\gamma = \beta L/v$, and the counterion concentration at which the protein elutes, C_B^R, is given by the following equation:

$$\gamma = \int_{C_B^0}^{C_B^R} \frac{dC_B}{k_P' - k_{P,\infty}'} \tag{5.11}$$

where $k_P' = (1-\varepsilon)\phi_g q_P / \varepsilon C_P$ is the protein retention factor at C_B, C_B^0 the initial counterion concentration, and $k_{P,\infty}'$ the protein retention factor for non-binding conditions. Based on the iSEC results, $k_{P,\infty}' \sim 0$. Combining eqs. 5.6 and 5.11 and integrating yield the following result:

$$\gamma = \frac{\left(C_B^R\right)^{z_P/z_B+1} - \left(C_B^0\right)^{z_P/z_B+1}}{A\left(z_P/z_B+1\right)} \tag{5.12}$$

where $A = \left(1-\varepsilon\right)\phi_g K_{P,B}\left(q_0/z_B\right)^{z_P/z_B}\Big/\varepsilon$. In practice, since z_P/z_B is expected to be large and C_B^0 is small, only the first term in the numerator of eq. 5.12 is important. For these conditions, $\gamma \sim \left(C_B^R\right)^{z_P/z_B+1}\Big/A\left(z_P/z_B+1\right)$ yielding a linear plot of $\log\gamma$ vs. $\log C_B^R$ with slope z_P/z_B+1. As shown in Fig. 5.4, experimental results for Nuvia S conform to the predicted trend and yield $z_P =$ 22.8±1.2. This result suggests that the stoichiometry of the protein ion exchange process is the same regardless of the counterion used. This would likely not be the case if any of these counterions were bound to the protein. Although the A-value and, hence, $K_{P,B}$, could not be determined from these data with any reasonable statistically significant precision because of the steepness of these curves, it is obvious that in terms of eluting strength calcium acetate is most effective as a result of its divalency, eluting the mAb at concentrations as low as 110 mM, while TBAH is least effective, requiring concentrations in excess of 350 mm for elution. Sodium and arginine are intermediate with regards to the eluting strength, both requiring concentrations between 200 and 300 mM for elution.

5.4.1.5. Protein adsorption equilibrium

Protein adsorption isotherms were obtained for different counterions and are shown in Fig. 5.5 with the amount bound, $\hat{q}_P$, expressed in mg of protein per mL of particle volume. The amount bound per mL of column volume can be obtained approximately by multiplying $\hat{q}_p$ times $1-\varepsilon$ where $\varepsilon = 0.37$ for uncompressed columns of Nuvia S.
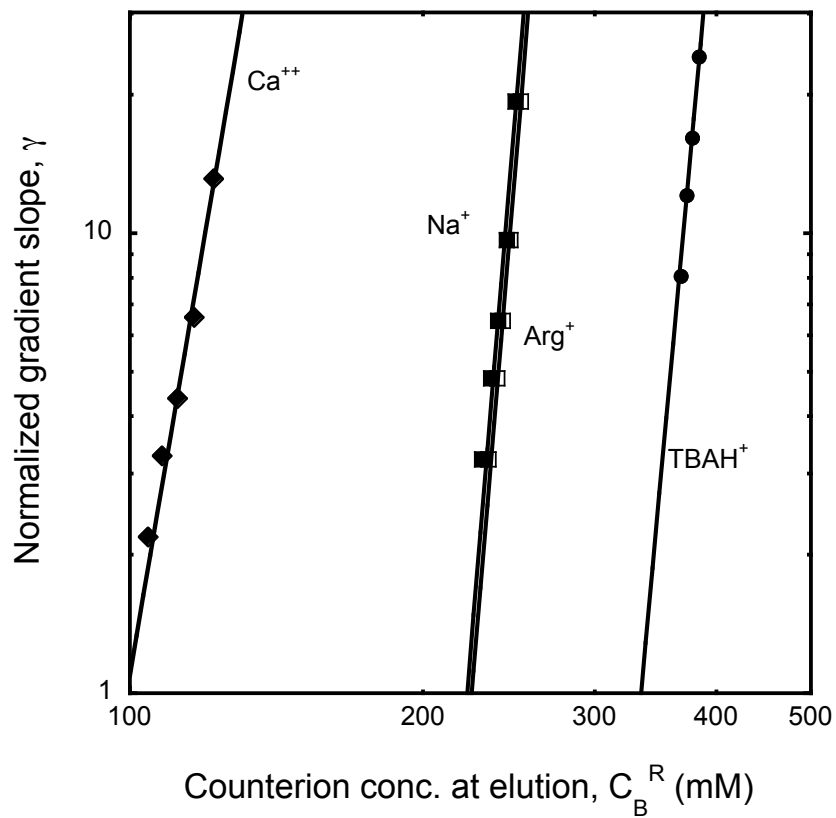
Fig. 5.4. LGE data for mAb on Nuvia S with different counterions in acetate buffers at pH 5.0. The slope of the lines is $z_P/z_B + 1$.

Table 5.4. Protein effective charge determined from LGE experiments for different counterions in acetate buffers at pH 5.0.

Counterion	z_P
TBAH$^+$	22.0±1.5
Na$^+$	24.5±2.5
Arg$^+$	24.4±1.1
Ca^{++}	22.8±1.8
Average	22.8±1.2
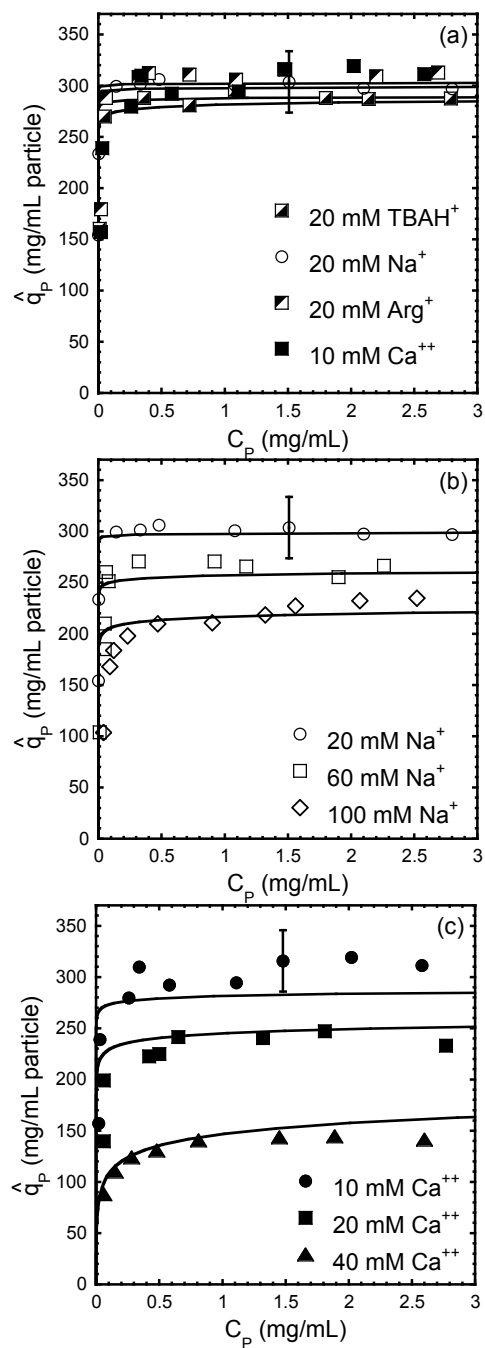
Fig. 5.5. mAb adsorption isotherms for Nuvia S in acetate buffers at pH 5.0. (a) isotherms with 20 mequiv/L concentrations of different counterions; (b) isotherms with different sodium concentrations; (c) isotherms with different calcium concentrations. Representative error bars shown are estimated from repeated measurements. The solid lines are calculated from the SMA model with parameters in Table 5.5.

As seen in Fig. 5.5, the mAb adsorption isotherm is highly favorable for all these conditions. Very similar binding capacities are obtained at 20 mM concentration of each monovalent counterion and at 10 mM concentration of calcium, suggesting that the equivalent counterion concentration is the main factor influencing how much protein binds. As seen for sodium and calcium, increasing the equivalent concentration reduces the amount of protein bound. Equation 5.5 was used to describe the relationship between protein bound and protein and salt concentration. The four parameters in this equation, z_P, q_0, $K_{P,B}$, and σ_P , were determined as follows. z_P was obtained from the LGE experiments, which are most sensitive for this purpose. q_0 was obtained from the counterion frontal analysis experiments for the favorable exchanges, which gave sharp transitions. K_{P,Na^+} and σ_P were obtained by regressing the mAb adsorption isotherms at different sodium acetate concentrations. Finally, the remaining $K_{P,B}$-values for TBAH, arginine, and calcium acetate were obtained from the following relationship:

$$K_{P,B} = \frac{K_{P,Na^+}}{\left(K_{B,Na^+}\right)^{z_P/z_B}} \tag{5.13}$$

using the K_{B,Na^+} -values from Table 5.5. The precision of the isotherm measurement is ±10%, primarily as a result of inaccuracies in determining the weights of the resin samples used and is indicated by the representative error bar included in Fig. 5.5. Thus, the SMA model fits the data within experimental error. This result is significant since the isotherm parameters determined for Na^+ are actually used to predict the isotherms in TBAH, arginine, and calcium together with the

Table 5.5. SMA parameters for mAb adsorption on Nuvia S in acetate buffers at pH 5.0 with different counterions. $q_0 = 0.25$ mequiv/mL, $z_P = 22.8$, $\sigma_P = 58\pm5$.

Counterion, B	$K_{P,B}$
TBAH$^+$	1.4×10^5
Na$^+$	1.0×10^3
Arg$^+$	0.20
Ca^{++}	2.1

independently determined equilibrium constants for the counterion exchanges. The agreement between the model and the results for different counterions and different salt concentrations indicates consistency with a stoichiometric exchange process being the principal mechanism for protein binding in Nuvia S.

5.4.1.6. Protein ion exchange kinetics

The kinetics of protein binding was determined from batch uptake experiments at 1 mg/mL mAb with the different counterions. The results, given in Fig. 5.6, reveal the most dramatic effects of the counterion. Although equilibrium is only attained in these runs for the 20 mM Ca^{++} case, it is obvious that the uptake rate is dramatically different for the different counterions. The rate is smallest for TBAH and highest for Arg^+ and Ca^{++}, despite the fact that the equilibrium binding capacity is essentially the same for all of these counterions for these conditions (cf. Fig. 5.5a). The initial rate is actually highest for 20 mM Ca^{++}. However, the mAb equilibrium binding capacity is also lower for these conditions. Since neither the solution diffusivity or hydrodynamic radius, nor the protein effective charge vary with the type of counterion, these results suggest that protein transport in Nuvia S is directly affected by interactions with the matrix functional groups, which, in turn is obviously influenced by the counterion.

5.4.1.7. Comparison with other cation exchangers

Two additional cation exchangers were tested in this work: UNOsphere S and Capto S. UNOsphere S is a macroporous cation exchanger with a backbone structure similar to that of Nuvia S, but without polymeric surface extenders [15]. The effective pore size of this material, also determined by iSEC, is 60 nm in radius, more than 10 times larger than the mAb hydrodynamic radius. On the other hand, Capto S is based on an agarose matrix grafted with
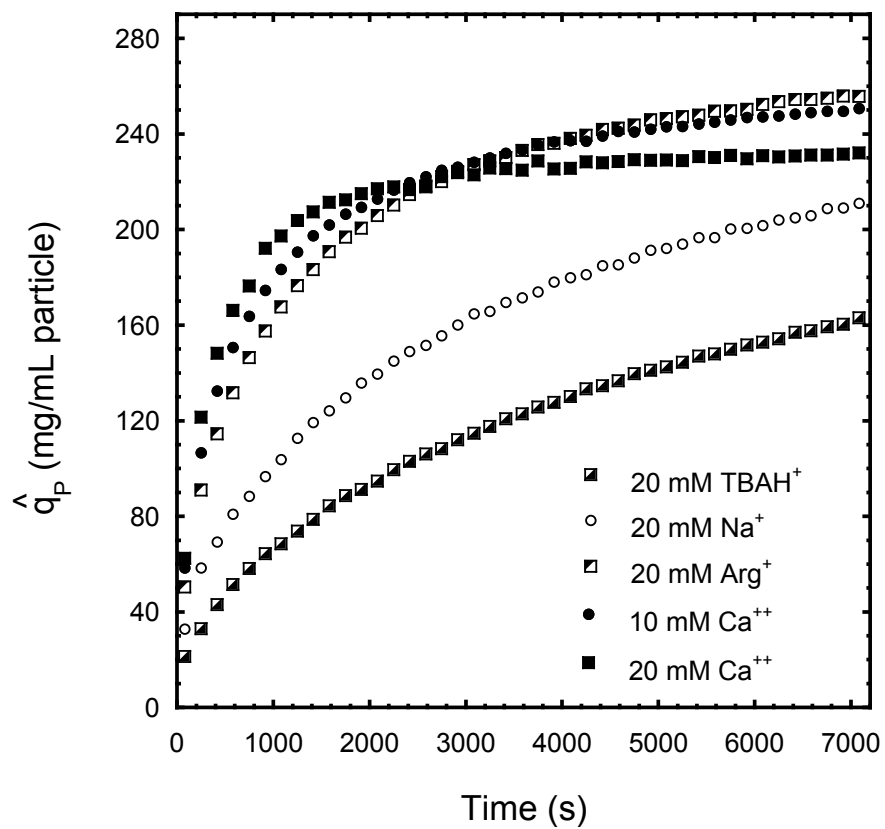
Fig. 5.6. Batch uptake curves for 1 mg/mL mAb on Nuvia S in acetate buffers with different counterions at pH 5.0. Legend values give the counterion concentration in mmol/L.

charged dextran polymers. Based on iSEC, the effective pore size of this material is less than about 5 nm at low ionic strength [15], similar to that of Nuvia S.

Figure 5.7 shows adsorption isotherms and batch uptake rates for UNOsphere S. The trends of the isotherms are similar to those found for Nuvia S, although a somewhat lower binding capacity is seen for 10 mM Ca^{++} compared to the same equivalent concentration of the monovalent counterions. On the other hand, a very different result is obtained for the uptake rates. In this case, the rate are very nearly the same, regardless of the counterion type. This result is consistent with the kinetics being controlled by diffusion of the mAb in the particle pores. Since the pores are large, and the counterion does not affect the mAb aqueous diffusivity, the uptake kinetics is the same.

The results for Capto S are given in Fig. 5.8. In this case both the isotherm and the batch uptake trends are similar to those observed for Nuvia S. Compared to UNOsphere S, the equilibrium binding capacity is much higher and similar to that obtained for Nuvia S at the same counterion concentration. Moreover, consistent with the Nuvia S results, the uptake rates increase markedly in the order $Ca^{++} > Arg^+ > Na^+ > TBAH^+$, with the fastest uptake rate obtained for 20 mM Ca^{++}. This consistency suggests that while quantitatively different, the basic transport mechanism associated with the counterion dependence is the same in both materials. Although the backbone structure is different, according to the respective manufacturers, both matrices contain charged polymeric surface extenders suggesting that they influence directly the protein adsorption characteristics.
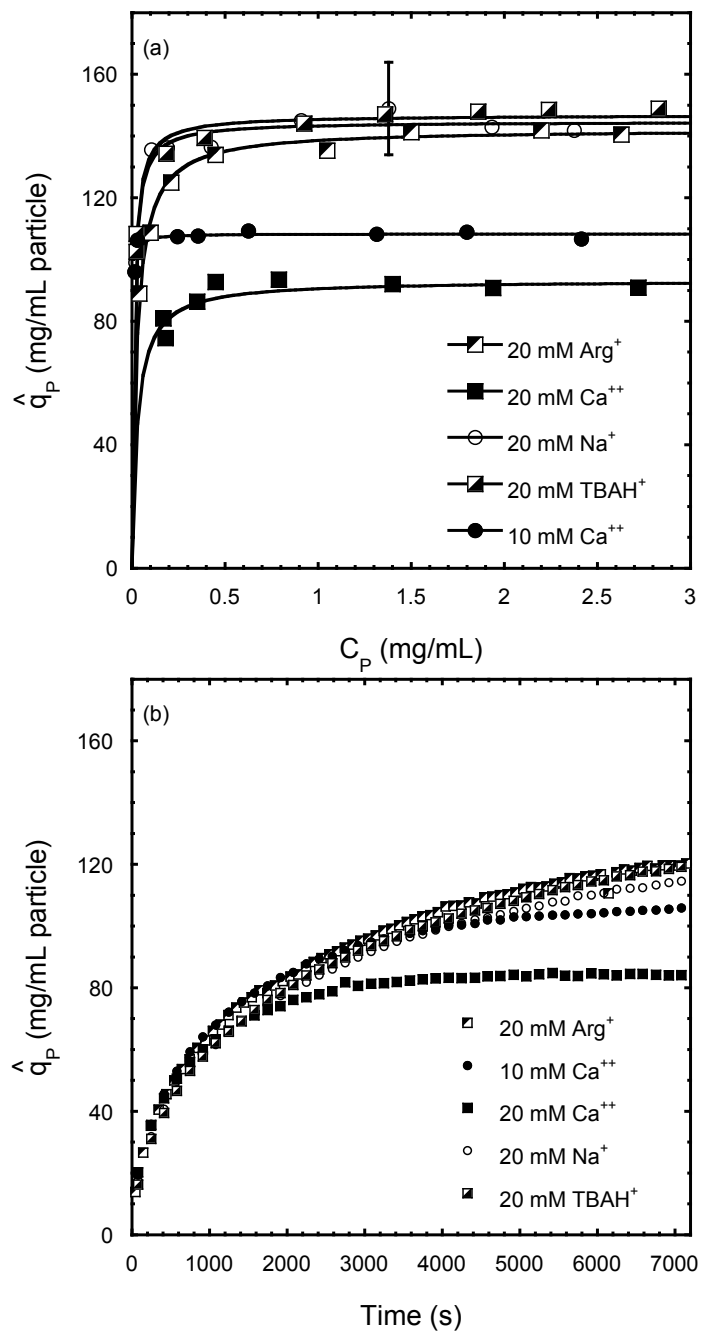
Fig. 5.7. mAb adsorption on UNOsphere S in acetate buffers at pH 5.0 with different counterions. (a) isotherms, (b) batch uptake of 1 mg/mL mAb. Lines in (a) are drawn as guides. The representative error bar shown is estimated from repeated measurements.
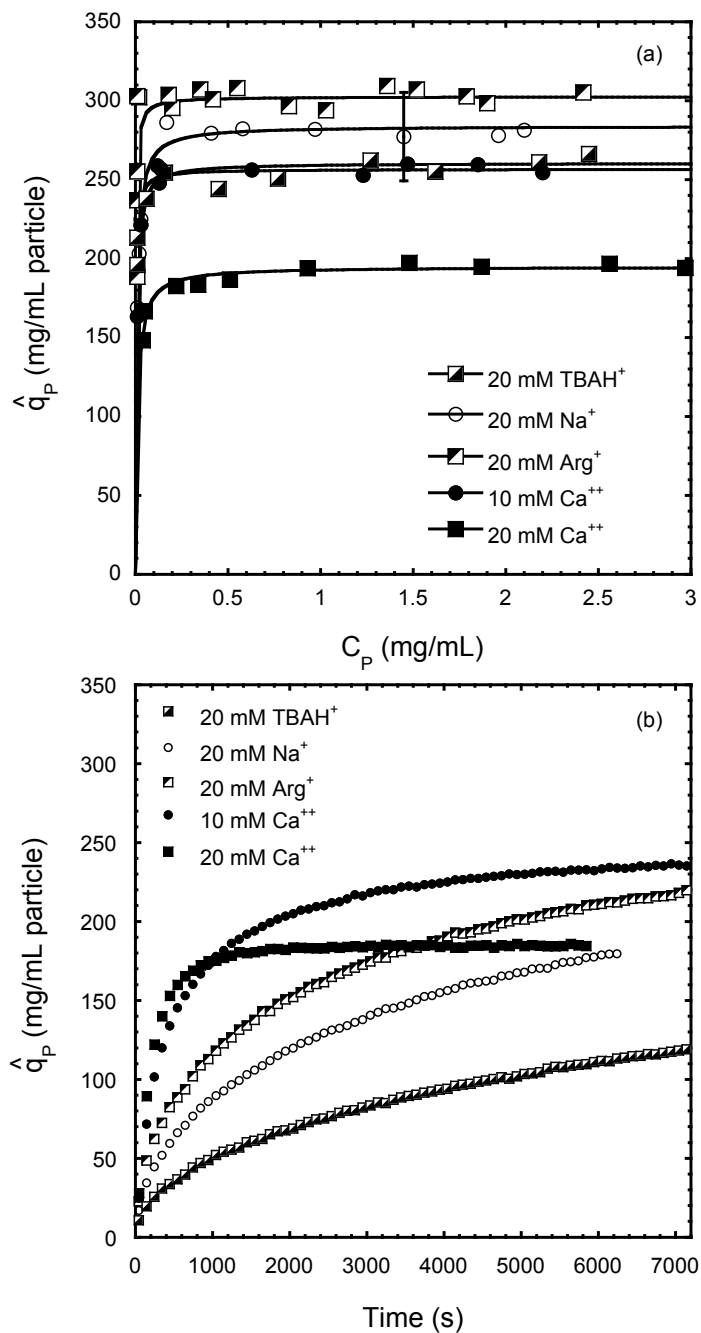
Fig. 5.8. mAb adsorption on Capto S in acetate buffers at pH 5.0 with different counterions. (a) isotherms, (b) batch uptake of 1 mg/mL mAb. Lines in (a) are drawn as guides. The representative error bar shown is estimated from repeated measurements.

5.4.1.8. Comparison with other proteins

Figure 5.9 shows the batch uptake behavior of lysozyme and lactoferrin for both UNOsphere S and Nuvia S. As seen in Fig. 5.9a and b, the rate behavior of lysozyme is also nearly independent of counterion type for both stationary phases, but the rate is obviously faster for Nuvia S than for UNOsphere S. For lactoferrin, the rate is again independent of counterion type for UNOsphere S, but much slower than for lysozyme and comparable to the rate observed for the mAb. On the other hand, a strong dependence of the rate of lactoferrin adsorption is seen for Nuvia S. In the case, the rate is slowest for $TBAH^+$ and fastest for Ca^{++}, consistent with the mAb results.

5.4.2. Discussion

It is apparent that, based on the iSEC results, the type of counterion has little effect on the structural properties of Nuvia S and suggesting that the charged polymer grafts form a network matrix which excludes neutral macromolecules, whose size is larger than about 4 nm in radius. As shown by iSEC results for UNOsphere S [15,17] without the polymer grafts, much large neutral macromolecules gain access to the particle interior. In neither case, the counterion type seems to influence this characteristic in a significant way. A preference for different counterions is, however, exhibited by Nuvia S. For monovalent counterions, Nuvia S favors arginine over sodium and sodium over TBAH. Calcium is also favored at low concentrations. Similar trends were also found for UNOsphere S and Capto S as examples shown in Fig. 5.10 suggesting that this behavior is primarily associated with the properties of the SP-groups in these materials, rather than by interactions with the resin backbone or with the grafted polymers. The type of counterion also affects the protein binding strength. As shown by the LGE results for Nuvia S, counterions that are favored by the resin result in weaker protein binding. In the high
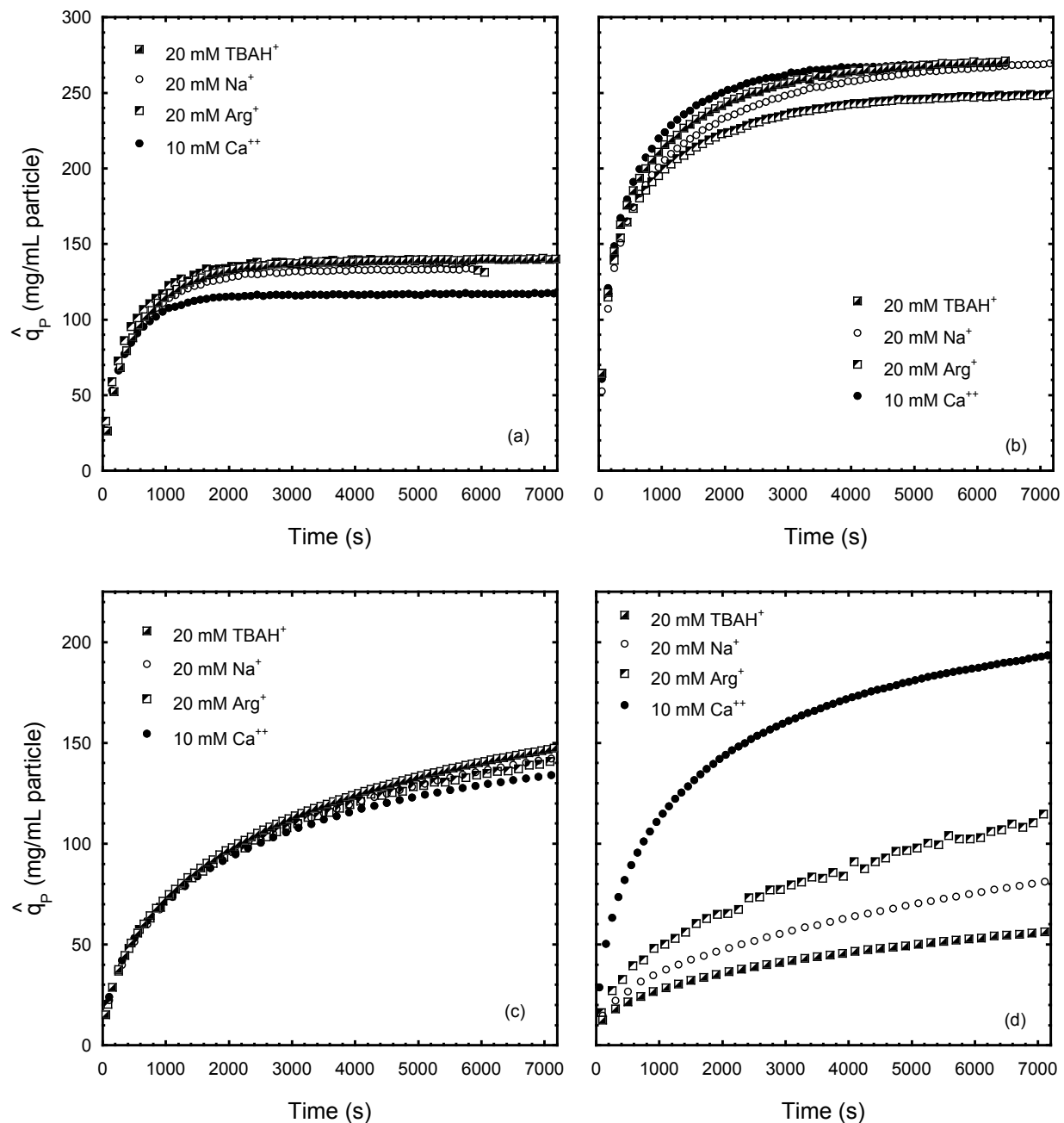
Fig. 5.9. Batch uptake of 1 mg/mL lysozyme and lactoferrin in acetate buffers at pH 5.0 with different counterions. (a) lysozyme on UNOsphere S; (b) lysozyme on Nuvia S; (c) lactoferrin on UNOsphere S; (d) lactoferrin on Nuvia S.
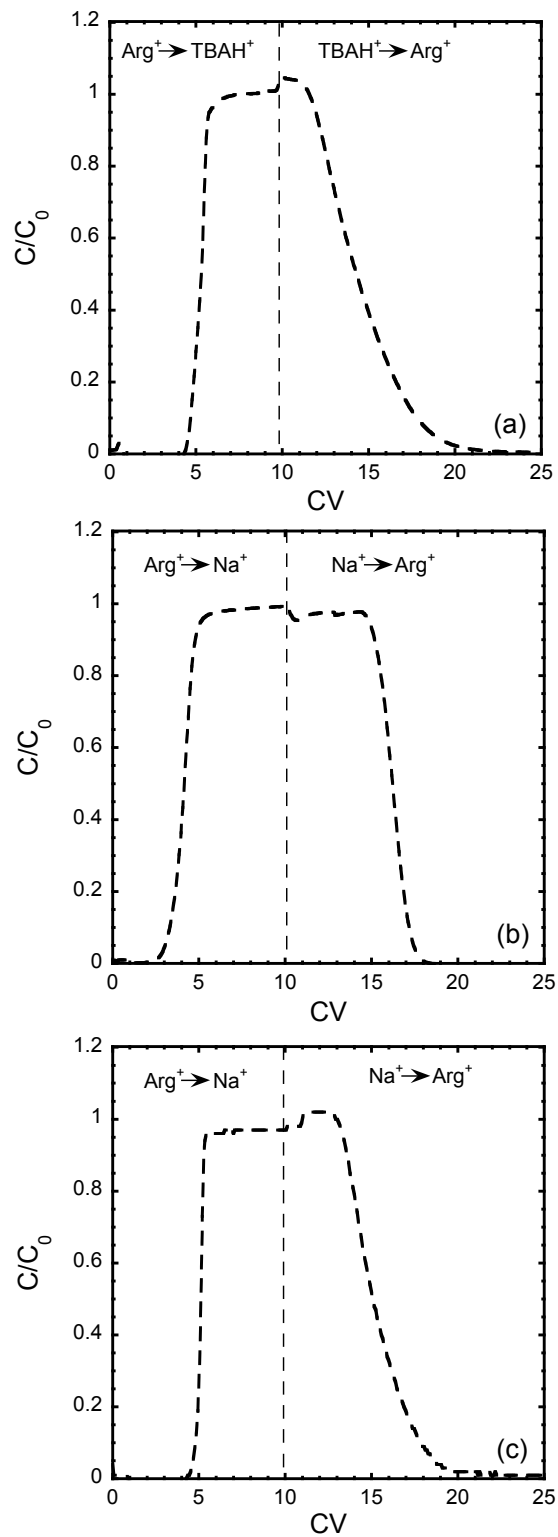
Fig. 5.10. Frontal analysis results for (a) Arg^+/$TBAH^+$ on Capto S, (b) Arg^+/Na^+ on Capto S, and (c) Arg^+/Na^+ on UNOsphere S exchanges in acetate at pH 5.0. C_0 = 20 mM.

concentration range, elution occurs at lower salt concentrations with calcium acetate, while much higher concentrations are needed to elute the protein in TBAH-acetate. Arginine and sodium acetate are intermediate, but in general it appears that the order of protein binding strength is opposite to the order of counterion affinity for the SP groups. This relationship also appears to exist in the lower salt concentration region where adsorption isotherms obtained for different counterions and different counterion concentrations are consistent with the SMA model with protein-counterion exchange equilibrium constants that are related to the K-values describing the affinity for the different counterions. These effects do not appear to be related to counterion binding to the protein since the effective binding charge was not affected. No effects of the counterions studied were also detected on protein solution diffusivity and, thus, hydrodynamic radius.

The most dramatic effect of the couterion type is by far that on the adsorption kinetics. The mAb results for Nuvia S show that while the equilibrium binding capacity at 20 mequiv/L concentrations is practically independent of counterion type, the uptake rate is vastly different. The mAb uptake rate is much higher for counterions that are favored by the SP-groups, which, in turn, result in weaker protein binding. The same trend is seen for adsorption of the mAb on Capto S and for the adsorption of lactoferrin on Nuvia S. No effect of the counterion type is seen, however, for any of these proteins with UNOsphere S, whose pores are quite large. Little effect is also seen on the adsorption rate of lysozyme in Nuvia S. However, in this case, the rate is already very fast in sodium acetate. Moreover, the lysozyme effective charge is much smaller than that of the mAb. For example, Carta et al. [17], give $z_P \sim 5$ for lysozyme in SP-Sepharose-FF suggesting that this protein is held much less strongly and can, accordingly, diffuse faster, regardless of the counterion.

The mechanism leading to the observed effect of the counterion type on the protein adsorption kinetics in the polymer-grafted exchangers is obviously complex. Based on the iSEC determinations, it is obvious that protein transport must occur within the apparently flexible network structure defined by the polymer grafts with continuous interactions between the protein and the resin's charged functional groups. Different theories have been advanced in the past to describe transport for these conditions. One theory assumes that transport is affected by an electrokinetic component [21]. Since there is no applied electrical potential gradient, the driving force for this mechanism can be thought to arise from the different diffusional mobilities of the protein and of the counterions that are replaced when the protein is bound [11]. Since the counterions' diffusional mobility in these matrices is certainly an order of magnitude larger than that of the protein, a large electrokinetic contribution to the protein mass transfer flux could be expected. The experimental trends obtained in this work, however, seem to debunk this theory. In fact, in our case, slower diffusing and higher valence counterions, which would be predicted to provide a smaller electrokinetic contribution, actually enhance the protein adsorption kinetics. Another possibility is that protein transport in these polymer-grafted matrices occurs according to a "hopping" mechanism driven by a chemical potential gradient, which has been advanced by Tao et al. [15] for polymer grafted ion exchangers. Since protein transport seems to occur in the flexible but spatially constraining network in these polymers grafted materials, single file diffusion (SFD) of protein molecules can be envisioned as discussed in Chapter 4. In this case, the protein diffusion rate would be expected to depend on the ability of protein molecules to hop into the nearest empty binding site. When protein binding is weaker, which occurs with counterions that are favored by the SP groups, this hopping process can be expected to be easier resulting in faster diffusional transport. This behavior is consistent with the experimental trends

observed for the mAb in Nuvia S and Capto S. It is also consistent with the behavior of lysozyme and lactoferrin. Lysozyme is a much smaller protein (~ 2 nm hydrodynamic radius), which allows greater mobility. On the other hand, lactoferrin, whose size is similar to that of the mAb, is bound very strongly. In fact, in LGE experiments with Nuvia S (Fig. 5.11), we observed that lactoferrin does not elute at Na^+ concentrations lower than about 520 mM. As a result, the adsorption kinetics is slower than that of the mAb, but still improves when Na^+ is replaced by Arg^+ or Ca^{++} and depressed further when Na^+ is replaced by $TBAH^+$. None of these effects are, of course, seen in UNOsphere S. In this case, the pores are large. While a solid diffusion contribution may still be present, intraparticle transport is largely dominated by diffusion within the particle macropores, which is unaffected by the couterion type and/or concentration.

5.5. Conclusions

The type of counterion used has relatively small effects on structural characteristics and adsorption equilibrium for protein binding in polymer grafted cation exchangers. However, large effects are seeing on the adsorption kinetics with protein adsorption rates increasing dramatically in the order $Ca^{++} > Arg^+ > Na^+ > TBAH^+$, which is the same as the order of affinity of the counterions for the SP groups in the exchanger. No effects on the adsorption rate are seen for a macroporous matrix in the absence of polymer grafts indicating that these trends are closely connected with the network structure created by introducing charged polymer grafts. The results suggest that the mechanism responsible for protein transport in these materials involve close interactions between diffusing protein molecules and the exchanger functional groups. Thus, protein mass transfer and adsorption equilibrium are interrelated. As a result, the driving force for diffusional transport in these materials is likely best expressed in terms of chemical potential gradients. From a practice viewpoint, our results suggest ways in which the adsorption kinetics
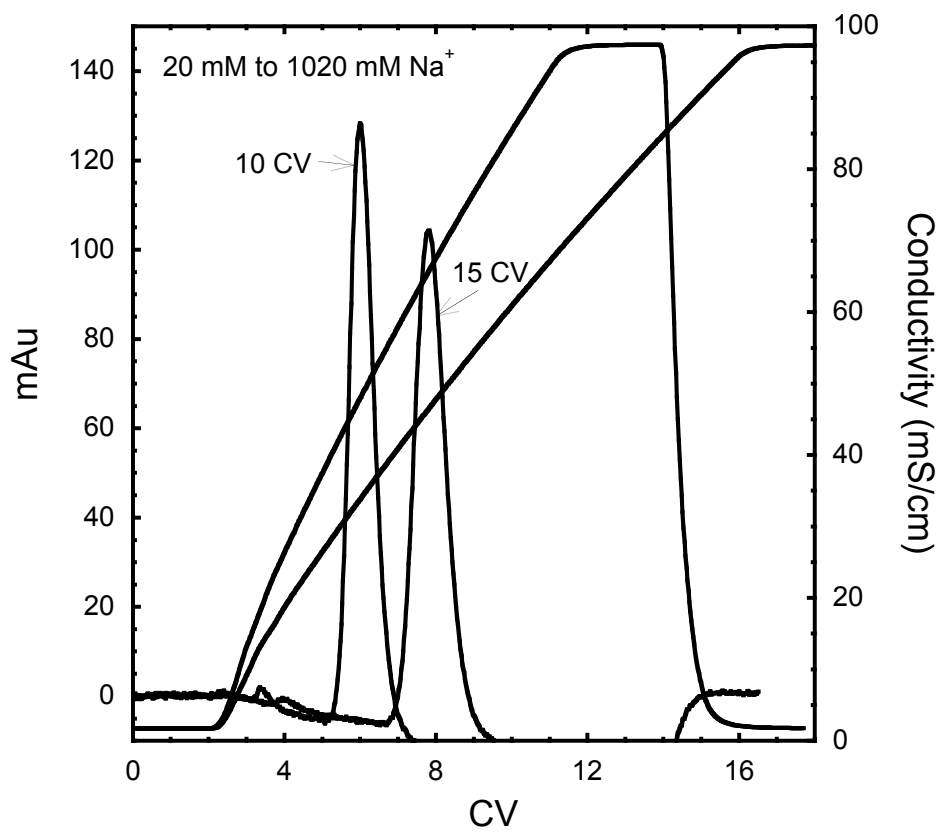
Fig. 5.11. Linear gradient elution chromatogram of lactoferrin on Nuvia S.

can be improved by utilizing different counterion species, without compromising equilibrium binding capacity. Moreover, the results suggest that care must be taken when predicting the kinetic performance of these materials in practical applications since the rates are potentially very different for different proteins and for different mobile phase compositions.

5.6. List of symbols

A parameter in mass action law model

C_i liquid phase concentration of component i, mol/L or mg/mL

C_0 total equivalent concentration, equiv/L

CV number of column volumes of mobile phase passed

D_0 diffusion coefficient, cm^2/s

k_i' retention factor of component i

$K_{i,j}$ ion exchange equilibrium constant

L   column length, cm

q_i concentration in adsorbed phase, mol/L or mg/mL

q_0 charge density, mol/L

$\hat{q}_i$ concentration averaged over the particle volume, mol/L or mg/mL

r_s hydrodynamic radius, nm

v mobile phase velocity, cm/s

z_i charge of ion i

Greek symbols

β gradient slope, mol/L s

ε extraparticle porosity

ε_p porosity of backbone matrix

ϕ_g volume fraction of adsorbent phase in the particle

γ normalized gradient slope ($=\beta L/v$), mol/L

σ_P hindrance parameter in SMA model

5.7. References

[1] U. Gottschalk, Process Scale Purification of Antibodies, Wiley & Sons, Hoboken, NJ, USA, 2009.

[2] M.E. Ladisch, Bioseparations Engineering – Principles, Practice and Economics, Wiley Interscience, New York, USA, 2001.

[3] R.K. Lewus, G. Carta, Ind. Eng. Chem. Res. 40 (2001) 1548

[4] G.Carta, A. Jungbauer, Protein Chromatography- Process development and Scale-up, Wiley-VCH, Weinheim, Germany, 2010.

[5] A.M. Lenhoff, J. Chromatogr. A 1218 (2011) 8748.

[6] R.K. Lewus, G. Carta, J. Chromatogr. A 865 (1999) 155.

[7] G. Jayaraman, S.D. Gadam, S.D., S.M. Cramer, J. Chromatogr. A, 630 (1993) 53.

[8] L.E. Weaver, G. Carta, Biotechnol. Progr. 12 (1996) 342.

[9] W. Kopaciewicz, M.A. Rounds, J. Fausnaugh, F.E. Regnier, J. Chromatogr. A, 266 (1983) 3.

[10] Yamamoto, S., Nakanishi, K., and Matsuno, R. Ion Exchange Chromatography of Proteins, Marcel Dekker, New York (1988).

[11] C.A. Brooks, S.M. Cramer, AIChE J. 38 (1992) 969.

[12] T. Arakawa, Y. Kita, D. Ejima, P. Gagnon, Prot. Pept. Lett 15 (2008) 544.

[13] G.V. Annathur, J.J. Buckley, K. Muthurania, N. Ramasubramanyan, J. Chromatogr. A 1217 (2010) 3783.

[14]   M.A. Holstein, S. Parimal, S.A. McCallum, S. M. Cramer, Biotechnol. Bioeng. 109 (2012) 176.

[15]   E.X. Perez-Almodovar, Y. Tao, G. Carta, Biotechnol. Progr., 27 (2011) 1264.

[16]   E.L. Cussler, Diffusion – Mass Transfer in Fluid Systems, 2nd ed., Cambridge University Press, Cambridge, UK, 1997.

[17]   G. Carta, A.R. Ubiera, T.M. Pabst, Chem. Eng. Technol. 28 (2005) 1252.

[18]   F. Helfferich, Ion Exchange, McGraw-Hill, NY, USA, 1962.

[19]   D.K. Hale, D.I. Pacham, K.W. Pepper, J. Am. Chem. Soc. 3129 (1952) 844.

[20]   S. Yamamoto, Biotechnol. Bioeng., 48 (1995) 444.

[21]   S.R. Dziennik, E.B. Belcher, G.A. Barker, M.J. de Bergalis, S.E. Fernandez, A.M. Lenhoff, Proc. Nat. Acad. Sci. 100 (2003) 420.

Chapter 6

Concluding Remarks

6.1. Conclusions

This study has brought to light unique features of different protein adsorbents that are based on a rigid, macroporous backbone formulated with hydrophilic polymers and known as UNOsphere. The Protein A version of this matrix, UNOsphere SUPrA contains relatively large pores and has a small particle size, yet it possess sufficient mechanical strength to be usable at high flow rates with moderate column pressures. The IgG batch adsorption kinetics on this material is fast and the breakthrough curves show substantial dynamic binding capacity at residence times of less than 1 min. The adsorption behavior of IgG can be modeled using a heterogeneous binding model. Pressure-flow curve results of the UNOsphere backbone show that the adsorbent is compressible to some extent when used in large scale columns, but that the compressibility of the packing is predictable using a newly developed model.

The polymer grafted cation exchanger version of UNOsphere, Nuvia S, incorporates polymeric surface extenders that impart unique protein adsorption properties. Both the protein binding capacity and the protein adsorption kinetics are enhanced by the grafted polymers. Images of protein movement within the particles obtained by CLSM reveal profound differences between protein transport in the macroporous backbone functionalized with short ligand chemistry and the polymer-grafted matrix. Very sharp intraparticle protein concentration profiles are seen for UNOsphere S, while diffuse profiles are seen for Nuvia S consistent with pore

diffusion and solid diffusion, respectively. The multicomponent protein adsorption behavior was also very different for the two matrices. Simultaneous and sequential adsorption results of two mAbs on UNOsphere S are consistent with pore diffusion accompanied by a continual displacement of one mAb by the other. Conversely, the Nuvia S results are consistent with a solid diffusion mechanism where adsorbed protein molecules cannot pass each other. A single file diffusion model describes the single and multi-component results obtained for the mAbs on Nuvia S.

Finally, while no adsorption kinetic effects were observed for UNOsphere S with different counterions, large effects were seen for the polymer-grafted matrix, Nuvia S, with protein adsorption rates increasing dramatically in the order $Ca^{++} > Arg^{+} > Na^{+} > TBAH^{+}$. This order is the same as the order of affinity of the counterions for the SP groups in the exchangers, suggesting that the mechanism responsible for protein transport in polymeric grafted matrices is highly associated with the strength of interaction between protein molecules and the charged polymeric surface extenders.

Overall, our results suggest ways in which the design of chromatographic systems can be improved. For example, in combination, the pressure flow model and the DBC model developed in Chapter 2 can be used to maximize productivity while satisfying pressure constraints. On the other hand, Chapter 3 and 4 showed that the use of polymer grafted materials like Nuvia S can be beneficial for capture steps where both higher adsorption capacities and kinetics are needed. Moreover, Chapter 5 presents ways to further improve the adsorption kinetics on polymer grafted matrices, without compromising equilibrium binding capacity, by utilizing different counterion species. The information provided in this thesis will help to develop other models that will describe the complex behavior observed in polymer grafted matrices. Furthermore, this thesis

provides the necessary tools and knowledge for both the effective design of chromatographic columns and the further development of new chromatographic materials.

6.2. Recommendations for future work

6.2.1. UNOsphere SUPrA

UNOsphere SUPrA has been shown to have a very large pore size, thus, a reduction of the pore size can show the same mass transfer behavior but increase the capacity of the material. Any size adjustment needs to be done carefully, because a reduction in pore size can also increase hindrance effects. The particle size can also be reduced to improve mass transfer on the material. A point of optimization exists for the production of a new resin in terms of properties, so particle size and pore size need to be optimized for a better capacity.

A better understanding of the relationship between the slow binding sites and the effect on mass transfer behavior is necessary. The heterogeneous model can be improved by adding more binding sites with different kinetic resistances. It is possible that this modification to the model would give a better explanation of the behavior observed at the breakthrough curves.

These studies were limited to single component (polyclonal IgG) uptake experiments. Multicomponent adsorption studies can be useful because in the purification step a combination of different sized aggregates sizes are present. It is not known what effects the presence of different proteins in the feed stream might have on this resin. The effects of these aggregates on the capture and elution of the protein of interest need to be addressed.

6.2.2. Nuvia S

CLSM proved to be a very useful tool for gaining insight into the transport mechanism of polymer grafted matrices. Therefore, experiments using different counterions (Arg^+, $TBAH^+$, and Ca^{++}) can provide more information on the transport mechanism responsible for the enhancement

caused by some counterions (Ca^{++} and Arg^+). Moreover, multicomponent experiments using these counterions will be useful to see if a different behavior is observed when compared to the Na^+ experiments already performed.

There are several adjustments that could be made in an attempt to improve Nuvia S characteristics. As discussed for the UNOsphere SUPrA in Section 6.2.1 reducing the particle size could improve mass transfer. Also the reduction of the length of the surface extenders should be studied to see how this affects adsorption equilibrium, adsorption kinetics and elution behavior. A point of optimization should exist where the elution behavior is less hindered.

Multicomponent desorption experiments can be performed to better understand the elution mechanism. A model for desorption kinetics on the polymer grafted material is needed. Probably a normal pore diffusion model with a hindrance factor will be enough. Furthermore, these experiments can also provide insight into the possibility of using the elution behavior to separate a large protein (e.g. mAb) from a small protein (e.g. lysozyme). A combination of CLSM and stirred-batch experiments can be completed to get the necessary information for both the modeling and the separation concepts.

Our studies with cation exchangers can be extended to anion exchangers with similar characteristics. Bio-Rad has recently developed a material with polymeric surface extenders containing positively charged groups (Nuvia Q). Preliminary studies with this material suggest an apparent pore radius of 8 nm (similar to that of Nuvia S) and a BSA binding capacity of over 300 mg/mL, consistent too with the results for mAb and lysozyme in Nuvia S. Similar experiments can be performed on this material using BSA as a model protein. Furthermore, anion exchangers are often used for the separation of pegylated proteins from unpegylated forms. Thus, pegylated BSA can also be studied. Pegylation is known to alter adsorption properties and

diffusion rates in ordinary macroporous resins but what happens in polymer grafted medias is unknown.

Appendix 1

Biomolecule Capture with Periodic Countercurrent Adsorption Systems

---

A1.1. Introduction

Periodic countercurrent (PCC) adsorption systems are used extensively in ion exchange and water purification systems for the removal of trace contaminants. In these applications, the adsorption isotherm is often nearly linear. As a result, the mass transfer zone is very broad and the breakthrough curve for a single column operation is very shallow, resulting in a poor utilization of the adsorption capacity. In these cases PCC systems, such that illustrated in Fig. A1.1, can be used to improve process efficiency [1]. These systems simulate a true countercurrent operation by switching multiple fixed-bed columns at periodic time intervals in a merry-go-round arrangement. Just a few columns in series normally provide a close approach to the behavior of an ideal countercurrent process, but without the complexities of actually moving individual particles against a countercurrently moving fluid. The switching can be obtained with a suitable system of valves so that ordinary fixed-bed columns can be used.

The advantages of PCC adsorption are well established for conditions where the adsorption isotherm is linear or nearly linear and detailed analyses have been published for these cases based on model simulations (e.g. refs. [2-5]) and on experiments (e.g. ref. [6]). Beside trace contaminant removal there has also been interest in applying PCC approaches to the adsorptive
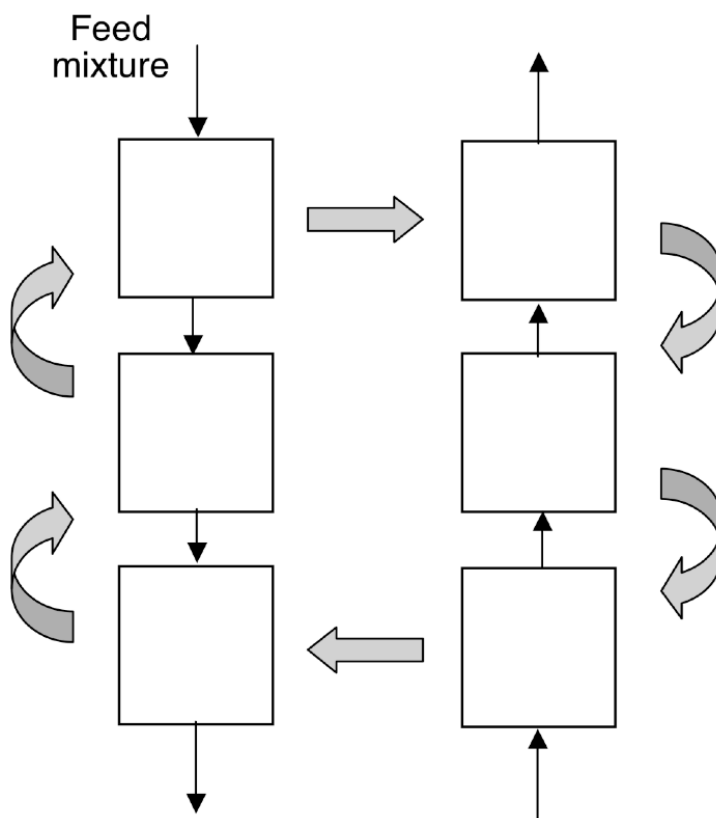
Fig. A1.1. Periodic countercurrent adsorption system. The individual columns are switched in position at periodic time intervals as indicated by the arrows. Note that each adsorption column spends equal time in the adsorption train (left) and in the desorption/regeneration train (right).

capture of biomolecules [7-8]. Arve and Liapis [8], for example, discussed a PCC system for biospecific adsorption and showed by numerical simulation that subdividing a single fixed bed in two could improve substantially the utilization of adsorption capacity but only for very short beds. More recently, other authors [9] have described equipment to implement PCC adsorption for protein capture in a biopharmaceutical manufacturing environment.

An important consideration in assessing the potential advantages of PCC systems for biomolecule capture applications is that the isotherm in bioadsorption is usually highly favorable, which results in relatively narrow mass transfer zones. As a result, the advantages of PCC adsorption over simpler one-column systems will depend strongly on the specific characteristics of the adsorbent and the operating conditions. Thus, in practice, detailed computer simulations or extensive experimentation will be needed to determine potential improvements. In order to simplify this task, this paper provides simple dimensionless design charts that can be used to assess potential advantages of PCC operations without having to recur to detailed computer simulations. The charts are also useful for preliminary design of optimum capture systems and complement previously published work that was limited to the linear isotherm case [3, 5] or based on approximate calculations for a saturation or irreversible isotherm [2].

A1.2. Mathematical model

The key assumptions made in the mathematical model used in this work are as follows:

1. Plug flow without axial dispersion;

2. Intraparticle mass transfer controlled by pore diffusion with negligible boundary layer mass transfer resistance;

3. Local equilibrium between adsorbed and pore fluid concentrations equilibrium; and

4.   Adsorption equilibrium described by Langmuir or constant-separation-factor isotherm.

These assumptions are quite reasonable for protein adsorption on stationary phases designed for industrial scale applications. The first assumption is justified by the fact that the reduced velocity, $v' = vd_p/D_0$, is usually greater than several hundreds in these applications [10]. As a result, that the c-term in the van Deemter equation and, hence, adsorption kinetics, is dominant as long as column packing is reasonably uniform and the hardware is well designed. The second assumption is justified for most open-pore adsorbents, such as those used for biospecific or affinity adsorption. In these cases, the Biot number, $Bi = k_f r_p/D_e$, which measures the relative importance of intraparticle and external mass transfer, is usually very large, so that the boundary layer resistance is negligible [11]. The third assumption is valid for most practical cases involving ion exchange or hydrophobic binding. However, even for biospecific adsorption, where the binding kinetics can be limiting in certain cases, the time constants for the formation of the ligand-protein bond are usually much smaller than diffusion times in porous particles so that local equilibrium prevails at each point within the particle. Finally, the last assumption is only a mathematical approximation. Obviously, the basic tenets of the Langmuir model (single site binding with no lateral interactions of the adsorbed molecules) are not met in reality by many protein adsorption systems. Nevertheless, the Langmuir model has been shown to be adequate for an accurate, albeit empirical, description of protein adsorption equilibrium in systems as diverse as ion exchange, hydrophobic interaction, and biospecific adsorption (e.g. see ref. [12]).

Based on the above assumptions, the following equations and boundary conditions can be used to describe the adsorption train of a PCC system:

$$\varepsilon \frac{\partial C}{\partial t} + (1 - \varepsilon)\frac{\partial \overline{q}}{\partial t} + u \frac{\partial C}{\partial z} = 0 \qquad (A1.1)$$

$$z = 0, \ C = C_F \tag{A1.1a}$$

$$\varepsilon_p \frac{\partial c}{\partial t} + \frac{\partial q}{\partial t} = \frac{D_e}{r^2} \frac{\partial}{\partial r}\left(r^2 \frac{\partial c}{\partial r} \right) \tag{A1.2}$$

$$r = 0, \ \frac{\partial c}{\partial r} = 0 \tag{A1.2a}$$

$$r = r_p, \ c = C \tag{A1.2b}$$

$$q = \frac{q_m bc}{1 + bc} \tag{A1.3}$$

where the average protein concentration in the particle, $\overline{q}$, given by:

$$\overline{q} = \frac{3}{r_p^3} \int_0^{r_p} \left(\varepsilon_p c + q \right) r^2 dr$$

(A1.4)

includes both adsorbed molecules as well as those that are present in the intraparticle macropores. Because of assumptions 3 and 4, combining eqs. A1.2 and A1.3 yields the following result:

$$\frac{\partial c}{\partial t} = \frac{D_e}{\varepsilon_p + \dfrac{q_m b}{\left(1 + bc \right)^2}} \frac{1}{r^2} \frac{\partial}{\partial r}\left(r^2 \frac{\partial c}{\partial r} \right) \tag{A1.5}$$

in place of eq. A1.2. In principle, analogous equations can be written to describe the desorption train. In practice, however, in bioprocess applications, the isotherm is extremely sensitive to the mobile phase composition. As a result, while the adsorption isotherm is generally quite favorable for the load step, conditions are usually such that essentially no binding occurs during elution. In this case, elution is completely diffusion limited and fast because the high concentration driving force. Furthermore, clean-in-place operations are often needed and these are generally dependent only on the time of exposure of the particles to the sanitizing agent. The net result is that the time

each adsorbent particle must spend in the desorption/regeneration train is approximately independent of the number of column sections or their length. Thus, we can assume that the switch time is given by:

$$t_{switch} = \frac{t_{reg}}{N_c}$$

(A1.6)

where t_{reg} is the time each particle must spend in the desorption/regeneration train and N_c is the number of columns in series, which is assumed to be the same for the adsorption and the desorption trains. Accordingly, the total cycle time, required for a column to go through the adsorption or the desorption train is $t_{cycle} = N_c\, t_{switch} = t_{reg}$. When this time is sufficient, a clean adsorbent bed is available at each switch so that only the loading columns need to be simulated. If we consider, for example, a system with 4 total columns (2 in the adsorption train and 2 in the desorption train), the total time spent by each particle in each train will be t_{reg}, while the switch time will be $t_{reg}/2$. Obviously, a different number of columns can be used in the adsorption and desorption trains. For instance, if only 1 column is used in the regeneration train, then the switch time must be equal to t_{reg} or greater regardless of the number of columns in series in the adsorption train.

The dimensionless form of eqs. A1.1-A1.5 is given by the following equations:

$$\frac{\varepsilon}{\Lambda}\frac{\partial X}{\partial \tau} + \frac{\partial \overline{Y}}{\partial \tau} + \frac{\partial X}{\partial \zeta} = 0$$

(A1.7)

$$\zeta = 0, \quad X = 1$$

(A1.7a)

$$\frac{\partial x}{\partial \tau} = \frac{n}{15}\frac{f(x)}{\rho^2}\frac{\partial}{\partial \rho}\left(\rho^2 \frac{\partial x}{\partial \rho}\right)$$

(A1.8)

$$\rho = 0, \quad \frac{\partial x}{\partial \rho} = 0$$

(A1.8a)

$$\rho = 1, \quad x = X \tag{A1.8b}$$

where the dimensionless variables are defined as follows:

$$X = \frac{C}{C_F} \tag{A1.9}$$

$$\bar{Y} = \frac{\bar{q}}{q_F} \tag{A1.10}$$

$$x = \frac{c}{C_F} \tag{A1.11}$$

$$\Lambda = \frac{(1-\varepsilon)q_F}{C_F} \tag{A1.12}$$

$$\tau = \frac{1}{\Lambda}\frac{ut}{L} \tag{A1.13}$$

$$\zeta = \frac{z}{L} \tag{A1.14}$$

$$\rho = \frac{r}{r_p}$$

(A1.15)

$$f(x) = \frac{\dfrac{\varepsilon_p}{q_m b} + \dfrac{1}{R}}{\dfrac{\varepsilon_p}{q_m b} + \dfrac{1}{\left(1 + \dfrac{1-R}{R}x\right)^2}} \tag{A1.16}$$

$$n = \frac{15(1-\varepsilon)D_e L}{r_p^2 u} \tag{A1.17}$$

$$R = \frac{1}{1 + bC_F}$$

(A1.18)

A numerical solution is required and was obtained by discretizing both the particle radial coordinate and the column axial coordinate by finite differences, the latter with a backwards scheme. The resulting ordinary differential equations were then integrated for a given switch period using subroutine DIVPAG of the International Mathematical and Statistical Library (IMSL), which uses Gear's method for stiff systems of ordinary differential equations. All calculations were done with a FORTRAN program available in our laboratory. In order to simulate the PCC switching of columns, at the end of each period, x and X values were reassigned according to Fig. 1 and the numerical integration repeated until reaching a periodic state. Calculations were done with a number of discretization points sufficiently large that their actual values did not affect the numerical results. For most difficult case, corresponding to $R = 0.01$, we used 50 axial and 39 radial discretization points. For each case, the cyclic calculation was repeated until the maximum effluent concentration at the outlet from the adsorption train was within 0.1 % of the value found in the previous cycle.

In dimensionless form, the model parameters are the total number of transfer units, n, the dimensionless total cycle time $\tau_p = ut_{cycle}/\Lambda L = uN_c t_{switch}/\Lambda L$, the isotherm parameter, R, the number of column sections in series, N_c, and the ratios ε/Λ and $\varepsilon_p/q_m b$. However, in practice, these two ratios are usually quite small and can be neglected for high-capacity adsorbents with favorable isotherms and dilute solutions, where the partition ratio, Λ, and the initial isotherm slope, $q_m b$, are both large. For these conditions, a general result can be found by setting a maximum outlet concentration at $\zeta = 1$ and calculating the number of transfer units required using different numbers of columns in series over a range of values of $n\tau_p = 15(1-\varepsilon)D_e t_{cycle}/\Lambda r_p^2$. The

product $n\tau_p$ is independent of residence time and can be estimated knowing adsorbent capacity, particle size, effective diffusivity, and the time required for desorption and regeneration of the adsorbent particles by taking $t_{cycle} = t_{reg}$.

A1.3. Results and discussion

Numerical results were obtained using typical values of $\varepsilon = 0.35$ and $\varepsilon_p = 0.5$ for $R = 0.01$, 0.1, 0.2, and 0.9. The two smaller values of R correspond to nearly rectangular, highly-favorable isotherms, while the largest one corresponds to a nearly linear isotherm. Although unlikely to be found in actual biomolecule capture systems, this case is included for comparison purposes. Results for $\Lambda = 10$ are given in Figs. A1.2-A1.3 for $X_{out} \leq 0.1$ in the periodic state with one, two, or three column sections in series. The corresponding results for $X_{out} \leq 0.01$ are given in Figs A1.4-A1.5. In both cases, the relative productivity is calculated as the ratio $n|_{N_c} / n|_{N_c=1}$ at the same value of the dimensionless switch period $n\tau_p$. For these conditions the effects of ε/Λ and $\varepsilon_p/q_m b$ are negligible, so that the same curves can also be used for larger values of Λ. For $R = 0.01$ and $X_{out} \leq 0.1$, the numerical solution for $N_c = 1$ is practically indistinguishable from the result for the irreversible isotherm limit ($R = 0$) predicted by the analytical solution of Cooper and Liberman [13]. The latter is approximated by the following equation valid for $n > 2.5$ [10]:

$$n = 1.03 + n\tau_p$$

(A1.19)

Increasing the number of column sections from $N_c = 1$ to 2 is seen to reduce n, and thus, the total column length, and to increase productivity by a maximum of about 24%.

However, the relative effect becomes increasingly less pronounced as $n\tau_p$ is increased. Moreover, increasing N_c further has only a small incremental effect, suggesting that subdividing the column in more than two sections would likely be unjustified.

The results for lower values of R shown in Fig. A1.3 mimic those in Fig. A1.2. The main difference is that as R is increased and the adsorption isotherm becomes less favorable, the relative productivity becomes somewhat less dependent on $n\tau_p$ but also more greatly influenced by N_c. Even with $R = 0.9$, however, the maximum improvement in productivity is only about 35% when $N_c = 2$.
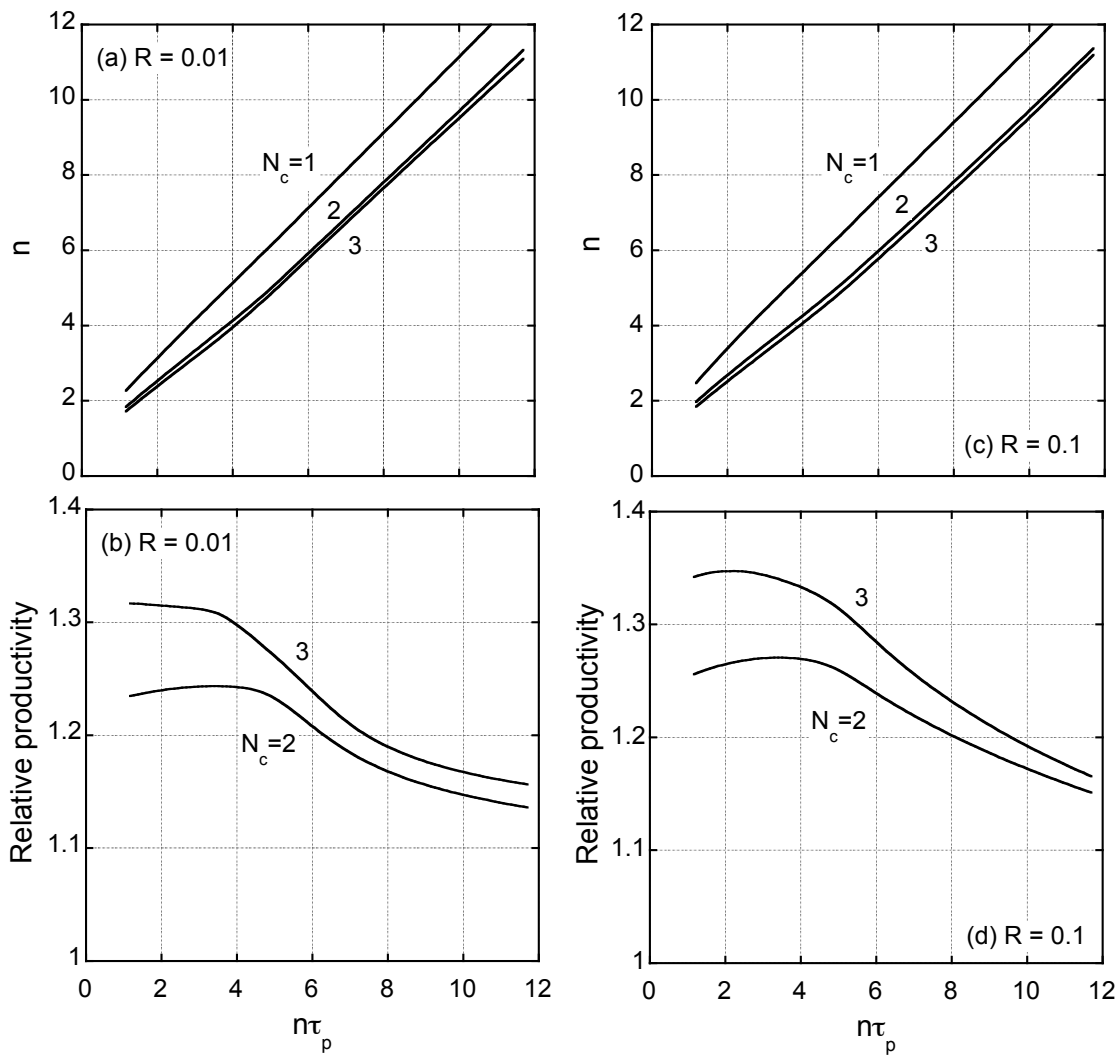
Fig. A1.2. Total number of transfer units required for $X_{out} \leq 0.1$ (top) and relative productivity (bottom) with different number of column sections in series. $R = 0.01$ for a and b; $R = 0.1$ for c and d.
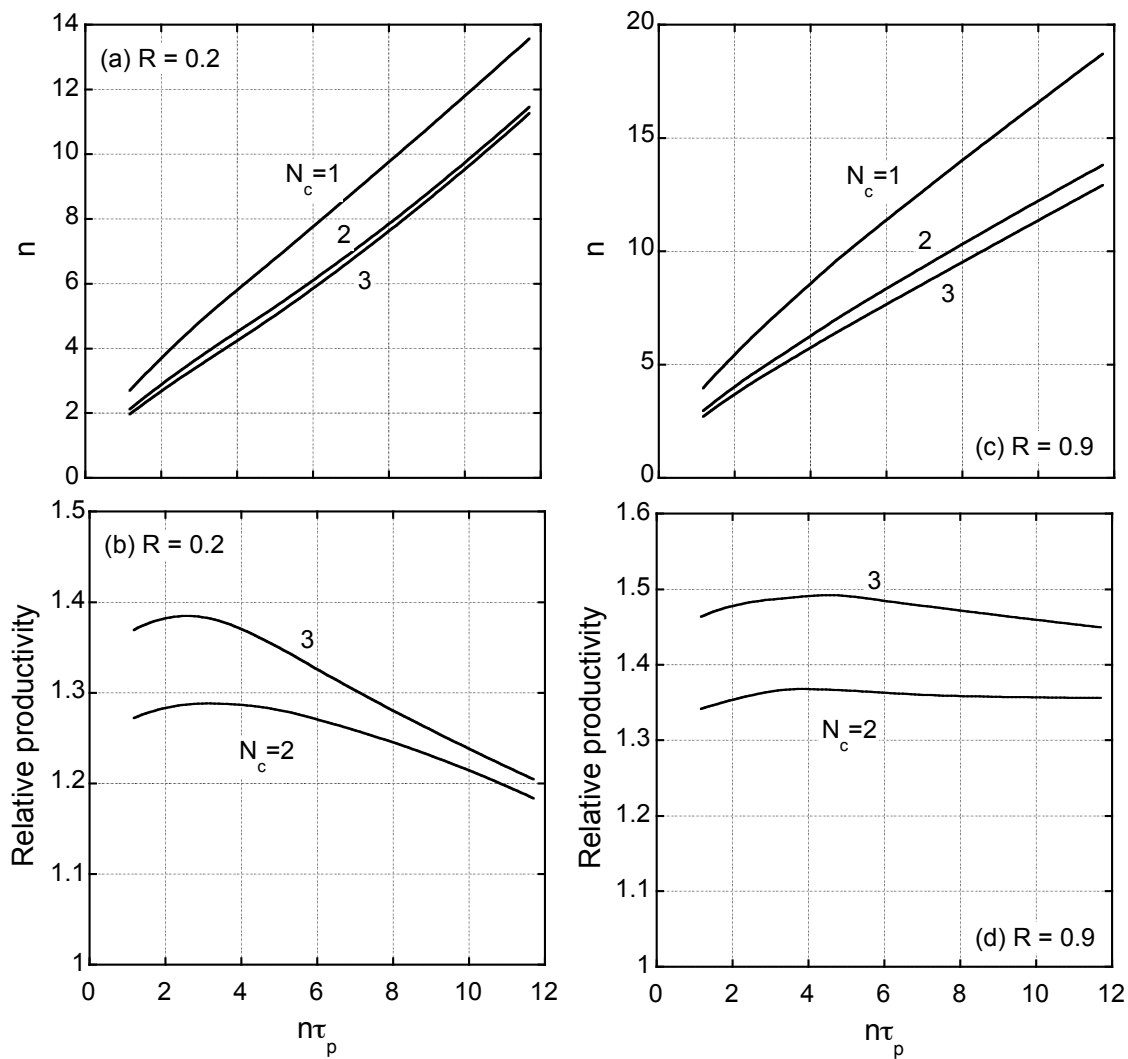
Fig. A1.3. Total number of transfer units required for $X_{out} \leq 0.1$ (top) and relative productivity (bottom) with different number of column sections in series. $R = 0.2$ for a and b; $R = 0.9$ for c and d.

The results for $X_{out} \leq 0.01$ shown in Figs. A1.4-A1.5 exhibit similar trends. The improvement with N_c is very similar in magnitude to the case of $X_{out} \leq 0.1$ when R is small, since the breakthrough curve is relative sharp and there is not much difference in the times at which values of $X_{out} = 0.1$ and $X_{out} = 0.01$ are reached. However, the improvement is more pronounced and the maximum shifts to higher $n\tau_p$-values when R is larger and the isotherm closer to linearity.

A1.4. Application example

The capture of IgG from a 1-mg/mL solution on the protein A adsorbent UNOsphere SUPrA (Bio-Rad Laboratories, Hercules, CA, USA) is used as an example. The relevant properties determined by Perez-Almodovar [14] are summarized in Table A1.1. We assume t_{cycle} = t_{reg} = 1,800 s and $X_{out} \leq 0.1$. The following values of the dimensionless parameters are obtained:

$$\Lambda = 24.4$$
$$\frac{\varepsilon}{\Lambda} = 0.0143$$
$$\frac{\varepsilon_p}{q_m b} = 0.000227$$
$$R = 0.0137$$
$$n\tau_p = 5.31$$

For these conditions, interpolating between the values read from Fig. A1.2a and A1.2b, we obtain n = 6.5, 5.3, and 5.1, using N_c = 1, 2, and 3, respectively. For a comparison, detailed simulations for the actual parameter values yield n = 6.61, 5.30, and 5.11, for N_c = 1, 2 and 3, respectively, practically indistinguishable from the values read from the figures. Note that in either case, the corresponding column lengths can be found if a superficial velocity is selected. At 600 cm/h (u = 0.167 cm/s), we obtain one column with L = 15 cm, two columns each 6.1 cm
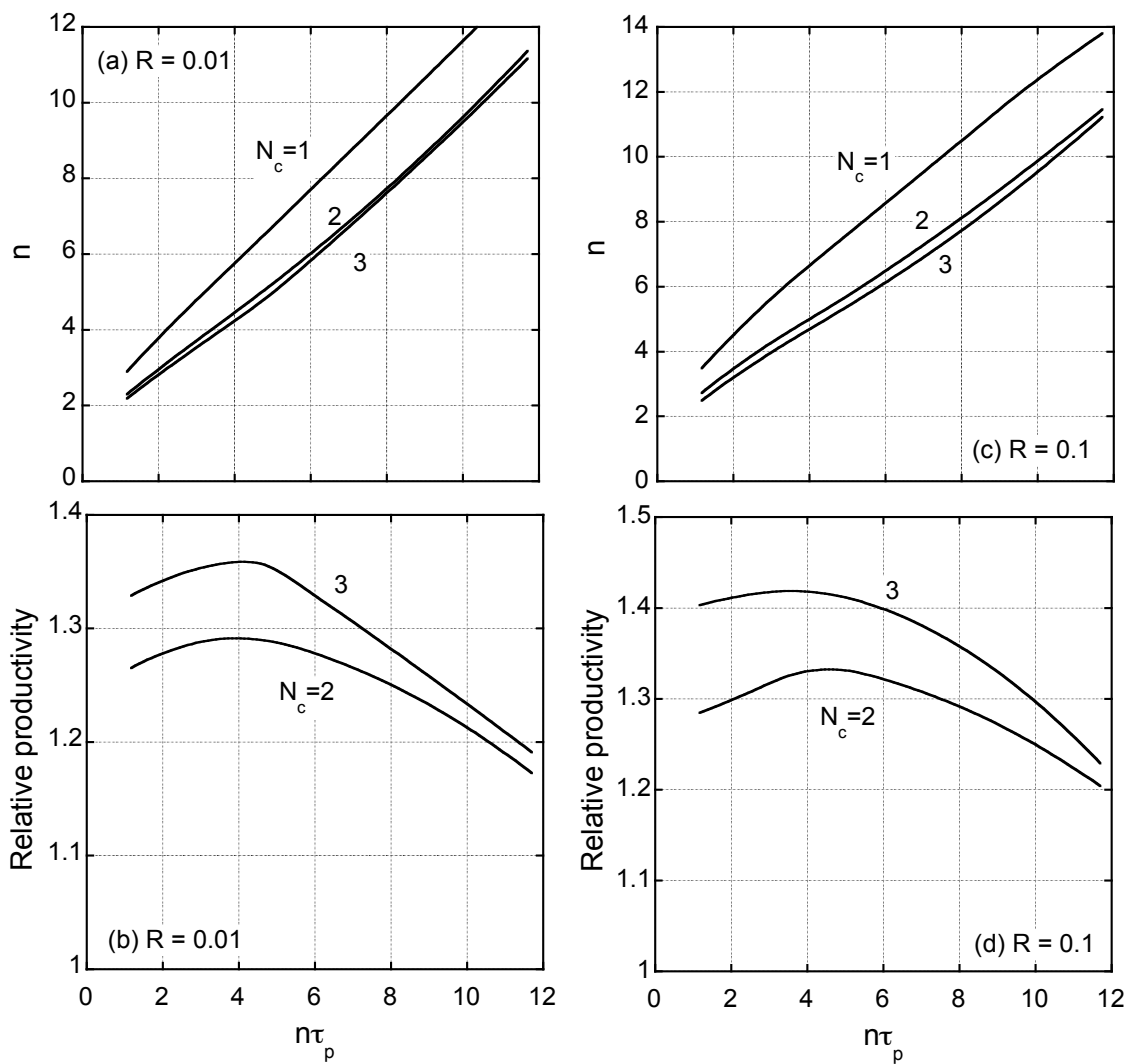
Fig. A1.4. Total number of transfer units required for $X_{out} \leq 0.01$ (top) and relative productivity (bottom) with different number of column sections in series. $R = 0.01$ for a and b; $R = 0.1$ for c and d.
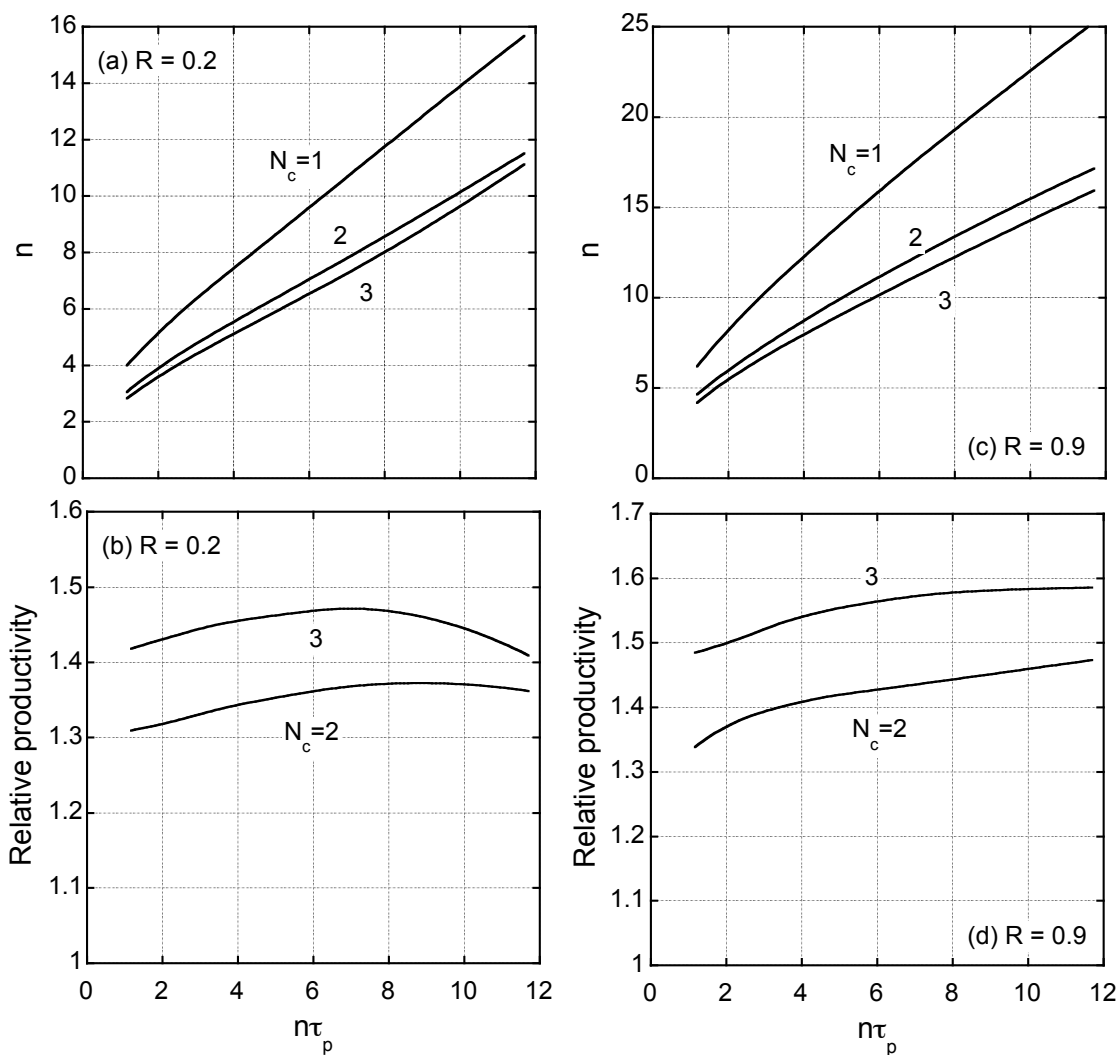
Fig. A1.5. Total number of transfer units required for $X_{out} \leq 0.01$ (top) and relative productivity (bottom) with different number of column sections in series. $R = 0.2$ for a and b; $R = 0.9$ for c and d.

Table A1.1. Parameter values for IgG capture on UNOsphere SUPrA (Perez-Almodovar and Carta [14]).

Parameter	Value	Units
d_p	57	μm
ε	0.35	
ε_p	0.62	
q_m	38	mg/mL particle
b	72	mL/mg
D_e	6.0×10^{-8}	cm^2/s

long, or three columns each 4.0 cm long. It should be noted that, in practice, there can be technological and procedural limitations to packing reliably and validating large diameter columns with very short bed heights. Clearly, such limitations need to be taken into account in the design of actual systems.

A1.5. Conclusions

The charts provided in this appendix allow rapid predictions of the periodic state performance of a PCC adsorptive process for conditions that are typically found in biochromatographic capture steps. Although the charts are provided only for a few different values of the dimensionless parameters, interpolation between values provides reasonably accurate predictions for practical cases using basic parameters describing the adsorption isotherm and the intraparticle pore diffusivity. The switching time is determined independently either experimentally or from models based on the time required to completely desorb and clean the adsorbent particles.

A1.6. List of symbols

b parameter in Langmuir isotherm (mL/mg)

c concentration in pore fluid (mg/mL)

C concentration in external fluid (mg/mL)

C_F feed concentration (mg/mL)

D_e effective intraparticle diffusivity (cm²/s)

L total length of adsorption train (cm)

n total number of transfer units in adsorption train $[=15(1-\varepsilon)D_e L/ur_p^2]$

N_c number of columns in series in the adsorption train

q adsorbed concentration (mg/mL)

$\overline{q}$ concentration averaged over particle volume (mg/mL)

q_F adsorbed concentration at equilibrium with feed (mg/mL)

q_m monolayer adsorption capacity in Langmuir model (mg/mL)

r radial coordinate (cm)

r_p particle radius (cm)

R isotherm parameter defined as $R=1/(1+bC_F)$

u superficial velocity (cm/s)

t time (s)

t_{cycle} total time required for a column to cycle through the adsorption train (s)

t_{reg} time required for elution, regeneration, and cleaning (s)

t_{switch} switch time (s)

x dimensionless pore fluid concentration $(=c/C_F)$

X dimensionless fluid phase concentration $(=C/C_F)$

Y dimensionless concentration in particle $(=q/q_F)$

z axial coordinate

Greek symbols

ε extraparticle porosity

ε_p intraparticle porosity

Λ partition ratio $[=(1-\varepsilon)q_F/C_F]$

ρ dimensionless radial coordinate $(=r/r_p)$

τ dimensionless time $(=ut/\Lambda L)$

τ_p dimensionless total cycle time $(=ut_{cycle}/\Lambda L)$

ζ dimensionless axial coordinate ($= z/L$)

A1.7. References

[1]   D.M. Ruthven, Principles of Adsorption and Adsorption Processes, Wiley, New York, 1984.

[2]   I. Neretnieks, Chem. Ing. Technik 47 (1975) 773.

[3]   U.G. Svedberg, Chem. Eng. Sci. 31 (1976) 345.

[4]   A.I. Liapis, D.W.T. Rippin, AIChE J. 25 (1979) 455.

[5]   H.J. Ortlieb, G. Bunke, D. Gelbin, Chem. Eng. Sci. 36 (1981) 1009.

[6]   G. Carta, R.L. Pigford, Ind. Eng. Chem. Fundam. 25 (1986) 677.

[7]   P.D. Liu, R.L. Pigford, AIChE Spring National meeting, Houston, TX, USA, 1987.

[8]   B.H. Arve, A.I. Liapis, Biotechnol. Bioeng. 32 (1988) 616.

[9]   M. Holzer, H. Osuna-Sanchez, L. David, Bioprocess International (2008) 74.

[10]   G. Carta, A.R. Ubiera, T.M. Pabst, Chem. Eng. Technol. 28 (2005) 1252.

[11]   M.D. LeVan, G. Carta, Adsorption and Ion Exchange, in D.W. Green (Ed.) Perry's Chemical Engineers' Handbook, Eighth Edition, Section 16, McGraw-Hill, New York, 2007.

[12]   T.E. Bankston, M.C. Stone, G. Carta, J. Chromatogr. A, 1188 (2008) 242.

[13]   R.S. Cooper, D.A. Liberman, Ind. Eng. Chem. Fundam. 9 (1970) 620.

[14]   E.X. Perez-Almodovar, G. Carta, J. Chromatogr. A, 1216 (2009) 8339.

Appendix 2

Effects of Polymeric Surface Extenders on Desorption

A2.1. Introduction

Desorption is, of course, an integral step in protein chromatography. Many processes used in biopharmaceutical production include a single load-wash-elute cycle where the protein is adsorbed at low ionic strength, unbound impurities are washed out also at low or intermediate ionic strength and the protein is finally recovered by elution at high salt concentration. In the case of macroporous matrices, desorption is expected to occur rapidly as shown in multiple studies [1-3]. Here salt diffuses quickly in the pores of a protein saturated particles causing the protein to detach from the adsorbent surface and concentrate in the pore fluid. With high capacity adsorbents, the protein concentration reaches high values in the pore fluid almost instantly providing a high diffusional driving force.

The behavior of polymer-grafted matrices is likely to be different. In this case, as shown, for example by iSEC, little space is available within the beads for unhindered diffusion. Thus, desorption could be expected to occur much more slowly than for macroporous matrices, particularly with regards to the removal of the last small percentage of preadsorbed protein. For example, in our chromatographic experiments for non-binding conditions (Fig. A2.1) we found that the mAb diffused extremely slowly in Nuvia S resulting in nearly complete exclusion. A paper recently published by Bowes et al. [4] used CLSM to study the desorption behavior of lactoferrin and lysozyme on a dextran-grafted material, SP-Sepharose XL, whose properties are similar to those seen in Nuvia S. They observed a desorption behavior where protein molecules
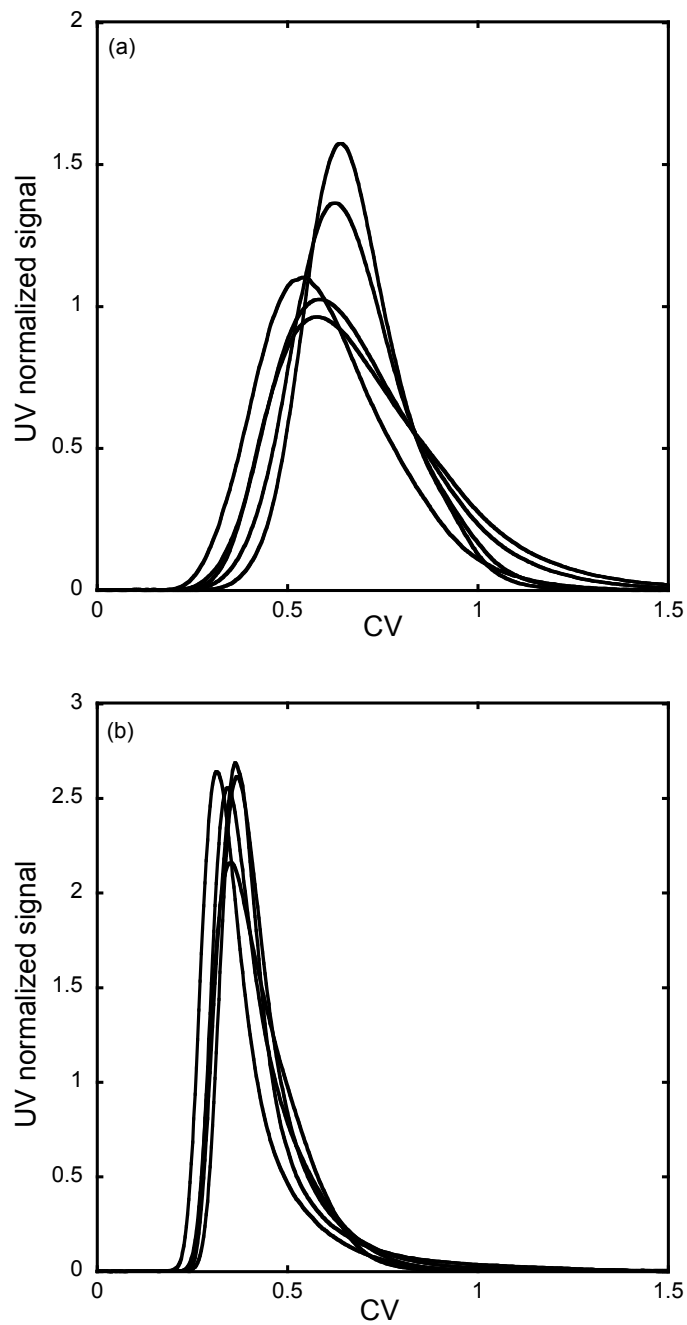
Fig. A2.1. Isocratic pulse response peaks under nonbinding conditions for mAb in 1 M NaCl for UNOsphere S (a) and Nuvia S (b). Flow rate for the curves shown were 0.1, 0.2, 0.5, 0.75, and 1 mL/min for both UNOsphere S and Nuvia S.

diffuse out progressively from the particle edge to its center. A lack of literature on the desorption behavior of proteins in polymer-grafted matrices motivated us to study the mAb desorption behavior on Nuvia S.

In order to study the desorption mechanism batch adsorption experiments were conducted by changing the salt concentration of protein-saturated beads in a stirred solution and measuring desorption rates by material balance. Additionally, to gain an insight into the desorption mechanism, CLSM experiments were performed as described in Section 3.2. In this case, the protein-saturated beads were exposed to a salt solution and samples were taken for imaging as described in Section 3.2. We postulated that exposing protein-saturated Nuvia S particles to high salt will result in high diffusional hindrance and, thus, slower desorption than in UNOsphere S.

A2.2. Experimental methods

A2.2.1. Materials

UNOsphere S and Nuvia S were obtained from Bio-Rad Laboratories (Hercules, CA, USA). Both are based on similar crosslinked polyacrylamide copolymers. UNOsphere S has an open macroporous structure and Nuvia S contains proprietary sulfonated polymeric surface extenders. A complete description and characterization of the materials can be found in Chapter 3.

A mAb with pI=8.2 was used for the experiments. This mAb is >99 % monomer as determined by size exclusion chromatography with a Superdex 200 column (GE Healthcare, Piscatway, NJ, USA). All other chemicals were purchased from Fisher Scientific (Pittsburgh, PA, USA). Desorption experiments were done at room temperature, 22±2 °C. Protein solutions were prepared in buffers containing 20 mM $NaCH_3COO$ adjusted to pH 5.0 with acetic acid and

the desorption buffers were 20 mM $NaCH_3COO$ + 100mM, 150 mM, 200 mM, or 300 mM NaCl.

A2.2.2. Methods

A2.2.2.1. Desorption kinetics

Protein desorption rates were measured by placing a known amount of adsorbent in 20 ml of protein solution in a vial and rotating end to end for approximately 6 hours. After reaching equilibrium, the solution was added to a 30 mL stirred batch apparatus described elsewhere [5, 6]. A specific volume of a 20 mM $NaCH_3COO$ + 3 M NaCl at pH 5 buffer was then added to reach a final NaCl concentration of 100 mM, 150 mM, 200 mM or 300 mM specifically. The total amount of protein desorbed at each time step was determined by material balance from the initial and current solution concentrations obtained from the UV absorbance at 280 nm.

A2.2.2.2. CLSM

As described in Section 3.3, confocal laser scanning microscopy (CLSM) was used to image the mAb movement within the resin beads. For this purpose, the mAb was conjugated with Rhodamine Green™-X dye, following the dye supplier instructions. The mAb was incubated in a solution containing the reactive dye with a dye-to-protein molar ratio of 3:1 in a pH 8.5 sodium bicarbonate buffer for 1 hour at room temperature. The unreacted dye was separated by size exclusion chromatography as described in Section 3.2 and the average labeling ratio was calculated by UV/Vis spectrophotometry.

Confocal microscopy was carried out batch-wise using 40% sucrose as a refractive index matching fluid (see Section 3.2). For the desorption experiments the resin samples were initially equilibrated with a mAb solution for 24 hours to obtain complete saturation. After equilibration,

the resin samples were separated from the mAb solution using a filter and added to an excess volume (10 mL) of the corresponding desorption buffer. The same procedure described in Section 3.2 was then followed to take the samples and image the fluorescence intensity profiles from each particles equatorial section.

A2.3. Results and discussion

A2.3.1. Desorption kinetics

The effects of salt concentration on the desorption rate are shown in Fig. A2.2 for UNOsphere S (a) and Nuvia S (b). The experiments were conducted on a stirred-batch apparatus. The plot shows the amount of mAb (mg) desorbed per mL of particle volume at different salt concentrations. The initial mAb loading on the particles was 150 mg/mL and 310 mg/mL for UNOsphere S and Nuvia S, respectively. As seen in Fig. A2.2a, desorption is essentially complete in about 200 s for 150, 200 and 300 mM NaCl, although the rates follow an unexpected trend related to the NaCl concentration. The initial rate of desorption is still fairly rapid for 100 mM NaCl. However, in this case, the rate slows down after the first 200 s. This behavior was explained by Hunter and Carta [7] since under these salt concentration the isotherm is expected to still be favorable. Thus, as the system settles on the new isotherm, the rate of desorption becomes small.

The results for Nuvia S (Fig. A2.2b) are qualitatively similar but quantitatively different from those obtained for UNOsphere S. The desorption rates follow the same trends seen in UNOsphere S, but slower rates were observed. For example at 150 mM NaCl the desorption process took more than 800 s to achieved equilibrium. Since the only difference between the two chromatographic materials is the surface extender polymers we can conclude that they are responsible for the observed behavior. As presented before in our chromatographic experiments
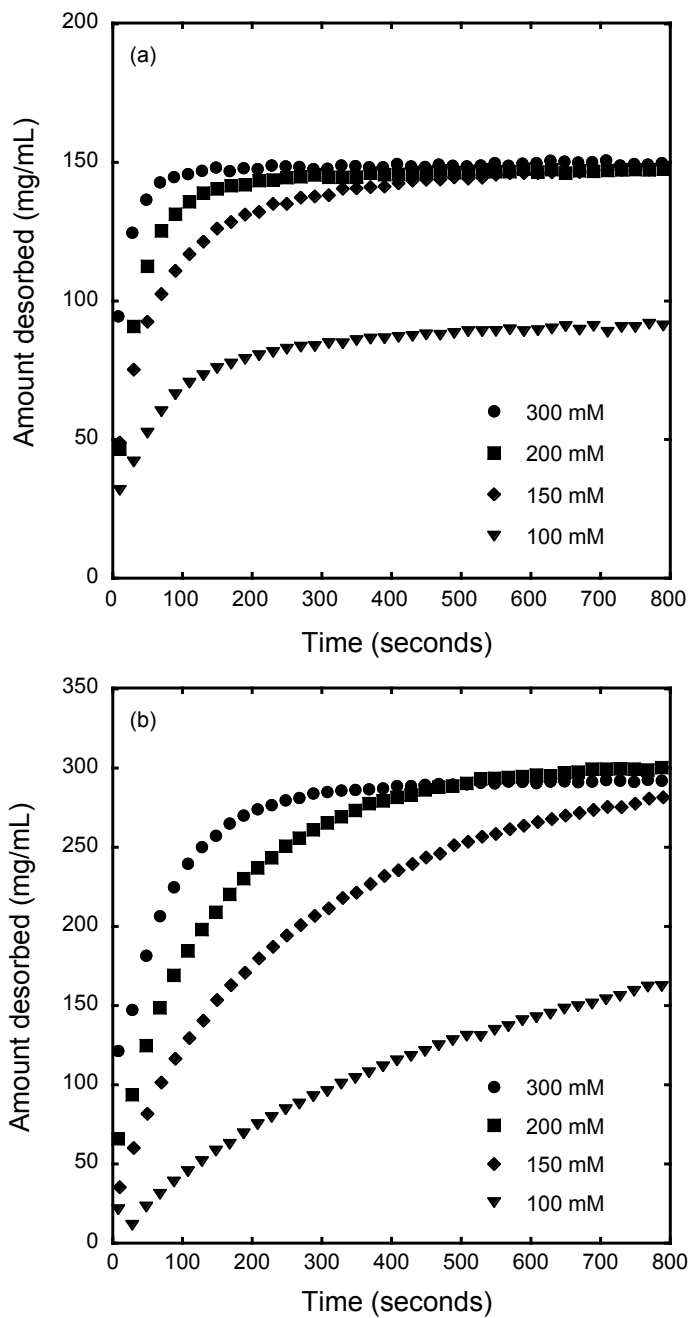
Figure A2.2. UNOsphere S (a) and Nuvia S (b) desorption using the batch uptake system at different salt concentration.

for non-binding conditions (Fig. A2.1) we found that the mAb diffused extremely slowly in Nuvia S resulting in nearly complete exclusion. Also as determined by iSEC in 1 M salt (Section 3.3.1) only glucose, only the 10 kDa (2.4 nm radius) dextran standard and a small fraction of the 40 kDa standard (4.7 nm radius) gained access to the pores. Since the radius of the mAb is comparable to that of the 40 kDa standard, hindrance effects must play an important role during the desorption process. To observe the mAb desorption behavior within the particle CLSM was then performed.

A2.3.2. CLSM

Figures A2.3 and A2.4 show the CLSM results for UNOsphere S for desorption in 300 and 150 mM salt, respectively. The results confirmed what was described in Section A2.3.1. The desorption process occurs very fast. It is very important to point out that the time scales for both the stirred-batch experiments and CLSM results are the same.

Figures A2.5 and A2.6 show the CLSM results for Nuvia S. In Nuvia S, the mAb desorbed from the particle edge accumulates near the particle center as observed before by Bowes et al. for other proteins and resins [4]. Since the interaction between the surface extenders and the protein do not occur under non-binding conditions (Fig. A2.1) the space available for diffusion out of the particle is very small as calculated from iSEC (see Section 3.3.1). Consequently, the mAb desorption process on Nuvia S is hindered by the surface extenders.

Figure A2.7 show a sketch of the mechanism hypothesized for the desorption process in an open pore for UNOsphere S (a-b) and in a pore filled with surface extenders Nuvia S (c-d). When a UNOsphere S particle is completely saturated (Fig. A2.7a) and then exposed to a solution with high NaCl concentration (Fig. A2.7b), salt diffuses quickly in the pores causing the protein to detach from the adsorbent surface and concentrate in the pore fluid. This then provides
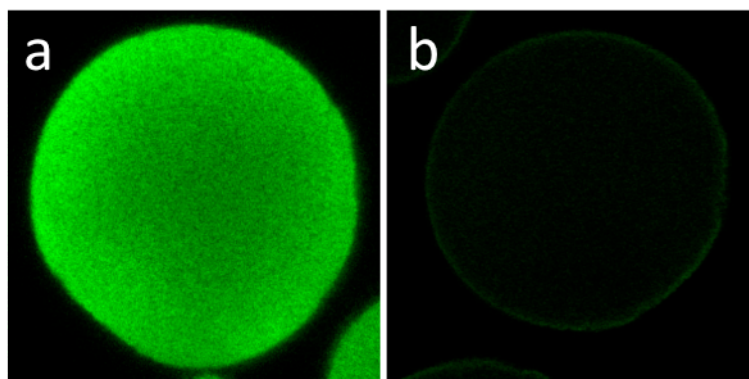
Figure A2.3. UNOsphere S CLSM desorption images for sodium acetate with 300 mM NaCl.

Different particles were observed at different times: (a) 0 s, 76 μm, (b) 40 s, 76 μm.
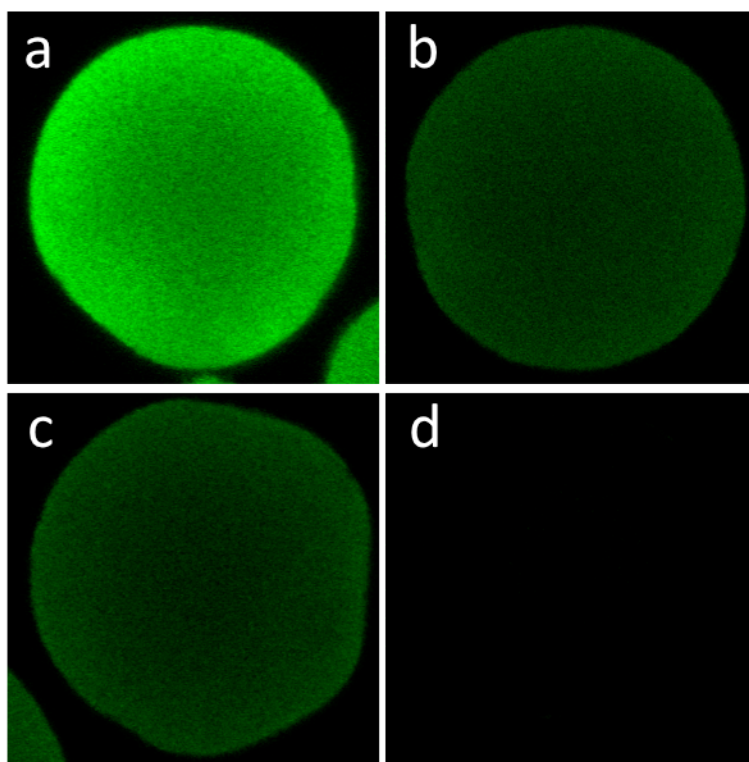
Figure A2.4. UNOsphere S CLSM desorption images for sodium acteate with 150 mM NaCl. (a) 0 s, 76 μm, (b) 30 s, 96 μm, (c) 120 s, 90 μm, (d) 12 min, 88 μm.
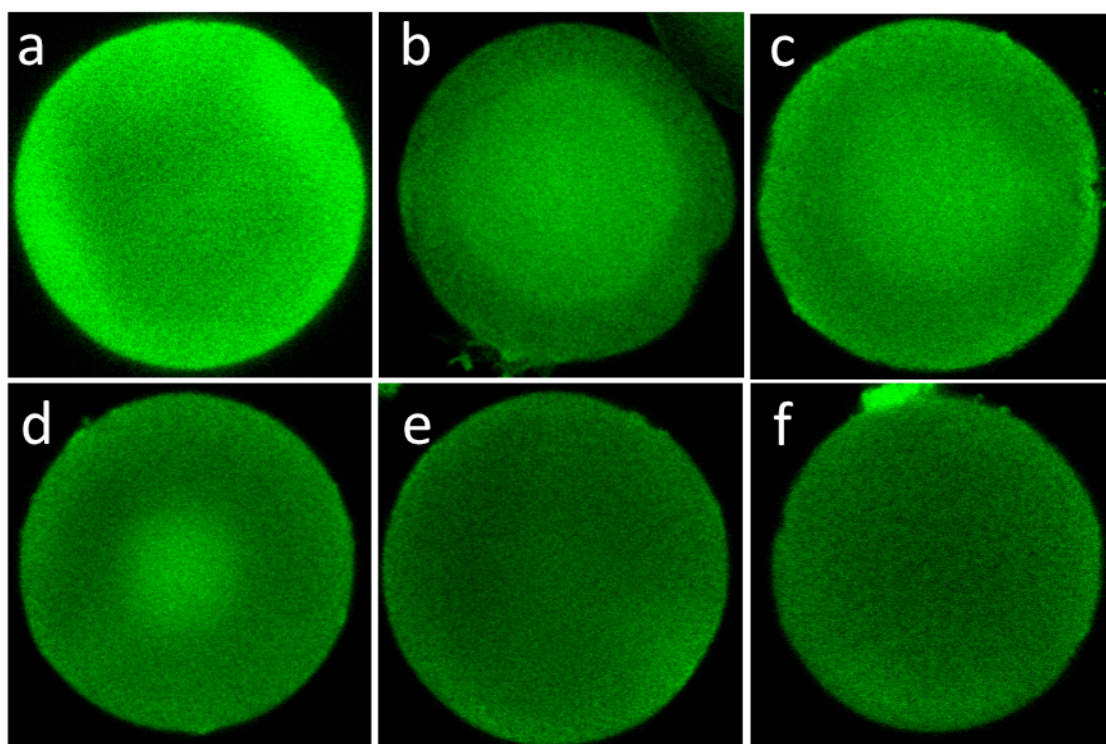
Figure A2.5. Nuvia S CLSM desorption images for sodium acetate with 100 mM NaCl. (a) 0 s, 80 μm, (b) 30 s, 79 μm, (c) 300 s, 85 μm, (d) 500 s, 84 μm, (e) 900 s, 88 μm, (f) 30 min, 81 μm.
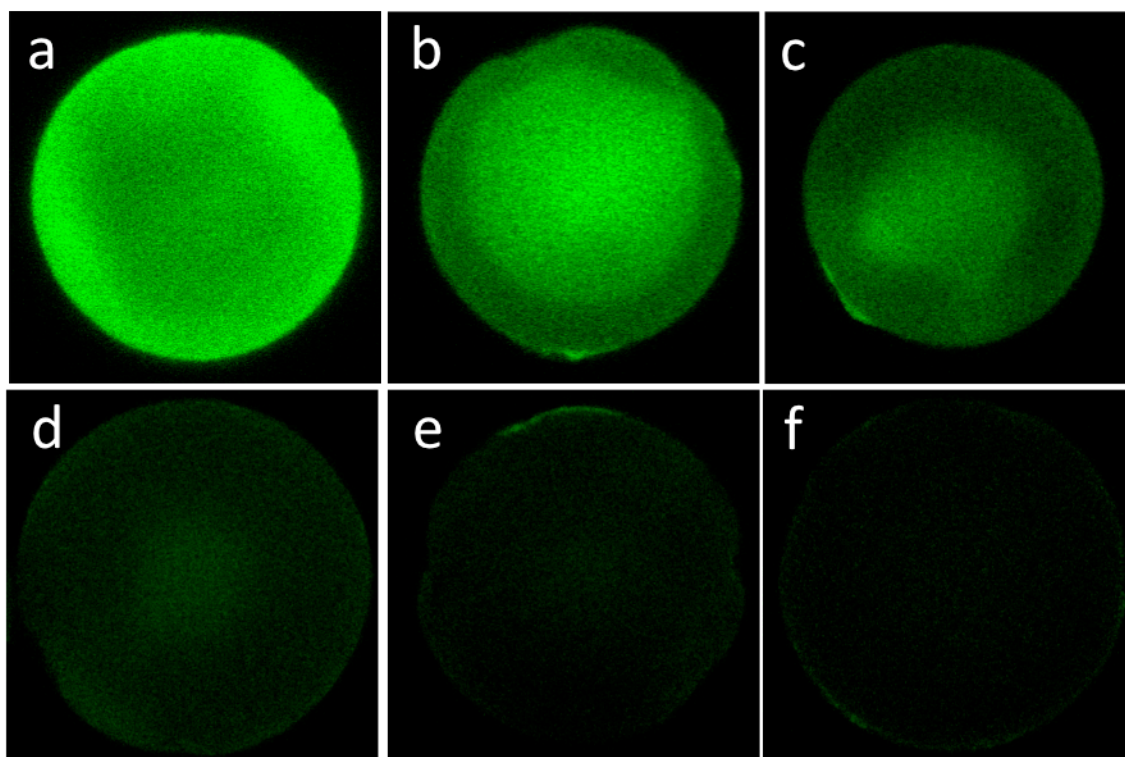
Figure A2.6. Nuvia S CLSM desorption 300 mM NaCl. (a) 0 s, 80 μm, (b) 30 s, 78 μm, (c) 300 s, 75 μm, (d) 500 s, 94 μm, (e) 900 s, 89 μm, (f) 30 min, 86 μm.
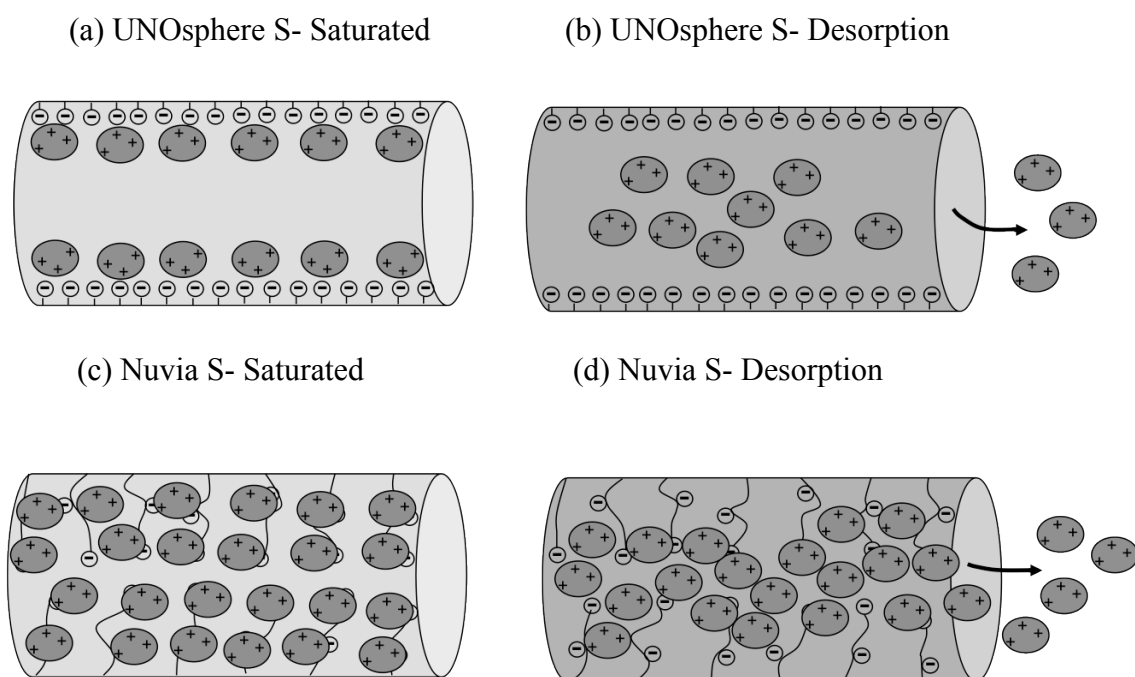
Figure A2.7. Desorption mechanism explanation. (a) UNOsphere S-Saturated, (b) UNOsphere S-Desorption, (c) Nuvia S-Saturated, and (d) Nuvia S- Desorption.

a high diffusional driving force. When partial desorption occurs, as in the case of 100 mM NaCl, only a small fraction of the bound protein will become free to diffuse out.

For the Nuvia S case (Fig. 2.7 c-d), the salt diffuses quickly in the pores of a protein saturated particle causing the protein to detach from the surface extenders; however, since the interaction between the protein and surface extender is absent, the protein needs to diffuse within the smaller space available between the surface extender phase. This will cause a diffusional hindrance effect and desorption will begin at the edge of the particle and eventually reach to its center.

A2.4. Conclusions

UNOsphere S material exhibited very fast desorption kinetics as observed by both Stirred-batch and CLSM results. This behavior is consistent with its macroporous structure. However, Nuvia S desorption kinetics was slower than that observed for UNOsphere S. The cause of the slower observed rates is that little space is available within the beads for unhindered diffusion because of the surface extender phase. CLSM results showed that the desorption process for the mAb occurs from the edge of the particle to its center which is consistent with a hindered diffusional process. From a technical point of view, the different desorption behavior observed on Nuvia S can be exploited for separations where the protein of interest and an impurity vary on size. The mAb desorption information discussed in this appendix provides essential knowledge for the continued development of new chromatographic medias.

A2.5. References

[1]   E.E. Graham, C.F. Fook, AIChE J. 28 (1982) 245.

[2]   H. Tsou, E.E. Graham, AIChE J. 31 (1985) 1959.

[3]   J.R. Conder, B.O. Hayek, Biochem. Eng. J. 6 (2000) 225.

[4]   B.D. Bowes, S.J. Traylor, S.M. Timmick, K.J. Czymmek, A.M. Lenhoff, Chem. Eng. Technol. 35 (2012) 91.

[5]   M.C. Stone, G. Carta, J. Chromatogr. A 1160 (2007) 206.

[6]   G. Carta, A.R. Ubiera, T.M. Pabst, Chem. Eng. Technol. 28 (2005) 1252.

[7]   A.K. Hunter, G. Carta, J. Chromatogr. A 930 (2001) 79.